The Potential of Storing Carbon Dioxide in Construction Materials through Mineralisation: A Mathematical Modelling Study

Liyuan Chen

Lady Margaret Hall

Department of Engineering Science

University of Oxford

Thesis submitted for

Doctor of Philosophy in Engineering Science

2025

Abstract

The rapid increase of anthropogenic carbon dioxide (CO_2) emissions continues to pose a critical challenge to achieving the temperature stabilisation targets of the Paris Agreement. While decarbonisation of energy systems and industrial processes is essential, it alone is insufficient to achieve net zero and negative emissions. Carbon dioxide removal (CDR) technologies are therefore necessary to address the historical CO_2 already present in the atmosphere. Among available CDR options, Direct Air Capture (DAC) offers a uniquely scalable approach as it extracts CO_2 directly from ambient air and is not geographically constrained by point source emissions. However, DAC must be paired with secure, durable and cost-effective storage to deliver meaningful climate benefits. Geological storage is effective but raises challenges in terms of site availability, transport infrastructure and public acceptance. The utilisation of CO_2 in construction materials such as cement, concrete, recycled concrete aggregates (RCA) and steel slag provides an alternative pathway that enables long term mineralisation of CO_2, simultaneously valorising industrial by products and promoting a circular economy.

Project 1 consolidates existing global knowledge through a comprehensive meta-analysis of 548 datasets concerning the CO_2 curing of cement and concrete, from 35 studies to enable cross-comparison. The analysis quantitatively identifies the most influential process parameters governing carbon dioxide uptake, with water-to-cement ratio, pre-curing duration, partial pressure, and exposure time identified as

the dominant variables. A machine-learning-based ensemble regression model, which combines Random Forest, Gradient Boosting, Support Vector Regression, and Ridge Regression, achieves high predictive accuracy (R^2 = 0.81), thereby providing a reliable tool for forecasting carbon dioxide uptake under diverse curing conditions. The results establish a quantitative foundation for the optimisation of curing protocols, achieving a predicted carbon dioxide uptake capability in the range of approximately 5-30%. Overall, this project clarifies the variability observed across previous experimental studies, provides a data-driven framework for the optimisation of carbon utilisation in cementitious materials, and establishes a predictive model capable of reliably estimating carbon dioxide uptake performance.

Project 2 evaluates the carbon removal performance of combining DAC with the carbonation of RCA. A process model was developed to examine the effects of key operational parameters on carbonation behaviour and energy use, and this was integrated with a life cycle assessment to determine the overall climate impact under realistic operating conditions. Two representative scenarios were considered: using high-purity CO_2 supplied from an external DAC system, and onsite carbonation with a low-purity CO_2 concentration. The results show that for one tonne of 90% carbonated RCA, the net outcome ranges from a removal of approximately 13 kg CO_2 to a net emission of about 14 kg CO_2, depending on the DAC technology, transport distance, and electricity carbon intensity. When low-purity CO_2 at around 1% concentration is used onsite, the overall carbon removal increases by approximately 70% compared with the use of pure CO_2. Overall, the life cycle assessment confirms that DAC–RCA

carbonation can achieve verifiable net CO_2 removal under low-carbon electricity and optimised logistics, providing a quantitative basis for evaluating carbon removal performance in built-environment applications.

Project 3 examines the comparative performance of steel slag carbonation as a carbon removal pathway, focusing on gas–solid and indirect aqueous routes. A process model and life cycle assessment were combined to quantify carbon dioxide uptake, energy demand, and net removal potential under consistent assumptions. The gas–solid route achieved faster reaction rates at elevated temperature and finer particle size, whereas the indirect route exhibited lower reactivity but reduced energy intensity. The life cycle results show that indirect carbonation performs better when the electricity carbon intensity is below 0.192 kg CO_2 per kWh, while gas–solid carbonation is more favourable in higher-intensity grids. Global scenario analysis across 37 countries indicates that approximately 81% can achieve net-negative outcomes, with carbon uptake ranging from about 0.07 to 0.30 kg CO_2 per kg slag depending on process conditions. Overall, the project demonstrates that steel slag carbonation is technically viable and can deliver meaningful net CO_2 removal when deployed within low-carbon energy systems.

Overall, these studies establish a systematic and quantitative framework for evaluating DACU-enabled CO_2 storage in construction materials. They contribute to scientific understanding by harmonising experimental data, building predictive and process models, and integrating techno-environmental assessment with global deployment scenarios. The findings provide actionable insights for researchers,

industry stakeholders, and policymakers seeking to design and implement carbon removal strategies that are technically robust, environmentally effective, and economically viable.

Acknowledgements

I am profoundly grateful to my supervisor, Professor Aidong Yang, who is the most outstanding mentor I have ever met. His professionalism, patience, efficiency and warmth have shaped my PhD in countless ways. My passion for academic research has, to a large extent, been inspired and sustained by his guidance. If I one day choose to pursue an academic career, it will be largely because he has set such an exemplary model of what it means to be both a scholar and a supervisor. I can only aspire to follow in his footsteps and to emulate the qualities that make him such an exceptional academic and mentor.

My sincere appreciation goes to my fellow group members and friends, including Yukun Zhang, Jiaying Pan, Sizhe Qiu, Jinyuan Zhang, Guokun Liu, Huiying Zhang, Dorcas Tuitoek, William Leonard, Alli Devlin, Nadja Yang, Xuesong Lu, Zi Huang, Franco Williams and Till Weidner. Their companionship, encouragement and the many discussions we shared have greatly enriched my PhD, both academically and personally.

I would like to thank my college advisor, Professor Xiaowen Dong, for his guidance and support during my doctoral studies. I am also grateful to the Lady Margaret Hall Academic Development Fund and the Rhodes Scholar Grants, whose financial support enabled me to attend academic conferences during my PhD.

Finally, I am deeply grateful to my parents, Mr. Hui Chen and Mrs. Yuchun Gao, for their unconditional love and unwavering support throughout my life. I am also

indebted to my best friend, Zijie Wang and Lyvying Lan, whose constant support and encouragement have meant so much to me. I hope that this work will make them proud. It is my sincere wish to be a source of pride for them, just as they have always been for me.

Completed my doctoral thesis at the age of 29, this milestone represents not only academic achievement but also deeply personal fulfilment. I am also grateful for the four years I have spent in the United Kingdom, which allowed me to experience a different world and broaden my horizons in ways that will stay with me for the rest of my life. Lastly, I would like to thank myself for being strong, diligent and persistent, for choosing the University of Oxford and for taking the courageous step of pursuing a doctoral degree. It has not been an easy path, but I am grateful that I had the determination to take this step and to persevere until today.

DOMINUS ILLUMINATIO MEA

Abbreviations

Abbreviation	Full Term
ACC	Accelerated Carbonation Curing
AODS	Argon Oxygen Decarburisation Slag
BFS	Blast Furnace Slag
BOFS	Basic Oxygen Furnace Slag
BPM	Bipolar Membrane
BPMED	Bipolar Membrane Electrodialysis
BSSF	Basic Slag Steelmaking Furnace
CCS	Carbon Capture and Storage
CCUS	Carbon Capture, Utilisation and Storage
CDR	Carbon Dioxide Removal
CDW	Construction and Demolition Waste
CF	Carbon Fibre
CLT	Cross-Laminated Timber
CMS	Carbon Management Strategy
DAC	Direct Air Capture
DACU	Direct Air Capture and Utilisation
DRI	Direct Reduced Iron
EAFS	Electric Arc Furnace Slag
GHG	Greenhouse Gas
HPC	High-Performance Concrete
LCA	Life Cycle Assessment
LFS	Ladle Furnace Slag

LOI	Loss on Ignition
LTH	Low-Temperature Hydrothermal
LVL	Laminated Veneer Lumber
ML	Machine Learning
MSE	Mean Squared Error
OC	Organic Carbon
OPC	Ordinary Portland Cement
PCC	Portland Cement Concrete
RA	Recycled Aggregate
RC	Reinforced Concrete
RCA	Recycled Concrete Aggregate
RH	Relative Humidity
SCM	Supplementary Cementitious Material
SSS	Stainless Steel Slag
SVR	Support Vector Regression
VODS	Vacuum Oxygen Decarburisation Slag

List of Figures and Tables

Table of Contents

Chapter 1 Introduction and Intended Contribution

1.1 Background

CO_2 emissions continuously rise due to the increase in global energy demand, reaching 37.4 Gt CO_2 in 2023 (IEA, 2024). To keep the global temperature at or below 1.5 °C, rapid and far-reaching transitions for CO_2 emissions reductions in energy, infrastructure (including transport and buildings), industrial systems, land, and urban areas are necessary. Different mitigation measures can be used, such as lowering energy and resource carbon emission intensity, the rate of decarbonisation, and atmospheric carbon dioxide removal (CDR). For the high-emissions sector, clean energy and decarbonisation are more efficient. Renewable energy, nuclear energy and fossil fuels with carbon dioxide capture and storage (CCS) in electricity generation can reduce energy systems' emissions. In industry, such reductions can be achieved by combining new and existing technologies and practices, including electrification, hydrogen, sustainable bio-based feedstocks, product substitution, and carbon capture, utilisation, and storage (CCUS). Although these measures could achieve most CO_2 emission reduction missions, they can't remove the anthropogenic CO_2 or achieve net-zero and negative emissions. At this point, the advantages of CDR become increasingly apparent.

As the crisis of climate change deepens, carbon dioxide Removal (CDR) from the atmosphere has been considered necessary to complement emissions reduction to keep the concentration of greenhouse gases under the budget level by the end of the

21st century (Qiu et al., 2022). The recently published State of Carbon Dioxide Removal report (Smith et al., 2023) estimates that a significant CDR requirement between 420 and 1,100 Gt CO_2 by 2100 is needed for the IPCC's 1.5°C scenarios. Among CDR options, direct air capture (DAC) removes CO_2 from the air through industrial processes, often resulting in a high-purity CO_2 gas product (Qiu et al., 2022). In recent years, remarkable advances have been made in DAC technologies, with adsorption- based and solvent-based options reaching high Technology Readiness Levels (8-9) while other processes such as electrochemical and other hybrid options are being further developed (Bisotti et al., 2024). Compared with carbon capture from point sources, DAC has higher energy requirements and costs due to the unique difficulty of separating CO_2 from air at a very low concentration (currently ~420 ppm) (Darton et al., 2020). However, this economical advantage is limited to industrial sources (i.e. power plant pollutants), the fact that DAC extracts CO_2 directly from the surrounding air means fewer limits on scaling and greater siting flexibility (Sodiq et al., 2023). Despite these advantages, DAC remains highly energy intensive. The total energy requirement typically ranges between 5 and 9 GJ per tonne CO_2, dominated by air-handling and sorbent regeneration processes. When integrated with utilisation pathways such as mineral carbonation, additional energy is required for CO_2 compression, transport and reaction. Consequently, the overall carbon removal efficiency depends strongly on the carbon intensity of the energy supply (Fasihi et al., 2019; Keith et al., 2018). This energy demand represents a key constraint on the large-scale deployment of DACU

and underpins the need for developing low-energy configurations in regions with decarbonised power systems (P. Wang et al., 2024).

Like carbon capture from point sources, DAC also requires long-term secure CO_2 storage. When geological storage is considered, the challenges include transportation pipelines, geological appraisal and preparation and, in some countries, regional availability of suitable storage sites (Budinis et al., 2018). As an alternative to geological storage, captured CO_2 can be stored in materials through the route of utilisation, ideally for a time period relevant to climate change mitigation, i.e., from multiple decades to 100s years (Hepburn et al., 2019). Materials that naturally align with such timescales are those used in the construction of buildings and infrastructures. Focusing on construction materials, concrete is the world's most widely used construction material, with an annual production of close to 30 billion tonnes (Provis et al., 2017). The worldwide demand for concrete is expected to grow further in the coming decades, especially in developing countries. An acute challenge facing the production of a key component of concrete, namely cement, is its high CO_2 emissions, which have attracted great attention as a significant target for industrial decarbonization (Habert et al., 2020). At the same time, CO_2 removal and storage in cement or concrete could be a positive pathway for offsetting emissions.

One of the options for storing CO_2 in cement is called CO_2 curing, a process that accelerates the carbonation reaction for absorbing more CO_2 quickly. Hepburn's research shows that its likelihood of release is low, which means it's a stable way to store CO_2 (Hepburn et al., 2019). Two opposite views are shown. (Cao et al., 2020)

suggests that cement plays a dual role including massive production emissions and carbonation absorption in the global carbon cycle like a sponge effect. Cementitious materials (mainly concrete) production is divided into four parts: Raw material Supply, Production & Construction, Use, and End-of-life according to the life cycle. CO_2 curing occurs in the use stage, when has a carbon emission reduction trend (Arehart et al., 2021). However, Ravikumar suggested that CO_2 curing or mixing might not produce a net climate benefit if one considers the capture, transport, utilisation, and uncertainty production processes (Ravikumar et al., 2021).

Another option for storing CO_2 in concrete is the carbonation of recycled concrete aggregate (RCA), a recycled material as part of non-hazardous construction and demolition wastes (CDW), usually concrete debris. The use of CDW-derived RCA to replace natural coarse aggregates in construction has been shown to significantly reduce the use of non-renewable energy and greenhouse gas emissions (Hossain et al., 2016). In 2021, CDW generation was around 2,600 Mt in China (Joseph et al., 2023), 500 ~600 Mt in both the US and India, and 100~200 Mt in several Europe countries (Wang et al., 2021). Despite disposal options with lower environmental impacts exist (Danish & Mosaberpanah, 2022), landfill remains a significant destination of CDW. The landfill proportion of CDW in India, China, US and Europe countries are currently at 99%, 75%, 25% and 10%, respectively (Chen et al., 2022); the concrete fractions of these unutilised materials thus represent considerable supply potential of RCA worldwide. Both pathways of CO_2 uptake in concrete are governed by well-established carbonation mechanisms. In conventional concrete, carbonation occurs as CO_2

diffuses through the pore structure, dissolves in pore water, and reacts with alkaline hydration products such as portlandite and calcium silicate hydrates (C–S–H) to form stable calcium carbonate ($CaCO_3$) and silica gel (Papadakis et al., 1991; Thiery et al., 2013). The overall process involves gas diffusion, dissolution, ionic reactions, and precipitation, which progressively densify the microstructure. In accelerated carbonation curing systems, the same reactions are enhanced under controlled temperature, humidity, and elevated CO_2 concentration, allowing rapid uptake within hours (Monkman & Shao, 2010). For RCA, residual mortar adhering to the aggregate surface contains portlandite and partially hydrated C–S–H that react through identical pathways, leading to the formation of carbonate phases that improve aggregate stability and contribute to permanent CO_2 storage (Kaddah et al., 2022; Liang et al., 2020).

Through the carbonation process, RCA can sequestrate CO_2, and the carbonated RCA can potentially be used for producing new concrete after mixing it with cement (Shuvo et al., 2024). It has been experimentally shown that the properties of recycled aggregate from ordinary concrete (OC) and high-performance concrete (HPC) could be improved by carbonation (Sereng et al., 2021); the improvement of RCA properties is affected by carbonation conditions such as RCA particle size, duration, and moisture contents (Zhan et al., 2014). Numerous RCA carbonation studies have recently been reported in literature. For example, the impacts of key factors on the degree of carbonation have been studied, including particle size (Leemann et al., 2023; Liu et al., 2021), CO_2 partial pressure (Ding et al., 2023; Xuan et al., 2017), duration (Li et al.,

2023; Pu et al., 2022), and RCA water/cement (w/c) ratio (Li et al., 2019; Tam et al., 2020). Across these studies, CO_2 uptake in the range between 10-21 kg/kg (dry) RCA has been reported. To predict the degree of carbonation, research has developed mechanistic and empirical models based on experimental observations. Mechanistic models formulate the coupled processes of CO_2 transport and reaction using reaction-diffusion frameworks that link Fickian diffusion, dissolution equilibria and carbonate precipitation (Ke et al., 2020; Thiery et al., 2013). For particulate systems such as RCA, diffusion-controlled and shrinking-core formulations are often used to describe the advance of the carbonated layer and its dependence on particle size and porosity. Empirical models calibrated to laboratory data relate carbonation depth or CO_2 uptake to parameters such as water–cement ratio, CO_2 concentration and exposure time (Xi et al., 2016; Pu et al., 2022; Li et al., 2023). Empirical models calibrated to laboratory data relate carbonation depth or CO_2 uptake to parameters such as water–cement ratio, CO_2 concentration and exposure time (Ding et al., 2023; Xuan et al., 2017; Liu et al., 2021).

With respect to environmental performance, life cycle assessments of CO_2-carbonated RCA consistently report reductions in global warming potential and primary energy demand relative to natural or untreated recycled aggregates, alongside lower natural aggregate depletion and the avoidance of landfill-related emissions when demolition waste is diverted to carbonation and reuse. The magnitude of the benefit is sensitive to electricity carbon intensity, CO_2 supply and transport, and site logistics, which

together govern whether net-removal outcomes are achieved in practice (e.g., Xiao et al., 2022).

Finally, another valuable waste that can play a role in storing CO_2 in concrete is steel slag from steel production. In 2023, global pig iron and raw steel production reached approximately 1,300 and 1,900 Mt, respectively, with over 75% of this output coming from six countries: China, India, Japan, Russia, the United States, and South Korea (Geological Survey, 2024). Most iron and steel are produced through two primary routes: the Blast Furnace-Basic Oxygen Furnace (BF-BOF) route and the Electric Arc Furnace (EAF) route. In the BF-BOF process, blast furnaces produce iron from iron ore, which is then converted into steel in a basic oxygen furnace, with some scrap metal added. These two steps generate byproducts known as blast furnace slag (BFS) and basic oxygen furnace slag (BOFS), respectively. In contrast, EAF produce steel primarily from recycled scrap metal, with electric arc furnace slag (EAFS) as a byproduct.

Steel slag, including both BOFS and EAFS, is produced at an estimated rate of 100-150 kg per tonne of raw steel. Approximately 72% of raw steel production is through the BOF process, while 28% is produced via EAF. In 2023, BFS production was estimated at 330-390 Mt, while steel slag production, including BOFS and EAFS, was estimated to range from 190 Mt to 290 Mt. For every tonne of pig iron produced, 250-300 kg of BFS is generated (Liu et al., 2021). Japan leads the world in steel slag utilisation with an impressive rate of 98.4%. The United States and Europe show similar rates, with the U.S. utilising 85.4% of its steel slag and Europe developed countries at 85.6%. In contrast, China, despite producing around 50% of the world's steel, utilises only 29.5%

of its steel slag, leaving a large portion unutilised. India lags even further behind, utilising just 15% to 20%, resulting in significant quantities being dumped and occupying land (Tiwari et al., 2016).

In future, steel slag's ability to store CO_2 is regarded as one of its most promising applications because its components readily react with CO_2 to form stable carbonates (Zhang et al., 2023). This carbonation process not only helps reduce atmospheric CO_2, addressing climate change concerns, but also enhances the slag's physical properties, making it more suitable for use in construction materials like cement and concrete. Additionally, utilising steel slag for CO_2 absorption provides an efficient way to recycle industrial waste, transforming a by-product of steel production into a valuable resource for carbon capture and storage. As global efforts to lower carbon emissions intensify, steel slag offers a cost-effective and sustainable solution for large-scale CO_2 sequestration.

The products of carbonated steel slag have numerous valuable applications, including construction materials, road infrastructure, and environmental remediation. Compared to untreated slag, carbonated steel slag shows enhanced performance, making it suitable for producing a range of green building materials, such as aggregates, cementitious materials, bricks, artificial coral, and self-healing concrete (Li & Wu, 2022) .Additionally, carbonated slag exhibits higher hydration activity, making it a more effective cement replacement (Chen et al., 2021). One particularly promising application is the use of carbonated steel slag as aggregates in concrete, especially for road construction. Due to the coarser particle size from agglomeration, it serves well

as coarse aggregate. Furthermore, combining carbonation with alkali activation has been shown to significantly improve the compressive strength of bricks (Wang et al., 2024), highlighting the value of carbonated steel slag in construction.

While significant progress has been made in carbon capture technologies and the understanding of potential use of construction materials for CO_2 storage, challenges remain in scaling these processes to meet the ambitious climate goals of the 21st century. The integration of DACU technology, though promising for net-negative emissions, must be carefully assessed within the broader industrial framework, particularly regarding energy consumption, material efficiency, and long-term CO_2 sequestration stability. Addressing these challenges will be crucial to transforming the construction industry into a key contributor to global carbon removal efforts.

1.2 Motivation and Objectives

This DPhil project investigates the feasibility of DACU in the construction industry, with a particular focus on CO_2 storage in cement, RCA, and steel slag. Unlike conventional decarbonisation technologies, DACU offers the potential to achieve net-negative emissions by removing CO_2 directly from ambient air. However, its large-scale implementation faces substantial challenges, including the energy intensity of DAC processes, the logistics of CO_2 transportation, and the energy requirements of carbonation chambers. Cement and concrete are prioritised because they represent the largest industrial sources of CO_2 emissions and possess inherent mineralogical capacity for permanent CO_2 binding through carbonation. RCA are also of growing

importance, offering a circular route to utilise construction and demolition waste while providing additional CO_2 storage potential. Steel slag, a by-product of iron and steel manufacturing, contains reactive oxides that make it particularly suitable for mineral carbonation. This research therefore aims to holistically assess the technical and environmental viability of DACU as a scalable carbon removal pathway, with an emphasis on integration into construction supply chains.

More specifically, this DPhil study comprises three individual research projects, and their objectives are enumerated as follows:

1. **Project 1** addresses cement and concrete carbonation by leveraging a comprehensive meta-analysis of CO_2 curing experiments. 548 data points from over 35 laboratories worldwide were compiled, but these datasets vary widely in experimental setups, measurement protocols, and reporting standards, resulting in uneven sample distribution and conflicting findings. To overcome these limitations, this project applies advanced data analytics and machine learning regression to identify the most influential parameters, quantify their relative importance, and provide evidence-based recommendations for optimising CO_2 curing protocols in future experiments and industrial applications.
2. **Project 2** investigates the potential of RCA carbonation as a CO_2 sink for DAC-derived emissions. Although RCA carbonation has been studied in various contexts, its integration with DAC to deliver net-negative emissions has not been comprehensively assessed. This project develops a representative process model of RCA carbonation to simulate CO_2 uptake under realistic operating conditions.

Based on these results, a life cycle assessment is conducted under multiple scenarios to evaluate net CO_2 removal potential, accounting for DAC energy demand, CO_2 transport modes, and electricity carbon intensity. The findings provide critical insights into the conditions under which DAC–RCA carbonation systems can achieve significant climate benefits.

3. **Project 3** investigates the carbonation of steel slag. While several steel slag carbonation technologies have been proposed, a systematic comparison under consistent process and material conditions is lacking. This project develops validated kinetic models for gas–solid and indirect carbonation routes, followed by a comparative LCA to quantify energy requirements, carbon footprints, and process efficiencies. A global scenario analysis further evaluates the regional feasibility of large-scale steel slag carbonation, particularly in countries with substantial slag stockpiles (e.g., China, India, Brazil), thereby informing policy and investment decisions for future deployment.

Collectively, these projects aim to provide a robust, quantitative basis for integrating DACU with construction material carbonation, enabling the construction sector to become an active contributor to global net-negative emission targets.

1.3 Thesis Structure

This thesis is presented in the integrated format, including a combination of conventional chapters and journal paper-based chapters. It consists of six chapters in total, including the introduction (Chapter 1), literature review (Chapter 2), three

research chapters (Chapters 3–5), and conclusions (Chapter 6). Each research chapter is based on a peer-reviewed journal paper or a manuscript under review. For consistency, the original sections, figures, tables, and equations in the published papers/manuscripts have been re-numbered in this thesis. The contents of 6 chapters are outlined as follows:

1. Chapter 1 introduces the global context of climate change mitigation, highlights the potential of construction materials as a durable CO_2 sink, and states the aims and intended contributions of this DPhil research.
2. Chapter 2 provides a critical review of the literature on DACU technologies, with a particular focus on their integration with construction materials such as cement and concrete, recycled concrete aggregates, and steel slag. It synthesises empirical evidence on CO_2 uptake, evaluates the theoretical sequestration capacity of these materials, and estimates their global-scale potential. The chapter also identifies major uncertainties and research gaps related to process optimisation, techno-economic feasibility, and life-cycle impacts, which motivate the modelling and assessments undertaken in the subsequent research chapters.
3. Chapter 3 presents a meta-analysis of 548 experimental datasets from 35 published studies on CO_2 curing studies of cement and concrete. Advanced data analytics and machine-learning regression are applied to identify the most influential parameters, quantify their effects, and provide predictive capability for CO_2 uptake under varied curing conditions. The results yield critical insights for experimental design and process optimisation.

4. Chapter 4 develops a mathematical model of industrial-scale RCA carbonation and couples it with life-cycle assessment under multiple scenarios. The chapter evaluates the net CO_2 removal potential of DAC–RCA carbonation systems, quantifies the impacts of CO_2 purity, transport mode, and electricity carbon intensity, and identifies the conditions under which this pathway can achieve significant climate benefits.
5. Chapter 5 compares gas-solid and indirect carbonation of steel slag through validated kinetic modelling and life-cycle assessment. The chapter quantifies energy demand, carbon footprints, and process efficiencies under consistent conditions and performs a global scenario analysis to determine regional feasibility in countries with large slag stockpiles.
6. Chapter 6 summarises the key findings of the three research projects, synthesises their contributions to the field of DACU-enabled CO_2 storage in construction materials, and discusses limitations and future research directions to facilitate large-scale implementation.

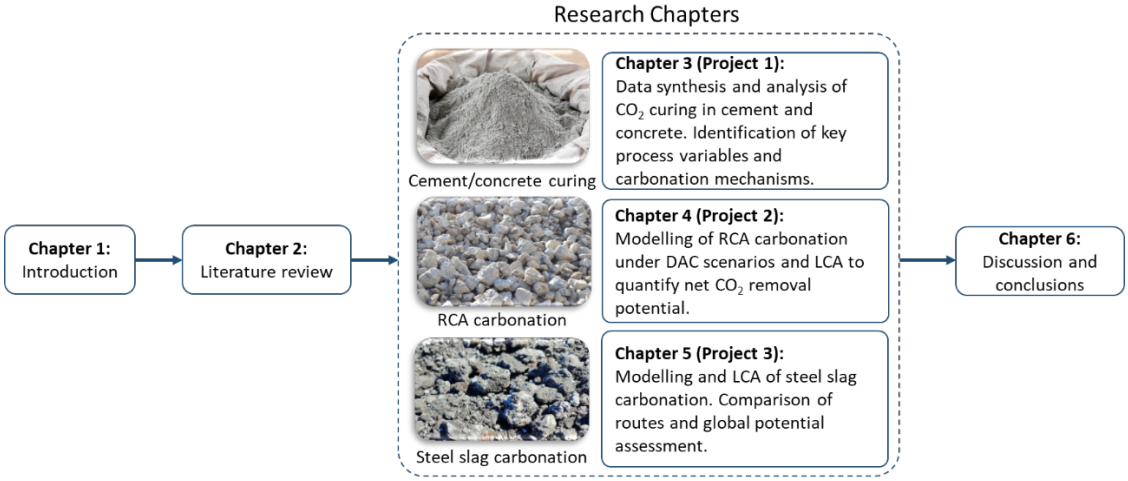

Figure 1-1 Structure of this thesis

The relationships among the three research projects are graphically illustrated in **Figure 1-1**. Project 1 conducts an extensive quantitative analysis of published CO_2 curing experiments on cement and concrete, employing statistical and machine learning methods to identify the dominant variables, quantify their interactions, and elucidate process mechanisms and practicable operating regimes. The evidence on parameter effects and feasible curing conditions informs the subsequent modelling work. Project 2 applies these insights to recycled concrete aggregate, for which experimental evidence is comparatively limited, by developing an industrially relevant carbonation model and undertaking a life cycle assessment to evaluate net CO_2 removal when integrated with DAC. Project 3 develops the modelling and assessment framework further by examining steel slag carbonation technologies in greater detail, comparing alternative carbonation routes, and assessing global deployment potential on the basis of material stock and energy system characteristics. Taken together, the three projects constitute a coherent research programme that progresses from data analysis to process modelling and system level evaluation, and ultimately to a global appraisal of the potential for DACU-enabled CO_2 storage in construction materials.

References

Arehart, J. H., Hart, J., Pomponi, F., & D'Amico, B. (2021). Carbon sequestration and storage in the built environment. *Sustainable Production and Consumption*, *27*, 1047–1063. https://doi.org/10.1016/j.spc.2021.02.028

Bisotti, F., Hoff, K. A., Mathisen, A., & Hovland, J. (2024). Direct Air capture (DAC) deployment: A review of the industrial deployment. *Chemical Engineering Science*, *283*, 119416. https://doi.org/10.1016/j.ces.2023.119416

Budinis, S., Krevor, S., Dowell, N. Mac, Brandon, N., & Hawkes, A. (2018). An assessment of CCS costs, barriers and potential. *Energy Strategy Reviews*, *22*, 61–81. https://doi.org/10.1016/j.esr.2018.08.003

Cao, Z., Myers, R. J., Lupton, R. C., Duan, H., Sacchi, R., Zhou, N., Reed Miller, T., Cullen, J. M., Ge, Q., & Liu, G. (2020). The sponge effect and carbon emission mitigation potentials of the global cement cycle. *Nature Communications*, *11*(1), 3777. https://doi.org/10.1038/s41467-020-17583-w

Chen, Z., Feng, Q., Yue, R., Chen, Z., Moselhi, O., Soliman, A., Hammad, A., & An, C. (2022). Construction, renovation, and demolition waste in landfill: a review of waste characteristics, environmental impacts, and mitigation measures. *Environmental Science and Pollution Research*, *29*(31), 46509–46526. https://doi.org/10.1007/s11356-022-20479-5

Chen, Z., Li, R., Zheng, X., & Liu, J. (2021). Carbon sequestration of steel slag and carbonation for activating RO phase. *Cement and Concrete Research*, *139*, 106271. https://doi.org/10.1016/J.CEMCONRES.2020.106271

Danish, A., & Mosaberpanah, M. A. (2022). A review on recycled concrete aggregates (RCA) characteristics to promote RCA utilization in developing sustainable recycled aggregate concrete (RAC). *European Journal of Environmental and Civil Engineering*, *26*(13), 6505–6539. https://doi.org/10.1080/19648189.2021.1946721

Ding, Y., Wu, J., Zhang, X., Xu, P., Ning, W., & Li, Y. (2023). Quality Improvement of Recycled Concrete Aggregate by Accelerated Carbonation under Different Pressure. *Journal Wuhan University of Technology, Materials Science Edition*, *38*(3), 623–631. https://doi.org/10.1007/s11595-023-2738-9

Fasihi, M., Efimova, O., & Breyer, C. (2019). Techno-economic assessment of CO2 direct air capture plants. *Journal of Cleaner Production*, *224*, 957–980. https://doi.org/10.1016/j.jclepro.2019.03.086

Geological Survey, U. (2024). *MINERAL COMMODITY SUMMARIES 2024*.

Habert, G., Miller, S. A., John, V. M., Provis, J. L., Favier, A., Horvath, A., & Scrivener, K. L. (2020). Environmental impacts and decarbonization strategies in the cement and concrete industries. *Nature Reviews Earth & Environment*, *1*(11), 559–573. https://doi.org/10.1038/s43017-020-0093-3

Hepburn, C., Adlen, E., Beddington, J., Carter, E. A., Fuss, S., Mac Dowell, N., Minx, J. C., Smith, P., & Williams, C. K. (2019). The technological and economic prospects for CO2 utilization and removal. *Nature*, *575*(7781), 87–97. https://doi.org/10.1038/s41586-019-1681-6

Hossain, Md. U., Poon, C. S., Lo, I. M. C., & Cheng, J. C. P. (2016). Comparative environmental evaluation of aggregate production from recycled waste materials and virgin sources by LCA. *Resources, Conservation and Recycling*, *109*, 67–77. https://doi.org/10.1016/j.resconrec.2016.02.009

IEA. (2024). *CO2 Emissions in 2023*.

Joseph, H. S., Pachiappan, T., Avudaiappan, S., Maureira-Carsalade, N., Roco-Videla, Á., Guindos, P., & Parra, P. F. (2023). A Comprehensive Review on Recycling of Construction Demolition Waste in Concrete. *Sustainability*, *15*(6), 4932. https://doi.org/10.3390/su15064932

Kaddah, F., Ranaivomanana, H., Amiri, O., & Rozière, E. (2022). Accelerated carbonation of recycled concrete aggregates: Investigation on the microstructure

and transport properties at cement paste and mortar scales. *Journal of CO2 Utilization*, *57*, 101885. https://doi.org/10.1016/j.jcou.2022.101885

Ke, X., Bernal, S. A., Provis, J. L., & Lothenbach, B. (2020). Thermodynamic modelling of phase evolution in alkali-activated slag cements exposed to carbon dioxide. *Cement and Concrete Research*, *136*, 106158. https://doi.org/10.1016/J.CEMCONRES.2020.106158

Keith, D. W., Holmes, G., St. Angelo, D., & Heidel, K. (2018). A Process for Capturing CO2 from the Atmosphere. *Joule*, *2*(8), 1573–1594. https://doi.org/10.1016/j.joule.2018.05.006

Leemann, A., Winnefeld, F., Münch, B., & Tiefenthaler, J. (2023). Accelerated carbonation of recycled concrete aggregates and its implications for the production of recycling concrete. *Journal of Building Engineering*, *79*, 107779. https://doi.org/10.1016/j.jobe.2023.107779

Li, L., & Wu, M. (2022). An overview of utilizing CO2 for accelerated carbonation treatment in the concrete industry. *Journal of CO2 Utilization*, *60*, 102000. https://doi.org/10.1016/j.jcou.2022.102000

Li, L., Ziyabek, N., Jiang, Y., Xiao, J., & Poon, C. S. (2023). Effect of carbonation duration on properties of recycled aggregate concrete. *Case Studies in Construction Materials*, *19*, e02640. https://doi.org/10.1016/j.cscm.2023.e02640

Li, Y., Zhang, S., Wang, R., Zhao, Y., & Men, C. (2019). Effects of carbonation treatment on the crushing characteristics of recycled coarse aggregates. *Construction and Building Materials*, *201*, 408–420. https://doi.org/10.1016/j.conbuildmat.2018.12.158

Liang, C., Lu, N., Ma, H., Ma, Z., & Duan, Z. (2020). Carbonation behavior of recycled concrete with CO2-curing recycled aggregate under various environments. *Journal of CO2 Utilization*, *39*, 101185. https://doi.org/10.1016/j.jcou.2020.101185

Liu, K., Xu, W., Sun, D., Tang, J., Wang, A., & Chen, D. (2021). Carbonation of recycled aggregate and its effect on properties of recycled aggregate concrete: A review. *Materials Express*, *11*(9), 1439–1452. https://doi.org/10.1166/mex.2021.2045

Liu, W., Teng, L., Rohani, S., Qin, Z., Zhao, B., Xu, C. C., Ren, S., Liu, Q., & Liang, B. (2021). CO2 mineral carbonation using industrial solid wastes: A review of recent developments. *Chemical Engineering Journal*, *416*, 129093. https://doi.org/10.1016/j.cej.2021.129093

Monkman, S., & Shao, Y. (2010). Carbonation Curing of Slag-Cement Concrete for Binding CO2 and Improving Performance. *Journal of Materials in Civil Engineering*, *22*(4), 296–304. https://doi.org/10.1061/(asce)mt.1943-5533.0000018

Papadakis, V. G., Vayenas, C. G., & Fardis, M. N. (1991). Experimental investigation and mathematical modeling of the concrete carbonation problem. *Chemical Engineering Science*, *46*(5-6), 1333-1338. https://doi.org/10.1016/0009-2509(91)85060-B

Monteiro, P. J., Miller, S. A., & Horvath, A. (2017). Towards sustainable concrete. Nature materials, 16(7), 698-699. https://doi.org/10.1016/j.cemconres.2017.02.009

Pu, Y., Li, L., Shi, X., Wang, Q., & Abomohra, A. (2022). Improving recycled concrete aggregates using flue gas based on multicyclic accelerated carbonation: Performance and mechanism. *Construction and Building Materials*, *361*, 129623. https://doi.org/10.1016/j.conbuildmat.2022.129623

Qiu, Y., Lamers, P., Daioglou, V., McQueen, N., de Boer, H.-S., Harmsen, M., Wilcox, J., Bardow, A., & Suh, S. (2022). Environmental trade-offs of direct air capture technologies in climate change mitigation toward 2100. *Nature Communications*, *13*(1), 3635. https://doi.org/10.1038/s41467-022-31146-1

Ravikumar, D., Zhang, D., Keoleian, G., Miller, S., Sick, V., & Li, V. (2021). Carbon

dioxide utilization in concrete curing or mixing might not produce a net climate benefit. *Nature Communications*, *12*(1), 855. https://doi.org/10.1038/s41467-021-21148-w

Darton, R. C., & Yang, A. (2020). Removing carbon dioxide from the air to stabilise the climate. In Advances in carbon management technologies (pp. 3-22). CRC Press.

Sereng, M., Djerbi, A., Metalssi, O. O., Dangla, P., & Torrenti, J.-M. (2021). Improvement of Recycled Aggregates Properties by Means of CO2 Uptake. *Applied Sciences*, *11*(14), 6571. https://doi.org/10.3390/app11146571

Shuvo, A. K., Sarker, P. K., & Shaikh, F. U. A. (2024). Efficacy of various accelerated carbonation techniques to improve recycled concrete aggregates: A comprehensive review. *Journal of Building Engineering*, *95*, 110257. https://doi.org/10.1016/j.jobe.2024.110257

Sodiq, A., Abdullatif, Y., Aissa, B., Ostovar, A., Nassar, N., El-Naas, M., & Amhamed, A. (2023). A review on progress made in direct air capture of CO2. Environmental Technology & Innovation, 29, 102991. https://doi.org/10.1016/j.eti.2022.102991

Stephen M Smith, Matthew Gidden, William F Lamb, Jan C Minx, & Oliver Geden. (2023). *A global, independent scientific assessment of Carbon Dioxide Removal*. https://www.stateofcdr.org/

Tam, V. W. Y., Butera, A., Le, K. N., & Li, W. (2020). Utilising CO2 technologies for recycled aggregate concrete: A critical review. In *Construction and Building Materials* (Vol. 250). Elsevier Ltd. https://doi.org/10.1016/j.conbuildmat.2020.118903

Thiery, M., Dangla, P., Belin, P., Habert, G., & Roussel, N. (2013). Carbonation kinetics of a bed of recycled concrete aggregates: A laboratory study on model materials. *Cement and Concrete Research*, *46*, 50–65. https://doi.org/10.1016/j.cemconres.2013.01.005

Tiwari, M., Bajpai, Dr. S., & Dewangan, Dr. U. (2016). Steel Slag Utilization — Overview

in Indian Perspective. *International Journal of Advanced Research*, *4*(8), 2232–2246. https://doi.org/10.21474/IJAR01/1442

Wang, B., Yan, L., Fu, Q., & Kasal, B. (2021). A Comprehensive Review on Recycled Aggregate and Recycled Aggregate Concrete. *Resources, Conservation and Recycling*, *171*, 105565. https://doi.org/10.1016/j.resconrec.2021.105565

Wang, P., Robinson, A. J., & Papadokonstantakis, S. (2024). Prospective techno-economic and life cycle assessment: a review across established and emerging carbon capture, storage and utilization (CCS/CCU) technologies. *Frontiers in Energy Research*, *12*. https://doi.org/10.3389/fenrg.2024.1412770

Wang, S., Wang, M., Liu, F., Song, Q., Deng, Y., Ye, W., Ni, J., Si, X., & Wang, C. (2024). A Review on the Carbonation of Steel Slag: Properties, Mechanism, and Application. *Materials*, *17*(9), 2066. https://doi.org/10.3390/ma17092066

Xi, F., Davis, S. J., Ciais, P., Crawford-Brown, D., Guan, D., Pade, C., Shi, T., Syddall, M., Lv, J., Ji, L., Bing, L., Wang, J., Wei, W., Yang, K.-H., Lagerblad, B., Galan, I., Andrade, C., Zhang, Y., & Liu, Z. (2016). Substantial global carbon uptake by cement carbonation. *Nature Geoscience*, *9*(12), 880–883. https://doi.org/10.1038/ngeo2840

Xiao, J., Zhang, H., Tang, Y., Deng, Q., Wang, D., & Poon, C. (2022). Fully utilizing carbonated recycled aggregates in concrete: Strength, drying shrinkage and carbon emissions analysis. *Journal of Cleaner Production*, *377*, 134520. https://doi.org/10.1016/j.jclepro.2022.134520

Xuan, D., Zhan, B., & Poon, C. S. (2017). Durability of recycled aggregate concrete prepared with carbonated recycled concrete aggregates. *Cement and Concrete Composites*, *84*, 214–221. https://doi.org/10.1016/j.cemconcomp.2017.09.015

Zhan, B., Poon, C. S., Liu, Q., Kou, S., & Shi, C. (2014). Experimental study on CO2 curing for enhancement of recycled aggregate properties. *Construction and Building Materials*, *67*, 3–7. https://doi.org/10.1016/j.conbuildmat.2013.09.008

Zhang, Y., Yu, L., Cui, K., Wang, H., & Fu, T. (2023). Carbon capture and storage technology by steel-making slags: Recent progress and future challenges. *Chemical Engineering Journal*, *455*, 140552. https://doi.org/10.1016/j.cej.2022.140552

Chapter 2 Literature Review

2.1 Introduction

The building and construction sector is responsible for a substantial portion of global carbon dioxide emissions, accounting for approximately 37% of energy and process related CO_2 emissions in 2022 (Ma et al., 2024). Within this figure, the embodied carbon associated with the materials, construction activities and end-of-life stages constitutes a significant share of the sector's overall emissions.

Cement production is among the most carbon-intensive industrial processes. It contributes between 5%-8% of global anthropogenic CO_2 emissions (Khaiyum et al., 2023). The emissions arise both from the combustion of fossil fuels for high-temperature processes and from the chemical decarbonation of limestone during clinker formation. Concrete, as the most widely used construction material globally, inherits the carbon burden of cement. Cement alone comprises only 10%-15% of concrete by volume yet is responsible for around 90% of concrete's carbon emissions of concrete (rpsgroup, 2024).

In response to these challenges, carbon capture and utilisation strategies that embed CO_2 into building materials offer promising avenues for dual benefits: carbon sequestration and potential improvements in material performance. These strategies draw on CO_2 from concentrated point sources or DAC and aim to convert it into stable forms through mineralisation, polymerisation or biological incorporation within construction materials.

This chapter delivers a critical review of building materials capable of absorbing and storing CO_2. The principal focus lies on concrete-based systems, including cement, fly ash, steel slag and RCA. Brief overviews of timber and polymer-based materials are also provided to present alternative carbon storage pathways, although they are not primary subjects in subsequent chapters.

2.2 CO_2 Sources for Mineralisation and Absorption

The core of this study is the potential of CO_2 storage in materials. Obviously, the first step is discussed where is the CO_2 from different sources of CO_2 represent different technologies with implications in energy consumption, cost-benefit, and feasibility.

2.2.1 Point Source Capture

Carbon dioxide is produced in many combustion processes, particularly during thermal power generation, including fossil, biomass, municipal waste and other waste to energy plants (Koytsoumpa et al., 2018). Generally, there are three major approaches for point source capture: pre-combustion capture, oxyfuel combustion capture and post-combustion. Oxyfuel combustion capture involves burning fuel in nearly pure oxygen so that the flue gas mainly consists of CO_2 and water vapor, which makes CO_2 separation easier after condensing the steam. Post-combustion carbon capture is the suitable choice in the near-to middle-term, since it can be retrofitted to the existing power plants compared to the other two approaches (Wu et al., 2014). In industry, there is a large amount of direct CO_2 emissions, which the companies have been trying to tackle. Pre-combustion capture and separation of CO_2 is possible to be

used under high concentration carbon dioxide environment. The pre-combustion capture refers to separation of CO_2 generated as a co-product of a process to convert a fossil fuel to a carbon-free fuel. In natural gas reforming and gasification, for example, pre-combustion is associated with the water gas shift reaction for converting the carbon monoxide and water to carbon dioxide and hydrogen and the removal of carbon dioxide (Kapetaki et al., 2015).

2.2.2 Direct Air Carbon Capture

DAC uses chemical or physical processes to separate CO_2 from ambient air. Given the homogeneous atmospheric CO_2 concentration levels around the world, DAC facilities can be deployed in locations that provide abundant cheap and carbon-free energy and/or that are close to pipeline infrastructure, underground storage, or utilization facilities for reducing the CO_2 transportation cost. Nowadays, the atmospheric CO_2 is around 425 ppm (NOAA Global Monitoring Laboratory, 2025), but still highly dilute compared to point sources, so DAC technologies require substantial energy and materials inputs. The role of DAC in climate change mitigation will heavily depend on process-design and resulting technoeconomic and environmental performances (Sanz-Pérez et al., 2016). Two types of technologies are presently considered promising from a technoeconomic perspective: solvent-based and sorbent-based. Solvent-based DAC typically relies on aqueous hydroxide solutions, such as potassium hydroxide and sodium hydroxide for capturing CO_2. It requires dedicated high-temperature (over 900 ℃) heat for CO_2 regeneration (Qiu et al., 2022). Such high temperatures need combusting energy dense fuels such as natural gas or hydrogen to

supply the heat. Sorbent-based DAC mostly uses amine materials bonded to a wide range of porous solid supports. It can function with lower temperature (80-120 ℃) heat for CO_2 regeneration, offering a larger variety of thermal energy supply options (e.g., heat pump, geothermal, and industrial waste heat) (Yamada, 2021).

2.3 CO_2 Uptake Potential in Construction Materials

2.3.1 Concrete

Concrete is the most widely used construction material in the world, with applications ranging from housing to infrastructure. It is essentially a composite of cement, which acts as the binder, and aggregates, which provide bulk, stiffness and strength (Bae et al., 2025). The typical composition of concrete is illustrated in **Figure 2-1,** where aggregates usually account for 60–80% of the total volume and cement paste provides the cohesive matrix. According to the *Concrete – Complementary British Standard* (British Standards Institution, 2015.), concrete can be categorised into designated concrete, designed concrete, prescribed concrete, standardised prescribed concrete and proprietary concrete. For many structural applications, designated concretes are most frequently specified, because of their reliability and suitability for housing, buildings and infrastructure. These concretes are normally designed for an intended service life of at least 50 years. A summary of representative mix proportions, cement or combination contents, and applications is available in Appendix A.1 **Table A-1** to **Table A-4**.

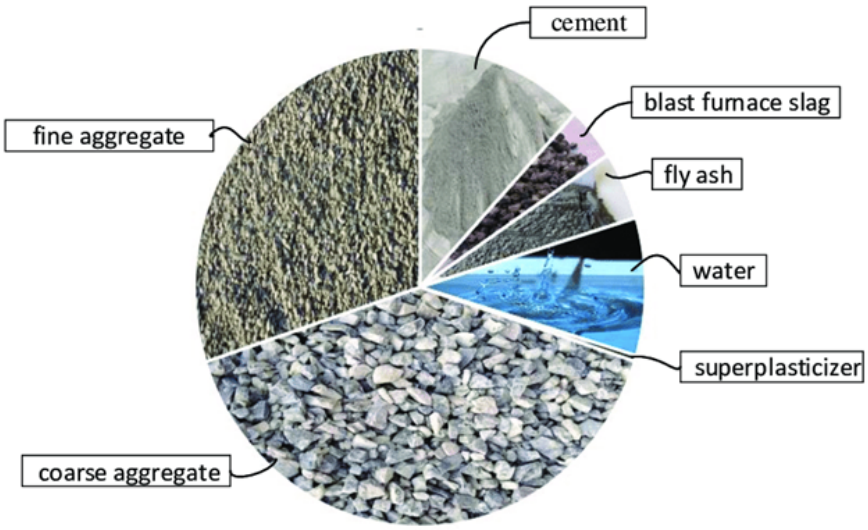

Figure 2-1 Concrete composition (Aïtcin, 2016)

In recent years increasing attention has been given to accelerated carbonation curing (ACC), which uses elevated CO_2 concentrations, controlled humidity, and in some cases mild pressure and temperature, to achieve rapid uptake of carbon dioxide. This approach has transformed the perception of concrete from a passive long-term sink into an active and engineered medium for CO_2 storage. In order to understand the role of concrete in carbon emissions and uptake, it is necessary to trace its production pathway from raw minerals to the hardened composite. The overall transformation is summarised in **Figure 2-2**, which shows the sequence from raw materials to final concrete. The process begins with the extraction of raw feedstocks, primarily limestone and clay, accompanied by minor constituents such as steel scoria and gypsum.

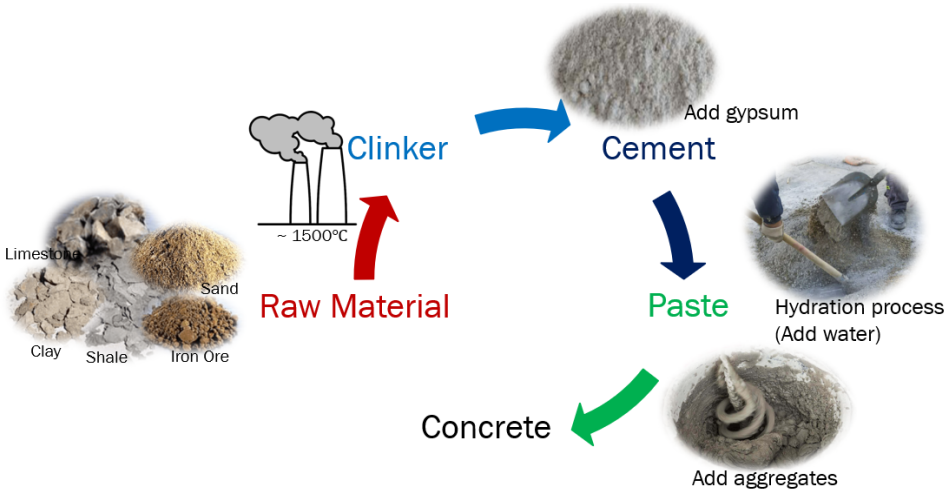

Figure 2-2 Concrete production line

A typical composition of Portland cement raw materials is listed in **Table 2-1**, with limestone contributing about 70% of the mass and serving as the dominant source of calcium carbonate. Clay provides aluminosilicate phases, sand contributes silica, steel scoria supplies iron oxide, and gypsum is later added as a setting regulator.

Table 2-1 Portland cement raw materials component

Cement Raw materials	***Chemical Composition***	***Percent content***
Limestone	$CaCO_3$	70%
	$MgCO_3,\ Na_2CO_3,\ K_2CO_3$	1%
Clay	$Al_2(OH)_4 \cdot Si_2O_5$	15%
	$Al_2(OH)_2 \cdot (Si_2O_5)_2$	
Sand	SiO_2	6%
Steel Scoria	Fe_2O_3	3%
Gypsum	$CaSO_4 \cdot 7H_2O$	5%

When subjected to high temperature calcination in the rotary kiln, these raw materials undergo decarbonation and solid-state reactions that yield the principal clinker

minerals. The decarbonation of limestone is the most significant reaction in terms of CO_2 release, shown as reaction (2-1).

$$CaCO_3 \xrightarrow{\text{heat}(\sim 800℃-900℃)} CaO + CO_2 \qquad (2-1)$$

Subsequent reactions produce belite, alite, tricalcium aluminate and calcium aluminoferrite, which together constitute the clinker phase assemblage, shown as reactions (2-2) to (2-5).

$$2CaO + SiO_2 \xrightarrow{\text{heat}(900℃-1100℃)} 2CaO \cdot SiO_2 \qquad (2-2)$$

$$2CaO \cdot SiO_2 + CaO \xrightarrow{heat(1300℃-1450℃)} 3CaO \cdot SiO_2 \qquad (2-3)$$

$$3CaO + Al_2O_3 \xrightarrow{\text{heat}(1100℃-1300℃)} 3CaO \cdot Al_2O_3 \qquad (2-4)$$

$$4CaO + Al_2O_3 + Fe_2O_3 \xrightarrow{\text{heat}(1100℃-1300℃)} 4CaO \cdot Al_2O_3 \cdot Fe_2O_3 \qquad (2-5)$$

A secondary reaction also occurs through the decomposition of magnesite, shown as reaction (2-6).

$$MgCO_3 \xrightarrow{\text{heat}(750℃)} MgO + CO_2[\text{side reaction}] \qquad (2-6)$$

The mixture of these crystalline phases, referred to collectively as clinker, is then ground together with a small amount of gypsum, and occasionally supplementary materials, to form cement. When cement is combined with water and aggregates, it produces fresh concrete, which subsequently hardens into the durable material used worldwide in modern construction.

Once placed in service, hardened concrete has the intrinsic ability to act as a sink for atmospheric CO_2 through the gradual process of carbonation. The process is

illustrated in **Figure 2-3**, which schematically depicts CO_2 transmission and carbonate formation within the cement matrix.

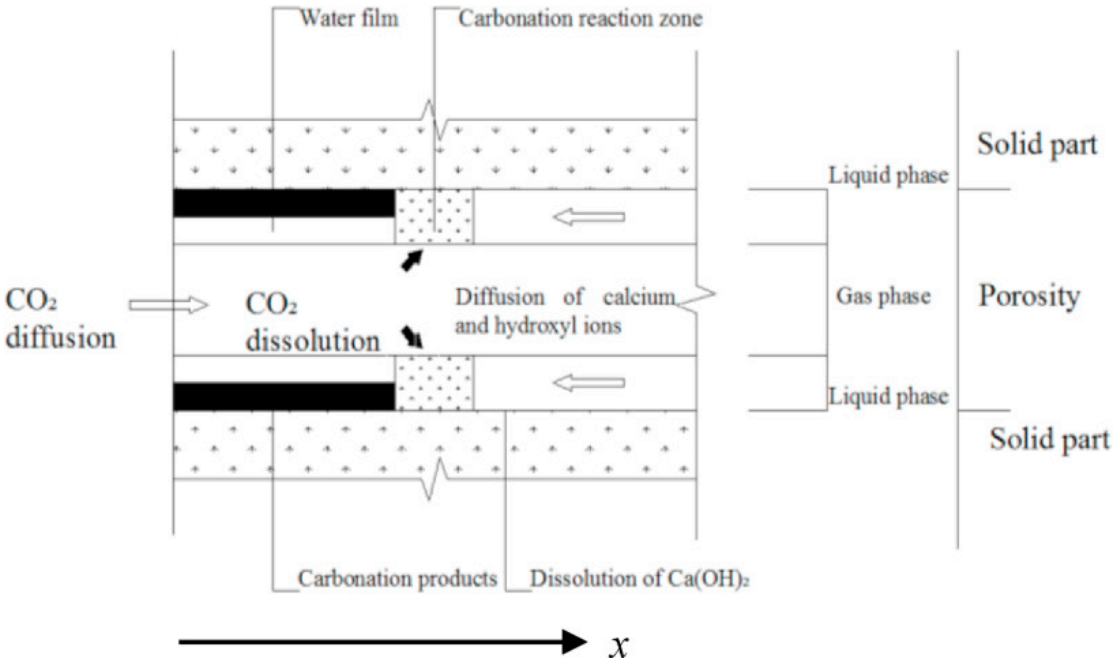

Figure 2-3 Schematic diagram of concrete carbonation and CO_2 transmission (Liu et al., 2020)

This mechanism involves the diffusion of CO_2 into the pore network, its dissolution in pore water, and subsequent reactions with alkaline hydration products. The ionic pathway has been reported in carbonation studies of cementitious materials (Xi et al., 2016) and can be expressed as reaction (2-7).

$$CO_2(g) \rightarrow CO_2(aq) + H_2O \rightarrow H_2CO_3 \rightleftharpoons HCO_3^- + CO_3^{2-} \qquad (2-7)$$

The dissolved carbonate and bicarbonate species then react with portlandite and calcium silicate hydrates (C–S–H), according to widely established carbonation reactions (2-8) to (2-11) (Li & Wu, 2022).

$$Ca(OH)_2 + CO_2 \rightarrow CaCO_3 + H_2O \qquad (2-8)$$

$$C - S - H + CO_2 \rightarrow CaCO_3 + SiO_2 \cdot nH_2O \qquad (2-9)$$

$$C_3S + (3-x)CO_2 + yH_2O \rightarrow C_xSH_y + (3-x)CaCO_3 \qquad (2-10)$$

$$C_2S + (2-x)CO_2 + yH_2O \rightarrow C_xSH_y + (2-x)CaCO_3 \qquad (2-11)$$

Mechanistically, carbonation in concrete involves several stages that have been documented in experimental and modelling studies (Akutagawa, 1991; Scrivener & Nonat, 2011): (i) penetration of CO_2 through the pore system by diffusion, governed by porosity and moisture content; (ii) dissolution of CO_2 in pore water, forming carbonic acid and carbonate species; (iii) release of calcium ions from portlandite and partially from C–S–H; (iv) precipitation of $CaCO_3$ in the pore space, progressively densifying the microstructure. While the formation of $CaCO_3$ densifies the matrix and may locally enhance compressive strength, the transformation of $Ca(OH)_2$ and the decalcification of C–S–H lower the alkalinity of the pore solution, reducing its protective capacity against steel corrosion. This process ultimately decreases the pH, induces shrinkage, and can lead to long-term deterioration of reinforced-concrete durability. Carbonation in concrete can nonetheless be beneficial when utilised under controlled curing or RCA treatment conditions, where it enhances densification and enables permanent CO_2 sequestration. However, in reinforced concrete structures exposed to natural environments, progressive carbonation lowers alkalinity, depassivates steel reinforcement and may compromise long-term durability.

In natural exposure conditions, this process is strongly dependent on relative humidity, with maximum uptake generally occurring between 50% and 70%. At lower humidity

the dissolution of CO_2 is insufficient, while at very high humidity saturated pores restrict gas ingress. Concretes with higher porosity, reduced curing or lower cover depths are particularly susceptible to rapid natural carbonation. From previous studies, the rate-limiting step of natural carbonation is generally the diffusion of CO_2 through the pore structure, as the chemical reactions between dissolved CO_2 and hydration products are comparatively fast under typical environmental conditions. By contrast, in ACC systems the same sequence of reactions occurs but under externally optimised conditions (Zhang & Shao, 2016). Elevated CO_2 partial pressure enhances dissolution and accelerates the carbonation front, while controlled humidity provides sufficient water for ion transport without blocking pore access. Mild heating can further increase diffusivity and reaction kinetics. Under such conditions, uptake that would normally take decades can be achieved within a few hours, with additional benefits such as increased early strength, reduced permeability and improved durability (Binder et al., 2023; El-Hassan, 2021). Moreover, demolition and recycling phases provide additional opportunities, as crushed concrete surfaces can be rapidly carbonated in dedicated reactors before reusing (Leemann et al., 2023).

In summary, concrete undergoes carbonation through well-known dissolution and precipitation reactions, but the rate and extent are highly dependent on exposure conditions. Natural carbonation contributes to long-term sequestration during service life, while accelerated carbonation curing represents a promising strategy for rapid and permanent CO_2 storage. This duality highlights the significance of concrete as both

a traditional structural material and a key player in engineered carbon management strategies.

2.3.2 Cement Products

Cement-based products, which include pastes, mortars and precast blocks, are central to CO_2 uptake in the construction sector. Their carbonation behaviour is governed by the mineral assemblage formed during clinker production and by the curing environment after mixing. Clinker is mainly composed of alite (C_3S), belite (C_2S), tricalcium aluminate (C_3A) and tetracalcium aluminoferrite (C_4AF). These phases not only provide mechanical strength upon hydration but also act as primary reactants during carbonation. The Bogue Calculation for clinkers can be reduced to the following formula (2-12) to (2-15) (Hewlett, 2019). It is assumed that four compounds C_3S, C_2S, C_3A and C_4AF exist in the clinker. The units of C_3S, C_2S, C_3A and C_4AF are the mass percentage of clinkers. The units of input values, including CaO, SiO_2, Al_2O_3 and Fe_2O_3 are the mass percentage of raw materials.

$$C_4AF = 3.043 \times Fe_2O_3 \qquad (2-12)$$

$$C_3AF = 2.650 \times Al_2O_3 - 1.692 \times Fe_2O_3 \qquad (2-13)$$

$$C_2S = -3.0710 \times CaO + 8.6024 \times SiO_2 + 5.0683 \times Al_2O_3 + 1.0785 \times Fe_2O_3 (2-14)$$

$$C_3S = 4.0710 \times CaO - 7.602 \times SiO_2 - 6.7187 \times Al_2O_3 - 1.4297 \times Fe_2O_3 (2-15)$$

The standard Bogue calculation refers to cement clinker rather than cement, but it can be adjusted for use with cement. The difference is between C2S (2-16) and C3S's formula (2-17), which brings in gypsum.

$$C_2S = -3.071 \times (CaO - 0.7 \times SO_3) + 8.602 \times SiO_2 + 5.068 \times Al_2O_3 + 1.079 \times Fe_2O_3 \quad (2-16)$$

$$C_3S = 4.071 \times (CaO - 0.7 \times SO_3) - 7.602 \times SiO_2 - 6.719 \times Al_2O_3 - 1.430 \times Fe_2O_3 \quad (2-17)$$

The mass percentage of CaO, SiO_2, Al_2O_3 and Fe_2O_3 are referred to in **Figure 2-4** (Bediako & Amankwah, 2015). Note that the above equations were used in this work for calculating the fractions of C_2S, C_3S, C_3AF and C_4AF in each experiment collated from the literature.

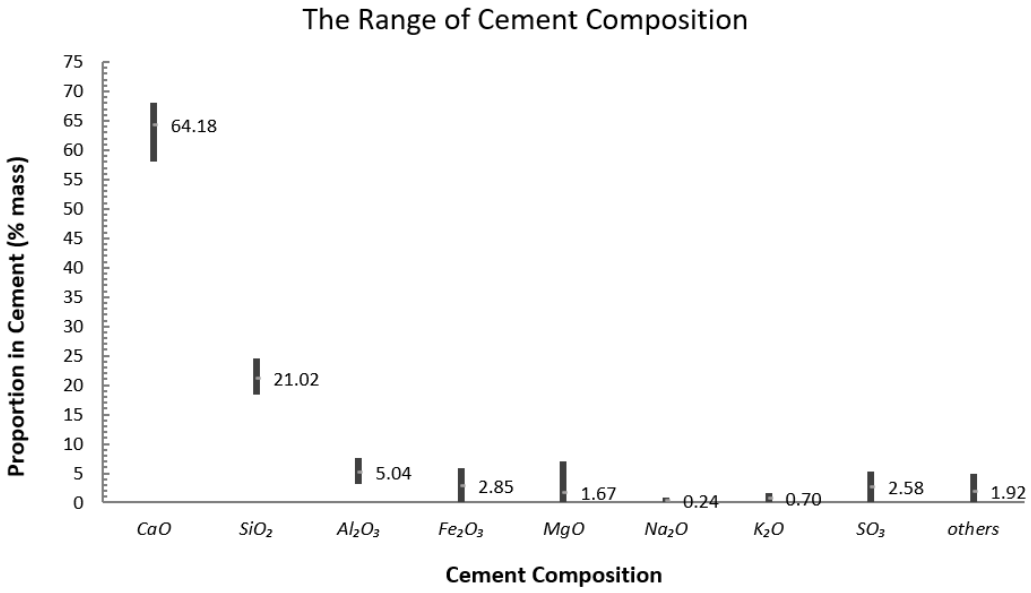

Figure 2-4 The range of cement composition

The Bogue calculation shows Portland cement's chemical composition and percent content in **Table 2-2** (Britannica, 2022).

Table 2-2 Portland cement clinker component

Compound	*abbreviation*	*Chemical composition*	*Percent content*
Belite or Di-Calcium silicate	C_2S	$2CaO \cdot Si_2O_3$	7%-32%
Alite or Tri-Calcium silicate	C_3S	$3CaO \cdot Si_2O_3$	45%-75%
Tri-Calcium Aluminate	C_3A	$3CaO \cdot Al_2O_3$	0%-13%
Tetra Calcium Aluminoferrite	C_4AF	$4CaO \cdot Al_2O_3 \cdot Fe_2O_3$	0%-18%

Carbon dioxide curing, which involves exposing cement-based products to concentrated CO_2 during early stages of application (before hardening), accelerates carbonation and substantially increases uptake. The principal clinker phases react as follows (2-18) to (2-20).

$$2CaO \cdot SiO_2 + 2CO_2 + xH_2O \xrightarrow{H_2O} 2CaCO_3 + SiO_2 \cdot xH_2O \qquad (2-18)$$

$$3CaO \cdot SiO_2 + 3CO_2 + xH_2O \xrightarrow{H_2O} 3CaCO_3 + SiO_2 \cdot xH_2O \qquad (2-19)$$

$$3CaO \cdot Al_2O_3 \cdot 6H_2O + 3CO_2 \xrightarrow{H_2O} 2Al(OH)_3 + 3CaCO_3 + 3H_2O \qquad (2-20)$$

These reactions show that alite, belite and tricalcium aluminate can directly mineralise CO_2 into stable carbonate phases. C_4AF is generally less reactive and often neglected in CO_2 curing considerations. At the same time, hydration reactions proceed in parallel, producing calcium hydroxide and additional C–S–H (Xi et al., 2016), shown as formula (2-21) and (2-22).

$$2(3CaO \cdot SiO_2) + 6H_2O \rightarrow 3CaO \cdot 2SiO_2 \cdot 3H_2O + 3Ca(OH)_2 \qquad (2-21)$$

$$2(2CaO \cdot SiO_2) + 4H_2O \rightarrow 3CaO \cdot 2SiO_2 \cdot 3H_2O + 3Ca(OH)_2 \qquad (2-22)$$

The portlandite formed then reacts further with CO_2, contributing to additional carbonation, as shown in (2-23).

$$3CaO \cdot 2SiO_2 \cdot 3H_2O + 3CO_2 \xrightarrow{H_2O} 3CaCO_3 \cdot 2SiO_2 \cdot 3H_2O \qquad (2-23)$$

In practice, the extent of these reactions depends strongly on curing conditions. Pre-cured treatments, often involving low-humidity environments or steam curing, are applied to reduce free water and create diffusion pathways for CO_2 (Shi et al., 2012; Zhang & Shao, 2016). Subsequent CO_2 curing is typically performed in chambers with controlled pressure (0.1–5 bars), temperature (20–60 °C) and CO_2 concentration, which can range from atmospheric levels to pure CO_2 depending on experimental design (Ahmad et al., 2017). During curing, water compensation by surface spraying may be employed to balance evaporation losses and sustain reaction kinetics (El-Hassan, 2021).

The outcome of CO_2 curing is twofold: significant uptake of CO_2, achieved within hours or days, and improved performance of cement products. Reported benefits include enhanced early strength, reduced porosity, improved dimensional stability and increased durability (Zhang & Shao, 2016). Subsequent hydration after CO_2 curing continues for weeks to months but contributes less to sequestration and more to long-term mechanical properties.

In summary, the carbonation of cement products is strongly linked to clinker mineralogy and curing environment. By integrating controlled CO_2 curing, these

materials can function not only as structural components but also as efficient and rapid CO_2 sinks, aligning cement manufacture with climate mitigation strategies through reduced net emissions.

2.3.3 Aggregates

As illustrated in **Figure 2-1**, aggregates, both fine and coarse, constitute the majority of the composition of concrete, typically accounting for 60–80% of the volume and approximately 75% of the weight. Fine aggregates, such as sand, are defined as particles smaller than 4.75 mm that pass through a No. 4 sieve. Coarse aggregates, such as gravel and crushed stone, are those retained on the sieve, usually larger than 4.75 mm in diameter. Given their large proportion, the type and origin of aggregates are highly relevant when assessing the overall CO_2 balance of concrete. Aggregates can be broadly classified into three categories: natural, manufactured, and recycled (Infante Gomes et al., 2021).

Natural aggregates are rock fragments obtained through mining, quarrying or dredging, which are used either directly or after processing such as crushing, washing and grading. Common examples include sand, gravel and crushed rock. From the standpoint of CO_2 uptake, natural aggregates are largely inert, consisting mainly of quartz, feldspar and stable carbonates. Their reactivity with atmospheric CO_2 under ambient conditions is negligible, and thus their contribution to sequestration in concrete is minimal (Vijerathne et al., 2024). For this reason, natural aggregates are

generally considered a passive filler rather than an active sink within the concrete matrix.

Manufactured aggregates are derived from industrial processes, often as by-products of metallurgical or energy production. These materials may undergo thermal or chemical transformation, and examples include iron and steel slags, pelletised fly ash and expanded clays. The key distinction is that many manufactured aggregates contain reactive oxides such as CaO and MgO, which are prone to carbonation. The carbonation reactions proceed as follows formular (2-24) to (2-28) (Sousanabadi Farahani et al., 2025).

$$CaO + CO_2 \rightarrow CaCO_3 \quad (2-24)$$

$$MgO + CO_2 \rightarrow MgCO_3 \quad (2-25)$$

$$Ca(OH)_2(s) + CO_2(g) \rightarrow CaCO_3(s) + H_2O\ (l) \quad (2-26)$$

$$2CaO \cdot SiO_2(s) + 2CO_2(g) \rightarrow 2CaCO_3(s) + SiO_2(s) \quad (2-27)$$

$$3CaO \cdot MgO \cdot 2SiO_2(s) + 4CO_2(g) \rightarrow 3CaCO_3(s) + MgCO_3(s) + 2SiO_2(s) \quad (2-28)$$

Because of this reactivity, manufactured aggregates can display significant CO_2 uptake potential under appropriate curing conditions. In contrast to ACC, which primarily carbonates hydration products such as portlandite and C–S–H within fresh or early-age cementitious matrices, aggregate carbonation mainly targets free oxides and latent mineral phases contained within the aggregates. This distinction is important, as aggregate carbonation is frequently used not only for CO_2 sequestration but also

for the stabilisation of potentially expansive components and the enhancement of aggregate durability. Their specific contributions to CO_2 sequestration will be explored in the following sections on steel slag (Section 2.3.4) and fly ash aggregates (Section 2.3.5).

Above all, while much of the discussion on carbonation has centred on cement paste, it is important to emphasise that cement only accounts for 7–15% of the total mass of concrete, whereas aggregates comprise almost 60–75% (Issa et al., 2000). This highlights the significance of aggregates in the carbon balance of concrete. Among these, RCA derived from the crushing of construction and demolition waste represents a key material for enhancing waste utilisation and promoting circularity in the construction sector (arahani et al., 2025).

The quality of RCA has been widely reported to be inferior to that of natural aggregates, largely due to the presence of adhered mortar and higher porosity. Aggregates are usually classified into recycled aggregates (RA) and recycled concrete aggregates (RCA), with the distinction being based on composition. RA often contains masonry and other non-concrete constituents, while RCA is primarily composed of crushed concrete fragments. This difference in composition is crucial, as it influences both performance and carbonation reactivity. RA is generally limited to use in concrete of strength classes up to C16/20, whereas RCA can be used in higher strength concretes up to C40/50 (Gonçalves & Brito, 2010). In practice, both RA and RCA are commonly restricted to a maximum of 20% substitution by weight of the coarse aggregate fraction. Consequently, most standards recommend that no more than 20%

of natural coarse aggregate be replaced with recycled aggregate in new structural concrete. Moreover, the applications of concrete incorporating RCA remain somewhat limited, particularly for structural elements (Zhan et al., 2014).

From a carbonation perspective, RCA are distinct from natural aggregates because they retain residual hardened cement paste on their surfaces. This residual mortar contains portlandite, partially hydrated C–S–H, and occasionally unreacted clinker fragments, which can undergo carbonation through the same pathways described previously for concrete (see formula (2-8) and (2-9) in Section 2.3.1).

Because of these reactions, RCA have a measurable though relatively modest capacity for CO_2 sequestration. Experimental studies indicate that RCA typically absorb only 0.4–0.8% of their mass as CO_2 (Xuan et al., 2016). Although this is significantly less than the uptake achievable by cement paste or manufactured aggregates, the very large quantities of demolition waste produced worldwide mean that RCA still represents a meaningful sink in aggregate carbon balances. Furthermore, carbonation has been observed to improve certain aggregate properties, such as increasing density and reducing water absorption, although excessive decalcification can negatively impact the interfacial transition zone in new concretes (Thomas et al., 2013).

In conclusion, RCA play a dual role as both a sustainable substitute for natural aggregates and a modest but non-negligible medium for CO_2 sequestration. Their uptake capacity is limited, but given the scale of construction and demolition waste, RCA represents an important area for further research. Future work is needed to more

accurately quantify their CO_2 uptake potential under different processing and curing regimes, and to integrate these processes into recycling practice at industrial scale.

2.3.4 Steel Slag

Most steel in Europe is produced via two basic routes: The Blast Furnace-Basic Oxygen Furnace (BF-BOF) route and the Electric Arc Furnace route (EAF). Blast furnaces produce iron from iron ore. In a second step a basic oxygen converter turns iron, with some additions of scrap, into steel. In these two steps, the byproducts are basic furnace slag (BFS) and basic oxygen furnace slag (BOFS), respectively. Therefore, based on the production process, we usually obtain either BFS alone or both BOFS and BFS simultaneously. Thus, it is important to consider this when conducting an LCA. Electric Arc Furnaces produce steel mostly from scrap collected for recycling, and from this process, electric arc furnace slag (EAFS) is made as a kind of byproduct. After getting molten steel, it will go into Argon Oxygen Decarburization (AOD) converter or vacuum Oxygen Decarburization (VOD) converter, both of these two processes used for refining stainless steel (Holappa et al., 2021). During these two processes, AODS and VODS existed. Finally, ladle metallurgical treatments take place in a ladle furnace (LF) which makes temperature adjustment easy. LF slag can be divided into water-cooled LF slag and air-cooled LF slay because of different technologies (Zhang et al., 2023) The LF slag (LFS) follows on the ladle to continuous casting (CC), and after the cast end, the slag is poured into a slag pot (LF-CCS). Therefore, the steelmaking process can make seven kinds of slag. The sequence in which they occur is shown in **Figure 2-5**.

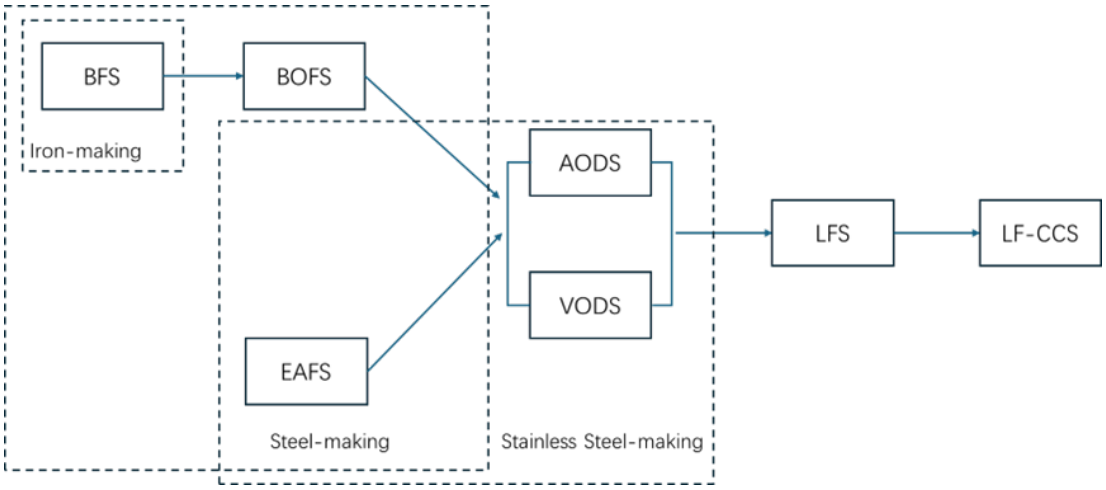

Figure 2-5 Slag types from iron and steel-production processes

The chemical compositions of BOF, EAF, AOD, LF and BF slags are broadly similar, differing mainly in the proportions of the major oxides. EAF slag typically contains the lowest CaO content and the highest iron content, whereas BOF slag also has a relatively high iron content and LF slag has much lower iron. Typial EAF and BOF oxide compositions are shown as **Table 2-3**. BF slag is distinguished by its higher silica content. Reported mineral phases in steel slags include olivine, merwinite, C_3S, β-C_2S, γ-C_2S (formed from β-C_2S on cooling), C_4AF, C_2F, RO phase (a CaO-FeO-MnO-MgO solid solution in which FeO is dominant), as well as free CaO and free MgO (Biava et al., 2024). These compositional and mineralogical characteristics strongly influence the reactivity and carbonation potential of each slag type. For example, slags with higher free CaO and β-C_2S contents generally exhibit greater CO_2 uptake capacity, whereas γ-C_2S is a non-hydraulic phase that contributes little to strength development but may carbonate slowly over extended time periods (Baras et al., 2023).

Table 2-3 Typical EAF and BOF oxide compositions (DiGiovanni et al., 2024)

Oxides	*EAF Slag*	*BOF Slag*
CaO	20%-40%	30%-50%
SiO_2	10%-20%	10%-15%
Al_2O_3	2%-10%	1%-3%
MgO	5%-15%	5%-15%
FeO_X	20%-40%	10%-30%
MnO	2.5%-5%	1%-5%
TiO_2	0.5%-1%	0.5%-2%
P_2O_5	0.5%-2%	1%-3%

The CO_2 carbonation by steel slag includes (i) direct carbonation and (ii) indirect carbonation. Direct carbonation is a simple approach of steel slag carbonation, which is achieved through the reaction of steel slag with CO_2 either in the aqueous or gaseous phase. It can be pre-treated but does not involve using dissolvent to extract the active components (such as Ca^{2+} or Mg^{2+}) from steel slag. Direct carbonation shows many advantages, such as simple process, convenient operation and less consumption of chemical reagent consumption (Wang et al., 2021). For direct carbonation, it concludes two possible methods: (i-a) gas-solid carbonation; (i-b) aqueous carbonation. The experimental procedure is typically carried out in an environmentally controlled chamber, as shown in **Figure 2-6**. In general, the mechanism of steel slag CO_2 storage is through carbonation or hydration combined carbonation, and the carbonation reactions follow as:

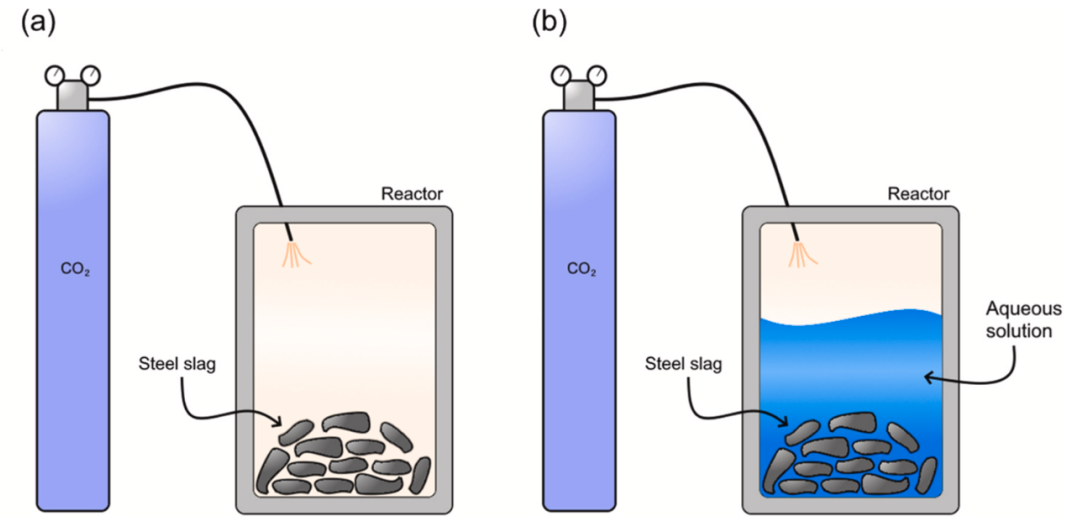

Figure 2-6 Schematic representation of an experimental for (a) direct gas-solid carbonation setup (b) aqueous carbonation setup (DiGiovanni et al., 2024)

(i-a) Gas-solid carbonation

The reaction proceeds by a rapid surface reaction-controlled step, followed by a slower product-layer diffusion-controlled stage. In the initial period, CO_2 and reactive ions directly contact the mineral surface, leading to fast nucleation of carbonates. As the carbonate layer thickens, it acts as a diffusion barrier that limits further transport of CO_2 and ions to the unreacted core, thereby slowing the overall reaction rate. In this case, reaction kinetics is well understood and can be enhanced to achieve accelerated carbonation by raising the reaction temperature, pressure or the CO_2 concentration (DiGiovanni et al., 2024). The relative humidity of the gas phase during direct gas–solid carbonation is usually maintained below 20%, to avoid excessive pore water that could hinder CO_2 diffusion into the solid surface. Usually, this reaction is under 350 to 600 centigrade (Tian et al., 2013). Besides, this process suffers from slow reaction kinetics and low conversion and always takes a very long time (Liu et al., 2021).

As the temperature increases, the CO_2 uptake increases, which is between 1% to 8% (per kg steel slag can store 0.01 kg-0.08 kg CO_2). It can be represented as equations (2-24) to (2-27).

(i-b) Aqueous carbonation

Gas–liquid–solid carbonation involves the reaction of CO_2 with a solid material in an aqueous or water-based medium. Compared with gas–solid carbonation, direct aqueous mineral carbonation is a multiphase reaction that can achieve relatively high CO_2 capture efficiency even at ambient temperature and atmospheric pressure, because CO_2 dissolves in water to form reactive carbonate species that readily react with calcium- or magnesium-bearing solids. Dissolved CO_2 forms carbonic acid, which subsequently dissociates to yield H^+, HCO_3^- and CO_3^{2-} ions that promote the dissolution and subsequent carbonation of steel slag minerals. During the reaction, the dissolution of alkaline oxides such as CaO and MgO increases the solution alkalinity, frequently resulting in pH values exceeding 11. Under these strongly alkaline conditions, CO_3^{2-} predominate and drive the final precipitation step, represented by equations (2-29) and (2-30).

$$CO_2(g) \rightarrow CO_2(aq) \qquad (2-29)$$

$$CO_2(aq) + H_2O\ (l) \rightarrow H_2CO_3(aq) \rightarrow H^+(aq) + HCO_3{}^-(aq) \rightarrow 2H^+(aq) + CO_3{}^{2-}(aq) \qquad (2-30)$$

Therefore, aqueous carbonation can occur either in brine or wastewater as a gas–liquid system, or in suspensions of solid particles as a gas–liquid–solid slurry. In such environments, protons (H^+) promote the dissolution of Ca^{2+} from the γ-C_2S phase. In

the gas–liquid system, as described by equations (2-31) to (2-33), $CaCO_3$(s) and SiO_2(s) precipitate and form a product layer on the surface of the calcium silicate phase. This product layer is a critical feature of the carbonation process because it acts as a diffusion barrier, thereby inhibiting further carbonation (DiGiovanni et al., 2024).

$$2CaO \cdot SiO_2(s) + 4H^+(aq) \rightarrow Ca^{2+}(aq) + SiO_2(s) + 2H_2O\ (l) \qquad (2-31)$$

$$Ca^{2+}(aq) + {CO_3}^{2-}(aq) \rightarrow CaCO_3(s) \qquad (2-32)$$

$$2CaO \cdot SiO_2(s) + 2\,{CO_3}^{2-}(aq) + 4H^+(aq) \rightarrow 2CaCO_3(s) + SiO_2(s) + 2H_2O\ (l) \qquad (2-33)$$

Then, the hydration reaction of *f*-CaO/MgO generates $Ca(OH)_2(s)$ and $Mg(OH)_2(s)$, as shown in equations (2-34) to (2-35). Due to the very low content of *f*-CaO/MgO in the steel slag, the carbonation of Ca/Mg-silicates aqueous suspension is the dominant reaction, as shown in equation (2-36)-(2-42). (Chen et al., 2021; DiGiovanni et al., 2024; Zhang et al., 2023)

$$CaO(s) + H_2O(l) \rightarrow Ca(OH)_2(s) \qquad (2-34)$$

$$MgO(s) + H_2O(l) \rightarrow Mg(OH)_2(s) \qquad (2-35)$$

$$Ca(OH)_2(s) + CO_2(aq) \rightarrow CaCO_3(s) + H_2O\ (l) \qquad (2-36)$$

$$Mg(OH)_2(s) + CO_2(aq) + 2H_2O(l) \rightarrow MgCO_3(s) + 3H_2O\ (l) \qquad (2-37)$$

$$2(2CaO \cdot SiO_2)(s) + CO_2(aq) + 3H_2O(l) \rightarrow 3CaO \cdot 2SiO_2 \cdot H_2O + CaCO_3(s) \qquad (2-38)$$

$$2(3CaO \cdot SiO_2)(s) + CO_2(aq) + 3H_2O(l) \rightarrow 3CaO \cdot 2SiO_2 \cdot H_2O + 3CaCO_3(s) \qquad (2-39)$$

$$3CaO \cdot 2SiO_2(s) \cdot 4H_2O(s) + 3\,CO_2(aq) \rightarrow 3CaCO_3(s) + 2(2SiO_2 \cdot H_2O) + 2H_2O\ (l) \qquad (2-40)$$

$$3(2\mathrm{MgO}\cdot \mathrm{Si}O_2)(s) + 4H_2O(l) \rightarrow 2Mg_3Si_2O_5(OH)_4(s) \qquad (2-41)$$

$$Mg_3Si_2O_5(OH)_4(s) + 3CO_2(aq) \rightarrow 3MgCO_3(s) + 2SiO_2 + 2H_2O(l) \qquad (2-42)$$

Compared with the direct carbonation of steel slag, indirect carbonation is a two-step process consisting of metal leaching and subsequent carbonate precipitation, as shown in **Figure 2-7.**

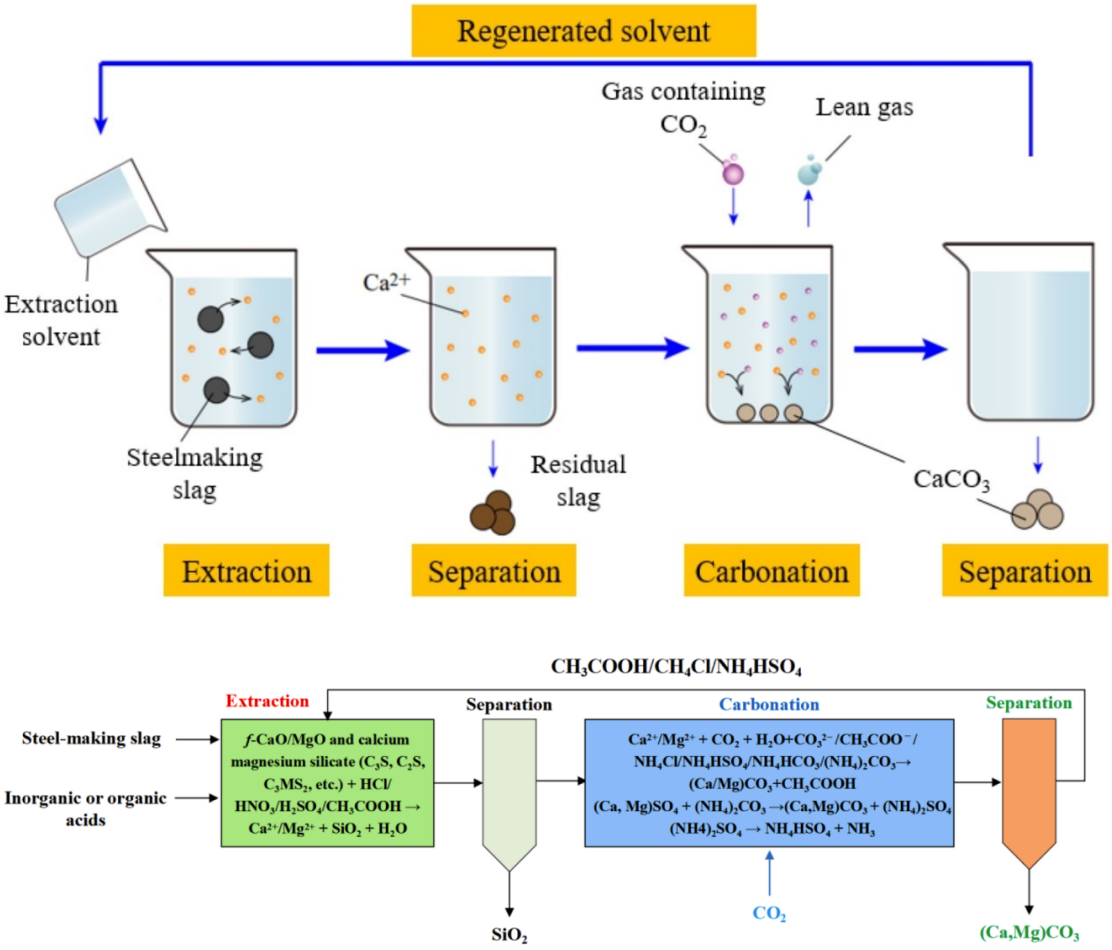

Figure 2-7 Indirect carbonation process of steelmaking slag (Chen et al., 2021)

Generally, the RO phase in steel slag (a solid solution of FeO-MnO-CaO-MgO) is known to have poor hydration activity. In fact, it has been determined that the RO phase with a high ratio of Fe/Mn can also be detrimental to the hydration activity of C2S. However,

the carbonation of the RO phase has been found to increase its hydration activity (Li et al., 2023).

In the first step, inorganic acids, organic acids or ammonium salts are used to extract Ca^{2+} and Mg^{2+} from the slag, leaving behind a silica-rich residue. In the second step, CO_2 is introduced into the leachate, where the dissolved metal ions react with carbonate species to form solid $CaCO_3$ or $(Ca,Mg)CO_3$ precipitates. The regenerated solvent can then be recycled for further leaching, enabling a closed-loop process with high CO_2 utilisation efficiency and a relatively pure carbonate product. In addition to carbon storage, carbonation improves the performance of slag for reuse. Carbonated slag is dimensionally stable, less prone to hydration expansion, and exhibits reduced leaching of trace metals. This enhances its suitability as aggregate, cement substitute, or raw material for precipitated calcium carbonate (PCC) production (Yildirim & Prezzi, 2011). As aggregate in concrete, carbonated slag can partially replace natural stone, reducing resource consumption and integrating carbon capture into construction practice. When processed into PCC, it provides high-purity carbonate products with commercial applications.

Despite these advantages, challenges remain for large-scale implementation. Energy requirements for grinding and pressurised carbonation, as well as variability in slag composition, affect the economics and consistency of the process. Moreover, regulatory acceptance for the widespread use of carbonated slag in structural applications is still developing. Further optimisation of reactor design, integration with steel plant operations, and standardisation of product quality are needed to fully

realise the potential of steel slag as a CO_2 sink. In summary, steel slag offers one of the most promising pathways for mineral carbonation within the construction sector. Its abundance, high reactivity, and dual benefits of CO_2 sequestration and material stabilisation make it a unique industrial by product with significant potential for climate mitigation. Continued research on process optimisation, life cycle performance, and practical utilisation will be essential to mainstream its application on a global scale. In the next section, the same analytical lens is applied to fly ash, which is less reactive on a mass basis but is available in large volumes and can be pelletised for efficient accelerated carbonation.

2.3.5 Fly Ash

Fly ash, a fine particulate by-product generated from the combustion of pulverised coal in thermal power plants, remains one of the most abundant industrial residues worldwide. Current annual production exceeds 500 Mt, and although significant amounts are incorporated into cement and concrete, vast quantities are still stored in landfills and ponds, posing environmental and land-use challenges (Uliasz-Bocheńczyk, 2024). From a CO_2 mitigation perspective, fly ash can contribute through two complementary routes: as a supplementary cementitious material (SCM), thereby indirectly lowering clinker-related emissions, and as a precursor for artificial aggregates subjected to accelerated carbonation for direct CO_2 sequestration.

Fly ash is chemical and mineralogically heterogeneous. According to ASTM standards, it is typically divided into Class F and Class C. Class F, produced from anthracite or

bituminous coal, is rich in amorphous aluminosilicate glass with low calcium content, while Class C, generated from sub-bituminous or lignite coal, contains higher CaO contents and occasionally residual free lime (Infante Gomes et al., 2021). This distinction is significant because carbonation reactivity depends strongly on calcium availability. Class C ashes exhibit higher affinity for CO_2, whereas Class F ashes rely more on the gradual reaction of aluminosilicate phases, giving them much lower uptake capacities (Fernández-Jiménez & Palomo, 2003; Uliasz-Bocheńczyk, 2024).

Fly ash as an SCM. When incorporated into blended cements, fly ash participates in pozzolanic reactions with calcium hydroxide released from clinker hydration, generating additional calcium silicate hydrates. From the perspective of carbonation, these hydrates and residual portlandite follow reaction pathways similar to those described previously for cement paste (Section 2.3.1). Fly ash is commonly classified into two types according to ASTM C618: Class C, which is rich in calcium, and Class F, which has lower calcium content. Class C ashes, with higher calcium contents, allow for modest direct carbonation, while Class F ashes are more inert. Nonetheless, the climate benefit of SCM utilisation lies not in direct CO_2 uptake but in clinker substitution. By replacing 15–30% of Portland cement, blended systems reduce emissions from limestone calcination, yielding a 15–30% reduction in embodied CO_2 (Scrivener et al., 2018; Wang et al., 2024). Recent experimental work has also shown that accelerated carbonation of fly ash–blended concretes can further improve CO_2 binding capacity, particularly under optimised humidity and curing conditions (Gaikwad & Sathe, 2025).

Fly ash as precursor for artificial aggregates. Beyond its role as SCM, fly ash can be agglomerated into pellets and subjected to accelerated carbonation curing, producing lightweight aggregates with both improved mechanical performance and stable CO_2 storage. The underlying mechanisms are analogous to those in steel slag carbonation (Section 2.3.4), involving dissolution of CO_2, mobilisation of calcium ions from reactive phases, and carbonate precipitation within pellet pores (Bouzoubaâ & Fournier, 2003). Carbonated pellets not only sequester CO_2 but also exhibit enhanced strength, reduced porosity, and lower water absorption. (Alptekin et al., 2025) reported uptake values of 30–100 kg CO_2 per tonne of fly ash, while recent studies have advanced this further: (Li et al., 2025) demonstrated the preparation of artificial aggregates from municipal solid waste fly ash cured with CO_2, achieving both high sequestration efficiency and improved aggregate quality, while (Ezu et al., 2024) developed porous construction materials from fly ash with enhanced uptake capacity through direct accelerated carbonation.

Fly ash carbonation improves not only CO_2 storage but also environmental safety. Leachability of toxic trace elements such as arsenic, selenium and mercury are reduced following carbonation, as these are often encapsulated within newly formed carbonate matrices (Alptekin et al., 2025). (Nawar et al., 2020) showed that high-CaO fly ash exhibited optimal CO_2 absorption at moderate water-to-solid ratios, pointing to a practical pathway for process optimisation. Furthermore, carbonation enhances dimensional stability and durability when fly ash is reused in concrete, reducing shrinkage and improving resistance to aggressive agents (Ukwattage et al., 2015;

Wang et al., 2024). From an LCA perspective, integrated carbonation and utilisation strategies provide clear advantages: (Uliasz-Bocheńczyk, 2024) demonstrated that coupling fly ash carbonation with CCUS frameworks can result in net negative emissions when flue gas is directly used, avoiding purification costs.

In summary, fly ash offers a dual contribution to carbon management strategies in construction. As SCM, it enables large-scale indirect reductions by lowering clinker demand, while as a feedstock for artificial aggregates it provides direct CO_2 sequestration. Although the inherent carbonation reactivity of fly ash is lower than that of steel slag, its sheer abundance and versatility make it indispensable in decarbonisation strategies. With the gradual decline of coal-fired power plants in some regions, attention is increasingly shifting towards legacy ash deposits. Recent studies highlight the potential of applying advanced carbonation methods, including high-pressure conditions and coupling with acid mine drainage or industrial effluents, to improve uptake (Zide et al., 2025). Future work should therefore prioritise optimising carbonation kinetics, ensure the environmental safety of carbonated products, and integrate these processes into circular construction systems.

2.3.6 Timber and Biomaterials

Timber represents one of the most established and effective natural carbon storage materials in the construction sector. Through photosynthesis, trees absorb atmospheric CO_2 and store it as carbon in cellulose, hemicellulose and lignin. This stored carbon can remain locked for decades or even centuries when timber is used

in long-lived construction products. In contrast with mineral-based pathways discussed in earlier sections, the carbon sequestration mechanism of timber originates from biological processes. As (Churkina et al., 2020) highlighted, the combination of high atmospheric CO_2 concentrations, extended growing seasons and warmer temperatures is projected to accelerate forest growth in the future, offering a significant opportunity to expand the resource base for bio-based construction.

Engineered timber products such as cross-laminated timber (CLT) and laminated veneer lumber (LVL) have emerged as viable alternatives to conventional concrete and steel in structural applications. Their production requires substantially less embodied energy and avoids the process of emissions associated with cement manufacture. More importantly, when deployed in large-scale construction such as mid-rise residential or commercial buildings, engineered timber provides long-term carbon storage. Unlike carbonation reactions in mineral systems, the storage in timber arises from biogenic carbon fixed during growth rather than subsequent reaction. The principle of CO_2 storage in timber material is illustrated in **Figure 2-8**.

For timber systems, end-of-life management is particularly important. Landfilling generally offers greater potential for long-term carbon retention than incineration, thereby contributing more effectively to emission reduction. However, considerations of land availability, environmental impacts and social acceptance must also be taken into account. Therefore, special attention should be given to the C1–C4 end-of-life stages when evaluating the overall carbon balance of timber-based construction.

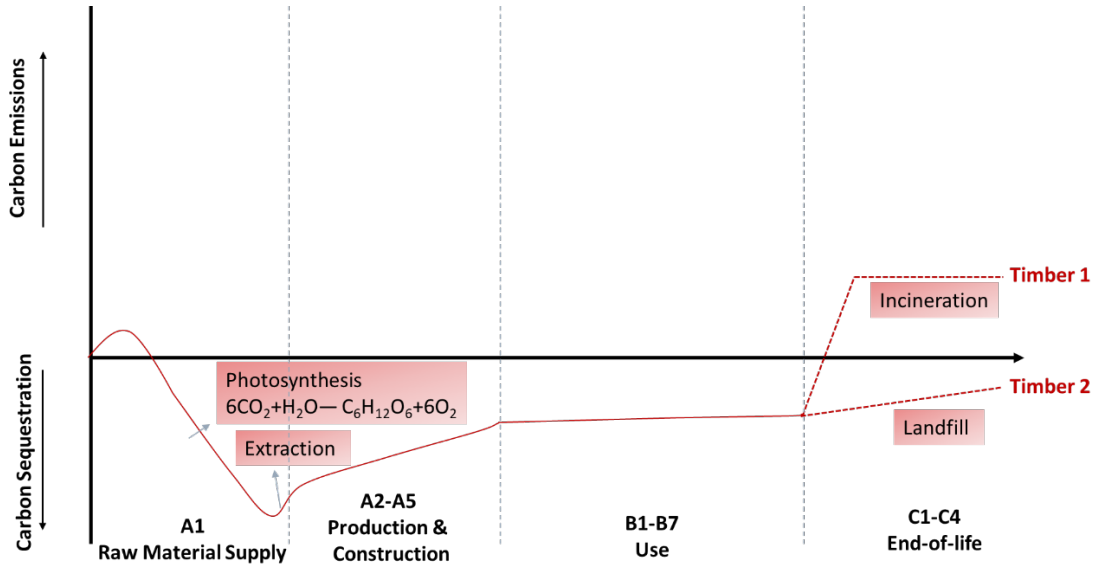

Figure 2-8 Principle of CO_2 storage in timber material

In addition to timber, a range of other biomaterials has attracted increasing attention for their potential to store atmospheric carbon in construction. Biochar cement filler is one of the most promising candidates. Produced by pyrolysis of biomass under limited oxygen conditions, biochar is a stable carbon-rich material with an aromatic structure that resists microbial degradation. When blended into cement, biochar not only retains carbon but also contributes to improved durability, reduced permeability and enhanced resistance to chloride ingress (Saniul Haque Mahi et al., 2025). The use of biochar aligns with circular economy principles, as it transforms agricultural or forestry residues into high-value construction inputs.

Bio-based plastics represent another pathway for embedding biogenic carbon into construction. These polymers, derived from plant-based feedstocks such as starch, sugarcane or lignin, retain the carbon captured during plant growth throughout their service life. Their applications in construction range from insulation foams to interior

finishing products, where their long service life extends the period of carbon storage (RameshKumar et al., 2020). Similarly, bio-based asphalt bitumen substitutes petroleum-derived binders with renewable plant-based oils or lignin derivatives, effectively incorporating atmospheric carbon into pavements and road infrastructure (Tupenaite et al., 2023). The advantage of these materials lies in their ability to displace fossil-based alternatives while simultaneously acting as carbon sinks.

The durability of carbon storage in bio-based materials depends critically on end-of-life management. If timber or bio-based materials are incinerated without carbon capture, the stored CO_2 is released back into the atmosphere, nullifying the benefit. Conversely, if materials are recycled into new construction products, cascaded into other uses, or sequestered in landfills under controlled conditions, carbon storage can be prolonged significantly (Gu et al., 2022). In this respect, engineered timber products offer particular promise because their large element sizes (e.g. CLT panels) are amenable to direct reuse in subsequent construction cycles.

The climate benefits of substituting conventional materials with bio-based alternatives extend beyond direct carbon storage. Life cycle assessment studies demonstrate that replacing reinforced concrete or steel with timber can reduce embodied greenhouse gas emissions of buildings by 30–60%, depending on regional energy mixes and design assumptions (Leskinen et al., 2018). When biochar fillers are integrated into cement or asphalt, further emission reductions are realised both through the avoided production of conventional materials and the permanence of biochar carbon. Similarly, bio-based polymers and asphalt contribute to reducing

dependency on fossil feedstocks, a crucial element of long-term decarbonisation strategies.

Recent advances have underscored the scalability of these approaches. For instance, (Churkina et al., 2020) estimated that global substitution of concrete and steel with timber in mid-rise buildings could store up to 700 Mt of CO_2 annually. More recent projections indicate that sustainable forest management combined with engineered timber construction could increase the total carbon stock in the built environment to several gigatonnes by 2050 (Gu et al., 2022). In parallel, biochar integration into cementitious composites has been demonstrated at pilot scale, showing both enhanced strength and carbon retention (Tupenaite et al., 2023). The use of lignin-based asphalt binders has similarly been advanced in Europe, where field trials demonstrate improved rutting resistance and reduced life-cycle emissions (Wang et al., 2025).

In summary, timber and bio-based construction materials provide one of the highest potentials for long-term carbon retention in the built environment. Their sequestration mechanism is fundamentally different from mineral carbonation, relying on photosynthetic uptake during biomass growth rather than chemical binding post-production. If maintained in durable structures and managed responsibly at end-of-life, these materials can lock away atmospheric carbon for decades to centuries, while simultaneously displacing the carbon-intensive production of concrete, cement and steel. The integration of timber, biochar, bio-based plastics and bio-based asphalt

into construction systems therefore represents a crucial strategy within the portfolio of approaches for reducing the climate impact of the built environment.

2.4 CO_2 Uptake Theoretical Potential in Construction Materials

Although the mechanisms of CO_2 uptake across different construction materials vary considerably, ranging from mineral carbonation in cementitious phases and industrial by-products to biogenic fixation in timber, the dominant chemical driver for inorganic systems is the presence of reactive CaO. When exposed to CO_2 under appropriate conditions, CaO can undergo carbonation reactions forming $CaCO_3$. Although $CaCO_3$ is generally considered a stable solid under ambient conditions, it can partially dissolve in water and react with dissolved CO_2 to form bicarbonate species under high CO_2 concentrations or in aqueous environments. Therefore, the CaO content provides a practical basis for estimating the theoretical maximum CO_2 storage potential. While other oxides such as MgO and alkali metal oxides may also participate in carbonation to a limited extent, their abundance and reactivity are typically lower and are thus regarded as secondary. For consistency and comparability across materials, the following assessment focuses primarily on CaO as the key reactive constituent.

The chemical compositions of representative materials are summarised in **Table 2-4**. These values illustrate the wide variation in CaO availability: Portland cement contains more than 60% CaO, explaining its relatively high carbonation capacity; RCA contain smaller fractions of CaO due to the dilution effect of natural aggregates; steel slags, depending on process origin, are also rich in CaO and MgO, which underpin their

strong mineral carbonation potential; fly ashes, especially Class C, contain moderate levels of CaO, while Class F ashes are predominantly siliceous and therefore exhibit lower uptake capacity.

Table 2-4 Calcium oxide (CaO) content of major construction materials relevant to CO_2 storage potential

Material	*Subtype*	*CaO content (wt%)*
Cement products	OPC	58.1 -64.18 (Bediako & Amankwah, 2015)
Natural aggregate	River sand	0.5 -1.1 (Nedeljković et al., 2021)
	Gravel	0.26 (Nedeljković et al., 2021)
Recycled concrete aggregate (RCA)	Fine	17.1 -27.5 (Limbachiya et al., 2007)
	Coarse	11.19 -16.86 (Limbachiya et al., 2007)
Steel slag	Blast furnace slag (BFs)	30 -42 (Mo et al., 2017)
	Basic oxygen furnace slag (BOFs)	40.82 -54.29 (Martins et al., 2021)
	Electric arc furnace slag (EAFs)	25.08 – 45.9 (Martins et al., 2021)
Fly ash	Class F	0.7 – 6.7 (Akbulut et al., 2024)
	Class C	11.5 – 29.0 (Akbulut et al., 2024)

In contrast, timber and other bio-based materials do not store CO_2 via carbonation but instead through the carbon already fixed in their biomass structure. The raw data on the chemical composition of concrete components and the elemental composition of timber and biomaterials are provided in Appendix A.1.

Table 2-5 Carbon content of timber and selected bio-based construction materials

Material type	*Subtype*	*Carbon content (wt%)*
Timber	–	49 – 51 ("Wood as Bio-Based Building Material," 2017)
Biomaterials	Biochar	59.24 – 82.77 (Wijitkosum & Jiwnok, 2019)
	Bio-based plastics	37.14 – 59.53 (Lombardi et al., 2024)
	Bio-based asphalt bitumen	30.52 – 77.01 (Bao et al., 2020)

Accordingly, the subsequent calculations of theoretical CO_2 storage capacity are derived by linking the CaO contents reported in **Table 2-4** and the carbon contents reported in **Table 2-5** with their respective stoichiometric conversion factors, while recognising that real-world storage values will depend on kinetics, exposure conditions, and processing routes.

Prior to analysing experimental data, theoretical CO_2 uptake levels are first calculated, to which the reported experimental measurements can be compared. For cement, the calculation can be performed directly from its phase composition. As indicated earlier in Table 2.6, C_2S, C_3S, C_3A and C_4AF account for 90–92% of cement. Among these, C_4AF,

whose mass fraction ranges from 0% to 18% in cement, rarely carbonates. According to the carbonation reactions presented in Equations (2-18) to (2-23), one mole of C_2S, C_3S and C_3A can absorb two, three and three moles of carbon dioxide, respectively. On a mass basis, one kilogram of C_2S, C_3S and C_3A can absorb 0.511 kg, 0.576 kg and 0.487 kg CO_2, respectively. The overall uptake in cement (C_t) can therefore be calculated as equation (2-43).

$$\begin{cases} C_t = 0.511x_0 + 0.576x_1 + 0.487x_2 \\ 0.07 \le x_0 \le 0.32 \\ 0.45 \le x_1 \le 0.75 \\ 0 \le x_2 \le 0.13 \\ 0 \le x_3 \le 0.18 \\ 0.02 \le x_4 \le 0.10 \\ x_0 + x_1 + x_2 + x_3 + x_4 = 1 \end{cases} \quad (2-43)$$

where x_0, x_1, x_2, x_3, x_4 are the mass fractions of C_2S, C_3S, C_3A, C_4AF, and gypsum, respectively; their ranges are according to **Table 2-2**.

For other inorganic construction materials such as recycled concrete aggregates, steel slags and fly ashes, the carbonation potential is estimated from their bulk CaO content. On a stoichiometric basis, one mole of CaO (molar mass 56 g/mol) reacts with one mole of CO_2 (molar mass 44 g/mol) to form $CaCO_3$. The ratio 44/56=0.785744/56 = 0.785744/56=0.7857 therefore represents the theoretical maximum uptake of CO_2 per unit mass of CaO. The corresponding uptake C_{inorg} (kg CO_2/kg material) is expressed as:

$$C_{inorg} = 0.7857 \times w_{CaO} \quad (2-44)$$

where w_{CaO} is the mass fraction of CaO in the material.

In contrast, timber and bio-based construction materials store CO_2 through biogenic carbon fixation rather than mineral carbonation. The relevant reaction is the oxidation of carbon to CO_2, where one mole of carbon (12 g/mol) corresponds to one mole of CO_2 (44 g/mol). The ratio 44/12=3.6744/12 = 3.6744/12=3.67 thus represents the theoretical maximum uptake per unit mass of carbon. Accordingly, the uptake C_{bio} is expressed as:

$$C_{bio} = 3.67 \times w_C \qquad (2-45)$$

In equation (42), w_C denotes the mass fraction of biogenic carbon in the dry material. For the bio-based materials considered in this analysis, the adopted w_C values are taken from **Table 2-5** and represent the typical carbon contents of timber, biochar, bio-based plastics, and bio-based asphalt (The results are presented in Appendix A.1 **Table A-7**).

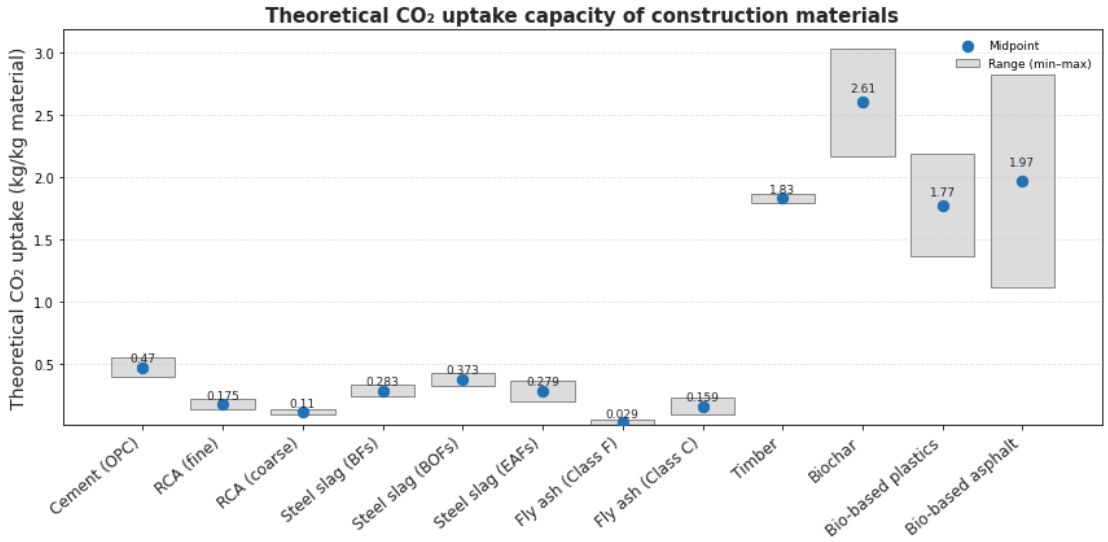

Figure 2-9 Theoretical CO_2 uptake capacity of construction materials

Figure 2-9 presents the theoretical CO_2 uptake capacities of representative construction materials, distinguishing between CaO-based mineral systems and C-based bio-derived products. The results reveal a marked contrast across material categories. Ordinary Portland cement (OPC) shows relatively high uptake values around 0.47–0.55 kg/kg material, reflecting its high CaO content. Recycled concrete aggregates and steel slags exhibit intermediate capacities, typically 0.09–0.43 kg/kg material, with slag displaying the highest potential among industrial by-products. Fly ash, particularly Class F, shows comparatively low values (0.005–0.05 kg/kg material), whereas Class C reaches up to 0.23 kg/kg material due to its higher CaO content.

2.5 Global Potential of CO_2 Uptake in Construction Materials

In order to estimate the global CO_2 storage potential of construction materials based on their theoretical uptake capacity, it is first necessary to establish the magnitude and distribution of their annual production. Cement constitutes by far the largest flow, with worldwide output reaching approximately 4,200 Mt in 2024 (World Population Review, 2025). This figure highlights its dominant role in the built environment, particularly in emerging economies where infrastructure expansion remains ongoing, while global growth overall has stabilized. RCA, while currently limited in scale, has been developing rapidly due to the increasing focus on circularity and the valorisation of construction and demolition waste. In 2024, global RCA production was estimated at 540 Mt, reflecting both the scale of demolition activities in industrialized regions and the gradual integration of recycled materials into mainstream construction practices (Younes et al., 2024).

Fly ash, a major by-product of coal combustion, continues to represent a substantial secondary material stream. In 2023, global production was estimated at 390 Mt, with notable regional variation linked to coal dependence (Sharma & Yadav, 2021). Within this total, approximately 234 Mt corresponds to Class F fly ash, typically characterized by low calcium content and longer-term pozzolanic activity, while 156 Mt corresponds to Class C fly ash, generally richer in calcium and more reactive. This distinction is crucial, as the different classes of fly ash not only determine potential applications in cementitious systems but also influence their capacity for mineral carbonation.

The steel industry also generates large quantities of mineral by-products. In 2023, global blast furnace slag (BFS) production was estimated in the range of 330–390 Mt (Liu et al., 2021), reflecting the volume of pig iron smelting, with approximately 250–300 kg of BFS produced per tonne of pig iron (Liu et al., 2021). In parallel, steel slag, encompassing both BOFS and EAFS, contributed an additional 190–290 Mt worldwide. Considering the distribution of steelmaking routes, with about 70% proceeding through the BOF process and 30% through the EAF process, the majority of this slag originates from BOF operations. Nevertheless, EAF slag remains a significant stream, particularly in regions with high scrap utilization.

Beyond mineral-based flows, renewable and bio-based materials also represent an important component of the global material system. Timber used in construction accounted for approximately 2,000 Mt globally in 2024 (Food and Agriculture Organization of the United Nations, 2024), with North America, Russia, China, and Brazil as the principal producers. Its widespread use reflects both traditional practices

and contemporary trends toward biogenic materials in low-carbon construction. Biomaterials, although quantitatively minor at present, are gaining increasing attention. Current global estimates suggest annual production of about 0.35 Mt of biochar (International Biochar Initiative, 2025) and 2 Mt of bioplastics (European Environment Agency, 2025), while bio-based bitumen remains only a negligible fraction of overall bitumen supply. Despite their relatively small scale compared to cementitious and metallurgical by-products, these biomaterials represent emerging alternatives with distinct properties and long-term growth potential.

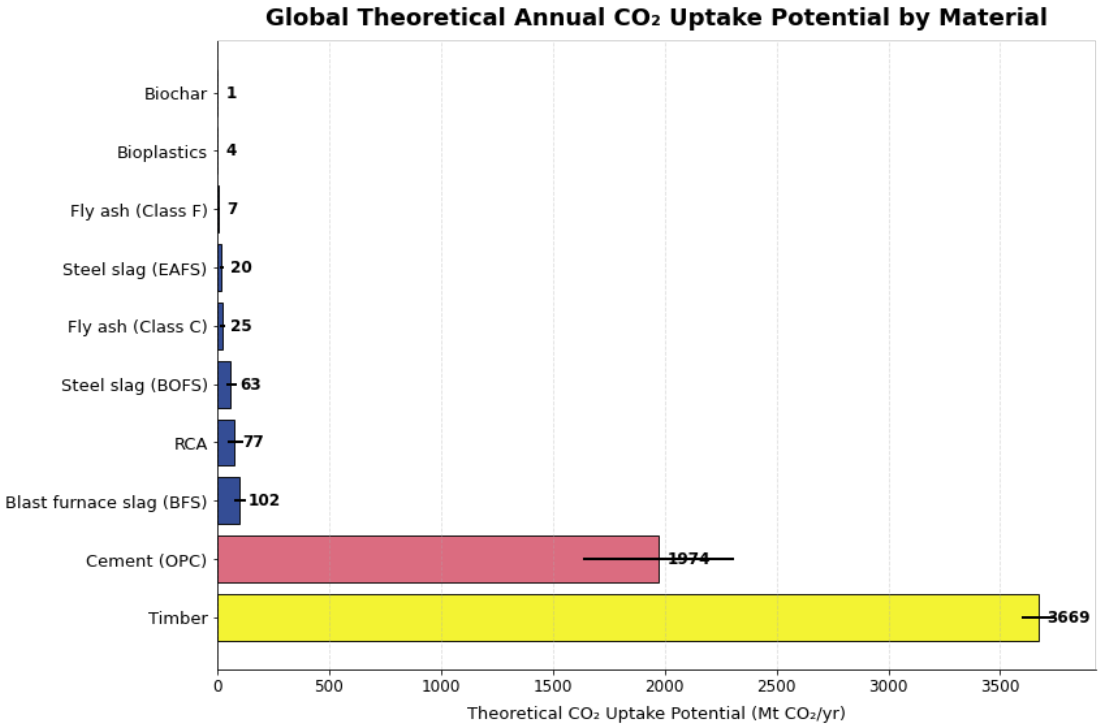

Figure 2-10 Global theoretical annual CO_2 uptake potential by material

Building on the theoretical CO_2 uptake values of individual materials calculated in Section 2.4, we further derive the corresponding global potentials by combining these uptake factors with annual production volumes. The aggregated results are presented

in **Figure 2-10** which illustrates the comparative scale of different material categories at the global level (The results are presented in Appendix A.1 **Table A-8**).

The results highlight substantial variation in the theoretical CO_2 uptake potential among construction materials, reflecting both the scale of global production and the chemical or biogenic composition of each stream. Cement represents the largest mineral-based contributor, with an uptake potential of 1.6–2.3 Gt CO_2 per year, consistent with its massive global output and high CaO content. RCA adds a further 48–117 Mt, while BFS contributes 78–129 Mt annually. Steelmaking slags also play an important role: BOFS and EAFS together amount to 54–118 Mt CO_2 per year, with BOFS dominating due to the prevalence of BOF steelmaking. Fly ash exhibits clear contrasts between types: Class F, though produced in larger quantities, accounts for 1–12 Mt, while Class C, despite its smaller volume, contributes 14–36 Mt owing to its higher CaO content. Collectively, these mineral carbonation materials provide an annual uptake potential of 1.83–2.72 Gt CO_2 (midpoint ~2.27 Gt).

The results highlight substantial variation in the theoretical CO_2 uptake potential among construction materials, reflecting both the scale of global production and the chemical or biogenic composition of each stream. Cement represents the largest mineral-based contributor, with an uptake potential of 1.6–2.3 Gt CO_2 per year, consistent with its massive global output and high CaO content. RCA adds a further 48–117 Mt, while BFS contributes 78–129 Mt annually. Steelmaking slags also play an important role: BOFS and EAFS together amount to 54–118 Mt CO_2 per year, with BOFS dominating due to the prevalence of BOF steelmaking. Fly ash exhibits clear

contrasts between types: Class F, though produced in larger quantities, accounts for 1–12 Mt, while Class C, despite its smaller volume, contributes 14–36 Mt owing to its higher CaO content. Collectively, these mineral carbonation materials provide an annual uptake potential of 1.83–2.72 Gt CO_2 (midpoint ~2.27 Gt).

Timber shows a theoretical storage potential exceeding 3.6–3.7 Gt CO_2 per year, although its widespread use in construction faces greater challenges compared with mineral-based materials, particularly in terms of durability, fire safety, and regulatory acceptance. Biomaterials such as biochar and bioplastics add ~4–5 Mt CO_2 per year, reflecting their emerging but still modest scale in comparison with major material flows. When combined, biogenic resources contribute 3.60–3.75 Gt CO_2 annually (midpoint ~3.67 Gt).

Overall, the global theoretical CO_2 uptake capacity from all considered materials is estimated at 5.43–6.47 Gt CO_2 per year (midpoint ~5.94 Gt). These results underscore the pivotal role of mineral-based construction materials, namely cement, RCA, steel slag, and fly ash, in shaping feasible carbon storage pathways, while also recognizing the significant theoretical potential of timber and other bio-based alternatives.

2.6 Summary and Key Research Gaps

This chapter has reviewed the current understanding of the CO_2 uptake potential of major construction materials. It first introduced the available sources of CO_2 for mineralisation and absorption, followed by a discussion of the principles and chemical processes that govern uptake in concrete, cement products, aggregates, steel slag, fly

ash, timber and biomaterials. The theoretical uptake capacities of both alkaline and bio-based construction materials were quantified, and when combined with their respective global production volumes they were shown to amount to an overall potential of between 5.4 and 6.5 Gt CO_2 yr^{-1}, comprising approximately 3.7 Gt CO_2 yr^{-1} from bio-based and 2.7–2.8 Gt CO_2 yr^{-1} from alkaline materials. This estimate aligns with previous global assessments, which identified a CO_2 storage potential of approximately 2.9 Gt CO_2 yr^{-1} for alkaline industrial residues (Renforth, 2019). The bio-based component is consistent with the upper range of recent evaluations, which report potentials of up to 3 Gt CO_2 yr^{-1} for bio-based carbon storage pathways including timber construction and biochar (Smith et al., 2023). These findings collectively highlight the substantial, though technically constrained, potential of both alkaline and bio-based materials to contribute to large-scale CO_2 mineralisation and removal within the construction sector. At the same time, important gaps in current knowledge remain. Most existing studies have been conducted under laboratory conditions and tend to focus on simplified systems, leaving many of the critical variables that influence carbonation underexplored. Factors such as particle size distribution, curing environment, reaction kinetics, and material heterogeneity have not been fully examined in relation to industrial practice. Moreover, the feasibility of scaling up these processes to match the very high production volumes characteristic of the construction sector has received limited attention. This lack of integration between laboratory findings and industrial conditions restricts our ability to translate theoretical uptake capacities into realistic assessments of mitigation potential.

Building on this review, the following chapters turn to a more detailed analysis of cement and concrete (Chapter 3), recycled concrete aggregate (Chapter 4) and steel slag (Chapter 5). These materials have been selected because they combine very large global production volumes with relatively high calcium oxide contents that determine their carbonation reactivity, and because they are closely embedded within established industrial supply chains. The subsequent chapters therefore address the identified gaps by modelling the carbonation processes in detail, investigating the role of key variables, embedding the results within life cycle assessment frameworks, and evaluating the global mitigation potential of these material systems under realistic industrial conditions.

References

Ahmad, S., Assaggaf, R. A., Maslehuddin, M., Al-Amoudi, O. S. B., Adekunle, S. K., & Ali, S. I. (2017). Effects of carbonation pressure and duration on strength evolution of concrete subjected to accelerated carbonation curing. *Construction and Building Materials*, *136*, 565–573. https://doi.org/10.1016/J.CONBUILDMAT.2017.01.069

Aïtcin, P.-C. (2016). Portland cement. In *Science and Technology of Concrete Admixtures* (pp. 27–51). Elsevier. https://doi.org/10.1016/B978-0-08-100693-1.00003-5

Akbulut, Z. F., Yavuz, D., Tawfik, T. A., Smarzewski, P., & Guler, S. (2024). Enhancing Concrete Performance through Sustainable Utilization of Class-C and Class-F Fly Ash: A Comprehensive Review. *Sustainability*, *16*(12), 4905. https://doi.org/10.3390/su16124905

Alptekin, F. M., Zanoletti, A., Depero, L. E., & Bontempi, E. (2025). Accelerated carbonation of municipal waste fly ash for carbon sequestration: a review. In *Environmental Chemistry Letters*. Springer Nature. https://doi.org/10.1007/s10311-025-01866-z

Bae, J.-H., Kil, T., Yun, T., & Yang, B. (2025). An intricately designed modeling of concrete carbonation utilizing reactive molecular dynamics and micromechanics. *Construction and Building Materials*, *489*, 142297. https://doi.org/10.1016/j.conbuildmat.2025.142297

Bao, D.-X., Yu, Y.-Y., & Zhao, Q.-M. (2020). Evaluation of the chemical composition and rheological properties of bio-asphalt from different biomass sources. *Road Materials and Pavement Design*, *21*(7), 1829–1843. https://doi.org/10.1080/14680629.2019.1568287

Baras, A., Li, J., Ni, W., Hussain, Z., & Hitch, M. (2023). Evaluation of Potential Factors Affecting Steel Slag Carbonation. *Processes*, *11*(9), 2590.

https://doi.org/10.3390/pr11092590

Bediako, M., & Amankwah, E. O. (2015). Analysis of Chemical Composition of Portland Cement in Ghana: A Key to Understand the Behavior of Cement. *Advances in Materials Science and Engineering*, *2015*, 1–5. https://doi.org/10.1155/2015/349401

Biava, G., Depero, L. E., & Bontempi, E. (2024). Accelerated Carbonation of Steel Slag and Their Valorisation in Cement Products: A Review. *Spanish Journal of Soil Science*, *14*. https://doi.org/10.3389/sjss.2024.12908

Binder, E., Königsberger, M., Díaz Flores, R., Mang, H. A., Hellmich, C., & Pichler, B. L. A. (2023). Thermally activated viscoelasticity of cement paste: Minute-long creep tests and micromechanical link to molecular properties. *Cement and Concrete Research*, *163*, 107014. https://doi.org/10.1016/J.CEMCONRES.2022.107014

Bouzoubaâ, N., & Fournier, B. (2003). Optimization of fly ash content in concrete: Part I: Non-air-entrained concrete made without superplasticizer. *Cement and Concrete Research*, *33*(7), 1029–1037. https://doi.org/10.1016/S0008-8846(03)00004-8

Britannica. (2022). *https://www.britannica.com/technology/cement-building-material/The-major-cements-composition-and-properties*.

British Standards Institution. (2015). *Concrete. Complementary British Standard to BS EN 206. Part 1, Method of specifying and guidance for the specifier.*

Chen, Z., Cang, Z., Yang, F., Zhang, J., & Zhang, L. (2021). Carbonation of steelmaking slag presents an opportunity for carbon neutral: A review. *Journal of CO2 Utilization*, *54*, 101738. https://doi.org/10.1016/j.jcou.2021.101738

Churkina, G., Organschi, A., Reyer, C.P.O. et al. Buildings as a global carbon sink. Nat Sustain 3, 269–276 (2020). https://doi.org/10.1038/s41893-019-0462-4

DiGiovanni, C., Hisseine, O. A., & Awolayo, A. N. (2024). Carbon dioxide sequestration through steel slag carbonation: Review of mechanisms, process parameters, and cleaner upcycling pathways. *Journal of CO2 Utilization*, *81*, 102736. https://doi.org/10.1016/j.jcou.2024.102736

El-Hassan, H. (2021). Accelerated Carbonation Curing as a Means of Reducing Carbon Dioxide Emissions. In *Cement Industry - Optimization, Characterization and Sustainable Application*. IntechOpen. https://doi.org/10.5772/intechopen.93929

European Environment Agency. (2025). *Global bio-based plastics production capacity*. European Environment Agency. https://www.eea.europa.eu/en/circularity/sectoral-modules/plastics/global-bio-based-plastics-production-capacity.

Ezu, A., Moukannaa, S., Kriskova, L., Illikainen, M., & Kilpimaa, K. (2024). Direct carbonation of porous materials produced from self-hardened paper mill fly ash. *Case Studies in Construction Materials*, *20*, e03243. https://doi.org/10.1016/J.CSCM.2024.E03243

Fernández-Jiménez, A., & Palomo, A. (2003). Characterisation of fly ashes. Potential reactivity as alkaline cements☆. *Fuel*, *82*(18), 2259–2265. https://doi.org/10.1016/S0016-2361(03)00194-7

Food and Agriculture Organization of the United Nations. (2024). *The state of the world's forests 2024*. Food and Agriculture Organization of the United Nations.

Gaikwad, P., & Sathe, S. (2025). Effect of fly ash on compressive strength, carbonation and corrosion resistance of reinforced concrete: a systematic review. *World Journal of Engineering*, *22*(1), 40–60. https://doi.org/10.1108/WJE-07-2023-0240

Gonçalves, P., & Brito, J. de. (2010). Recycled aggregate concrete (RAC) – comparative analysis of existing specifications. *Magazine of Concrete Research*, *62*(5), 339–346. https://doi.org/10.1680/macr.2008.62.5.339

Gu, H., Nepal, P., Arvanitis, M., & Alderman, D. (2022). Carbon Impacts of Engineered Wood Products in Construction. In *Engineered Wood Products for Construction*. IntechOpen. https://doi.org/10.5772/intechopen.99193

Holappa, L., Kekkonen, M., Jokilaakso, A., & Koskinen, J. (2021). A Review of Circular Economy Prospects for Stainless Steelmaking Slags. *Journal of Sustainable Metallurgy*, *7*(3), 806–817. https://doi.org/10.1007/s40831-021-00392-w

Infante Gomes, R., Brazão Farinha, C., Veiga, R., de Brito, J., Faria, P., & Bastos, D. (2021). CO2 sequestration by construction and demolition waste aggregates and effect on mortars and concrete performance - An overview. *Renewable and Sustainable Energy Reviews*, *152*, 111668. https://doi.org/10.1016/J.RSER.2021.111668

International Biochar Initiative. (2025, March 25). *2023 Global Biochar Market Report*. International Biochar Initiative. https://biochar-international.org/news/global-biochar-market-soars-to-600-million-in-2023-setting-the-stage-for-future-growth/

Issa, S., Islam, M., Issa, M., Yousif, A., & Issa, M. (2000). Specimen and Aggregate Size Effect on Concrete Compressive Strength. *Cement, Concrete, and Aggregates*, *22*(2), 103–115. https://doi.org/10.1520/CCA10470J

Kapetaki, Z., Brandani, P., Brandani, S., & Ahn, H. (2015). Process simulation of a dual-stage Selexol process for 95% carbon capture efficiency at an integrated gasification combined cycle power plant. *International Journal of Greenhouse Gas Control*, *39*, 17–26. https://doi.org/10.1016/j.ijggc.2015.04.015

Khaiyum, M. Z., Sarker, S., & Kabir, G. (2023). Evaluation of Carbon Emission Factors in the Cement Industry: An Emerging Economy Context. *Sustainability*, *15*(21), 15407. https://doi.org/10.3390/su152115407

Koytsoumpa, E. I., Bergins, C., & Kakaras, E. (2018). The CO2 economy: Review of CO2 capture and reuse technologies. In *Journal of Supercritical Fluids* (Vol. 132, pp.

3–16). Elsevier B.V. https://doi.org/10.1016/j.supflu.2017.07.029

Leemann, A., Winnefeld, F., Münch, B., & Tiefenthaler, J. (2023). Accelerated carbonation of recycled concrete aggregates and its implications for the production of recycling concrete. *Journal of Building Engineering*, *79*, 107779. https://doi.org/10.1016/j.jobe.2023.107779

Leskinen, P., Cardellini, G., González-García, S., Hurmekoski, E., Sathre, R., Seppälä, J., Smyth, C., Stern, T., & Verkerk, P. J. (2018). *Substitution effects of wood-based products in climate change mitigation* (From Science to Policy). European Forest Institute. https://doi.org/10.36333/fs07

Li, L., & Wu, M. (2022). An overview of utilizing CO2 for accelerated carbonation treatment in the concrete industry. *Journal of CO2 Utilization*, *60*, 102000. https://doi.org/10.1016/J.JCOU.2022.102000

Li, W., Cao, M., Wang, D., & Chang, J. (2023). Increase in volume stability of RO phases in steel slag by combined treatment of alkali and dry carbonation. *Construction and Building Materials*, *396*, 132345. https://doi.org/10.1016/j.conbuildmat.2023.132345

Li, Z., Wu, Z., Long, Q., Feng, W., Liu, S., & Yuan, X. (2025). Preparation of municipal waste incineration fly ash artificial aggregate using CO_2 curing and its properties. Journal of CO2 Utilization, 93, 103042. https://doi.org/10.1016/J.JCOU.2025.103042

Limbachiya, M. C., Marrocchino, E., & Koulouris, A. (2007). Chemical–mineralogical characterisation of coarse recycled concrete aggregate. *Waste Management*, *27*(2), 201–208. https://doi.org/10.1016/J.WASMAN.2006.01.005

Liu, P., Yu, Z., & Chen, Y. (2020). Carbonation depth model and carbonated acceleration rate of concrete under different environment. *Cement and Concrete Composites*, *114*, 103736. https://doi.org/10.1016/j.cemconcomp.2020.103736

Liu, W., Teng, L., Rohani, S., Qin, Z., Zhao, B., Xu, C. C., Ren, S., Liu, Q., & Liang, B.

(2021). CO2 mineral carbonation using industrial solid wastes: A review of recent developments. *Chemical Engineering Journal*, *416*, 129093. https://doi.org/10.1016/j.cej.2021.129093

Lombardi, F., Bartolucci, L., Cordiner, S., Costa, G., Falsetti, A., Mele, P., Mercurio, M., Mulone, V., & Sorino, D. (2024). Chemical-Physical Characterization of Bio-Based Biodegradable Plastics in View of Identifying Suitable Recycling/Recovery Strategies and Numerical Modeling of PLA Pyrolysis. *Waste and Biomass Valorization*, *15*(3), 1653–1670. https://doi.org/10.1007/s12649-023-02159-8

Ma, M., Zhou, N., Feng, W., & Yan, J. (2024). Challenges and opportunities in the global net-zero building sector. *Cell Reports Sustainability*, *1*(8), 100154. https://doi.org/10.1016/j.crsus.2024.100154

Martins, A. C. P., Franco de Carvalho, J. M., Costa, L. C. B., Andrade, H. D., de Melo, T. V., Ribeiro, J. C. L., Pedroti, L. G., & Peixoto, R. A. F. (2021). Steel slags in cement-based composites: An ultimate review on characterization, applications and performance. *Construction and Building Materials*, *291*, 123265. https://doi.org/10.1016/J.CONBUILDMAT.2021.123265

Mo, K. H., Ling, T. C., Alengaram, U. J., Yap, S. P., & Yuen, C. W. (2017). Overview of supplementary cementitious materials usage in lightweight aggregate concrete. *Construction and Building Materials*, *139*, 403–418. https://doi.org/10.1016/J.CONBUILDMAT.2017.02.081

Nawar, A., Ali, M., Waqas, A., Javed, A., Iqbal, N., & Khan, R. (2020). Effect of Different Activation Processes on CaO/Fly Ash Mixture for CO2 Capture. *Energy and Fuels*, *34*(2), 2035–2044. https://doi.org/10.1021/acs.energyfuels.9b03520

Nedeljković, M., Visser, J., Nijland, T. G., Valcke, S., & Schlangen, E. (2021). Physical, chemical and mineralogical characterization of Dutch fine recycled concrete aggregates: A comparative study. *Construction and Building Materials*, *270*, 121475. https://doi.org/10.1016/J.CONBUILDMAT.2020.121475

NOAA Global Monitoring Laboratory. (2025, August). *Trends in Atmospheric Carbon Dioxide: Mauna Loa CO_2 Monthly Mean Data*. Https://Gml.Noaa.Gov/Ccgg/Trends/.

Peter Hewlett, M. L. (2019). *Lea's Chemistry of Cement and Concrete*.

Qiu, Y., Lamers, P., Daioglou, V., McQueen, N., de Boer, H.-S., Harmsen, M., Wilcox, J., Bardow, A., & Suh, S. (2022). Environmental trade-offs of direct air capture technologies in climate change mitigation toward 2100. *Nature Communications*, *13*(1), 3635. https://doi.org/10.1038/s41467-022-31146-1

RameshKumar, S., Shaiju, P., O'Connor, K. E., & P, R. B. (2020). Bio-based and biodegradable polymers - State-of-the-art, challenges and emerging trends. *Current Opinion in Green and Sustainable Chemistry*, *21*, 75–81. https://doi.org/10.1016/J.COGSC.2019.12.005

Renforth, P. (2019). The negative emission potential of alkaline materials. *Nature Communications*, *10*(1). https://doi.org/10.1038/s41467-019-09475-5

rpsgroup. (2024). *REDUCING EMBODIED CARBON IN CEMENT AND CONCRETE THROUGH PUBLIC PROCUREMENT IN IRELAND Building a better working world*.

S. Akutagawa, F. L. J. N. M. H. B. M. L. J. D. and A. S. K. (1991). Effects of Loading History on Fracture Properties of Concrete. *ACI Materials Journal*, *88*(2). https://doi.org/10.14359/1965

Saniul Haque Mahi, M., Abdul Mun-Im-Dinar, M., & Ashravi Ridoy, T. (2025). *Biochar as a Sustainable Cement Replacement for Enhancing Concrete Composite Properties: A Review*. https://doi.org/10.70028/sgm.v1i2.24

Sanz-Pérez, E. S., Murdock, C. R., Didas, S. A., & Jones, C. W. (2016). Direct Capture of CO_2 from Ambient Air. *Chemical Reviews*, *116*(19), 11840–11876. https://doi.org/10.1021/acs.chemrev.6b00173

Scrivener, K. L., John, V. M., & Gartner, E. M. (2018). Eco-efficient cements: Potential

economically viable solutions for a low-CO2 cement-based materials industry. *Cement and Concrete Research*, *114*, 2–26. https://doi.org/10.1016/J.CEMCONRES.2018.03.015

Scrivener, K. L., & Nonat, A. (2011). Hydration of cementitious materials, present and future. *Cement and Concrete Research*, *41*(7), 651–665. https://doi.org/10.1016/J.CEMCONRES.2011.03.026

Sharma, R., & Yadav, R. N. (2021). FLY ASH GENERATION-UTILIZATION, GOVERNMENT INITIATIVES IN INDIA AND OTHER DIVERSE APPLICATIONS: A REVIEW. *Journal of Advanced Scientific Research*, *12*(01), 9–20. https://doi.org/10.55218/JASR.202112102

Shi, C. (2004). Steel Slag—Its Production, Processing, Characteristics, and Cementitious Properties. *Journal of Materials in Civil Engineering*, *16*(3), 230–236. https://doi.org/10.1061/(ASCE)0899-1561(2004)16:3(230)

Sousanabadi Farahani, H., Hosseini Zadeh, A., Hu, J., Hawkins, C., & Kim, S. (2025). Carbonation reaction of recycled concrete aggregates (RCA): CO2 mass consumption under various treatment conditions. *Cleaner Materials*, *15*, 100296. https://doi.org/10.1016/J.CLEMA.2025.100296

Smith, S., Geden, O., Gidden, M., Lamb, W., Nemet, G., Minx, J., ... & Vaughan, N. (2024). The state of carbon dioxide removal. https://doi.org/10.17605/OSF.IO/W3B4Z

Thomas, C., Setién, J., Polanco, J. A., Alaejos, P., & Sánchez De Juan, M. (2013). Durability of recycled aggregate concrete. *Construction and Building Materials*, *40*, 1054–1065. https://doi.org/10.1016/J.CONBUILDMAT.2012.11.106

Tian, S., Jiang, J., Chen, X., Yan, F., & Li, K. (2013). Direct Gas–Solid Carbonation Kinetics of Steel Slag and the Contribution to In situ Sequestration of Flue Gas CO_2 in Steel-Making Plants. *ChemSusChem*, *6*(12), 2348–2355. https://doi.org/10.1002/cssc.201300436

Tupenaite, L., Kanapeckiene, L., Naimaviciene, J., Kaklauskas, A., & Gecys, T. (2023). Timber Construction as a Solution to Climate Change: A Systematic Literature Review. *Buildings*, *13*(4), 976. https://doi.org/10.3390/buildings13040976

Ukwattage, N. L., Ranjith, P. G., Yellishetty, M., Bui, H. H., & Xu, T. (2015). A laboratory-scale study of the aqueous mineral carbonation of coal fly ash for CO2 sequestration. *Journal of Cleaner Production*, *103*, 665–674. https://doi.org/10.1016/J.JCLEPRO.2014.03.005

Uliasz-Bocheńczyk, A. (2024). A Comprehensive Review of CO2 Mineral Sequestration Methods Using Coal Fly Ash for Carbon Capture, Utilisation, and Storage (CCUS) Technology. Energies, 17(22), 5605. https://doi.org/10.3390/en17225605

Vijerathne, D., Wahala, S., & Illankoon, C. (2024). Impact of Crushed Natural Aggregate on Environmental Footprint of the Construction Industry: Enhancing Sustainability in Aggregate Production. *Buildings*, *14*(9). https://doi.org/10.3390/buildings14092770

Wang, C., Jiang, H., Miao, E., Wang, Y., Zhang, T., Xiao, Y., Liu, Z., Ma, J., Xiong, Z., Zhao, Y., & Zhang, J. (2024). Accelerated CO2 mineralization technology using fly ash as raw material: Recent research advances. *Chemical Engineering Journal*, *488*, 150676. https://doi.org/10.1016/J.CEJ.2024.150676

Wang, J., Zhong, M., Wu, P., Wen, S., Huang, L., & Ning, P. (2021). A Review of the Application of Steel Slag in CO_2 Fixation. *ChemBioEng Reviews*, *8*(3), 189–199. https://doi.org/10.1002/cben.202000021

Wang, S., Kim, J., & Qin, T. (2024). Mineral carbonation of iron and steel by-products: State-of-the-art techniques and economic, environmental, and health implications. *Journal of CO2 Utilization*, *81*, 102707. https://doi.org/10.1016/J.JCOU.2024.102707

Wang, Z., Huo, S., Steubing, B., Meng, F., Long, Y., Schjønberg, M. S., Birkved, M., Corona, B., & Cao, Z. (2025). Lignin-based asphalt pavements can create

permanent carbon storage and substantial climate benefits. *Resources, Conservation and Recycling*, *215*, 108080. https://doi.org/10.1016/J.RESCONREC.2024.108080

Wijitkosum, S., & Jiwnok, P. (2019). Elemental Composition of Biochar Obtained from Agricultural Waste for Soil Amendment and Carbon Sequestration. *Applied Sciences*, *9*(19), 3980. https://doi.org/10.3390/app9193980

Wood as bio-based building material. (2017). In *Performance of Bio-based Building Materials* (pp. 21–96). Elsevier. https://doi.org/10.1016/B978-0-08-100982-6.00002-1

World Population Review. (2025). *Cement Production by Country 2025*. World Population Review. https://worldpopulationreview.com/country-rankings/cement-production-by-country

Wu, X., Yu, Y., Qin, Z., & Zhang, Z. (2014). The advances of post-combustion CO2 capture with chemical solvents: Review and guidelines. *Energy Procedia*, *63*, 1339–1346. https://doi.org/10.1016/j.egypro.2014.11.143

Xi, F., Davis, S. J., Ciais, P., Crawford-Brown, D., Guan, D., Pade, C., Shi, T., Syddall, M., Lv, J., Ji, L., Bing, L., Wang, J., Wei, W., Yang, K.-H., Lagerblad, B., Galan, I., Andrade, C., Zhang, Y., & Liu, Z. (2016). Substantial global carbon uptake by cement carbonation. *Nature Geoscience*, *9*(12), 880–883. https://doi.org/10.1038/ngeo2840

Xuan, D., Zhan, B., & Poon, C. S. (2016). Assessment of mechanical properties of concrete incorporating carbonated recycled concrete aggregates. *Cement and Concrete Composites*, *65*, 67–74. https://doi.org/10.1016/j.cemconcomp.2015.10.018

Yamada, H. (2021). Amine-based capture of CO2 for utilization and storage. *Polymer Journal*, *53*(1), 93–102. https://doi.org/10.1038/s41428-020-00400-y

Yildirim, I. Z., & Prezzi, M. (2011). Chemical, Mineralogical, and Morphological

Properties of Steel Slag. *Advances in Civil Engineering*, *2011*, 1–13. https://doi.org/10.1155/2011/463638

Younes, A., Elbeltagi, E., Diab, A., Tarsi, G., Saeed, F., & Sangiorgi, C. (2024). Incorporating coarse and fine recycled aggregates into concrete mixes: mechanical characterization and environmental impact. *Journal of Material Cycles and Waste Management*, *26*(1), 654–668. https://doi.org/10.1007/s10163-023-01834-1

Zhan, B., Poon, C. S., Liu, Q., Kou, S., & Shi, C. (2014). Experimental study on CO2 curing for enhancement of recycled aggregate properties. *Construction and Building Materials*, *67*, 3–7. https://doi.org/10.1016/j.conbuildmat.2013.09.008

Zhang, D., & Shao, Y. (2016). Early age carbonation curing for precast reinforced concretes. *Construction and Building Materials*, *113*, 134–143. https://doi.org/10.1016/j.conbuildmat.2016.03.048

d

Zhang, Y., Yu, L., Cui, K., Wang, H., & Fu, T. (2023). Carbon capture and storage technology by steel-making slags: Recent progress and future challenges. *Chemical Engineering Journal*, *455*, 140552. https://doi.org/10.1016/j.cej.2022.140552

Zide, S., Ho, H. J., Iizuka, A., Petersen, J., Vadapalli, V. R. K., Petrik, L., & Ojumu, T. (2025). Direct mineral carbonation of fly ash under high pressure using acid mine drainage: Effects of solid-to-liquid ratio, stirring speed and CO2 pressure. *Environmental Progress & Sustainable Energy*, *44*(2), e14545. https://doi.org/10.1002/ep.14545

Chapter 3 Curing of Cement: Data Analysis and Regression Modelling

3.1 Introduction

As one of the CO_2 utilisation/absorption options, CO_2 curing of cement during the manufacturing of (fresh) cement paste (or mortar) and concrete has been investigated under various conditions in different studies. The CO_2 uptake is commonly used to quantify the material's capacity to store CO_2, providing a normalized metric for comparing different mixtures and curing conditions. It is generally defined as the ratio of the actual amount of CO_2 sequestered by the material to its theoretical maximum uptake capacity, expressed as a percentage. The theoretical maximum is calculated based on the stoichiometric carbonation potential of reactive oxides (e.g., CaO) in the binder, whereas the actual uptake can be determined experimentally through mass gain, gas flow balance, or chemical analysis of carbonates. In the current literature, eight factors influencing the cement/concrete CO_2 curing results have been identified, including: water to cement (w/c) ratio (Wang et al., 2017), pre-cured time (Chen & Gao, 2019), CO_2 concentration (Rostami et al., 2012), environmental temperature and relative humidity (RH) (Wang et al., 2019), curing exposure time (Zhang et al., 2016), subsequent hydration time (Li & Ling, 2020) and specimen thickness (Sun et al., 2016). **Table 3-1** summarises the principal parameters reported in the literature together with their typical ranges and qualitative influence on CO_2 uptake efficiency.

Table 3-1 Principal parameters influencing CO_2 curing performance in cement and concrete

Parameter	*Reported influence on CO_2 uptake*	*Representative range*
Water-to-cement ratio (w/c)	Non-linear: moderate ratios (~0.4–0.5) favour uptake due to balanced porosity and moisture	0.3–0.6
Pre-curing time	Short pre-curing (<24 h) enhances early-stage CO_2 reactivity	0–48 h
CO_2 concentration	Uptake increases with concentration up to ~20%, then plateaus	5–50 %
Temperature	Moderate increase (20–60 °C) accelerates reaction kinetics	20–80 °C
Relative humidity (RH)	Optimum around 50–70 %; too high limits diffusion	30–90 %
Curing exposure time	Rapid increase during first 24 h, then asymptotic	1–72 h
Subsequent hydration time	Longer hydration promotes carbonate stabilisation	1–28 days
Specimen thickness	Thicker samples reduce diffusion and overall uptake	10–50 mm

Water to cement ratio is an important parameter for concrete manufacturing, typically dictated by the target strength; a broadly followed trend is that the CO_2 uptake increases at reduced w/c ratio. Pre-cured process refers to the treatment of the material in preparation for the subsequent CO_2 curing. A longer pre-cured time generally shows a positive impact on the CO_2 uptake. CO_2 curing exposure time appears to be one of the key influencing factors. The data collected can be divided

into two categories: short curing (less than 2 hours) and long curing (from multiple hours up to one day). Besides, some experiments recorded results of much longer duration of curing, which are in days or even months. However, such extensively long curing might be not practically relevant given the typical time duration for cement or concrete application. Generally, the CO_2 uptake increases along with the increase of exposure time, although the impact appears to be more significant in the longer curing experiments than the shorter ones. This suggests that long curing might be more suitable for improved CO_2 uptake, although this needs to be balanced with other considerations such as costs and operational feasibility. CO_2 concentration (or partial pressure) appears to be another very important factor. Most experiments take pure CO_2 gas, at different pressures. The adopted pressure is linked to energy consumption and therefore has an impact on economic efficiency; finding suitable CO_2 concentration and pressure to satisfy the CO_2 partial pressure thus requires broader considerations.

CO_2 curing temperature and RH are known to affect CO_2 uptake as well. However, in most experimental studies, these parameters are maintained at approximately room temperature and within a relative humidity range of 50–70%. Within this range, carbonation performance is governed by a balance between gas diffusion and moisture availability. At higher temperatures, the reaction rate generally increases due to enhanced diffusion and reaction kinetics, but excessive heating can accelerate water loss and reduce the amount of dissolved CO_2 available for carbonation. Similarly, relative humidity exerts a non-linear influence: insufficient humidity limits CO_2

dissolution, while excessively high humidity saturates the pore network and restricts gas ingress. Consequently, moderate humidity levels around 50–60% and near-ambient temperatures are typically found to yield the highest CO_2 uptake efficiency. The thickness of cement/concrete sample is crucial in CO_2 curing; a thicker sample limits CO_2 penetration (relative) depth, reducing the reaction zone and overall uptake. Additionally, thicker samples accumulate carbonation products that block pores at the outer layer, increasing diffusion resistance and further hindering CO_2 absorption.

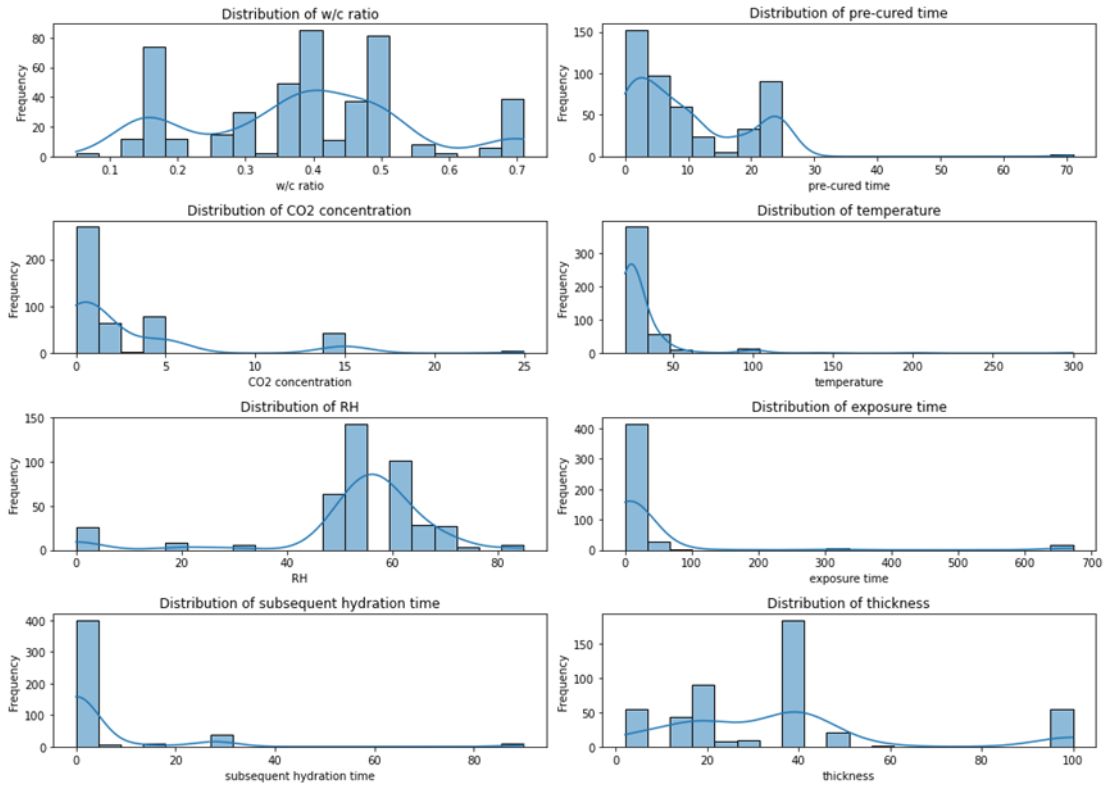

Figure 3-1 Data distribution and frequency (w/c ratio, pre-cured time, CO_2 concentration, temperature, RH, exposure time, subsequent hydration time and thickness

Surprisingly, such impacts, especially the interactive effects of these factors, have not been systematically analysed in the past, despite the fact that quite a number of experimental tests have been reported. In this study, 548 data from 35 studies

reported in literature are analysed; their distributions along the eight aforementioned features aforementioned are shown in **Figure 3-1** For clarity, datasets were sequentially numbered and grouped by reference; within each reference, entries were ordered to reflect distinctions across the eight features. The complete list of dataset IDs is provided in Appendix A.2 and the corresponding references in Appendix A.2 **Table A-9**.

Ideally, the data points should be relatively evenly distributed across the range of each factor to allow a balanced evaluation of their influence. However, the current literature exhibits highly skewed distributions. Most studies on CO_2 partial pressure are concentrated in the range of 0.1–0.3 bar, with very limited data above 0.5 bar, which restricts the understanding of high-pressure carbonation performance. CO_2 exposure time is mostly in the short-term range of 1–6 h, and very few studies investigate prolonged curing beyond 12 h, leaving long-term reaction kinetics largely unknown. Water-to-cement ratio is predominantly reported between 0.40–0.50, whereas the behaviour of systems with lower w/c ratios (<0.35) or higher w/c ratios (>0.55) remains insufficiently investigated.

For pre-cured time, most studies focus on early ages within 0–6 h, with almost no data on delayed CO_2 curing (>24 h). Subsequent hydration time is typically limited to 1–3 days, providing little information about the contribution of long-term hydration to total CO_2 uptake. Specimen thickness is commonly in the narrow range of 10–20 mm, whereas thicker elements (>30 mm) have rarely been tested. Considering that different cement-based and concrete products often have diverse shapes and cross-

sectional dimensions, it is necessary to investigate the influence of thickness systematically. Such studies would help clarify how diffusion path length and carbonation front progression vary with element geometry and would provide more representative guidance for practical applications. Similarly, curing temperature and relative humidity are mostly kept near ambient conditions (20–25 °C, 50–70 %), resulting in a lack of data on elevated temperatures or controlled humidity environments.

This uneven distribution of experimental conditions limits the robustness of statistical modelling and may bias conclusions towards the most frequently tested parameter ranges. Future studies should systematically expand the coverage of under-represented factors. In particular, there is a need for tests with higher CO_2 pressures above 0.5 bar, longer exposure durations beyond 12 h, a wider range of water-to-cement ratios, delayed pre-cured times, extended hydration periods and greater specimen thicknesses. Addressing these gaps would enable a more comprehensive and representative analysis of CO_2 curing performance and provides the motivation for the systematic feature-importance analysis presented in Section 3.3.

By systematically comparing the experimental conditions and results reported in the literature, this chapter addresses three key aspects. First, it identifies the factors that significantly influence CO_2 curing and quantifies their relative importance. Second, it characterises the interactions among these factors to reveal how they collectively affect CO_2 uptake. Third, it develops a machine-learning-based regression model that quantitatively relates CO_2 uptake to the influencing factors, thereby enabling reliable

prediction and providing a data-driven tool for process optimisation. Together, these analyses help mitigate the knowledge gap caused by the uneven distribution of experimental studies in the existing literature but also provide guidance for the design of future CO_2 curing experiments and the optimisation of curing protocols for cement- and concrete-based products.

3.2 Single Factor Analysis

Water to cement ratio. **Figure 3-2** shows data from R32 (In all figures, the dataset reference numbers are presented in square brackets (e.g., R32 is displayed as [32])) in terms of how w/c ratio affects CO_2 uptake at different lengths of CO_2 curing period (which itself is an important factor, see below) (Wang et al., 2017). These experiments were conducted under 24 hours pre-cured, 14.985 bars CO_2 partial pressure, and 40 °C CO_2 curing temperature.

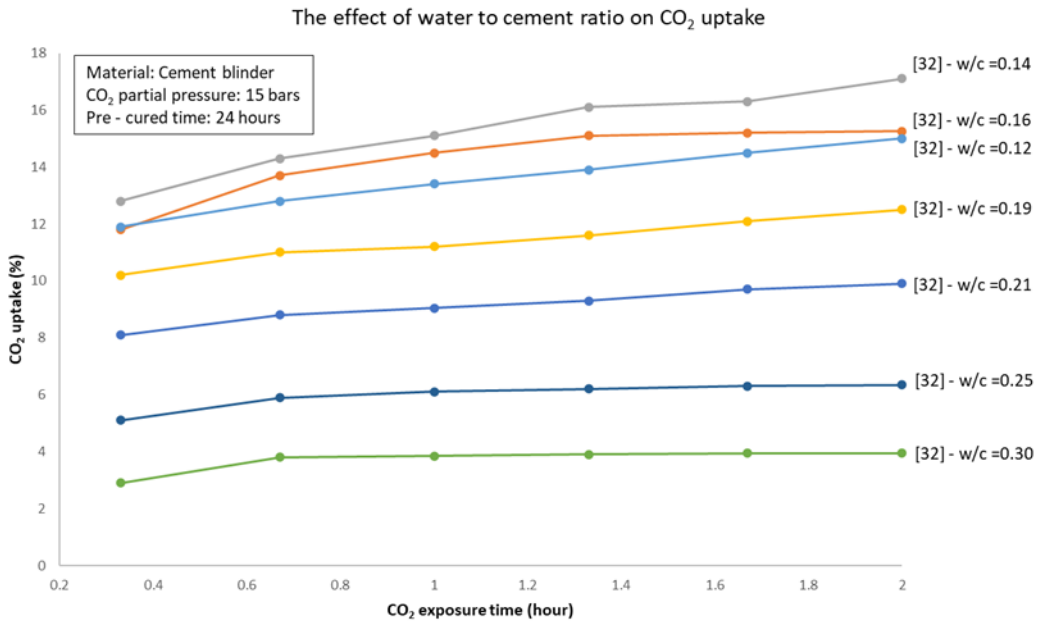

Figure 3-2 The effect of water to cement ratio on CO_2 uptake-R32

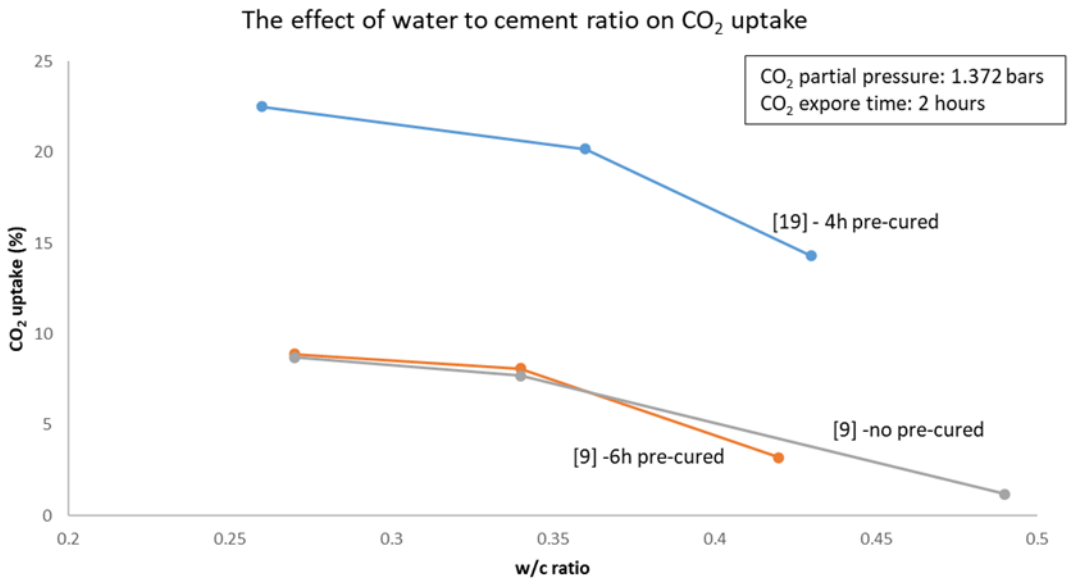

Figure 3-3 The effect of water to cement ratio on CO_2 uptake-R9+R19

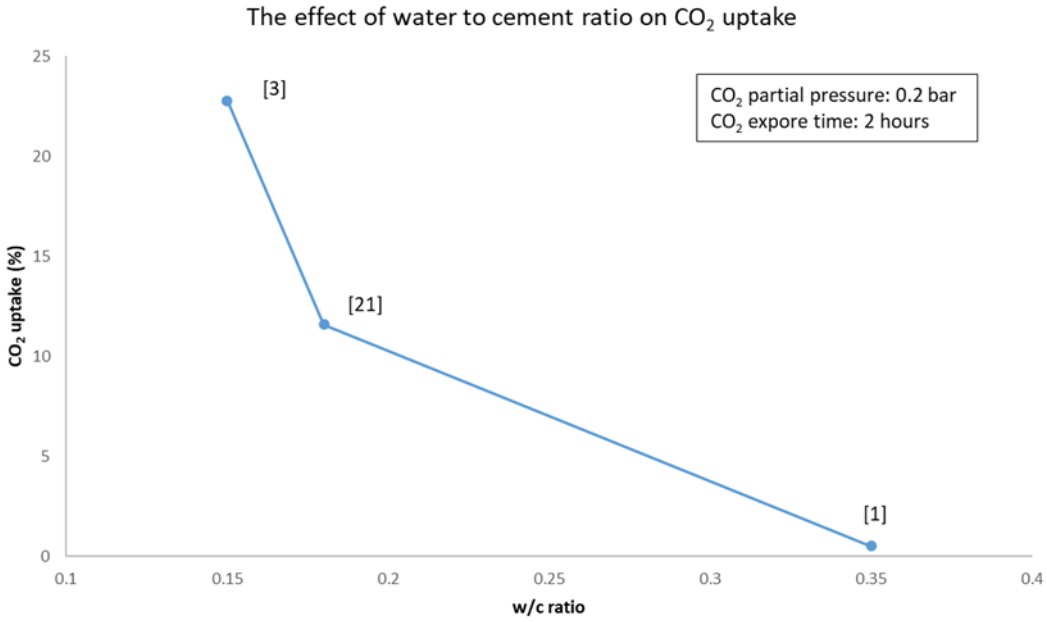

Figure 3-4 The effect of water to cement ratio on CO_2 uptake-R1+R3+R21

Figure 3-3 shows two different w/c ratio raw materials in R19 (Shi & Wu, 2008a) and one set of data in R9 (Zakir Morshed & Shao, 2013). The experiments in R19 were under 4 hours pre-cured, 1.372 bars CO_2 partial pressure, 22 ℃ CO_2 curing temperature, and 2 hours exposure time. The experiments in R9 were under 1.485

bars CO_2 partial pressure, 22 ℃ CO_2 curing temperature, 2 hours exposure time and without pre-cured. **Figure 3-4** includes three mixed data from R1 (Chen & Gao, 2019), R3 (Li & Ling, 2020), and R21 (Zhan et al., 2019). They could be put into one plot because of their similar experimental conditions particularly in terms of the CO_2 partial pressure (less than 1 bar).

Due to the difference in experimental settings, these data do not show an agreed quantitative relationship between w/c ratio and CO_2 update. However, the trend that is broadly followed is that the CO_2 uptake increases at reduced w/c ratio. However, a turning point also exists, which is around 0.14, below which the CO_2 uptake could reduce (see **Figure 3-4**). The observed optimum w/c ratio could be related to the residual water in cement paste, whose role during the CO_2 curing is twofold. One is that pore water is essential for the dissolution of CO_2 gas (therefore the w/c ratio should not be too low), another is that the saturation of microspores (the degree of which increases with w/c ratio) would hinder the further gaseous diffusion from outside through the material, leading to the faster accumulation of precipitations on the surface which would further hamper CO_2 uptake (Wang et al., 2017). However, one needs to realize that w/c ratio, as an important parameter for concrete manufacturing (which normally ranges from 0.4 to 0.7, depending on the target strength), may not be suitable for wide manipulation for CO_2 curing purposes, although understanding its impact could help evaluate the potential of CO_2 uptake by the manufacturing of different (strength) classes of concrete.

Pre-cured time. Generally, pre-cured refers to the treatment of the material in preparation for the subsequent CO_2 curing (Zhang et al., 2020). This process is typically under ambient pressure in either open air or a closed chamber (with specific temperature and relative humidity). **Figure 3-5** shows a set of experimental data which were obtained in such experimental settings, except the two data from R6 where hydration was applied.

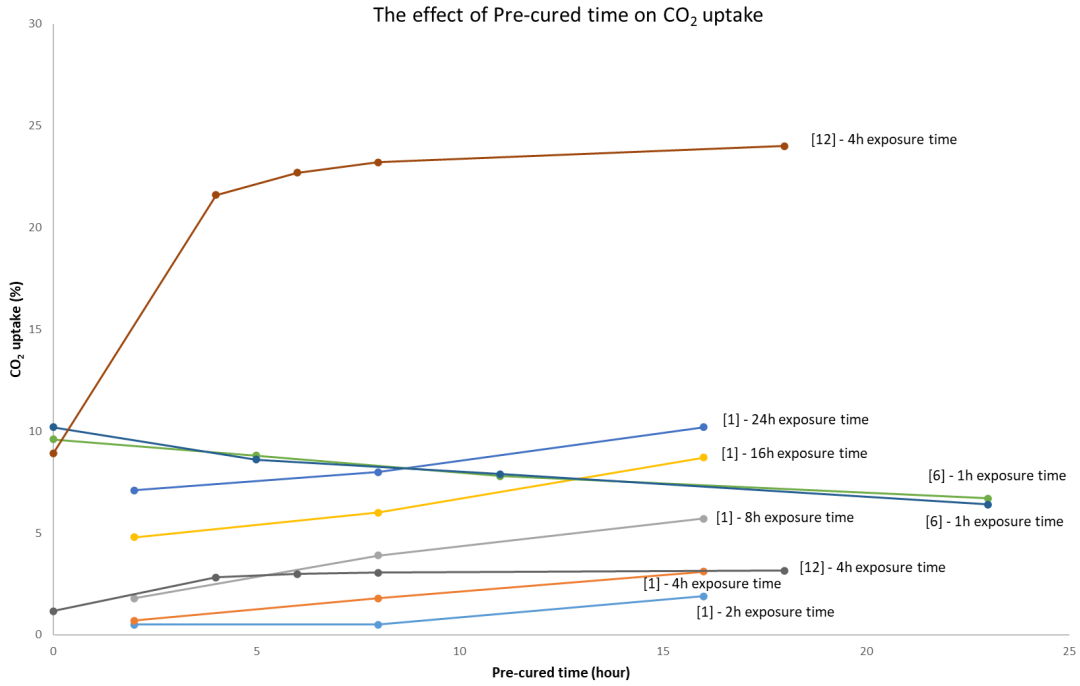

Figure 3-5 The effect of pre-cured time on CO_2 uptake

Except in the data from R6, longer pre-cured time generally shows a positive impact on the CO_2 uptake. This trend can be attributed to the fact that the pre-cured process reduces the w/c ratio of the binder through evaporation, which enhances subsequent carbonation by increasing the porosity and facilitating CO_2 diffusion (Wang et al., 2017). However, the effect of pre-cured time on CO_2 uptake will be less if w/c ratio is

lower. This means if the mass of original free water is less, the degree of water loss (as generally happens in pre-cured) will be reduced. From **Figure 3-5**, R12's w/c ratio is 0.4, which is a common w/c ratio in concrete manufacture. Under this condition, 4-hour pre-cured period appears to have made a significant impact on CO_2 uptake.

CO_2 curing exposure time. CO_2 curing exposure time appears to be one of the key influencing factors. The data collected can be divided into two categories: short curing (less than 2 hours) and long curing (from multiple hours up to one day). Besides, some experiments recorded results of much longer duration of curing, which are in days or even months. However, such extensively long curing might be not practically relevant given the typical time duration for cement or concrete application.

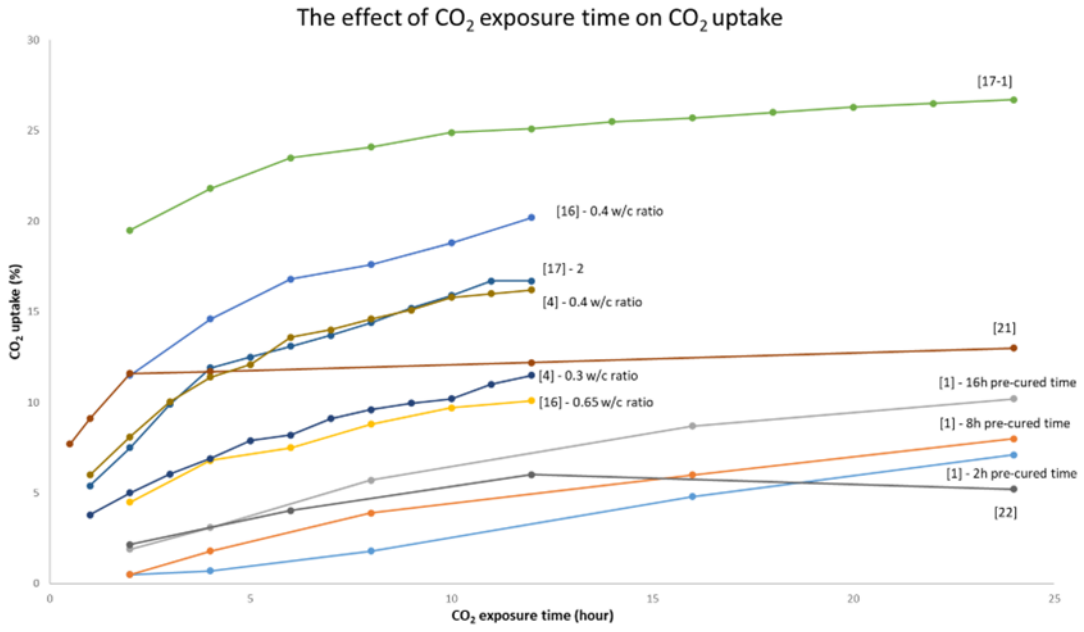

Figure 3-6 The effect of CO_2 exposure time on CO_2 uptake (longer duration)

For the long curing category, **Figure 3-6** shows the data from R1 (Chen & Gao, 2019), R4 (Zhang & Shao, 2016), R16 (Liu, 2016), R17 (Zhang et al., 2016), R21 (Zhan et al.,

2019) and R22 (Zhang et al., 2021), which presents exposure time from 2 hours to 24 hours.

For the short curing category, **Figure 3-7** shows the data from R7 (Rostami et al., 2011), R9 (Zakir Morshed & Shao, 2013), R11 (Shao & Morshed, 2015), R13 (Rostami et al., 2012), R20 (Wang et al., 2019), R32 (Wang et al., 2017), which presents exposure time less than 2 hours.

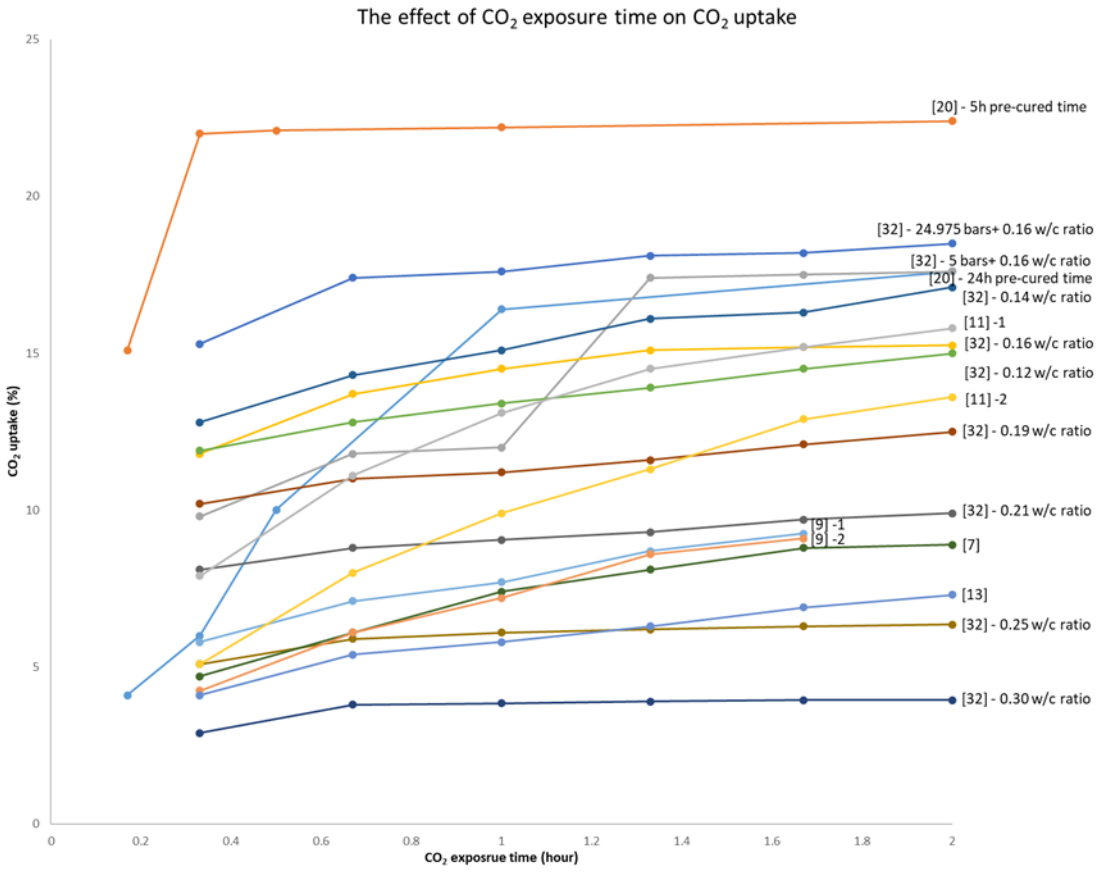

Figure 3-7 The effect of CO_2 exposure time on CO_2 uptake (shorter duration)

Generally, the CO_2 uptake increases along with the increase of exposure time, although the impact appears to be more significant in the longer curing experiments than the shorter ones. This suggests that the range of long curing might be more

suitable for improved CO_2 uptake, although this needs to be balanced with other considerations such as costs and operational feasibility.

CO_2 concentration (or partial pressure). This appears to be another very important factor. **Figure 3-8** shows the data from R3 (Li & Ling, 2020), R15 (Shao, 2010), R19 (Shi & Wu, 2008) and R32 (Wang et al., 2017), which suggests that the CO_2 uptake generally increases along with the increase of the CO_2 partial pressure, which is particularly significant at the lower range (below 5 bars). Most experiments used pure CO_2 gas, where the difference mostly came from the applied pressure which is linked to energy consumption and therefore has an impact on economic efficiency. Thus, finding suitable CO_2 concentration and pressure to satisfy the CO_2 partial pressure requires broader considerations.

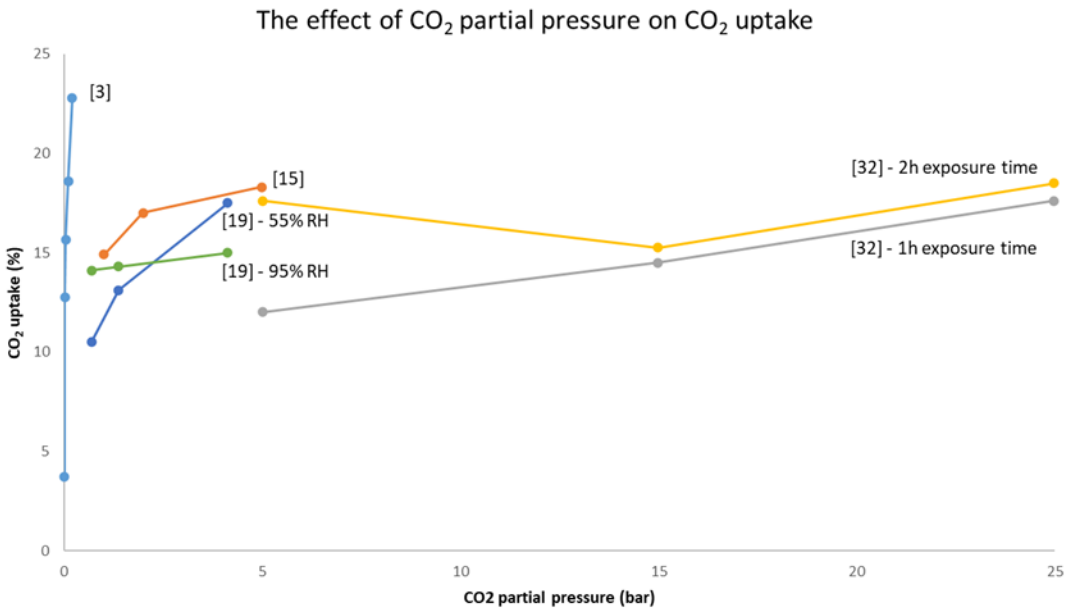

Figure 3-8 The effect of CO_2 partial pressure on CO_2 uptake

Other factors. CO_2 curing temperature is known to affect CO_2 uptake, as shown in **Figure 3-9**. However, CO_2 curing is hard to be performed under a high temperature (over 40℃) in the manufacturing process. Therefore, adopting a temperature significantly deviating from ambient conditions is impractical. Another factor, relative humidity, is known to have an impact as well, although in most experiments it was set to a similar range of typical ambient conditions (i.e., between 50% to 70%). The above two factors are thus not considered further in the following analyses.

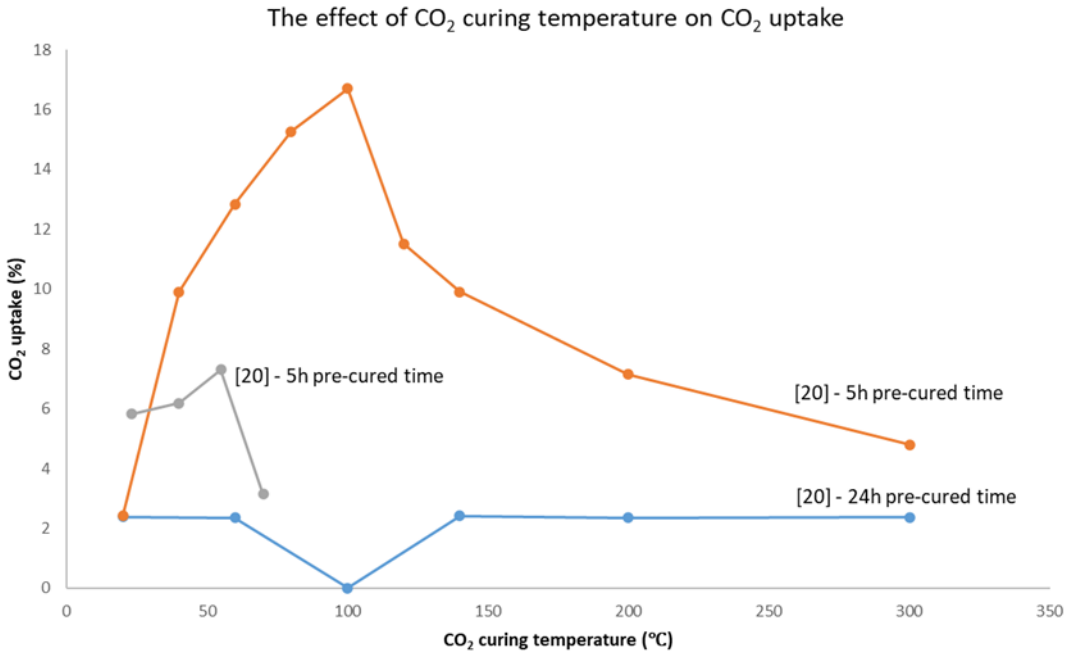

Figure 3-9 The effect of CO_2 curing temperature on CO_2 uptake

Similarly, subsequent hydration time can influence the final CO_2 uptake; its effect is therefore included in the subsequent analysis. Specimen thickness may also affect the diffusion path and, consequently, the degree of carbonation; this factor is included in the analysis to assess how geometric characteristics of the specimens influence CO_2 curing performance. Nevertheless, no systematic and comprehensive investigation of

these two influencing factors has been conducted in existing experiments, which underscores the importance of performing an integrated analysis of their effects in the present study.

To identify the key parameters affecting CO_2 uptake, a comprehensive feature importance analysis was conducted using Python (scikit-learn, pandas, numpy). Multiple complementary methods were applied, including Random Forest impurity-based importance, permutation importance (Random Forest and Gradient Boosting), Pearson correlation, mutual information, and Lasso regression coefficients. The features were ranked for each method, and the average rank was used as an aggregated importance score to ensure robustness.

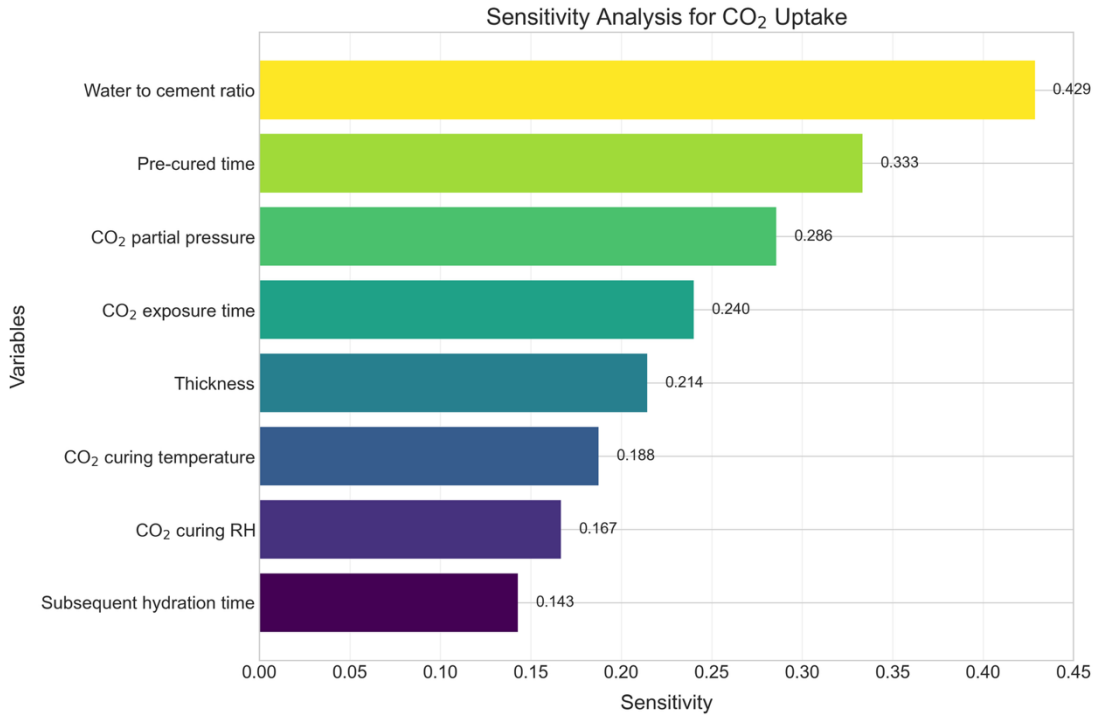

Figure 3-10 Feature importance in CO_2 curing process

The results are summarized in **Figure 3-10**. Water-to-cement ratio shows the greatest influence (0.429), followed by pre-cured time (0.333), CO_2 partial pressure (0.286), and CO_2 exposure time (0.240). These findings indicate that mixture proportion and early-age process parameters play a dominant role in determining CO_2 uptake. Thickness shows a moderate effect, reflecting its influence on diffusion path length, whereas curing temperature and relative humidity contribute less under the examined conditions. Subsequent hydration time exhibits the lowest importance, suggesting that most CO_2 sequestration occurs during the curing stage rather than during later hydration.

3.3 Machine-Learning-Based Regression Analysis of CO_2 curing

3.3.1 Purpose and Methodology

The objective of this analysis was to establish a robust predictive relationship between process variables and CO_2 uptake in order to enable quantitative prediction and subsequent response evaluation. Conventional multiple linear regression was first applied using three key factors: x_1 representing water-to-cement ratio, x_2 representing CO_2 partial pressure and $x_3$representing CO_2 exposure time, with the response variable y representing CO_2 uptake. The resulting model $y = 8.8997 - 5.5155x_1 + 1.1795x_2 + 0.2441x_3$ resulted in an R^2 of only 0.216, indicating poor predictive performance. The low R^2 confirmed that simple parametric models were inadequate for capturing the nonlinear and interacting effects present in the data. Consequently, a machine-learning-based nonlinear regression framework was

implemented in Python using the scikit-learn library, which allows flexible model construction and is well suited to capturing complex interactions among variables.

The compiled dataset initially consisted of 548 data points obtained from published studies. Non-numerical fields were removed, and all numerical predictors were standardised to zero mean and unit variance using StandardScaler. A Random Forest Regressor (RandomForestRegressor, n_estimators = 200, max_depth = 10, random_state = 42) was first trained as a preliminary model to identify anomalous observations. Residuals, defined as predicted minus measured CO_2 uptake, were examined, and points with physically implausible uptake values (outside 0–40 %) or standardised residuals greater than three standard deviations were flagged as outliers. This procedure identified 83 extreme points (≈15 % of the dataset), including dataset R6, which displayed trends inconsistent with the remaining data (**Figure 3-5**). These anomalous points were removed to ensure that the retained data exhibited physically plausible behaviour and consistent experimental trends. After screening, 465 valid observations remained.

While the removal of these 83 data points improved the overall consistency and interpretability of the dataset, it also introduces potential limitations that warrant consideration. Excluding anomalous values reduces the influence of measurement errors or inconsistent reporting but may also limit the representation of rare or extreme curing conditions. Some of the removed observations could reflect valid yet unconventional process regimes, such as atypical binder compositions or CO_2 pressures, which remain underexplored in the literature. Consequently, the refined

dataset provides a robust basis for modelling dominant carbonation trends under standard experimental conditions but may underestimate variability near the edges of the parameter space. Future work involving controlled experiments under broader curing conditions would be valuable to verify whether these excluded data points represent genuine anomalies or distinct carbonation behaviours.

The cleaned dataset was randomly divided into training (80 %, 372 samples) and testing (20 %, 93 samples) subsets. Several regression algorithms were trained on the training set, including support vector regression (SVR) with a radial basis function kernel, random forest, gradient boosting, and ridge regression. For the SVR model, hyperparameters were optimised by grid search with five-fold cross-validation, exploring $C \in [50,100,200,500]$, $\gamma \in \{\text{scale}, \text{auto}, 0.01, 0.1, 1\}$ and $\epsilon \in [0.1,0.2,0.5]$. Random forest and gradient boosting regressors were trained with 200 estimators, maximum depths of 10 and 6 respectively, and a fixed random seed (42) for reproducibility. Ridge regression was performed with an L_2-penalty parameter $\alpha = 1.0$. The final predictive model was a weighted ensemble combining the four regressors, with weights $\omega = [0.3, 0.3, 0.2, 0.2]$. The ensemble prediction was computed as equation (3-1).

$$\hat{y} = 0.3\hat{y}_{RF} + 0.3\hat{y}_{GB} + 0.2\hat{y}_{SVR} + 0.2\hat{y}_{Ridge} \qquad (3-1)$$

where $\hat{y}_{RF}$, $\hat{y}_{GB}$, $\hat{y}_{SVR}$ and $\hat{y}_{Ridge}$ denote the predictions of the individual models. Higher weights were assigned to the tree-based models owing to their superior

nonlinear predictive performance, while SVR and ridge contributions were retained to improve generalisation.

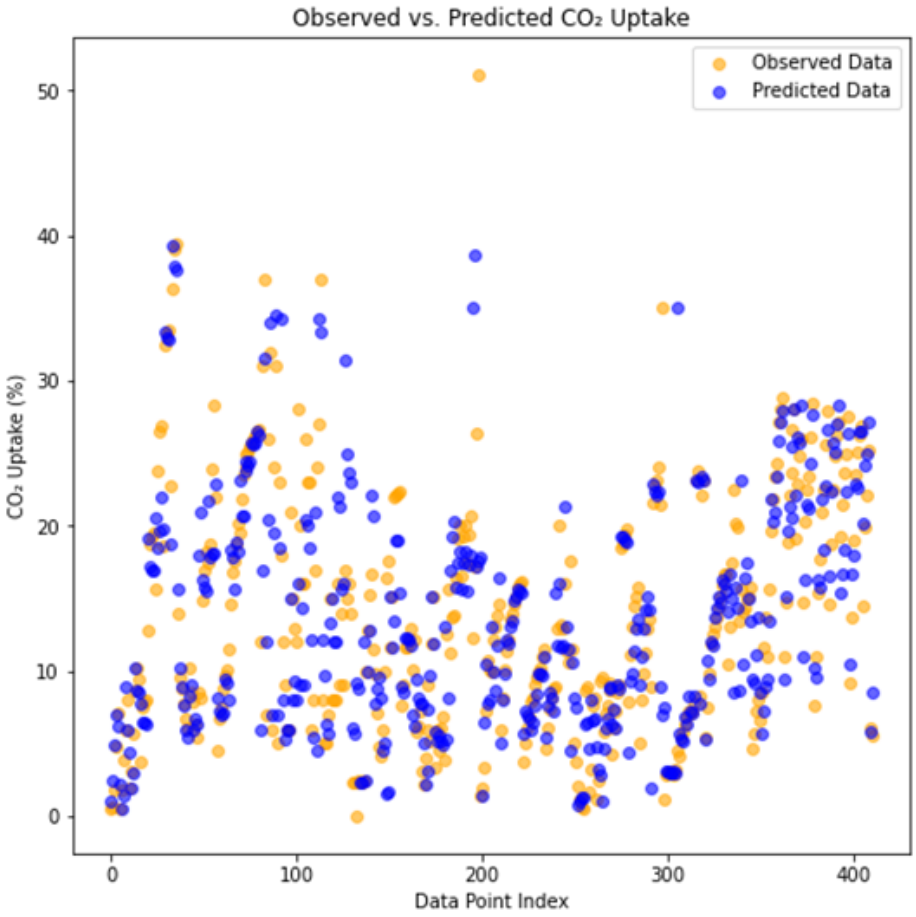

Figure 3-11 Observed and predicted CO_2 uptake before outlier removal

Model performance was evaluated on the test set using the coefficient of determination (R^2) and mean squared error (MSE). The ensemble achieved a higher R^2 than any single model, demonstrating enhanced robustness and predictive accuracy. **Figure 3-11** compares the observed CO_2 uptake values with predictions from the preliminary random forest model prior to outlier removal, illustrating the need for rigorous data screening.

3.3.2 Response and Interaction Analysis

The trained ensemble model was then used to explore the effects of individual process parameters on CO_2 uptake. Single-factor response analyses were performed by systematically varying each parameter across its observed or practically relevant range while holding the other variables constant at representative default values (water-to-cement ratio = 0.60, pre-cured time = 2 h, CO_2 pressure = 1 bar, curing temperature = 25 °C, relative humidity = 55 %, exposure time = 24 h, thickness = 50 mm, subsequent hydration time = 2 days). The studied parameter was then varied across its range (e.g. water-to-cement ratio 0–0.9, CO_2 pressure 0–30 bars, exposure time 0–120 h) to generate predicted response curves. Predicted trends were compared with binned experimental averages to ensure plausibility and to identify monotonic, saturation-type or non-monotonic behaviours.

Finally, three-dimensional (3D) response surfaces were generated to investigate the combined effects of key variables. Water-to-cement ratio (WC) and CO_2 partial pressure (P), which are chosen as primary axes due to their practical relevance to mixture design and process control. CO_2 exposure time (T) was considered at three representative values (2 h, 24 h and 48 h) to capture the progression of uptake behaviour, while all remaining variables were fixed at their median values. A physics-informed reference surface was first constructed by normalising each variable to the range [0,1], shown as equation (3-2).

$$\begin{cases} x = \dfrac{WC - WC_{min}}{WC_{max} - WC_{min}} \\ z = \dfrac{P - P_{min}}{P_{max} - P_{min}} \\ t = min\left(\dfrac{T}{48}, 1\right) \end{cases} \quad (3-2)$$

where x, z and t denote the normalised water-to-cement ratio, CO_2 pressure and exposure time, respectively, with t truncated at 48 h to represent saturation. Using these variables, a mechanistically consistent functional form $F_{phys}(x, z, t)$ was specified to represent the expected monotonic and saturation-type effects of each parameter, with a mild interaction between WC and P. The surface was scaled by the median CO_2 uptake (y_{med}) and clipped to [$0.8\,y_{min}$, $1.2\,y_{max}$] for physical plausibility, shown as equation (3-3).

$$y(WC, P, T) = F_{phys}(x, z, t, y_{med}, y_{min}, y_{max}) \quad (3-3)$$

The explicit functional form used in this study is equation (3-4).

$$y(WC, P, T) = y_{med}(1 - 0.8x)(0.6 + 0.8z)(0.4 + 0.9(1 - e^{-2t}) + 0.1y_{med}\sin(\pi x)\sin(\pi xz) \quad (3-4)$$

In parallel, a model-based surface was generated using the trained ensemble regression model. For each grid point, a feature vector $K(WC, P, T)$ was assembled with other variables fixed at their medians, standardised using the fitted scaler, and passed to the predictive model to obtain CO_2 uptake predictions, shown as equation (3-5).

$$\hat{y}(WC, P, T) = f_{ensemble}K(WC, P, T) \quad (3-5)$$

where $f_{ensemble}$ denotes the final weighted ensemble model combining random forest, gradient boosting, support vector regression and ridge regression.

The two surfaces were plotted for the three selected exposure times. The physics-informed surface provided a smooth and mechanistically interpretable baseline, whereas the machine-learning-based surface captured more irregular patterns directly inferred from the experimental data. Comparing these two representations highlights where the model-predicted trends agree with theoretical expectations and where deviations occur, offering a more nuanced understanding of process behaviour and supporting optimisation of CO_2 curing conditions.

3.3.3 Model Performance

The predictive performance of the final weighted ensemble model was evaluated using the independent testing subset. This model was chosen on the basis of its superior performance on the independent test set compared with the alternative models, achieving a coefficient of determination R^2 of 0.81. This indicates that more than 80 % of the variance in CO_2 uptake was explained by the selected model. The corresponding mean squared error (MSE) was 15.28, giving a root mean squared error of approximately 3.9 %. Given that the observed CO_2 uptake values span a range of roughly 0–40 % with a standard deviation of about 11.5 %, this level of error is considered small relative to the natural variability of the data and therefore acceptable for practical prediction purposes.

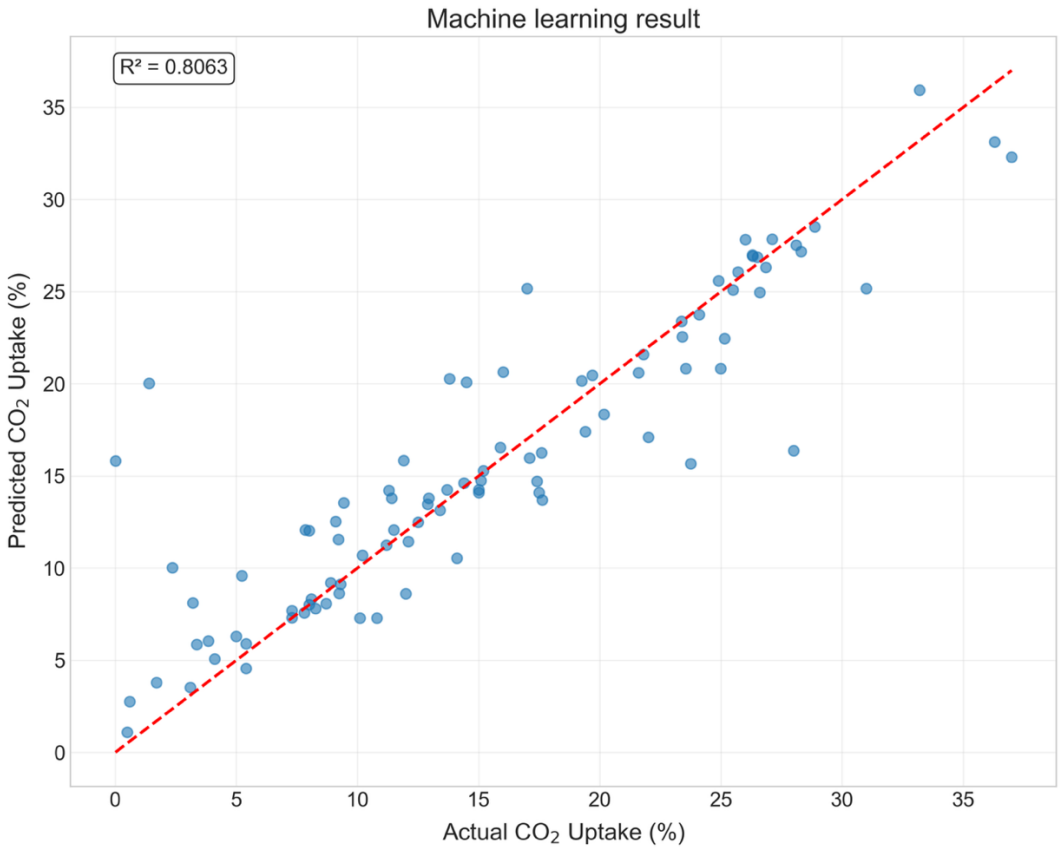

Figure 3-12 Actual vs Predicted CO_2 uptake with R^2 score

Model performance is further illustrated in **Figure 3-12**, which compares measured and predicted CO_2 uptake values. The predictions closely follow the experimental measurements, and the residuals exhibit an approximately symmetric distribution without systematic bias. These results demonstrate that the ensemble model effectively captures the dominant nonlinear relationships between process parameters and CO_2 uptake. The satisfactory predictive accuracy provides a robust foundation for subsequent interpretation of model outputs, including feature importance quantification, single-factor response analysis and three-dimensional interaction assessment.

3.3.4 Single Factor Response Analysis

For each of the eight features, a single-factor response plot was generated by systematically varying the selected feature across its observed range while keeping all other variables at their median values computed from the cleaned dataset. A physics-informed reference response was then constructed by applying a mechanistically motivated functional form such as monotonic, saturation type or bell shaped, chosen on the basis of experimental trends identified in Section 3.2. This reference curve was scaled to the median CO_2 uptake and clipped to remain within 80–120 % of the observed range to ensure physical plausibility. In parallel, 200 evenly spaced points were generated across the feature range, standardised using the fitted StandardScaler, and used as inputs to the trained ensemble regression model to obtain machine-learning predictions, which were plotted as the blue curve. The original experimental observations were plotted as semi-transparent grey scatter points to show the data distribution, and the feature range was divided into 10 equal-width bins to calculate mean CO_2 uptake in each bin. These binned averages were plotted as orange markers, with marker size scaled in proportion to the number of samples in each bin to indicate data density.

To enable direct comparison between machine-learning predictions and theoretically expected behaviours, physics-informed reference responses were constructed for each of the eight investigated features. The observed range of each variable was normalised to the interval [0,1], where x denotes the normalised value of the investigated variable and y represents the corresponding predicted CO_2 uptake

response. The median CO_2 uptake of the harmonised dataset (y_{med}) was used as a scaling baseline.

Table 3-2 Physics-informed reference responses for single-factor analysis

Variable	Physics-informed reference response (normalised form)
Water-to-cement ratio	$y = y_{med} \times (1 - 0.8x)$
Pre-cured time	$y = y_{med} \times \left(0.5 + 0.5(1 - e^{-3x})\right)$
CO_2 partial pressure	$y = y_{med} \times (0.6 + 0.8x)$
CO_2 curing temperature	$y = y_{med} \times (0.7 + 0.6x)$
CO_2 curing RH	$y = y_{med} \times \left(0.6 + 0.8e^{-8(x-0.5)^2}\right)$
CO_2 exposure time	$y = y_{med} \times \left(0.4 + 0.9(1 - e^{-2x})\right)$
Thickness	$y = y_{med} \times (1.2 - 0.7x)$
Subsequent hydration time	$y = y_{med} \times (1.1 - 0.6x)$

For each feature, a mechanistically motivated functional form was selected based on the experimental trends identified in Section 3.2 and the underlying carbonation mechanisms. These functions include monotonic increases or decreases, saturation-type growth, and bell-shaped dependencies that reflect physically interpretable behaviour observed in carbonation kinetics. The resulting expressions define the

expected single-factor response of CO_2 uptake to each variable and are summarised in **Table 3-2**.

In **Figure 3-13**, the red curve is the physics-consistent trend traced from the real experimental data analysed in Section 3.2, whereas the blue dashed curve is the machine-learning prediction trained on data extracted from 35 studies. The two curves are not fully consistent: the red line shows a smooth, monotonic decrease with increasing w/c, while the blue line is more piecewise, with a mild rise at low w/c, a step-like increase and short plateau around w/c ≈ 0.40–0.50, and then a near-flat segment at higher w/c. Even so, both curves convey a compatible overall message, higher w/c does not improve, and generally diminishes or flattens, CO_2 uptake. The weak marginal correlation shown in the panel (≈ 0.094) and the substantial scatter of grey points, together with binned averages that peak locally around w/c ≈ 0.45–0.50, explain why the ML curve deviates from the strictly decreasing red trend.

These discrepancies are considered acceptable as they can be attributed to realistic sources of variability, including: (i) uneven data coverage across w/c, with relatively few measurements below approximately 0.2 and above 0.6, which biases non-parametric fits in these regions; (ii) inter-study heterogeneity in mixture constituents (cement type, supplementary cementitious materials, fillers, admixtures) and in concomitant process parameters (CO_2 pressure, exposure time, temperature, relative humidity, specimen geometry), meaning that w/c is partially confounded with other variables in the compiled literature; (iii) variability in CO_2 uptake measurements, arising from differences between mass-gain and chemical analyses and from

normalisation by cement or binder content; and (iv) heteroscedastic experimental noise and small-sample effects within certain bins, which lead to local deviations. Taken together, these factors explain why the physics-consistent trend (red curve) and the model prediction (blue curve) are not perfectly aligned. Nonetheless, the two curves exhibit consistent direction, curvature and magnitude, and the observed differences are comparable to the experimental uncertainty of the dataset. The deviation is therefore considered acceptable and does not compromise the validity of the inferred trend.

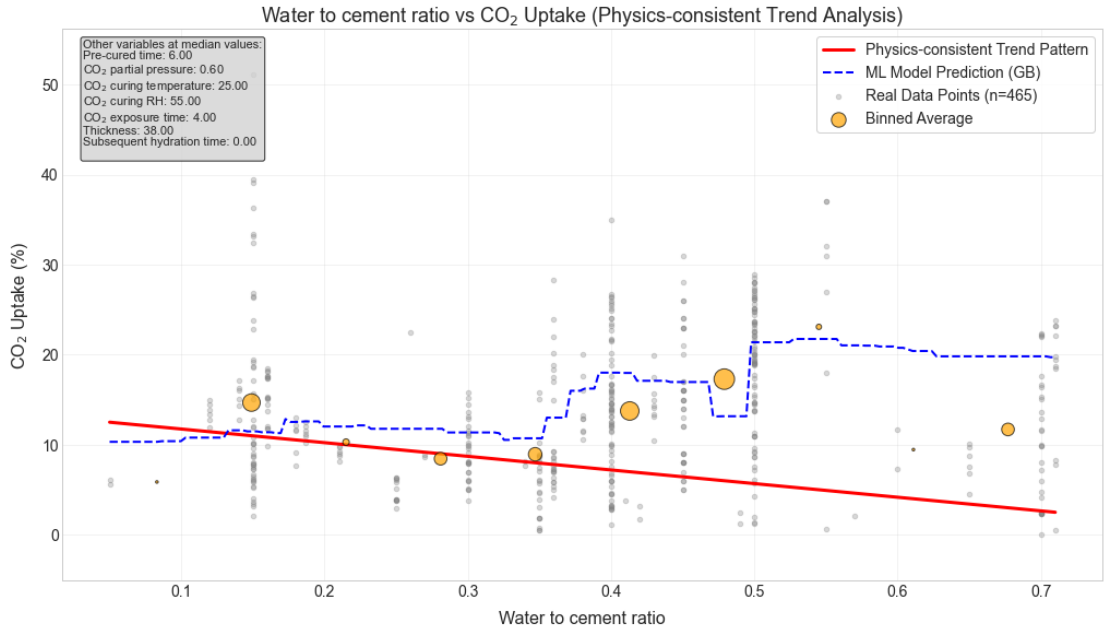

Figure 3-13 Predicted CO_2 uptake trend of water-to-cement ratio

Figure 3-14 to **Figure 3-20** illustrate the single-factor analyses for the seven remaining process variables, with red lines representing physics-consistent trends derived from experimental data and blue dashed lines representing machine-learning (ML) predictions from the compiled dataset. Although the agreement between the two

curves is not perfect, particularly at parameter extremes where data density is low, the ML model reproduces the overall trends with acceptable fidelity. The observed discrepancies can be explained by three main factors: (i) the uneven distribution of available data across the parameter ranges, leading to bias in regions with few experimental points, (ii) variations in curing protocols and measurement techniques across studies, and (iii) intrinsic experimental noise, which introduces scatter into reported CO_2 uptake values.

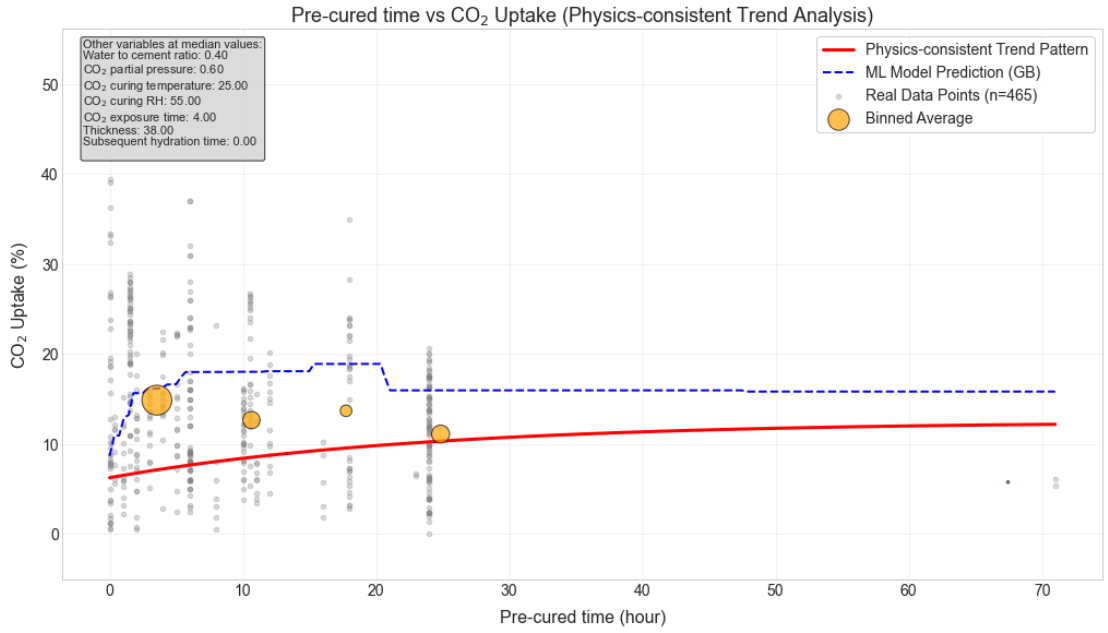

Figure 3-14 Predicted CO_2 uptake trend of pre-cured time

Pre-cured time (shown as **Figure 3-14**) shows a gradual increase in CO_2 uptake as the pre-cured period extends, with a tendency towards plateauing beyond approximately 24 h. This behaviour reflects the competing effects of early hydration: a short pre-cured period retains sufficient porosity for gas transport, whereas extended pre-cured allows further hydration and pore refinement, which eventually limits CO_2 penetration.

The ML prediction slightly overestimates uptake in the mid-range (10–30 h), suggesting that literature data in this range may be biased towards experiments reporting relatively higher carbonation efficiencies.

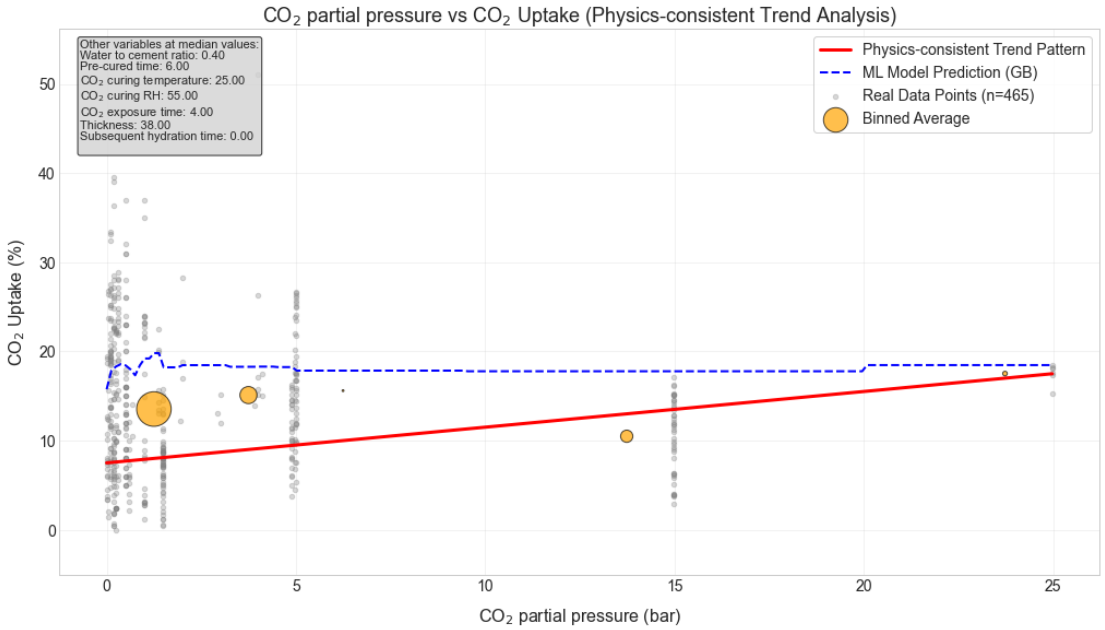

Figure 3-15 Predicted CO_2 uptake trend of CO_2 partial

CO_2 partial pressure (shown as **Figure 3-15**) exhibits a clear positive correlation with uptake. The red line indicates an approximately linear increase within the available range (0–25 bars), consistent with the expectation that higher CO_2 concentrations drive faster reaction kinetics by increasing the chemical potential gradient. The ML curve closely follows the experimental trend except for a small overprediction in the high-pressure region, likely due to the limited number of high-pressure tests in the database. This result reinforces the practical recommendation that elevated CO_2 concentrations are beneficial for accelerated curing, although economic and safety considerations must also be taken into account.

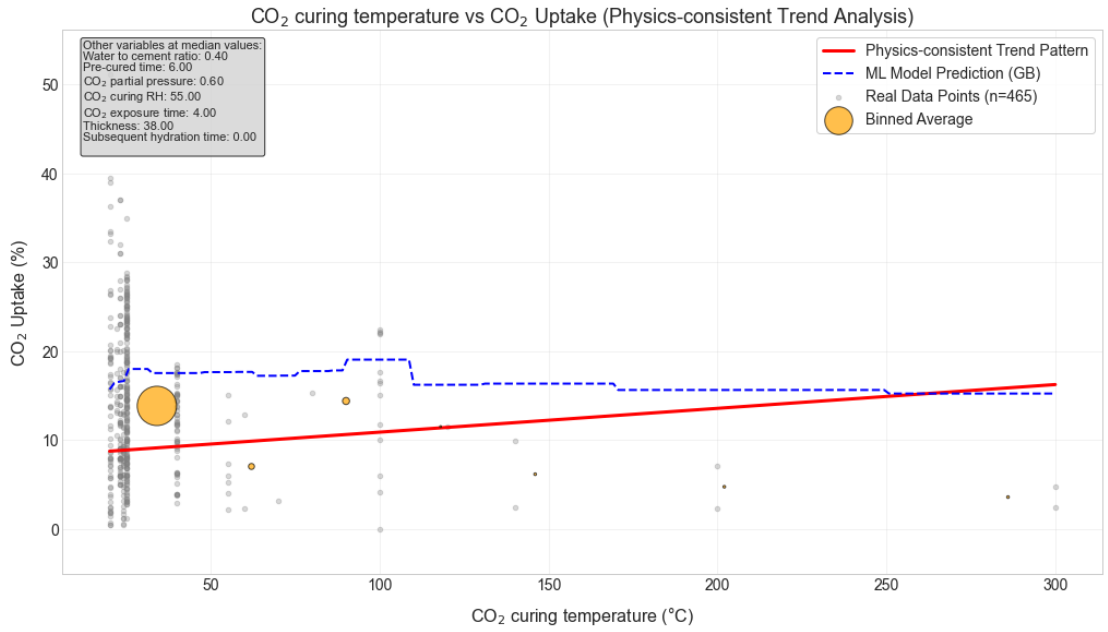

Figure 3-16 Predicted CO_2 uptake trend of temperature

For curing temperature (shown as **Figure 3-16**), the overall effect is relatively weak within the investigated range (ambient to 100 °C). A slight positive slope is observed, indicating that higher temperatures promote CO_2 diffusion and reaction rates. However, the scatter of the raw data is significant, and both the experimental and ML curves show only a modest increase. This suggests that temperature alone is not a dominant factor under the studied conditions and that efforts to significantly raise curing temperature may not yield proportionally large gains in uptake.

The effect of relative humidity (RH) (shown as **Figure 3-17**) follows a bell-shaped trend, peaking at around 50–60 %. This observation is physically meaningful: sufficient moisture is required to dissolve CO_2 and form carbonic acid, yet excessive water content can fill the pores and hinder gas transport. The ML prediction reproduces the peak reasonably well but slightly underestimates uptake at very high RH values, which

may reflect experimental differences in how humidity was controlled. This result confirms that careful RH control is crucial in practical curing chambers to maximise uptake efficiency.

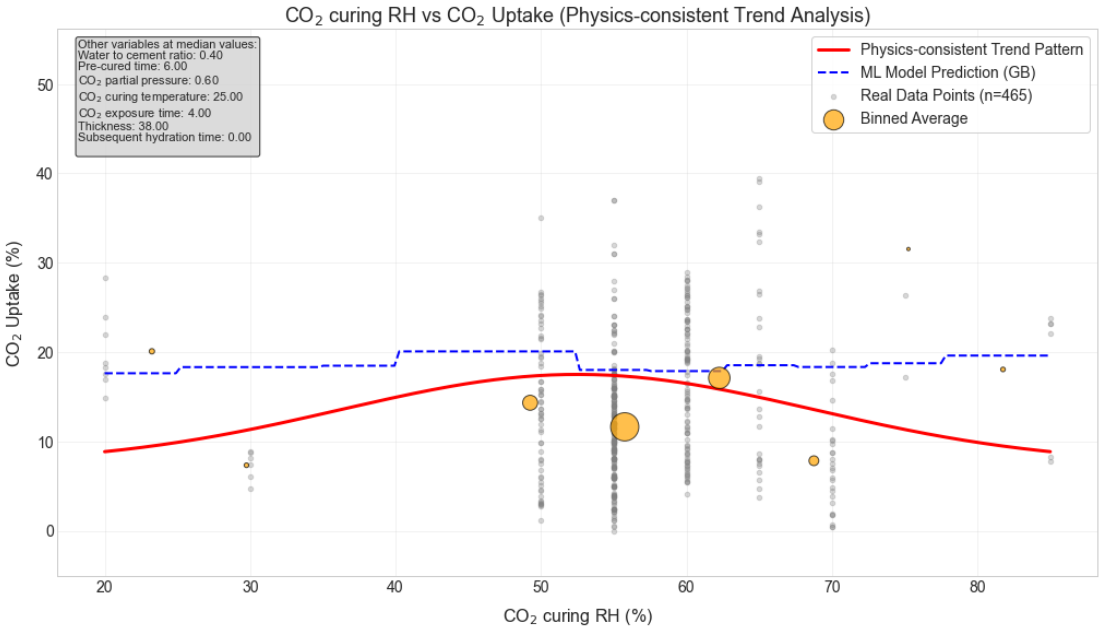

Figure 3-17 Predicted CO_2 uptake trend of RH

Exposure time (shown as **Figure 3-18**) demonstrates a rapid increase in uptake during the early curing period, followed by a plateau after roughly 48–72 h. This behaviour is consistent with diffusion-controlled carbonation kinetics, where the reaction front gradually penetrates deeper into the material until the majority of accessible $Ca(OH)_2$ is carbonated. The ML model slightly overpredicts uptake at very long curing times, likely due to the scarcity of data beyond 72 h. These findings suggest that excessively long curing times may offer diminishing returns and that optimising exposure duration can improve process efficiency.

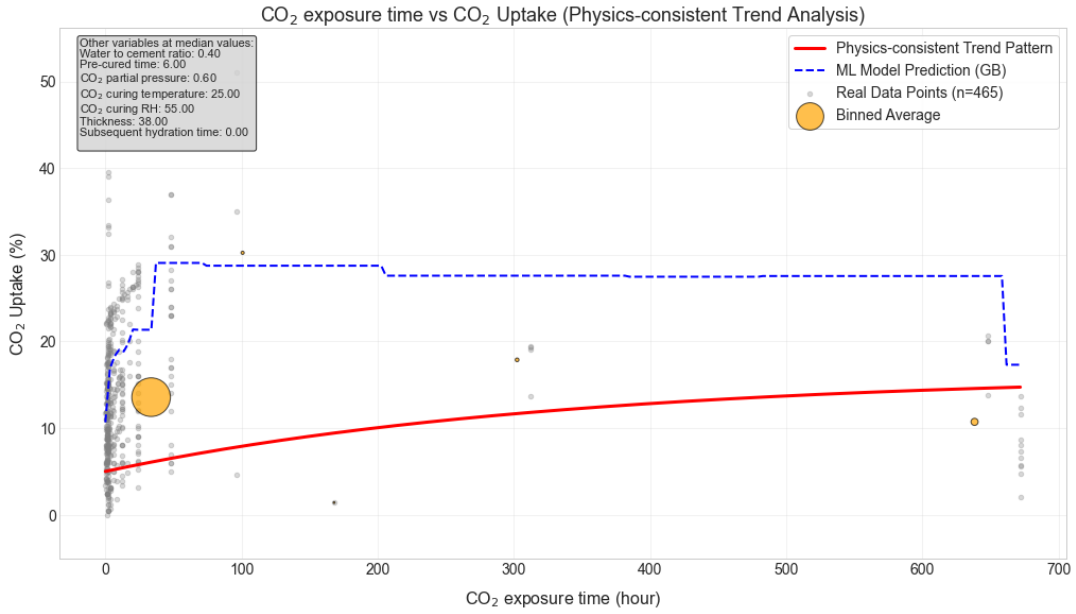

Figure 3-18 Predicted CO_2 uptake trend of exposure time

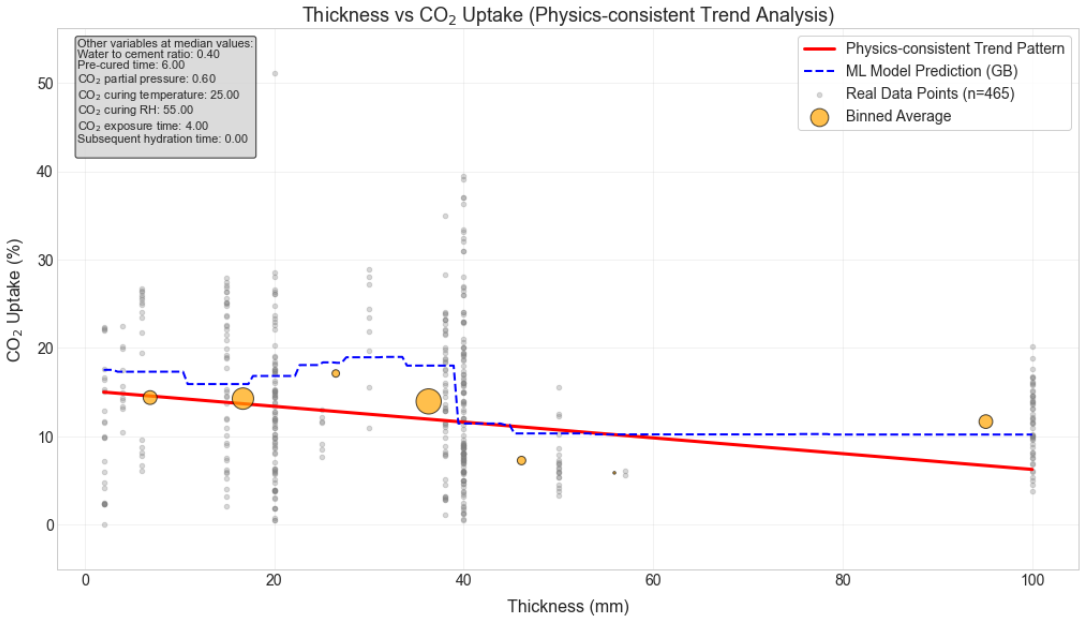

Figure 3-19 Predicted CO_2 uptake trend of thickness

Specimen thickness (shown as **Figure 3-19**) shows a negative correlation with CO_2 uptake, with thinner specimens consistently achieving higher uptake levels. This is attributed to the shorter diffusion path length in thinner samples, which allows more complete carbonation during the exposure period. The ML curve matches the

experimental trend well but slightly underestimates uptake for very thin specimens (<20 mm), possibly because these data are underrepresented in literature. This trend highlights the importance of considering component geometry when designing CO_2 curing protocols.

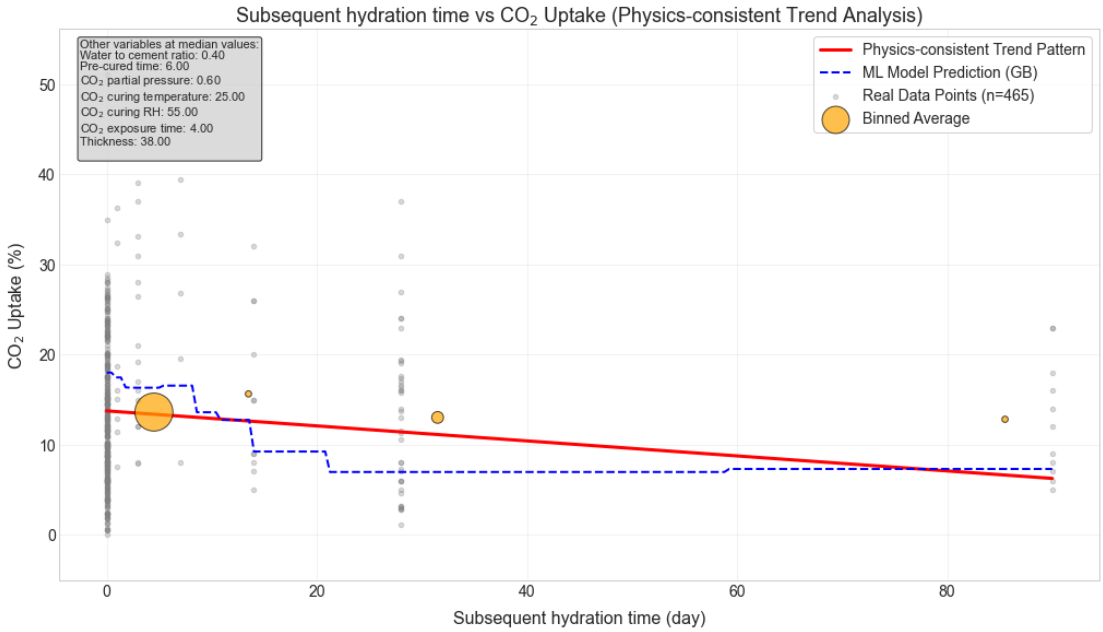

Figure 3-20 Predicted CO_2 uptake trend of subsequent hydration time

Finally, subsequent hydration time (shown as **Figure 3-20**) reveals a slight but consistent decrease in CO_2 uptake with prolonged hydration. This can be explained by the progressive filling of capillary pores by hydration products, which reduces the effective diffusivity of CO_2. The ML prediction captures this downward trend but exhibits a slightly flatter slope, likely because of the limited number of long-term hydration data points. In practice, this finding suggests that CO_2 curing should ideally be applied before substantial hydration has occurred to maximise carbonation potential.

Collectively, these single-factor analyses demonstrate that the machine-learning model not only captures the general direction of parameter effects but also reproduces key physical trends across a broad experimental dataset. The results provide quantitative evidence that parameters such as CO_2 partial pressure, exposure time and specimen thickness exert the strongest influence on CO_2 uptake, while others such as curing temperature and subsequent hydration time have more moderate effects. These findings emphasise the need to consider multiple factors simultaneously, as their combined effects may not be simply additive.

Therefore, Section 3.3.5 further explores the interactions between key variables by constructing three-dimensional response surfaces. These surfaces enable the visualisation of combined effects, for example the interplay between water-to-cement ratio, CO_2 partial pressure and exposure time, thus providing a more complete picture of how to optimise curing conditions for maximum CO_2 uptake.

3.3.5 Three-Dimensional Response Surface Analysis

Water-to-cement ratio is generally determined by the mixed design of the cementitious material and is typically fixed before casting, while pre-cured time is a process parameter that is usually pre-set in production. These two factors, together with CO_2 partial pressure, are among the most influential parameters identified in the feature importance analysis (**Figure 3-10**). In this study, water-to-cement ratio and CO_2 partial pressure were selected as the two primary axes for constructing the three-

dimensional response surfaces, since they represent fundamental material and process variables with strong physical relevance and clear controllability in practice.

Two types of three-dimensional response surfaces are first constructed. The physics-consistent trend surfaces are generated using monotonic and saturating functional forms that reflect expected carbonation behaviour, in which CO_2 uptake decreases with increasing water-to-cement ratio, increases with CO_2 pressure, and approaches a plateau with extended exposure. These surfaces are scaled to the median CO_2 uptake observed in the dataset and provide smooth, interpretable representations that serve as a mechanistic baseline. In parallel, ML prediction surfaces are produced using the Gradient Boosting Regressor, evaluated on a dense grid of water-to-cement ratio and CO_2 pressure combinations. These surfaces directly reflect the underlying experimental data and capture non-linearities and local variations that cannot be represented by simple mechanistic expressions.

Inspection of the raw ML response surfaces reveals localised peaks, abrupt gradients and irregular structures that are not fully consistent with physically plausible trends and which are partly attributable to data sparsity, experimental noise and the non-parametric nature of the model. To distinguish robust patterns from such artefacts, a third set of surfaces is therefore generated by applying a two-dimensional Gaussian smoothing filter to the ML predictions. The smoothing is implemented in Python using the scipy.ndimage.gaussian_filter function, which convolves the predicted uptake grid with a Gaussian kernel. This procedure attenuates high-frequency fluctuations and isolated spikes, while retaining the broader curvature imposed by the data-driven

model. The smoothed ML surfaces are not intended to enforce agreement with the physics-consistent trends, but rather to provide a clearer visualisation of the dominant tendencies implied by the ML predictions and to highlight regions where discrepancies persist.

At 2 h exposure (shown as **Figure 3-21**), the physics-consistent surface predicts CO_2 uptake in the range of approximately 1–8 %, with a smooth, nearly linear increase with CO_2 pressure and only a modest influence of water-to-cement ratio. The raw ML surface yields higher uptake levels (about 11–20 %) and exhibits several local maxima at low w/c and high pressure, together with irregular variations at the margins of the parameter space. After smoothing, the ML surface retains the elevated uptake in the low w/c and high-pressure region, but spurious sharp features are suppressed. The comparison indicates that, while both approaches identify low to moderate w/c ratios and increased pressure as favourable, the ML-based predictions suggest a stronger dependence on mixture design than indicated by the mechanistic baseline.

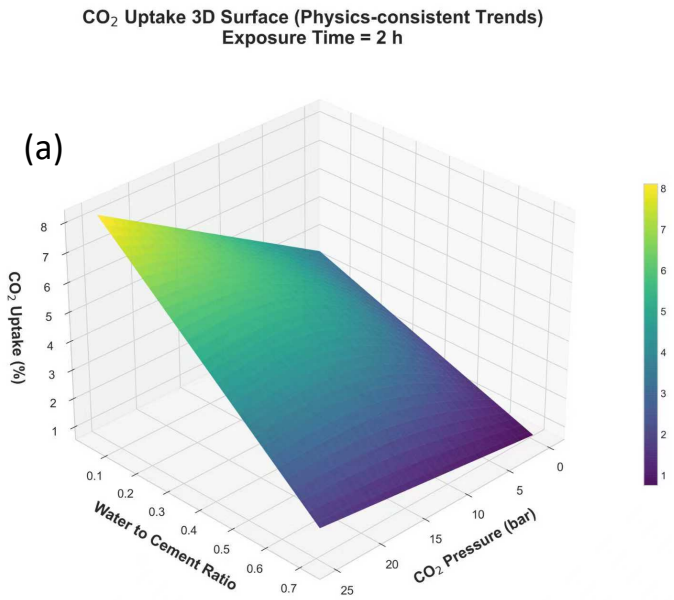

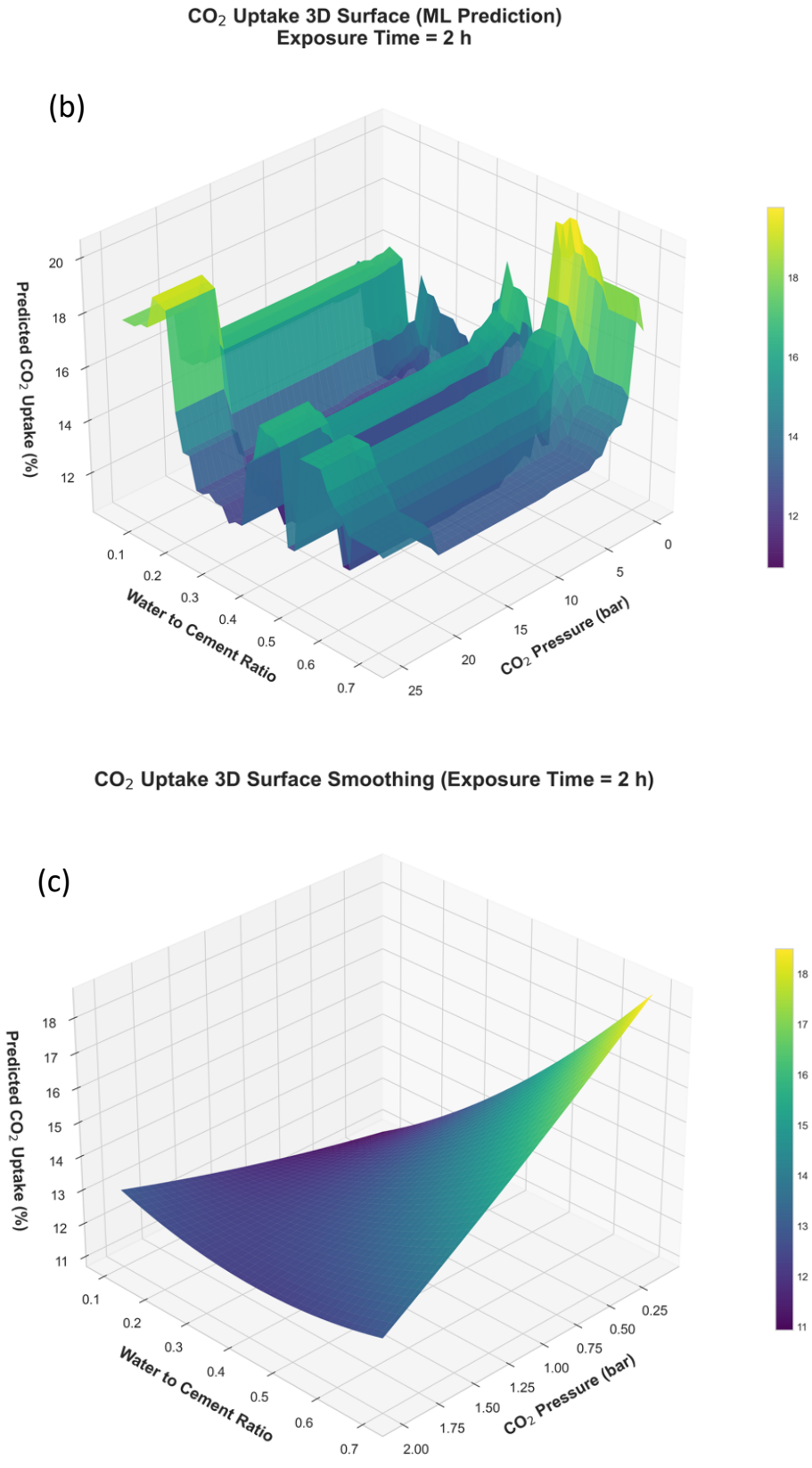

Figure 3-21 3D surfaces of CO_2 uptake as a function of water-to-cement ratio and CO_2 pressure at 2 h exposure: (a) physics-consistent model, (b) raw machine-learning prediction, and (c) smoothed machine-learning surface

At 24 h exposure (shown as **Figure 3-22**), both physics-consistent and ML-based surfaces show increased uptake relative to 2 h. The physics-consistent surface remains monotonic and gradually curved, with uptake up to about 16 %. The raw ML surface predicts values up to roughly 28 %, with pronounced interaction between w/c ratio and CO_2 pressure, especially at w/c ≤ 0.4. The smoothed ML surface clarifies these trends by removing small-scale oscillations but still indicates steeper gradients than the physics-consistent model in certain regions. This divergence suggests that the empirical model captures features driven by specific experimental datasets that are not fully represented in the simplified mechanistic formulation and underlines the need for cautious interpretation in sparsely sampled regions.

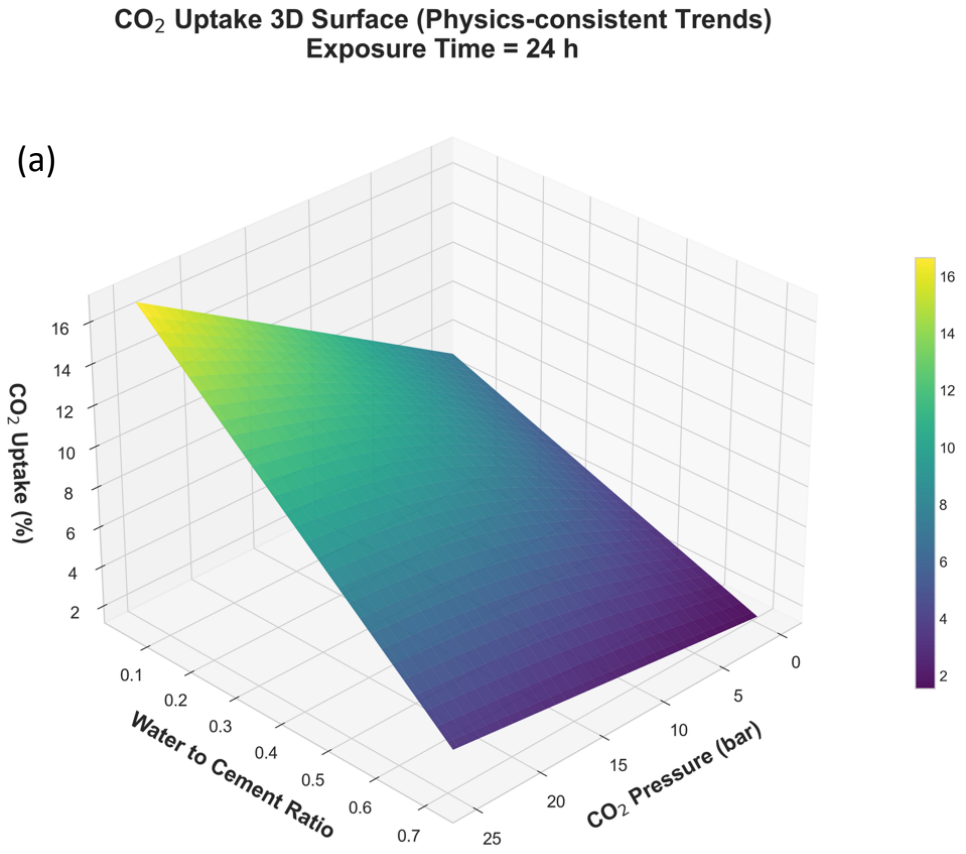

(b)

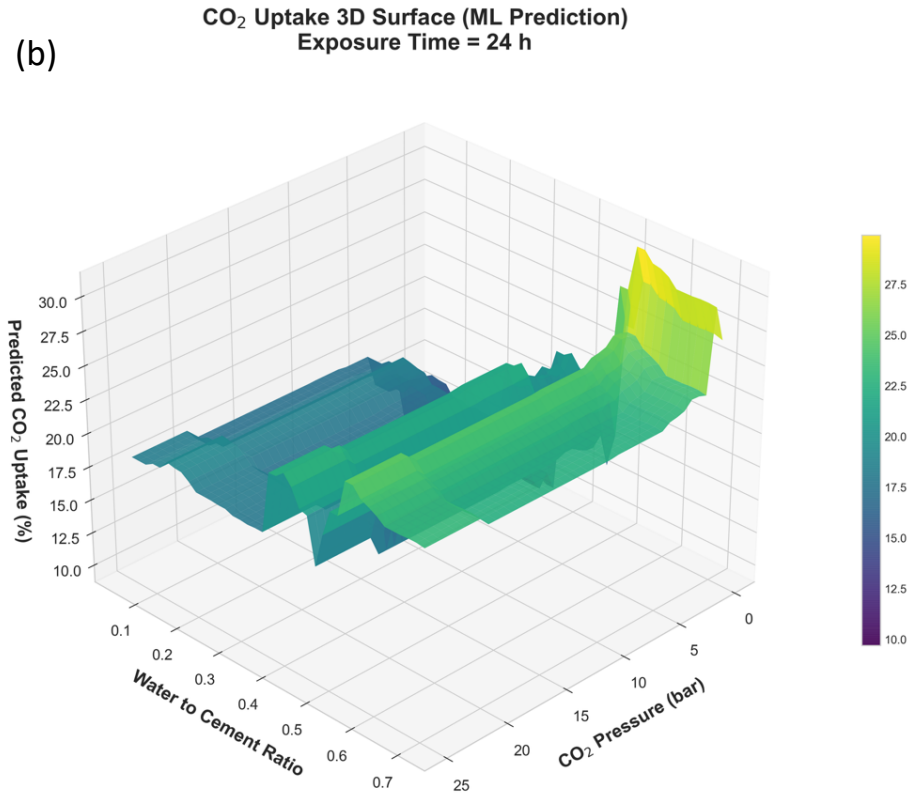

CO_2 Uptake 3D Surface Smoothing (Exposure Time = 24 h)

(c)

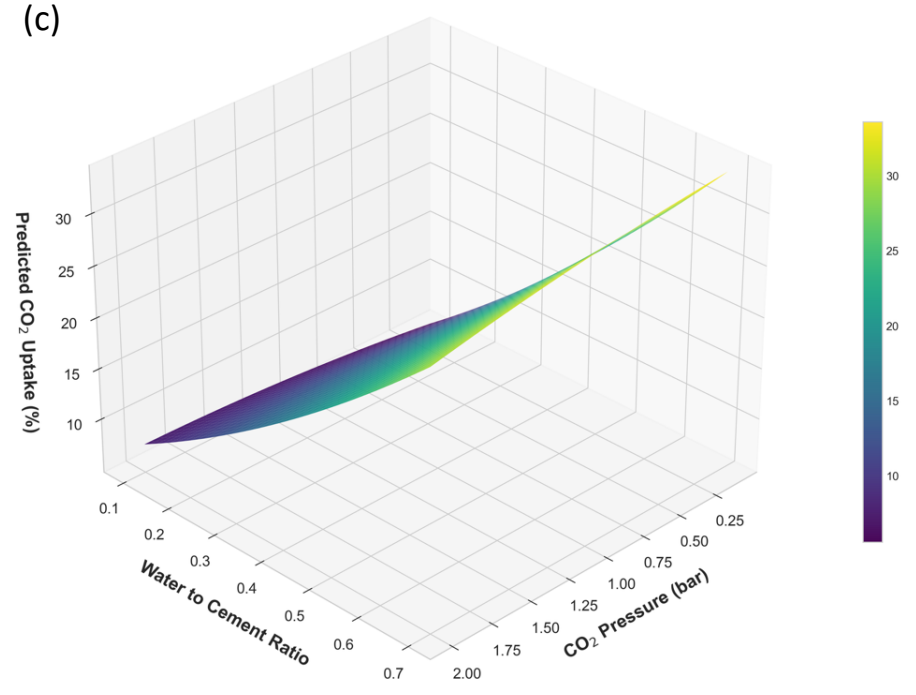

Figure 3-22 3D surfaces of CO_2 uptake as a function of water-to-cement ratio and CO_2 pressure at 24 h exposure: (a) physics-consistent model, (b) raw machine-learning prediction, and (c) smoothed machine-learning surface

At 48 h exposure (shown as **Figure 3-23**), both modelling approaches indicate that uptake approaches a plateau, with diminishing sensitivity to further increases in CO_2 pressure beyond approximately 15–20 bars. The physics-consistent surface shows uptake in the range of about 3–20 %, while the ML-based predictions extend to approximately 35 % in favourable conditions. The smoothed ML surface emphasises the plateau region and reduces visually distracting artefacts, yet differences relative to the physics-consistent surface remain, particularly at extreme combinations of low w/c and high pressure. These discrepancies highlight both the capacity of ML methods to extrapolate trends suggested by the data and their sensitivity to uneven data coverage.

(a)

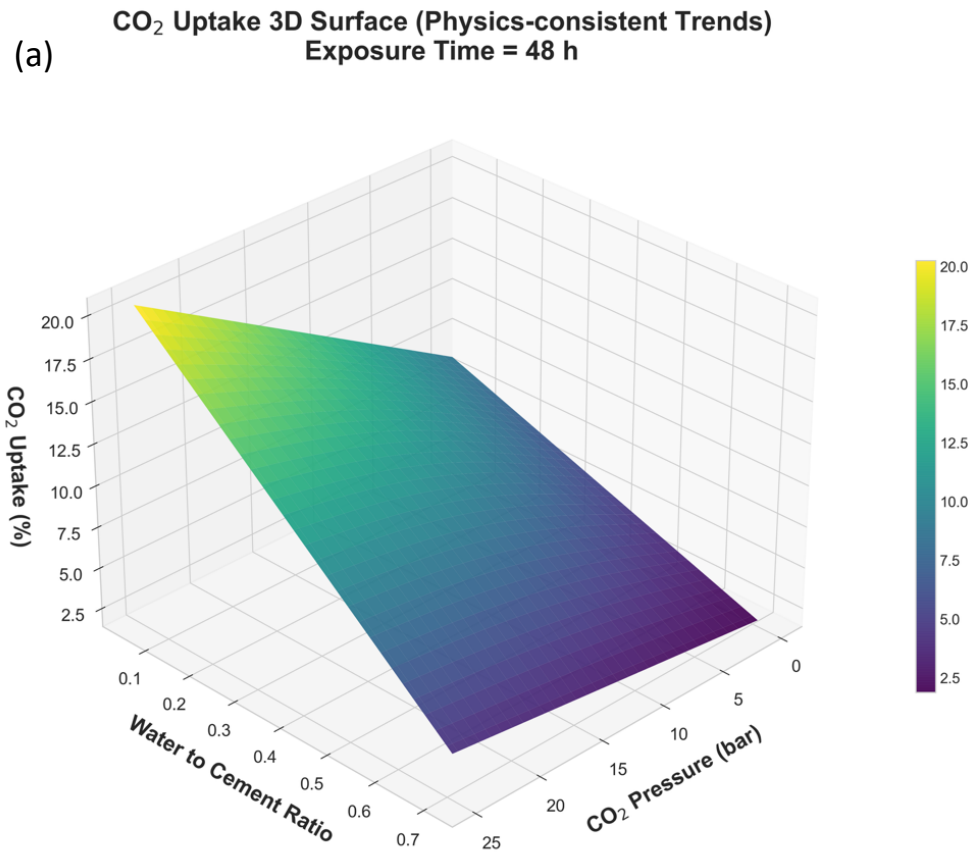

(b)

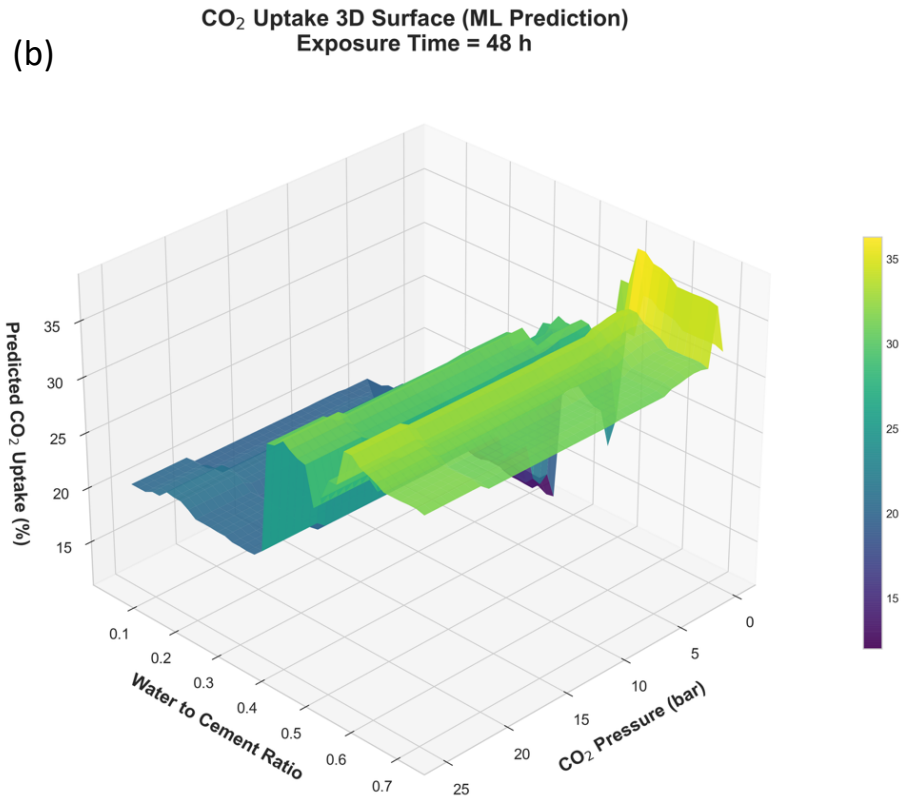

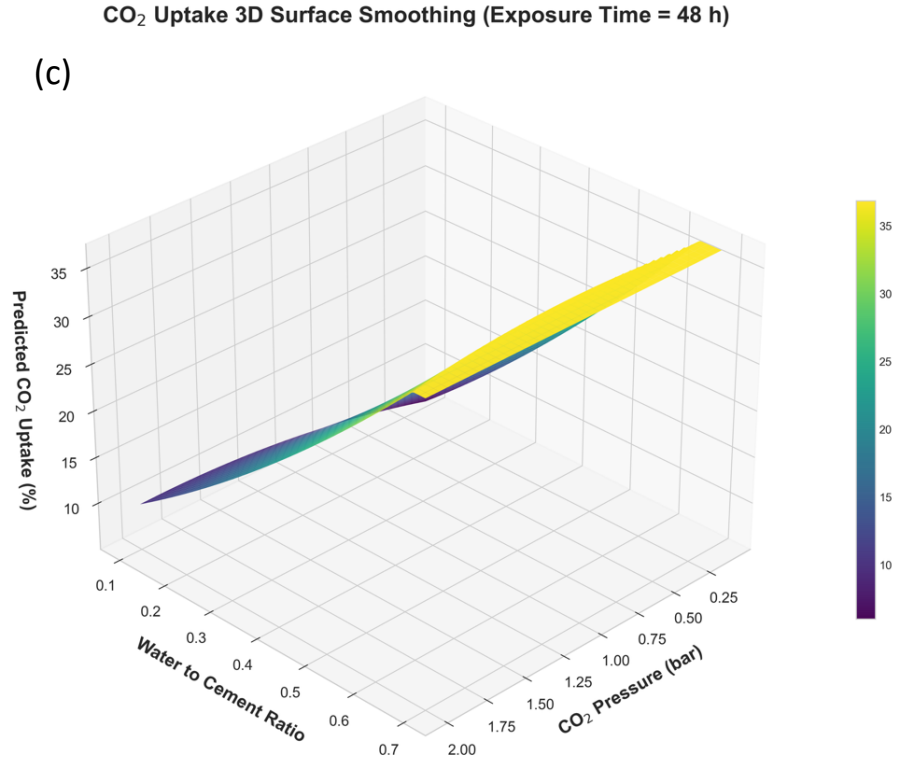

(c)

Figure 3-23 3D surfaces of CO_2 uptake as a function of water-to-cement ratio and CO_2 pressure at 48 h exposure: (a) physics-consistent model, (b) raw machine-learning prediction, and (c) smoothed machine-learning surface

Overall, the physics-consistent surfaces provide smooth and physically interpretable trends that are robust against noise but inherently limited in their ability to reproduce complex non-linear interactions. The ML-based surfaces, including their smoothed counterparts, offer a more detailed representation of the parameter space and can indicate potentially advantageous operating regions, but they are constrained by data quality and coverage and do not guarantee physical fidelity outside the observed domain. Taken together, the combined use of mechanistic, raw ML and smoothed ML surfaces offers a transparent and critical framework: agreement between surfaces increases confidence in predicted trends, whereas persistent differences signal domains where additional targeted experiments and refined modelling are required.

3.4 Conclusion

This chapter has compiled and systematically analysed more than five hundred experimental datasets on CO_2 curing of cementitious materials, encompassing a wide range of curing conditions and compositional parameters. The data confirm that CO_2 uptake is primarily controlled by water-to-cement ratio, pre-curing duration, temperature, relative humidity, CO_2 partial pressure, and exposure time, together with specimen thickness and subsequent hydration. The majority of studies were conducted under curing temperatures of 20–30 °C and relative humidity levels between 55 % and 70 %. Longer pre-curing durations were generally favourable, particularly when the water-to-cement ratio was relatively high. Lower ratios enhanced CO_2 uptake provided that workability was maintained, typically above 0.14. Increases in CO_2 pressure and curing duration improved uptake, although economic

and operational constraints impose practical limits. After screening for completeness and internal consistency, 465 datasets were retained for the subsequent machine-learning analysis.

The single-variable analyses revealed physically coherent trends: CO_2 uptake increased with pressure and exposure duration, exhibited a bell-shaped dependence on relative humidity with an optimum around 50–60 %, and declined with increasing specimen thickness and extended hydration. These relationships align with established reaction–diffusion mechanisms governing carbonation in cementitious systems.

A key methodological outcome of this chapter is the development of three complementary three-dimensional response surfaces to quantify and visualise the combined effects of water-to-cement ratio, CO_2 pressure, and curing duration. The physics-consistent surfaces describe monotonic, mechanistically grounded relationships, predicting uptake between approximately 0.01 and 0.20 kg CO_2 kg^{-1} binder and clearly exhibiting a plateau beyond 15–20 bars. The ML prediction surfaces, constructed using the Gradient Boosting Regressor, provide a higher-resolution depiction of the response space, capturing non-linear interactions and local variations that are not represented by the idealised mechanistic forms. These models predict maximum uptakes approaching 0.35 kg CO_2 kg^{-1} binder. A third set of Gaussian-smoothed ML surfaces is introduced to improve interpretability by attenuating local irregularities and experimental noise while preserving the broader curvature defined by the data. The smoothed surfaces highlight dominant tendencies within the ML

predictions and reveal areas of divergence from the physics-consistent results, indicating potential data sparsity or model overfitting.

Together, these three modelling approaches provide a coherent and critical framework for interpreting the relationships between process parameters and CO_2 uptake. The physics-consistent surfaces reproduce mechanistic behaviour but underestimate the quantitative magnitude of uptake. The ML predictions achieve greater numerical accuracy but are less interpretable and sensitive to data heterogeneity. The smoothed ML surfaces occupy an intermediate position, clarifying overall tendencies while exposing inconsistencies at the margins of the parameter space. The convergence of predictions across most of the parameter domain strengthens confidence in the general trends identified, whereas the remaining discrepancies point to priority areas for targeted experimental validation and data expansion.

In summary, this chapter establishes a harmonised and statistically robust foundation for the quantitative analysis of CO_2 curing. The combined use of mechanistic, data-driven, and post-processed models consolidates physical interpretation with empirical correlation, enabling a systematic characterisation of how key process variables govern CO_2 uptake. The findings strengthen the methodological basis for predictive modelling of accelerated carbonation in cementitious materials and provide a reproducible framework for future experimental design and comparative evaluation across curing systems.

References

Chen, T., & Gao, X. (2019). Effect of carbonation curing regime on strength and microstructure of Portland cement paste. *Journal of CO2 Utilization*, *34*, 74–86. https://doi.org/10.1016/j.jcou.2019.05.034

Li, X., & Ling, T. C. (2020). Instant CO2 curing for dry-mix pressed cement pastes: Consideration of CO2 concentrations coupled with further water curing. *Journal of CO2 Utilization*, *38*, 348–354. https://doi.org/10.1016/j.jcou.2020.02.012

Liu, T. (2016). Effect of early carbonation curing on concrete resistance to weathering carbonation. McGill University (Canada).

Rostami, V., Shao, Y., & Boyd, A. J. (2011). Durability of concrete pipes subjected to combined steam and carbonation curing. *Construction and Building Materials*, *25*(8), 3345–3355. https://doi.org/10.1016/j.conbuildmat.2011.03.025

Rostami, V., Shao, Y., & Boyd, A. J. (2012). Carbonation Curing versus Steam Curing for Precast Concrete Production. *Journal of Materials in Civil Engineering*, *24*(9), 1221–1229. https://doi.org/10.1061/(asce)mt.1943-5533.0000462

Shao, Y. (2010). *Beneficial Use of Carbon Dioxide in Precast Concrete Production Final Report*.

Shao, Y., & Morshed, A. Z. (2015). Early carbonation for hollow-core concrete slab curing and carbon dioxide recycling. *Materials and Structures/Materiaux et Constructions*, *48*(1–2), 307–319. https://doi.org/10.1617/s11527-013-0185-3

Shi, C., & Wu, Y. (2008). Studies on some factors affecting CO2 curing of lightweight concrete products. *Resources, Conservation and Recycling*, *52*(8–9), 1087–1092. https://doi.org/10.1016/j.resconrec.2008.05.002

Sun, K., Zhou, X., Gong, C., Ding, Y., & Lu, L. (2016). Influence of paste thickness on coated aggregates on properties of high-density sulphoaluminate cement concrete. *Construction and Building Materials*, *115*, 125–131.

https://doi.org/10.1016/j.conbuildmat.2016.04.018

Wang, D., Noguchi, T., & Nozaki, T. (2019). Increasing efficiency of carbon dioxide sequestration through high temperature carbonation of cement-based materials. *Journal of Cleaner Production*, *238*. https://doi.org/10.1016/j.jclepro.2019.117980

Wang, T., Huang, H., Hu, X., Fang, M., Luo, Z., & Guo, R. (2017). Accelerated mineral carbonation curing of cement paste for CO2 sequestration and enhanced properties of blended calcium silicate. *Chemical Engineering Journal*, *323*, 320–329. https://doi.org/10.1016/j.cej.2017.03.157

Zakir Morshed, A., & Shao, Y. (2013). Influence of moisture content on co2uptake in lightweight concrete subject to early carbonation. *Journal of Sustainable Cement-Based Materials*, *2*(2), 144–160. https://doi.org/10.1080/21650373.2013.797373

Zhan, B. J., Xuan, D. X., Poon, C. S., & Shi, C. J. (2019). Mechanism for rapid hardening of cement pastes under coupled CO2-water curing regime. *Cement and Concrete Composites*, *97*, 78–88. https://doi.org/10.1016/j.cemconcomp.2018.12.021

Zhang, D., Asce, S. M., Cai, ; Xinhua, & Shao, Y. (2016). *Carbonation Curing of Precast Fly Ash Concrete*. https://doi.org/10.1061/(ASCE)MT.1943

Zhang, D., Cai, X., & Jaworska, B. (2020). Effect of pre-carbonation hydration on long-term hydration of carbonation-cured cement-based materials. *Construction and Building Materials*, *231*. https://doi.org/10.1016/j.conbuildmat.2019.117122

Zhang, D., & Shao, Y. (2016). Early age carbonation curing for precast reinforced concretes. *Construction and Building Materials*, *113*, 134–143. https://doi.org/10.1016/j.conbuildmat.2016.03.048

Zhang, S., Ghouleh, Z., Liu, J., & Shao, Y. (2021). Converting ladle slag into high-strength cementing material by flue gas carbonation at different temperatures. *Resources, Conservation and Recycling*, *174*.

https://doi.org/10.1016/j.resconrec.2021.105819

Chapter 4 Assessing the Net Carbon Removal Potential by a Combination of Direct Air Capture and Recycled Concrete Aggregates Carbonation

This chapter is based on (with minor edits) the following published paper: Chen, Liyuan, and Aidong Yang. "Assessing the net carbon removal potential by a combination of direct air capture and recycled concrete aggregates carbonation." *Resources, Conservation and Recycling* 212 (2025): 107940.

Liyuan Chen, as the first author, contributed to Writing – original draft, Visualization, Software, Methodology, Formal analysis, Data curation, Conceptualization. Aidong Yang, as the corresponding author, contributed to Writing – review & editing, Supervision, Conceptualization.

Summary

Removing and storing CO_2 from the atmosphere has an important role in combating climate change. This study assessed the CO_2 removal potential of combining direct air capture with carbonation of RCAs (shown as **Figure 4-1**). An industrial-scale RCA carbonation process model quantified key parameters' impacts on carbonation duration and energy consumption. Furthermore, a lifecycle analysis evaluated scenarios of two cases: (i) using pure CO_2 with transportation between DAC and carbonation, and (ii) onsite production of low-purity CO_2. For 90% carbonation of 1 tonne of RCA, the performance of case-i scenarios ranged from ~13 kg net CO_2 removal to ~14 kg net CO_2 emission, influenced by DAC technology, transport option,

and electricity carbon intensity. In case-ii scenarios, 1% CO_2 feed purity achieved 70% greater CO_2 removal than using pure CO_2. This work provides an initial indication of the potential of this scheme while revealing key factors to investigate in future experimental exploration.

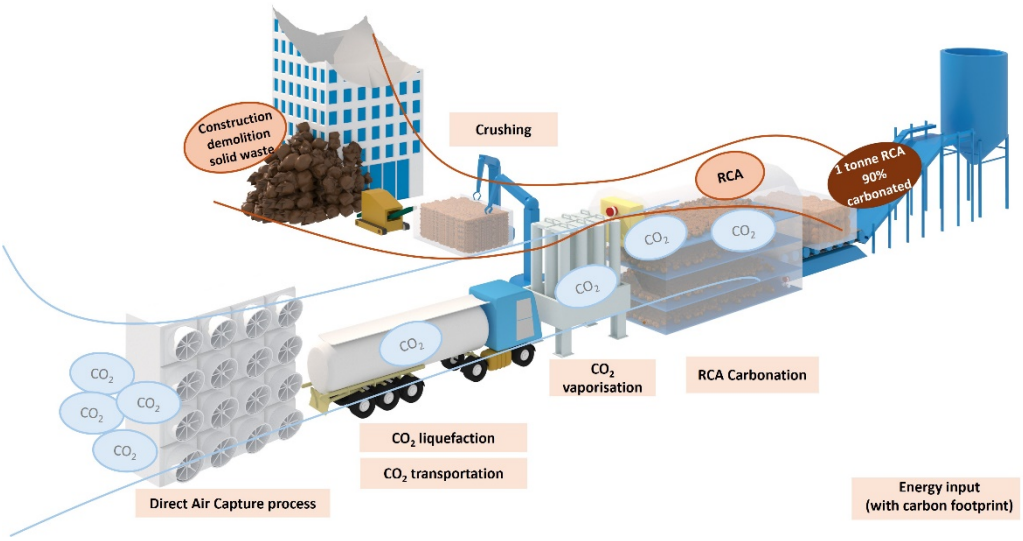

Figure 4-1 Recycled concrete aggregates carbonation process

4.1 Introduction

As the crisis of climate change deepens, carbon dioxide Removal (CDR) from the atmosphere has been considered necessary to complement emissions reduction to keep the concentration of greenhouse gases under the budget level by the end of the 21st century (Qiu et al., 2022). The recently published State of Carbon Dioxide Removal report (Smith et al., 2023) estimates that a significant CDR requirement between 420 and 1,100 Gt CO_2 by 2100 is needed for the IPCC's 1.5°C scenarios. Among CDR options, direct air capture (DAC) removes CO_2 from air through industrial processes, often resulting in a high-purity CO_2 gas product (Qiu et al., 2022). In recent years, remarkable

advances have been made in DAC technologies, with adsorption-based and solvent-based options reaching high Technology Readiness Levels (8-9) while other processes such as electrochemical and other hybrid options are being further developed (Bisotti et al., 2024). Compared with carbon capture from point sources, DAC has higher energy requirements and costs due to the unique difficulty of separating CO_2 from air at a very low concentration (currently ~420 ppm)(Richard C Darton, 2020). However, this economical advantage is limited to industrial source (i.e. power plant pollutants), the fact that DAC extracts CO_2 directly from the surrounding air means fewer limits on scaling and greater siting flexibility (Sodiq et al., 2023). Like carbon capture from point sources, DAC also requires long-term secure CO_2 storage. When geological storage is considered, the challenges include transportation pipelines, geological appraisal and preparation and, in some countries, regional availability of suitable storage sites (Budinis et al., 2018). As an alternative to geological storage, captured CO_2 can be stored in materials through the route of utilisation, ideally for a time period relevant to climate change mitigation, i.e., from multiple decades to 100s years (Hepburn et al., 2019). Materials that naturally align with such timescales are those used in the construction of buildings and infrastructures. In particular, concrete as the construction material used globally in the largest quantity has been known to be able to absorb CO_2 through chemical reaction processes (Xi et al., 2016), leading to secure CO_2 storage.

Very relevant to storing CO_2 in concrete is recycled concrete aggregate (RCA), a recycled material as part of non-hazardous construction and demolition wastes (CDW),

usually the concrete debris. The use of CDW-derived RCA to replace natural coarse aggregates in construction has been shown to significantly reduce the use of non-renewable energy and greenhouse gas emissions (Hossain et al., 2016). In 2021, CDW generation was around 2,600 Mt in China (Joseph et al., 2023), 500 ~600 Mt in both the US and India, and 100~200 Mt in several Europe countries (Wang et al., 2021). Despite disposal options with lower environmental impacts exist (Danish & Mosaberpanah, 2022), landfill remains a significant destination of CDW. The landfill proportion of CDW in India, China, US and Europe countries are currently at 99%, 75%, 25% and 10%, respectively (Chen et al., 2022); the concrete fractions of these unutilized materials thus represent considerable supply potential of RCA worldwide.

Through the carbonation process, RCA can sequestrate CO_2, and the carbonated RCA can potentially be used for producing new concrete after mixing it with cement (Shuvo et al., 2024). It has been experimentally shown that the properties of recycled aggregate from ordinary concrete (OC) and high-performance concrete (HPC) could be improved by carbonation (Sereng et al., 2021); the improvement of RCA properties is affected by carbonation conditions such as RCA particle size, duration, and moisture contents (Zhan et al., 2014). Numerous RCA carbonation studies have recently been reported in literature. For example, the impacts of key factors on the degree of carbonation have been studied, including particle size (Leemann et al., 2023; Liu et al., 2021), CO_2 partial pressure (Ding et al., 2023; Xuan et al., 2017), duration (Li et al., 2023; Pu et al., 2022), and RCA water/cement (w/c) ratio (Li et al., 2019; Tam et al., 2020). Across these studies, CO_2 uptake in the range between 10-21 kg/kg (dry) RCA

has been reported. To predict the degree of carbonation, mathematical modelling efforts have been made based on either a mechanistic understanding of the underlying physical and chemical processes (Thiery et al., 2013) or regression using experimental data (Fang et al., 2017). Besides, the environmental benefits of carbonated RCA with the CO_2 resource from CCS, compared with natural and recycled aggregates, have been studied (e.g., Xiao et al., 2022).

Despite the strong desire to find alternatives to geological storage of CO_2 produced by CDR (and DAC in particular) and the existing studies on absorbing CO_2 by RCA, the potential of using the carbonation of RCA as a sink for CO_2 captured from the atmosphere through DAC is yet to be assessed. This research gap means the important question remains unanswered regarding the net CO_2 removal potential by a technical scheme that combines DAC with RCA carbonation. This study presents the mathematical modelling of an industrial-scale carbonation process for treating RCA to store CO_2 derived from DAC. Informed by the results of carbonation process modelling, life cycle assessment (LCA) is carried out under multiple scenarios to quantify net CO_2 removal potential, taking into account DAC, CO_2 transport as well as RCA carbonation, to develop an understanding of how technological choices and the carbon intensity of power supply are likely to affect the performance of such a carbon removal and storage scheme in its possible future deployments.

4.2 Methodology

Here, a description of the RCA materials considered in this work is presented, followed by the modelling approaches applied to the RCA carbonation process and the rest of the LCA. Unless provided in this section, the values of the model parameters adopted in different parts of the modelling work are detailed in the Appendix B.1 **Table B-1**.

4.2.1 RCA Materials

The RCA is assumed to be supplied by crushing concrete demolition solid waste, with the characteristics depending on the original reinforced concrete applications. Six types of RCA (RCA1 to RCA6) are considered in this study. Each type is characterized by water-to-cement ratio (w/c ratio), cement content, CaO mass percentage in cement and density. In particular, the w/c ratio and cement content in RCA1 to RCA6 were set with reference to established concrete classes RC20/25, RC25/30, RC28/35, RC30/37, RC35/45, RC40/50, respectively (British Standards Institution, 2023), with the purpose to cover a range of each property (0.45 -0.5 for w/c ratio; 240 -340 kg/m^3 concrete for cement content) as possessed by concrete commonly encountered in CDW. CaO mass percentage of the cement content is assumed to be 65% for all RCA types, which is a typical value for Portland cement (Aïtcin & Flatt, 2015). RCA density depends on the type of concrete; the higher the w/c ratio, the lower the density (Malaiskiene et al., 2017). Here, the density of RCA5 is used as a reference (Sereng et al., 2021); the densities of other RCA types (with their exact values unknown) are

approximated through adjustment to the reference. The characteristics of these RCA types are given in the Appendix B.1 **Table B-2**.

4.2.2 Modelling of RCA Carbonation

4.2.2.1 Description of the RCA Carbonation Process

An enclosed chamber with reference dimensions of $10m^3$ (10m x 1m x 1m) is considered to host a bed of RCA particles, with a bed porosity of 0.4. For simplicity, carbonation that has already occurred to the RCA particles prior to the modelled carbonation process is ignored in the main simulation study. However, the potential impact of partial carbonation of the concrete content in CDW is separately explored (see Section 4.3.2.4). The feed gas that contains CO_2 is supplied from one end of the chamber, travelling through the bed across the length, with a fan to overcome the pressure drop caused by the resistance of the RCA particles to the gas flow. The carbonation process takes place at ambient conditions of 293.15 K, 1 bar, and with 70% relative humidity. To avoid an excessive level of CO_2 remaining in the exhaust gas that leaves the chamber, an operating strategy is considered, which continuously reduces the feed gas flow rate, when necessary, to limit the flow rate of CO_2 in the exhaust to below 0.1% of that in the feed gas. Since the carbonation rate progressively reduces as the process continues, the operation is stopped once 90% of the maximum degree of carbonation has been reached, to avoid prolonged unproductive operation.

4.2.2.2 Mathematical Model of the Carbonation Chamber

To predict carbonation across the chamber, a multi-compartmental 1-D model is established in which the chamber is divided into n compartments along its length; n=100 has particularly been adopted in the simulation analysis to ensure accuracy. Each compartment is assumed to be well-mixed, connected to its down-stream neighbour by the gas flow.

$$\frac{dC_{CO_2}(j)}{dt} = \frac{-R(j) + Q_{in}(j) \times C_{CO_{2in}}(j) - Q_{out}(j) \times C_{CO_2}(j)}{V(j)} \qquad (4-1)$$

Equation (4-1) presents the mass balance of CO_2 in the gas phase of compartment j, j = 1, 2, 3, …, n. $C_{CO_2}(j)$ (kg/m^3) is CO_2 concentration in the gas phase. $C_{CO_{2in}}(j)$ (kg/m^3) is CO_2 concentration of the gas entering compartment j, which is either the concentration of the feed gas if j = 1, or that leaving the previous compartment (j-1). $Q_{in}(j)$ (m^3/s) and $Q_{out}(j)$ (m^3/s) are the velocity of the gas entering and leaving the compartment, respectively. $V(j)$ (m^3) is the gas phase volume of the compartment. $R(j)$ (kg/s) is the carbonation rate, i.e. the rate at which CO_2 is removed from the gas phase and transferred to the RCA particles. t (s) is the time.

$$Q_{out}(j) = Q_{in}(j) - \frac{R(j)}{G_t \times M_{CO_2}} \qquad (4-2)$$

where G_t (mol/m^3) is the CO_2 mole in chamber. M_{CO_2} (kg/mol) is molar moss of CO_2. The carbonation rate, $R(j)$, is essentially the rate of increase in the CO_2 uptake by the RCA particles in compartment j:

$$R(j) = \frac{dCu(j)}{dt} \quad (4-3)$$

The total CO_2 uptake by time t, $Cu\,(j)$ (kg) can be calculated by the following equation:

$$C_u(j) = \frac{a_{max} \times F_d \times m_{RCA}(j)}{\rho_{RCA}} \quad (4-4)$$

where a_{max} (kg/m^3) is the maximum CO_2 uptake per unit volume of RCA. $m_{RCA}(j)$ (kg) is the mass of RCA in compartment j. F_d is the fraction of RCA that is carbonated by time t. ρ_{RCA} (kg/m^3) is RCA density. a_{max} can be calculated by the following equations:

$$a_{max} = a_{th} \times w \quad (4-5)$$

$$a_{th} = \beta \times C_e \times M_{CaO} \times M_r \quad (4-6)$$

In equation (4-5), the coefficient w is introduced to offer an adjustment to the theoretical maximum CO_2 uptake (a_{max}), with a value of 0.3 determined from previously reported observations (Thiery et al., 2013; Zhan et al., 2014).

a_{th} (kg/m^3) represents the theoretical maximum CO_2 uptake, dictated by the CaO content in the RCA that is theoretically available for carbonation. C_e (kg/m^3) is cement content. M_{CaO} (kg CaO /kg cement) is the CaO content in cement. M_r is the molar mass ratio of CO_2 to CaO. β (% of CaO carbonated) is the proportion of CaO that can be converted to $CaCO_3$ during the RCA carbonation.

$$\beta = f_{CaO} \times \alpha_H \quad (4-7)$$

where f_{CaO} is the ratio of the mass molar of CaO in C_2S, C_3S and C_3A to the mass

molar of CaO in clinker. α_H is hydration degree and can be estimated as a function of water to cement ratio in cement, w/c, by an empirical equation(Bejaoui & Bary, 2007):

$$\alpha_H = 0.239 + 0.745tanh[3.62(w/c - 0.095)] \qquad (4-8)$$

From equations (4-3) and (4-4), the following is obtained:

$$R(j) = \frac{dCu(j)}{dt} = \frac{a_{max} \times m_{RCA}(j)}{\rho_{RCA}} \frac{d\,F_d}{dt} \qquad (4-9)$$

To calculate $\frac{d\,F_d}{dt}$, an existing expression derived for F_d is used (Xi et al., 2016) which, as in other numerical studies (e.g.,Thiery et al., 2013), assumes a spherical shape for RCA particles. This is a simplification of the actual shapes resulting from crushing, to make the modelling tractable. F_d is modelled as a function of the carbonated diameter of an RCA particle (D_0, in m):

$$F_d = \begin{cases} 100\% - \dfrac{\int_a^b \frac{\pi}{6}(D - D_0)^3 dD}{\int_a^b \frac{\pi}{6} D^3 dD} \times 100\% \ (a \geq D_0) \\ 100\% - \dfrac{\int_{D_0}^b \frac{\pi}{6}(D - D_0)^3 dD}{\int_a^b \frac{\pi}{6} D^3 dD} \times 100\% (a < D_0 < b) \\ 100\% \ (b < D_0) \end{cases} \qquad (4-10)$$

where a (m) and b (m) are the minimum and maximum diameters of RCA particles in given size distribution, D (m) is the diameter of RCA particles, it's in range of a and b. Note that equation (4-10) assumes an even distribution of the RCA particle size between the size range (a to b).

$\frac{d\,F_d}{dt}$ can then be obtained by:

$$\frac{d\,F_d}{dt} = \frac{d\,F_d}{dD_0} \times \frac{dD_0}{dt} \qquad (4-11)$$

The detailed expression for $\frac{d\,F_d}{dD_0}$, derived from equation (4-10), is provided in the Appendix B.1 **Table B-3**. Furthermore,

$$\frac{dD_0}{dt} = 2 \times \frac{dd_0}{dt} \qquad (4-12)$$

where d_0 refers to the thickness of the carbonated layer of an RCA particle. Adopting the diffusion-controlled carbonated kinetics ((Nilsson, 2011; Papadakis et al., 1991)):

$$\frac{dd_0}{dt} = \frac{C_{CO_2} \times D_{CO_2}}{d_0 \times a_{max}} \qquad (4-13)$$

a_{max} is defined in equation (4-5). C_{CO_2}(kg/m^3) is the CO_2 concentration in the gas phase. D_{CO_2} (m^2/s) is the effective diffusivity of CO_2 and depends on numerous factors, such as carbonation temperature and relative humidity, water to cement ratio of concrete and other properties of concrete. In this study, it is estimated using equation (4-14) (Papadakis et al., 1991):

$$D_{CO_2} = \left[B \times \varepsilon_p \times \left(1 - \frac{RH}{100}\right)\right]^2 \qquad (4-14)$$

where ε_p is the cement paste porosity and B (m/s$^{1/2}$) is a constant. RH is relative humidity during RCA carbonation. The cement paste porosity ε_p can be described by the following formula (4-15) (Fagerlund, 2006):

$$\varepsilon_p = \frac{w/c - K \cdot \alpha_H}{w/c + 0.32} \qquad (4-15)$$

w/c is the water to cement ratio, K is a coefficient mainly determined by the chemical contraction, i.e. the reduction in specific volume when free water is bound chemically in the cement gel. It has previously been reported that the age of concrete

can affect carbonation rate through a gradually reducing diffusivity. Yoon et al., 2007 presented correlations between diffusivity and age for concrete of three w/c ratios. Since such information for all the six RCA types is not available, the explicit impact of aging has not been included in the current work.

4.2.2.3 Calculation of Energy Consumption

Energy consumption in RCA carbonation occurs in two steps, namely the crashing of demolition waste to RCA particles and the operation of the carbonation chamber fan for gas supply, both in the form of electricity. The crashing electricity demand, E_c (kWh/kg), can be computed using equation (4-16):

$$E_c = 0.01 W_i \left(\frac{1}{\sqrt{D_p}} - \frac{1}{\sqrt{d_m}} \right) \qquad (4-16)$$

where d_m (m) and D_p (m) are the initial and final particle diameters, respectively. W_i (kWh/kg) is the working index for recycled concrete aggregates (Cui & Sheikh, 2010). D_p takes the average of the upper and lower limits of the RCA particles (i.e. a and b in equation (4-10)).

To calculate fan energy consumption, the following equation is used:

$$E_f = \frac{1}{\varphi} \int_0^{t_c} \left\{ P_{in} Q_{in} \frac{\gamma}{\gamma - 1} \left[\left(\frac{P_{out}}{P_{in}} \right)^{\left(1 - \frac{1}{\gamma}\right)} - 1 \right] \right\} dt \qquad (4-17)$$

$$P_{out} = P_{in} + \Delta p \qquad (4-18)$$

E_f (J) is the energy consumption of the fan for the carbonation time duration, t_c (s). Q_{in} (m^3/s) is the inlet gas flowrate of the fan. P_{in} (Pa) and P_{out} (Pa) are the inlet

and out pressure of the fan, respectively. γ is the heat capacity ratio. φ is efficiency coefficient. To calculate the pressure drop Δp in carbonation chamber to be overcome by the fan, the following method is adopted (Sivakumaran et al., 2014):

$$f_p = \frac{\Delta p}{L_c} \frac{D_p}{\rho_{gas} v_s^2} \left(\frac{{\epsilon_b}^3}{1 - \epsilon_b} \right) \quad (4-19)$$

$$f_p = \frac{150}{Gr_p} + 1.75 \quad (4-20)$$

$$Gr_p = \frac{R_e}{(1 - \epsilon_b)} \quad (4-21)$$

$$R_e = \frac{\rho_{gas} v_s D_p}{\mu} \quad (4-22)$$

f_p is the packed bed friction factor, R_e and Gr_p are the original and the modified Reynolds number, respectively. ρ_{gas} (kg/m^3) is the density of the fluid. v_s (m/s) is the gas flow velocity. μ (Pa·s) is the dynamic viscosity of the fluid. ϵ_b is the bed porosity.

4.2.3 Life Cycle Assessment

Two distinct cases are considered for supplying CO_2 to the carbonation chamber, leading to different LCA treatments. The more complex case, in which a DAC facility produces pure CO_2, involves the delivery of CO_2 to the RCA carbonation site through liquefaction, transportation and vaporisation. In contrast, the simpler case considers low-purity CO_2 to be produced by a DAC facility, which would require lower energy input than the production of pure CO_2. However, the low-purity CO_2 product will be a mixture of CO_2 and air, which is impractical to transport through liquefaction as in the

case of pure CO_2. To circumvent this difficulty, the DAC facility is assumed to be collocated with the carbonation chamber, hence a much-simplified supply chain. **Figure 4-2** shows the scope of the LCA for the case involving pure CO_2 (the simpler supply chain with low-purity CO_2 is not separately shown). For both cases, the functional unit chosen for the LCA is 1 tonne of RCA (with the mass referring to that before carbonation) carbonated to 90%, that is, the achieved CO_2 uptake reaches 90% of the maximum value (as quantified by a_{max} in equation (4-5)).

For the DAC facility that produces pure CO_2, two relatively mature DAC technologies are considered. DAC Option 1 is based on wet scrubbing by Carbon Engineering (Keith et al., 2018). In this process, an alkali solvent is used to absorb CO_2 in an air contractor; the regeneration of the spent solvent is aided by the calcination of $CaCO_3$ and re-carbonation, primarily driven by thermal energy from natural gas. The process is designed such that the CO_2 released by natural gas combustion is also captured, thus the product contains CO_2 originating from both air and natural gas. This means that only part of the CO_2 supplied from this process to RCA carbonation is captured from air (quantified in Appendix B.1 **Table B-4**). DAC Option 2 is based on solid sorbent by Climeworks (Deutz & Bardow, 2021). This process involves adsorption of CO_2 on solid sorbent particles and subsequent desorption to regenerate the sorbent and release captured CO_2. The energy consumed included both electricity and heat, with the latter particularly for the desorption step. Following the treatment by (Deutz & Bardow, 2021), the heat demand is assumed to be met by heat pump which in turn consumes

electricity, thus the total energy demand of DAC Option 2 is met by electricity only. Unlike Option 1, all CO_2 supplied by this option originates from air.

Unlike DAC technologies producing pure CO_2, very little experimental work has been done to-date on DAC to produce low-purity CO_2, although potentially feasible options have previously been suggested. In a solid sorbent-based process, this could be achieved by regenerating the adsorption bed using hot air, instead of steam (Elfving et al., 2021). Also, membrane-based DAC could produce CO_2 at lower purities (Fujikawa et al., 2021). Due to the lack of data, the energy consumption by low-purity DAC has been modelled theoretically in this work (see below).

On the side of RCA supply to the carbonation chamber, the entire process generally includes various handling steps for separation and crushing, and transport (Xiao et al., 2022). Among the handling steps, only crushing is considered in this analysis as it represents a major energy demand, associated with carbon emissions. As in conventional CDW disposal, RCA is unlikely transported from the demolition site over an excessively long distance and would therefore be processed at a nearby site instead; such a transport requirement is assumed to be comparable to that of conventional CDW disposal (Soni et al., 2022), hence not an extra burden to be borne by the RCA carbonation scheme. Therefore, transport of RCA is excluded in this analysis. Note that this simplification may introduce inaccuracies; more importantly, the RCA transport step clearly needs to be considered in a study where the full system of RCA carbonation is to be assessed not with reference to conventional CDW disposal.

Figure 4-2 shows a cradle-to-gate scope of the LCA, encompassing all processes from raw material preparation and CO_2 capture to the completion of carbonation, while excluding the use and end-of-life stages of the carbonated products. The captured pure CO_2 is first liquefied and then transported to the carbonation site, where it is re-vaporised before feeding to the carbonation chamber. Considering the likely scale of operation where the amount of CO_2 to be consumed will be restricted by the RCA availability in the implementation at a given location, tanker-based transport of CO_2 is assumed as opposed to the use of a pipeline. More specifically, two different options for (road) transport in terms of fuel type are considered, namely diesel and electricity. All other steps, including DAC, liquefaction, vaporisation, crashing and carbonation (for fan use), involve the consumption of electricity. These energy consumption data have been gathered from literature sources and are detailed in the Appendix B.1 **Table B-4**.

The overall CO_2 emissions from the entire lifecycle include (i) the direct emission from the consumption of diesel fuel in the transportation step, (ii) the indirect emissions from the consumption of electricity at various steps, and (iii) the direct emission from the exhaust of the carbonation chamber due to the incomplete uptake of CO_2 (despite the strategy for controlling feed gas flowrate described in Section 4.2.2.1; determined by simulation). For (ii), the level of emissions depends on the carbon intensity of electricity, for which three representative countries, namely China (high), the United States (medium), and France (low) are considered. Furthermore, China and the US are among the top CDW producing countries (Joseph et al., 2023), while France is a top

CDW producing country in Europe (Akhtar & Sarmah, 2018). All the emission factors data are presented in the Appendix B.2 **Table B-5**.

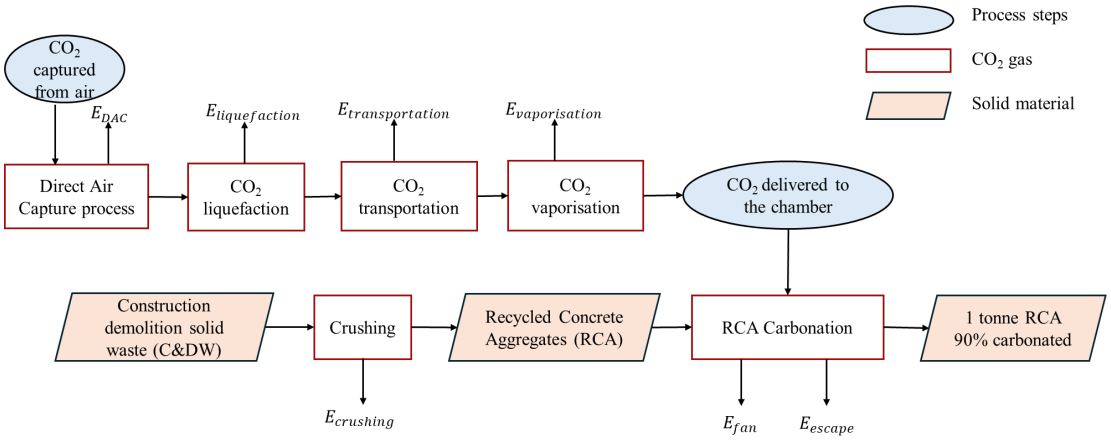

Figure 4-2 Life cycle of RCA carbonation with pure CO_2 supplied by DAC

The equation for calculating total net CO_2 removal (R_{total}) from the air is presented as:

$$R_{total} = R_{DAC} - (E_{DAC} + E_{liquefaction} + E_{vaporisation} + E_{transportation} + E_{crushing} + E_{fan} + E_{escape}) \quad (4-23)$$

In this equation, all the "E" terms refer to emissions due to energy use, except E_{escape} which is the CO_2 direct emission from the carbonation chamber because of the incomplete CO_2 uptake. R_{DAC} is the CO_2 removed from air through DAC. Note that R_{DAC} by Option 1 is lower than that by Option 2 when both options are set to supply the same amount of CO_2 to the carbonation chamber. This is because the CO_2 product delivered by the Option-1 process contains not only CO_2 captured from air but also that generated within the process due to the combustion of natural gas. In contrast, the Option-2 process produces CO_2 that is only originated from air.

For the case using low-purity CO_2, the CO_2 gas produced by DAC is injected into the carbonation chamber directly. Therefore, the liquefaction, transportation and vaporisation processes are excluded. The RCA carbonation step remains the same. As there are currently no well-established DAC processes producing non-pure CO_2, theoretical estimation of the energy (electricity) consumption, Elc_{low} (MJ/kg CO_2) was carried out, with reference to the energy consumption by DAC Option 2 introduced above (Elc_{opt2}):

$$Elc_{low} = \frac{Elc_{th-low}}{Elc_{th-pure}} \times Elc_{opt2} \qquad (4-24)$$

where Elc_{th-low} and $Elc_{th-pure}$ are the theoretical minimum energy consumption for achieving low-purity (as a function of the purity achieved) and that for producing pure CO_2, respectively. The details of the calculation of the two terms are presented in the Appendix B.1 **Table B-6**. Like DAC option 2, the DAC for producing low-purity CO_2 is assumed to source CO_2 only from air.

Combining the above two cases and their more detailed variants leads to a list of 12 LCA scenarios, as shown in **Table 4-1**. These include 12 scenarios for the case with pure CO_2, resulting from the combination of two DAC options, two transportation fuels and three countries. Besides, low-purity CO_2 to investigate a range of CO_2 product purity (20% -100% v/v) is discussed, with reference to the US (medium carbon intensity) as the location.

4.2.4 Model Features and Assumptions

Before presenting the modelling results, it is necessary to define the methodological features and underlying assumptions that frame the scope of the RCA carbonation analysis. This section establishes the physical configuration, boundary conditions, and parameter definitions adopted in the process model, together with the simplifications required for its integration with life cycle assessment. Clarifying these methodological foundations ensures transparency and reproducibility in interpreting the results that follow.

Table 4-1 LCA scenarios for RCA carbonation with pure CO_2

Scenario	DAC approach		Transportation		Country		
	Option 1	Option 2	Diesel	EVs	China	US	France
1	●		●		●		
2	●		●			●	
3	●		●				●
4	●			●	●		
5	●			●		●	
6	●			●			●
7		●	●		●		
8		●	●			●	
9		●	●				●
10		●		●	●		
11		●		●		●	
12		●		●			●

4.2.4.1 Model Features

The model represents a continuous carbonation process in which RCA, derived from construction and demolition waste, is treated in an enclosed chamber supplied with CO_2 captured via DAC. The reference reactor has internal dimensions of $10m^3$ (10m x 1m x 1m) and is treated as a fixed bed with constant porosity and uniform gas flow. The functional unit for the LCA is defined as one tonne of RCA carbonated to 90% of its theoretical CO_2 uptake capacity, determined from the reactive CaO content of the cementitious phase. The system boundary encompasses DAC operation, CO_2 conditioning (liquefaction, compression, transport and vaporisation), RCA crushing, fan operation for gas circulation, and off-gas management. Transport of RCA from demolition sites is excluded because it occurs in both the baseline and carbonation scenarios.

Six RCA types (RCA1–RCA6) are modelled to represent a range of structural concrete grades with different water–cement ratios and cement contents. The CaO fraction in the cementitious component is fixed at 65%, representing ordinary Portland cement. All RCA types are assumed to be initially uncarbonated, and the theoretical CO_2 uptake is determined stoichiometrically from the available reactive CaO. The carbonation target is defined as 90% of this capacity. Gas flow through the RCA bed is described using established fixed-bed equations, and gas properties are assumed to remain uniform throughout the reactor. Carbonation kinetics follow a diffusion-controlled mechanism combining both external film transfer and intra-particle diffusion. Local CO_2 concentration and conversion are resolved as functions of bed depth, particle size

and time. Particle size is assumed uniform for each simulation, typically ranging between 0.1 and 1.0 cm. The process temperature is maintained at ambient conditions, and the heat released by the mildly exothermic carbonation reaction is neglected because of its limited effect on gas properties and transport.

Two DAC configurations are incorporated in the model. The first is a solvent-based system that employs natural gas for heat, with complete capture of combustion-derived CO_2, while the second is a solid-sorbent system powered entirely by electricity. For low-purity CO_2 supply, a simplified DAC model estimates electricity demand as a function of product purity relative to the minimum work of separation. Low-purity DAC units are assumed to be located on site, eliminating the need for long-distance CO_2 transport. Electricity demand for DAC, fans, CO_2 conditioning, and crushing is calculated using grid carbon intensities for the United Kingdom, the United States, China and France. CO_2 transport, where applicable, assumes a reference distance of 500 kilometres, considering both diesel and electric transport options. The LCA focuses on the global warming potential, expressed in kilograms of CO_2 equivalent, and assumes steady-state operation for all processes.

4.2.4.2 Model Assumptions

The model assumes that RCA properties are homogeneous within each type, with no significant variation in mineral composition or porosity. Gas distribution within the carbonation chamber is considered uniform, and pressure drop is assumed constant along the bed. All reactive CaO is assumed to be accessible for carbonation up to 90% conversion, with no pore blockage or diffusion limitation beyond this level. The

thermal effects associated with carbonation are treated as negligible and do not affect gas temperature or reaction kinetics. DAC and carbonation reactors are assumed to operate continuously under stable conditions without interruptions or load variations. Environmental co-benefits from avoided landfill disposal and substitution of natural aggregates are recognised qualitatively but excluded from the quantitative net-removal calculations. Grid emission factors and equipment efficiencies are fixed at 2023 baseline values and are not adjusted for future decarbonisation trajectories. Together, these assumptions provide a transparent and consistent framework for quantifying CO_2 uptake, energy demand and net removal performance of DAC–RCA systems.

4.3 Results and Discussion

4.3.1 Results of Modelling the RCA Carbonation process

4.3.1.1 Comparison of Simulation Results with Experimental Data

Experimental data for RCA carbonation are scarce in literature. Nevertheless, four experimental tests reported in (Sereng et al., 2021) were found suitable to be simulated by our model for comparison. Details about experimental conditions and the comparison between simulation results and experimental data are provided in Appendix B.1 **Table B-7**.

Figure 4-3 shows that the simulated values exhibit consistent trends with experimental values under changing experimental settings, in terms of dropping in

CO_2 uptake (1) from test 1 to 2 and from test 3 to 4, due to the increase in particle size; and (2) from test 1 to test 3, due to decrease in w/c ratio.

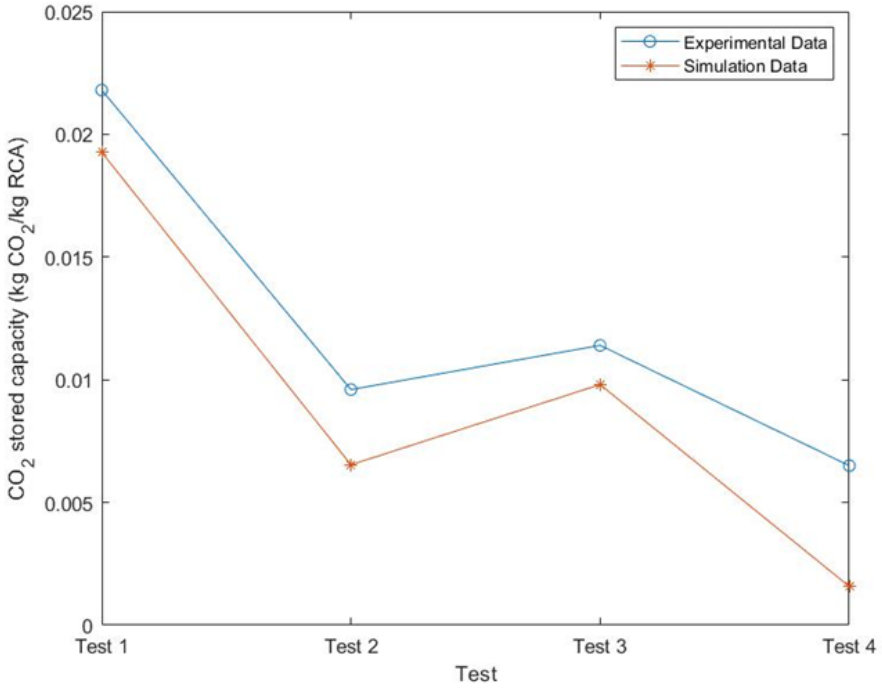

Figure 4-3 Comparison of RCA carbonation experimental data and model prediction

However, the model appears to somewhat underestimate the CO_2 uptake. The many mechanisms and parameters involved in the model mean that it is hard to pinpoint to the most plausible factors contributing to the underestimation, although a rather direct possibility is the discrepancy between the assumed RCA particle size profile (an even distribution across the size range, stated following equation (4-10)) and the actual distribution. The information of the latter is not available, however if the samples included more fine particles than an even distribution represents, the carbonation rate would be greater than predicted. Given the fact that the model was primarily parameterised using literature information and not calibrated to the data, the model can be regarded being capable of correctly capturing the impact of key

factors and has therefore been used for predictive explorations in this study. Nevertheless, it should be noted that the apparent underestimation by the model could lead to a lower CO_2 removal potential predicted by the LCA. It also calls for future improvements of the model for a higher accuracy.

4.3.1.2 Simulation Analysis of the Carbonation Chamber

Here, we show the results of simulating the RCA carbonation chamber with specific RCA type, CO_2 concentration, and average particle size. Unless specified otherwise, the default choices of these factors are RCA type 4, 20% CO_2 and 0.25 cm, respectively. Besides, the particle size distribution range is determined by empirical values from experiments (Gomes et al., 2015), normally around 0.1 -1 cm.

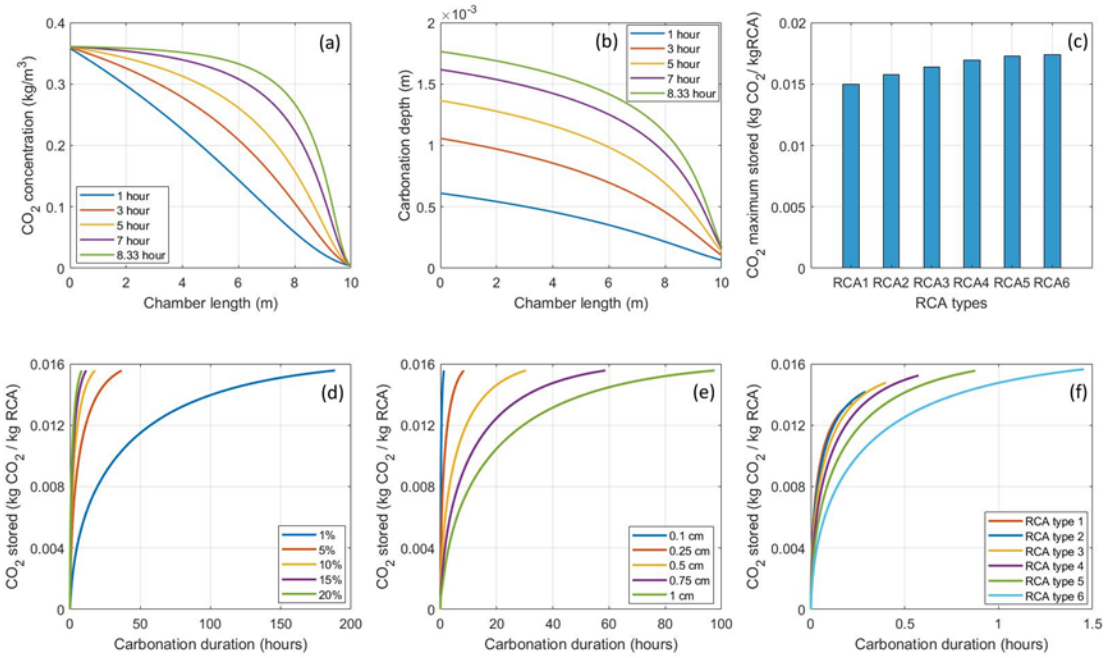

Figure 4-4 RCA carbonation process simulation results. (a) CO_2 concentration changes along the chamber length; (b) carbonation depth changes along the chamber length; (c) CO_2 maximum stored in RCA types; (d)-(f): impact on CO_2 uptake dynamics of factors including (d) CO_2 concentrations; (e) average RCA particle size; (f) RCA types. In subplots (a) and (b), the time point of "8.33 hour" corresponds to the end of simulated operation

Under the default settings, the dynamics of the carbonation process, obtained through dynamic simulation using the model presented in Section 4.2.2.2, are shown in **Figure 4-4 (a) and (b)**. At the beginning of the process, the CO_2 concentration declines quickly along the length of the chamber (see **Figure 4-4(a)**), because the un-carbonated RCA reacts consumes a significant amount of CO_2 at the forefront. As time progresses, the decline in CO_2 concentration becomes insignificant in the early part of the RCA bed where the degree of carbonation becomes high (as shown by the carbonation depth in **Figure 4-4(b)**); the "saturated" region in the bed extends as the carbonation process continues, until the operation ends when 90% of carbonation is reached.

Between RCA types, **Figure 4-4(c)** (based on equation (4-5)) shows that their maximum CO_2 uptake increases from 0.014 kg to 0.018 kg CO_2 per kg RCA, which reflects the increase in their cement content and hence the amount of CaO available for carbonation. Besides, the water-to-cement ratio also impacts the maximum uptake through hydration degree (as per equations (4-6), (4-7), and (4-8)). **Figure 4-4(d)** (based on dynamic simulation) further shows the time required for carbonating each type of RCA to 90% with pure CO_2 and an average particle size of 0.25 cm, which ranges from 0.2 to 1.5 hours. The increase in carbonation time is caused by the reduction in the water-to-cement ratio from RCA type 1 to 6, which leads to the reduction in the CO_2 diffusion coefficient (as per equations (4-14) and (4-15)).

Referring to RCA type 4, **Figure 4-4(e)** and **Figure 4-4(f)** (both based on dynamic simulation) further show the impact of CO_2 concentration (at an average particle size

of 0.25 cm) and average particle size (at 20% CO_2). One can see that a low CO_2 concentration and a large RCA particle size can significantly prolong the carbonation process. CO_2 concentration in the gas flow represents the overall mass transfer driving force and hence directly controls the rate of carbonation. On the other hand, a larger particle size means a thicker carbonated layer that the CO_2 gas needs to diffuse through, hence a greater mass transfer resistance. While it is desirable to adopt higher CO_2 concentrations and smaller particle sizes to accelerate the carbonation process, the potential tradeoff needs to be considered between the energy costs of DAC (increase with CO_2 concentration), crashing (increase with the reduction in particle size) and the fan use (increase with prolonged carbonation), which will be discussed in next section.

As a final note, the dimensions of the carbonation chamber adopted for the above simulations (10m x 1m x 1m) are indicative of an industrial-scale operation. When the dimensions are altered, it would not alter the carbonation time when pure CO_2 is used, as long as the RCA type and particle size remains unchanged. With a low-purity CO_2 feed, a much-enlarged chamber could experience a remarkable reduction in the CO_2 concentration along the path of the gas flow, leading to significant decreases in carbonation rate over a large fraction of the chamber. In such cases, using multiple rationally sized chambers in parallel might be preferred.

4.3.2 Results of LCA

4.3.2.1 Net Carbon Removal in the Case with Pure CO_2 Capture

With reference to RCA type 4 and an average particle size of 0.25 cm, **Figure 4-5** shows LCA results (obtained from applying equation (4-23)) of twelve scenarios assuming 500 km one-way transportation distance, for 1 tonne of RCA carbonated to 90% with pure CO_2. Each scenario's result consists of one circle and a pie chart. The black dashed circle represents the amount of CO_2 that is removed from the air by DAC to meet the requirement for feeding the carbonation chamber, thus the size of this circle corresponds to the value of R_{DAC} (See Appendix B.1 **Table B-4**), which varies between the two DAC options. Scenarios 1-6 use DAC option 1 with R_{DAC} = 12.63 kg, while scenarios 7-12 use DAC option 2 with R_{DAC} = 16.42 kg. The pie chart represents all carbon-emitting processes across the lifecycle and their proportions, corresponding to the "E" terms in equation (4-23). When the size of the pie chart is within the black dashed line, it indicates that the scheme that combines DAC and RCA carbonation can achieve net CO_2 removal from the atmosphere. Conversely, if the carbon emissions, arising from the consumption of electricity or transport fuel across the supply chain, exceed the amount of CO_2 removed from air by DAC, the process is considered as causing net emissions and hence not fulfilling the purpose of CDR.

Figure 4-5 shows that out of the 12 scenarios assessed, 8 scenarios (scenario 1,2,3,5,6,9,12) yield net removal in the range of 0.11 kg to 12.43 kg CO_2 from 90% carbonation of 1 tonne of RCA; 4 scenarios (scenario 7,8,10,11) yield net emissions in

the range of 1.05 kg to 13.92 kg (detailed data are provided in the Appendix B.1Table B-8 Supplementary LCA results **Table B-8** .

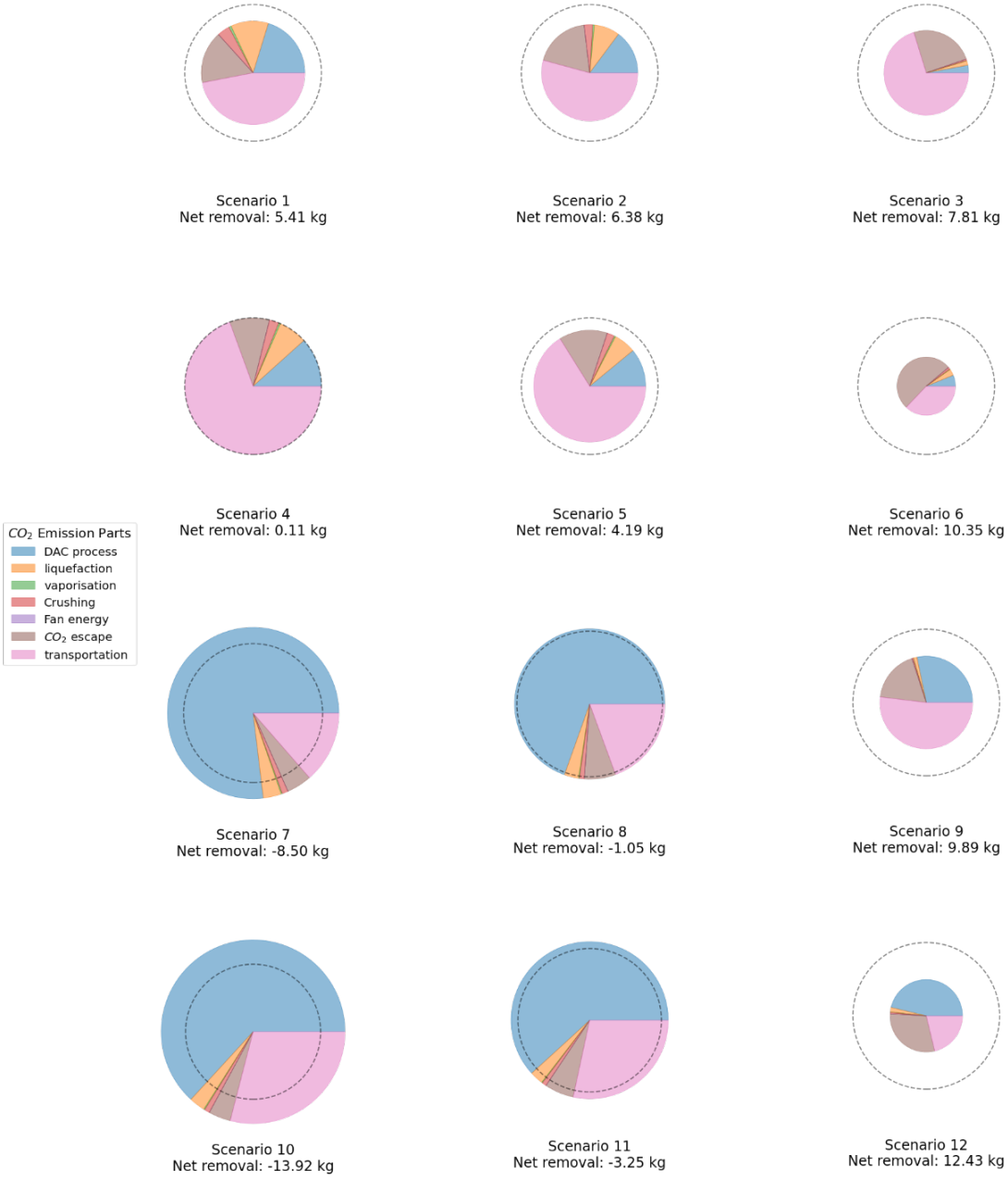

Figure 4-5 lifecycle net CO_2 removal by scenarios of RCA carbonation combined with DAC producing pure CO_2. For each scenario, the pie denotes (gross) CO_2 emissions across life cycle; the size of the dashed circle (relative to the size of the pie) represents gross CO_2 removal by DAC. When the size of the dashed circle is smaller (larger) than that of the pie, net negative (positive) CO_2 removal occurs

Among these scenarios, the best removal effect is achieved by scenario 12, by a combination of DAC option 2 and EVs with application in Iceland. It is worth noting that the same combination becomes the worst-case scenario when placed in China. Among the sources of CO_2 emissions, the most significant ones are transportation, DAC and CO_2 escape in RCA carbonation. Transportation is the most significant one in scenario 3, accounting for 70%; and in scenarios 1, 2, 4, 5 and 9, in the range of 47% to 69%. The share of CO_2 emissions by the DAC process dominates scenarios 7, 8, 10-12, ranging from 46% to 77%.

In scenarios 6, CO_2 escape is the main sources of CO_2 emissions, at 51%. Emissions by fan energy consumption is insignificant in all scenarios shown in **Figure 4-5**, where pure CO_2 is always used for carbonation. However, fan energy consumption is affected by the CO_2 concentration for carbonation; this will be discussed in section 4.3.2.3. Between the two DAC options, Option 1 has lower energy consumption than Option 2, which has a positive impact on net CO_2 removal. Between the three countries, the net CO_2 removal results in the third column (France) in **Figure 4-5** are significantly better than those in the first and second columns (China and US), due to the low carbon intensity of grid electricity in France. The emission of transportation is impacted by fuel, carbon emission factor and distance. EV trucks can reduce the emissions compared to diesel trucks when the electricity carbon intensity is sufficiently low, as in the case of the US and France, but not China. In the above analysis, DAC and transportation have clearly been identified as the two most significant sources of emissions due to energy consumption. Therefore, further

analyses are conducted on the impact of transport distance and on the use of DAC the produces low-purity CO_2 at a lower energy cost than that of capturing pure CO_2.

4.3.2.2 Impact of Transportation in the Case with Pure CO_2

Here, the assessment of scenarios 1-12 is repeated with varying transportation distances up to 2000 km (essentially altering the value of the $E_{transportation}$ term in equation (4-23)), with detailed results as shown in **Figure 4-6**.

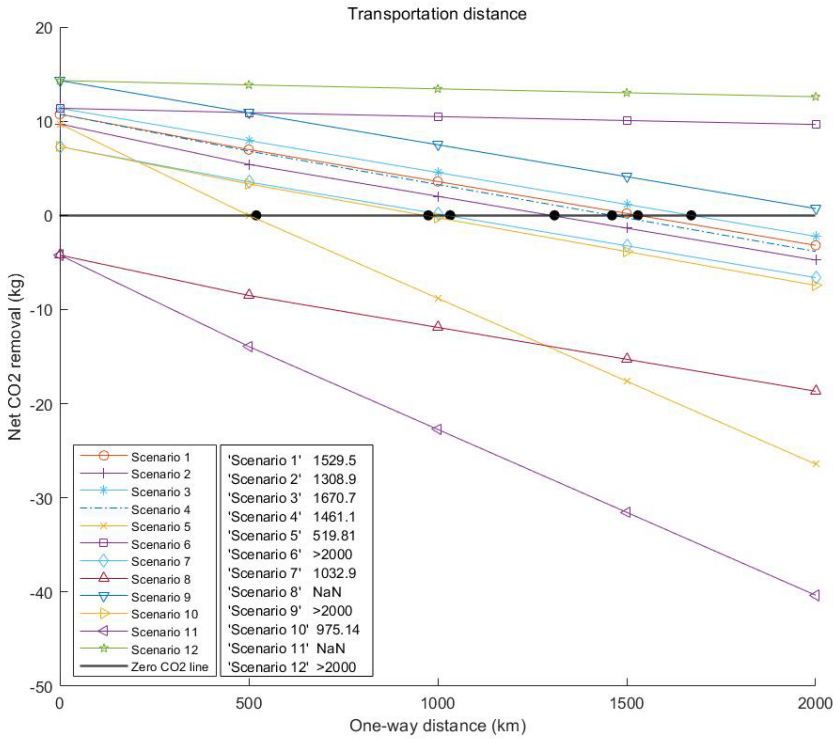

Figure 4-6 The relationship between net CO_2 removal and transportation distance

The two scenarios (7 and 10) previously identified as causing net CO_2 emissions would remain so even without transportation; the increase in transport distance would only lead to further deterioration of their performance. Oppositely, under scenarios 6 and 12, which were identified as most promising for delivering net CO_2 removal, variation

in transportation distance poses little impact on their performance, primarily due to their low overall burden of CO_2 emissions compared to CO_2 captured by DAC. Among the other scenarios, some of them could switch from net removal to net emissions as the transportation distance increases particularly beyond ~500 km which indicates a critical distance between DAC and RCA carbonation sites with today's energy system considered in this study.

4.3.2.3 Impact of CO_2 Concentration in the Case with Low-purity CO_2 Capture

With reference to RCA type 4 and an average particle size of 0.25 cm, **Figure 4-7** shows the results of low-purity CO_2 concentration impact (obtained primarily through running dynamic simulations using the model presented in Section 4.2.2.2), where the components include only RCA crashing, carbonation and on-site DAC.

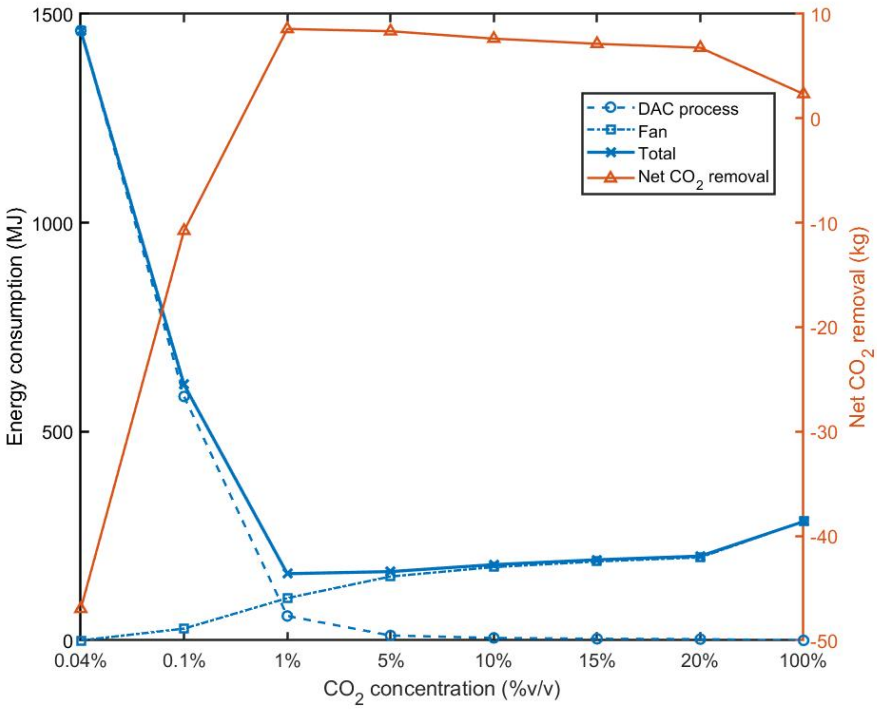

Figure 4-7 Energy consumption and net CO_2 removal at different CO_2 purity levels (with onsite DAC)

It is clear that when air is directly used for carbonation, which means no energy is consumed for DAC, the fan energy for the RCA carbonation process (calculated using equation (4-17)) will be prohibitively high, which is due to the extremely large volume of air to be supplied to complete the carbonation target. This leads to a very high level of overall energy consumption, and hence significant net CO_2 emissions. The excessive fan energy consumption reduces dramatically as the CO_2 concentration increases, while the DAC energy consumption (calculated using equation (4-24)) gradually increases. The total energy consumption and corresponding net CO_2 removal reaches a minimum level when the CO_2 concentration is around 1%, beyond which the fan energy consumption soon becomes negligible while DAC energy conception further increases mildly. Compared to a DAC system producing pure CO_2, the net carbon removal by a DAC system producing 1% CO_2 is 8.57 kg and 73% higher than the former, showing a desirable compromise between energy consumptions of DAC and carbonation.

4.3.2.4 Other Considerations

In the above analysis, RCA particles supplied to carbonation have been assumed to possess no pre-carbonation, which essentially means that all the CaO contained in concrete that is available for carbonation has not been reacted with CO_2. However, the concrete content of CDW, from which RCA is derived, has gone through a service life prior to demolition. Previous studies have shown that a significant amount of CO_2 can be absorbed by cement during the service life of buildings or infrastructures, particularly at surface layers of construction components where contact with air

occurs (Cao et al., 2020; Xi et al., 2016). When partially carbonated concrete is crushed into small-size RCA particles (typically in mm), these carbonated layers are most likely turned to (fully) carbonated RCA particles, which are mixed with un-carbonated RCA particles derived from the inner content of concrete components beneath the carbonated layers that is yet to react with CO_2. When such a mixture of RCA particles is subject to carbonation, the carbonated fraction would be present as inert particles, while the uncarbonated fraction would go through the reaction with CO_2 as depicted earlier in this study. Still on the basis of 1 tonne RCA, the attainable (gross) CO_2 uptake through carbonation (originally originating from CO_2 removal by DAC) will reduce in correspondence with the pre-carbonation degree. On the side of energy consumptions and CO_2 emissions, the same amount of crush energy will still be required which (as shown in **Figure 4-5**) is an insignificant element of total energy consumption. On the other hand, most of the significant energy demands (and hence CO_2 emissions) along the CO_2 supply chain, such as those of DAC and CO_2 transport, will scale with the CO_2 requirement which in turn reduces as the attenable CO_2 uptake decreases. Based on the above analysis, the net CO_2 removal potential of 1 tonne of mixed RCA particles (calculated by subtracting gross CO_2 emissions from gross CO_2 uptake, cf. equation (4-23)), whether negative or positive, would approximately scale with the uncarbonated fraction of the RCA particles.

Finally, this study solely focused on the net CO_2 removal of RCA carbonation combined with DAC, as a potential contributor to climate change mitigation. As in any industrial process, this scheme will inevitably have wider environmental impacts. Large-scale

deployment of DAC technologies, for example, have already received attention regarding potential adverse impacts such as terrestrial ecotoxicity and metal depletion(Qiu et al., 2022). Transport of CO_2, particularly when driven by diesel, will generate well-documented impacts on human and environmental health (find a good ref on diesel trucks' impact). As an example on the positive side, the processing of CDW into RCA, apart from the CO_2 sequestration potential through carbonation, could lead to beneficial replacement of natural coarse aggregates with resource savings (Hossain et al., 2016). These additional impacts deserve proper consideration in a more comprehensive assessment.

4.4 Conclusion

Through LCA informed by mathematical modelling, this work has presented an assessment of the potential of net CO_2 removal by a scheme that combines DAC and RCA carbonation. The mathematical modelling of an RCA carbonation chamber allowed us to predict the impacts of RCA types, CO_2 feed concentration and RCA particle size on CO_2 storage potential, carbonation process duration and the fan energy requirement. For the RCA types considered, the simulation results show that a maximum of 0.014 kg -0.017 kg CO_2 uptake by 1 kg of RCA. To achieve 90% of the maximum CO_2 uptake, the carbonation process with an average particle size of 0.25cm takes 0.21-0.45 hour with pure CO_2. This time range increases to 8.33 to 188.5 hours when low-purity CO_2 concentration is applied varying from 20% to 1%. Particle size can also significantly impact the duration: an average 0.1 cm particle size needs 1.12

hours to achieve the 90% carbonation with 20% CO_2, which increases to 97.11 hours at a particle size of 1 cm.

In LCA, a total of 12 scenarios were assessed with the functional unit of 90% carbonation of 1 tonne of RCA. When a DAC facility produces pure CO_2 which is transported by 500 km, the greatest net CO_2 removal is predicted to be 12.43kg, which occurs in France, thanks to its low carbon footprint in electricity supply. In contrast, net CO_2 emissions as high as 13.92 kg could be caused when the scheme is implemented in locations with significant emissions from energy use. Among the lifecycle emissions across all scenarios, those from energy use are dominated by DAC and transportation. A sensitivity analysis on transport distance suggests that multiple scenarios could switch from net CO_2 removal to net CO_2 emissions when the distance between DAC and carbonation sites exceeds 500 km. On the other hand, the assessment of on-site DAC feeding carbonation with low-purity CO_2 reveals a tradeoff in energy consumption between DAC and the fan used by the carbonation chamber, suggesting an optimal CO_2 purity of around 1% and a corresponding 8.57 kg of net CO_2 removal.

Overall, this theoretical study suggests that combining DAC with RCA carbonation is a potentially viable option for CDR, if it is implemented at favorable engineering conditions and at locations with low carbon footprint in energy supply. However, RCA carbonation experiment data are currently still lacking; consistent and systematic testing across different RCA characteristics and carbonation conditions is highly desirable. Besides, carbonation experiments at industrially relevant scale are yet to be

conducted to verify existing theoretical models. Meanwhile, there is significant space for the further development of DAC technology, particularly for producing low-purity CO_2. Finally, this work has solely focused on net CO_2 removal through RCA carbonation combined with DAC; an assessment of wider environmental impacts is required to comprehensively evaluate the value of this scheme.

References

Akhtar, A., & Sarmah, A. K. (2018). Construction and demolition waste generation and properties of recycled aggregate concrete: A global perspective. *Journal of Cleaner Production*, *186*, 262–281. https://doi.org/10.1016/J.JCLEPRO.2018.03.085

Bejaoui, S., & Bary, B. (2007). Modeling of the link between microstructure and effective diffusivity of cement pastes using a simplified composite model. *Cement and Concrete Research*, *37*(3), 469–480. https://doi.org/10.1016/j.cemconres.2006.06.004

Bisotti, F., Hoff, K. A., Mathisen, A., & Hovland, J. (2024). Direct Air capture (DAC) deployment: A review of the industrial deployment. *Chemical Engineering Science*, *283*, 119416. https://doi.org/10.1016/j.ces.2023.119416

British Standards Institution. (2019). *Concrete - complementary British Standard to BS EN 206 Part 2: Specification for constituent materials and concrete.*

Budinis, S., Krevor, S., Dowell, N. Mac, Brandon, N., & Hawkes, A. (2018). An assessment of CCS costs, barriers and potential. *Energy Strategy Reviews*, *22*, 61–81. https://doi.org/10.1016/j.esr.2018.08.003

Cao, Z., Myers, R. J., Lupton, R. C., Duan, H., Sacchi, R., Zhou, N., Reed Miller, T., Cullen, J. M., Ge, Q., & Liu, G. (2020). The sponge effect and carbon emission mitigation potentials of the global cement cycle. *Nature Communications*, *11*(1), 3777. https://doi.org/10.1038/s41467-020-17583-w

Chen, Z., Feng, Q., Yue, R., Chen, Z., Moselhi, O., Soliman, A., Hammad, A., & An, C. (2022). Construction, renovation, and demolition waste in landfill: a review of waste characteristics, environmental impacts, and mitigation measures. *Environmental Science and Pollution Research*, *29*(31), 46509–46526. https://doi.org/10.1007/s11356-022-20479-5

Cui, C., & Sheikh, S. A. (2010). Experimental Study of Normal- and High-Strength

Concrete Confined with Fiber-Reinforced Polymers. *Journal of Composites for Construction*, *14*(5), 553–561. https://doi.org/10.1061/(ASCE)CC.1943-5614.0000116

Danish, A., & Mosaberpanah, M. A. (2022). A review on recycled concrete aggregates (RCA) characteristics to promote RCA utilization in developing sustainable recycled aggregate concrete (RAC). *European Journal of Environmental and Civil Engineering*, *26*(13), 6505–6539. https://doi.org/10.1080/19648189.2021.1946721

Deutz, S., & Bardow, A. (2021). Life-cycle assessment of an industrial direct air capture process based on temperature–vacuum swing adsorption. *Nature Energy*, *6*(2), 203–213. https://doi.org/10.1038/s41560-020-00771-9

Ding, Y., Wu, J., Zhang, X., Xu, P., Ning, W., & Li, Y. (2023). Quality Improvement of Recycled Concrete Aggregate by Accelerated Carbonation under Different Pressure. *Journal Wuhan University of Technology, Materials Science Edition*, *38*(3), 623–631. https://doi.org/10.1007/s11595-023-2738-9

Elfving, J., Kauppinen, J., Jegoroff, M., Ruuskanen, V., Järvinen, L., & Sainio, T. (2021). Experimental comparison of regeneration methods for CO2 concentration from air using amine-based adsorbent. *Chemical Engineering Journal*, *404*, 126337. https://doi.org/10.1016/J.CEJ.2020.126337

Fagerlund, G. (2006). *Porosity and specific surface of Portland cement paste : an analysis of experimental work performed by Åke Grudemo during the years 1973-1979* (Vol. 3133). Division of Building Materials, LTH, Lund University.

Fang, X., Xuan, D., & Poon, C. S. (2017). Empirical modelling of CO2 uptake by recycled concrete aggregates under accelerated carbonation conditions. *Materials and Structures*, *50*(4), 200. https://doi.org/10.1617/s11527-017-1066-y

Fujikawa, S., Selyanchyn, R., & Kunitake, T. (2021). A new strategy for membrane-based direct air capture. In *Polymer Journal* (Vol. 53, Issue 1, pp. 111–119).

Springer Nature. https://doi.org/10.1038/s41428-020-00429-z

Gomes, P. C. C., Ulsen, C., Pereira, F. A., Quattrone, M., & Angulo, S. C. (2015). Comminution and sizing processes of concrete block waste as recycled aggregates. *Waste Management*, *45*, 171–179. https://doi.org/10.1016/j.wasman.2015.07.008

Hepburn, C., Adlen, E., Beddington, J., Carter, E. A., Fuss, S., Mac Dowell, N., Minx, J. C., Smith, P., & Williams, C. K. (2019). The technological and economic prospects for CO2 utilization and removal. *Nature*, *575*(7781), 87–97. https://doi.org/10.1038/s41586-019-1681-6

Hossain, Md. U., Poon, C. S., Lo, I. M. C., & Cheng, J. C. P. (2016). Comparative environmental evaluation of aggregate production from recycled waste materials and virgin sources by LCA. *Resources, Conservation and Recycling*, *109*, 67–77. https://doi.org/10.1016/j.resconrec.2016.02.009

Joseph, H. S., Pachiappan, T., Avudaiappan, S., Maureira-Carsalade, N., Roco-Videla, Á., Guindos, P., & Parra, P. F. (2023a). A Comprehensive Review on Recycling of Construction Demolition Waste in Concrete. *Sustainability*, *15*(6), 4932. https://doi.org/10.3390/su15064932

Keith, D. W., Holmes, G., St. Angelo, D., & Heidel, K. (2018). A Process for Capturing CO2 from the Atmosphere. *Joule*, *2*(8), 1573–1594. https://doi.org/10.1016/j.joule.2018.05.006

Leemann, A., Winnefeld, F., Münch, B., & Tiefenthaler, J. (2023). Accelerated carbonation of recycled concrete aggregates and its implications for the production of recycling concrete. *Journal of Building Engineering*, *79*, 107779. https://doi.org/10.1016/j.jobe.2023.107779

Li, L., Ziyabek, N., Jiang, Y., Xiao, J., & Poon, C. S. (2023). Effect of carbonation duration on properties of recycled aggregate concrete. *Case Studies in Construction Materials*, *19*, e02640. https://doi.org/10.1016/j.cscm.2023.e02640

Li, Y., Zhang, S., Wang, R., Zhao, Y., & Men, C. (2019). Effects of carbonation treatment on the crushing characteristics of recycled coarse aggregates. *Construction and Building Materials*, *201*, 408–420. https://doi.org/10.1016/j.conbuildmat.2018.12.158

Liu, K., Xu, W., Sun, D., Tang, J., Wang, A., & Chen, D. (2021). Carbonation of recycled aggregate and its effect on properties of recycled aggregate concrete: A review. *Materials Express*, *11*(9), 1439–1452. https://doi.org/10.1166/mex.2021.2045

Malaiskiene, J., Skripkiunas, G., Vaiciene, M., & Karpova, E. (2017). The influence of aggregates type on W/C ratio on the strength and other properties of concrete. *IOP Conference Series: Materials Science and Engineering*, *251*, 012025. https://doi.org/10.1088/1757-899X/251/1/012025

Nilsson, L.-O. (2011). *CO 2-cycle in cement and concrete Part 7: Models for CO 2-absorption. A new model for CO 2-absorption of concrete structures*. www.byggnadsmaterial.lth.se

Papadakis, V. G., Vayenas', C. G., & Fardis, M. N. (1991). EXPERIMENTAL INVESTIGATION AND MATHEMATICAL MODELING OF THE CONCRETE CARBONATION PROBLEM. In *Chemicd Engineering Science* (Vol. 46, Issue 516).

Pierre-Claude Aïtcin, & Robert J Flatt. (2015). *Science and Technology of Concrete Admixtures*. Elsevier Science.

Pu, Y., Li, L., Shi, X., Wang, Q., & Abomohra, A. (2022). Improving recycled concrete aggregates using flue gas based on multicyclic accelerated carbonation: Performance and mechanism. *Construction and Building Materials*, *361*, 129623. https://doi.org/10.1016/j.conbuildmat.2022.129623

Qiu, Y., Lamers, P., Daioglou, V., McQueen, N., de Boer, H.-S., Harmsen, M., Wilcox, J., Bardow, A., & Suh, S. (2022). Environmental trade-offs of direct air capture technologies in climate change mitigation toward 2100. *Nature Communications*, *13*(1), 3635. https://doi.org/10.1038/s41467-022-31146-1

Richard C Darton, A. Y. (2020). Removing Carbon Dioxide from the Air to Stabilise the Climate. In *Advances in Carbon Management Technologies* (1st Edition, pp. 3–22).

Sereng, M., Djerbi, A., Metalssi, O. O., Dangla, P., & Torrenti, J.-M. (2021). Improvement of Recycled Aggregates Properties by Means of CO2 Uptake. *Applied Sciences*, *11*(14), 6571. https://doi.org/10.3390/app11146571

Shuvo, A. K., Sarker, P. K., & Shaikh, F. U. A. (2024). Efficacy of various accelerated carbonation techniques to improve recycled concrete aggregates: A comprehensive review. *Journal of Building Engineering*, *95*, 110257. https://doi.org/10.1016/j.jobe.2024.110257

Sivakumaran, K. S., Korol, R. M., & Fan, X. (2014). Energy absorption potential of concrete floors containing secondary (shrinkage and temperature) reinforcements. *Frontiers of Structural and Civil Engineering*, *8*(3), 282–291. https://doi.org/10.1007/s11709-014-0269-3

Sodiq, A., Abdullatif, Y., Aissa, B., Ostovar, A., Nassar, N., El-Naas, M., & Amhamed, A. (2023). A review on progress made in direct air capture of CO2. *Environmental Technology & Innovation*, *29*, 102991.

Soni, A., Das, P. K., Hashmi, A. W., Yusuf, M., Kamyab, H., & Chelliapan, S. (2022). Challenges and opportunities of utilizing municipal solid waste as alternative building materials for sustainable development goals: A review. *Sustainable Chemistry and Pharmacy*, *27*, 100706. https://doi.org/10.1016/j.scp.2022.100706

Stephen M Smith, Matthew Gidden, William F Lamb, Jan C Minx, & Oliver Geden. (2023). *A global, independent scientific assessment of Carbon Dioxide Removal*. https://www.stateofcdr.org/

Tam, V. W. Y., Butera, A., Le, K. N., & Li, W. (2020). Utilising CO2 technologies for recycled aggregate concrete: A critical review. In *Construction and Building*

Materials (Vol. 250). Elsevier Ltd. https://doi.org/10.1016/j.conbuildmat.2020.118903

Thiery, M., Dangla, P., Belin, P., Habert, G., & Roussel, N. (2013). Carbonation kinetics of a bed of recycled concrete aggregates: A laboratory study on model materials. *Cement and Concrete Research*, *46*, 50–65. https://doi.org/10.1016/j.cemconres.2013.01.005

Wang, B., Yan, L., Fu, Q., & Kasal, B. (2021). A Comprehensive Review on Recycled Aggregate and Recycled Aggregate Concrete. *Resources, Conservation and Recycling*, *171*, 105565. https://doi.org/10.1016/j.resconrec.2021.105565

Xi, F., Davis, S. J., Ciais, P., Crawford-Brown, D., Guan, D., Pade, C., Shi, T., Syddall, M., Lv, J., Ji, L., Bing, L., Wang, J., Wei, W., Yang, K.-H., Lagerblad, B., Galan, I., Andrade, C., Zhang, Y., & Liu, Z. (2016). Substantial global carbon uptake by cement carbonation. *Nature Geoscience*, *9*(12), 880–883. https://doi.org/10.1038/ngeo2840

Xiao, J., Zhang, H., Tang, Y., Deng, Q., Wang, D., & Poon, C. (2022). Fully utilizing carbonated recycled aggregates in concrete: Strength, drying shrinkage and carbon emissions analysis. *Journal of Cleaner Production*, *377*, 134520. https://doi.org/10.1016/j.jclepro.2022.134520

Xuan, D., Zhan, B., & Poon, C. S. (2017). Durability of recycled aggregate concrete prepared with carbonated recycled concrete aggregates. *Cement and Concrete Composites*, *84*, 214–221. https://doi.org/10.1016/j.cemconcomp.2017.09.015

Yoon, I. S., Çopuroğlu, O., & Park, K. B. (2007). Effect of global climatic change on carbonation progress of concrete. *Atmospheric Environment*, *41*(34), 7274–7285. https://doi.org/10.1016/j.atmosenv.2007.05.028

Zhan, B., Poon, C. S., Liu, Q., Kou, S., & Shi, C. (2014). Experimental study on CO2 curing for enhancement of recycled aggregate properties. *Construction and Building Materials*, *67*, 3–7. https://doi.org/10.1016/j.conbuildmat.2013.09.008

Chapter 5 Comparative assessment of accelerated carbonation of steel slag for CO_2 removal

Summary

This study evaluates steel slag carbonation as a carbon dioxide removal pathway through process modelling, life cycle assessment (LCA), and global scenario analysis. Two routes were investigated: gas solid and indirect carbonation. The gas solid model, validated against experimental data, achieved rapid carbonation under optimised conditions of high temperature and fine particle size. Indirect carbonation, optimised for particle size and CO_2 partial pressure, demonstrated lower reactivity but reduced energy intensity. LCA results indicate that indirect carbonation performs best when electricity carbon intensity is below 0.192 kg CO_2/kWh, while gas solid carbonation is preferable in higher intensity grids. A global analysis across 37 countries shows that approximately 81% achieve negative emissions, with net CO_2 removal strongly dependent on electricity mix. This represents a potential solution that combines the economic reuse of steel slag with CO_2 storage, thereby simultaneously addressing both waste management and emissions reduction challenges. Overall, steel slag carbonation is technically viable and offers meaningful climate benefits when integrated with low carbon energy systems.

5.1 Introduction

The iron and steel industry (ISI) is a major source of energy consumption and contributes roughly 25% of global industrial greenhouse gas (GHG) emissions (Ren et

al., 2021). In response, steel production has seen some notable advancements, including greater reliance on electric arc furnaces (EAFs), the implementation of CCS technologies, experimentation with hydrogen as an alternative fuel (Devlin et al., 2023), and increased efforts to recycle and repurpose steel slag. Yet, despite these improvements, steel slag as a by-product continues to present environmental concerns. While new technologies have been effective in cutting CO_2 emissions, reducing the actual amount of steel slag, particularly the large stockpiles that have accumulated over time, remains a significant challenge.

In 2023, global pig iron and raw steel production reached approximately 1,300 Mt and 1,900 Mt, respectively, with over 75% of this output coming from six countries: China, India, Japan, Russia, the United States, and South Korea (Geological Survey, 2024). Most iron and steel are produced through two primary routes: the Blast Furnace-Basic Oxygen Furnace (BF-BOF) route and the Electric Arc Furnace (EAF) route. In the BF-BOF process, blast furnaces produce iron from iron ore, which is then converted into steel in a basic oxygen furnace, with some scrap metal added. These two steps generate byproducts known as blast furnace slag (BFS) and basic oxygen furnace slag (BOFS), respectively. In contrast, electric arc furnaces produce steel primarily from recycled scrap metal, with electric arc furnace slag (scrap-EAFS) as a byproduct. To reduce raw material costs and CO_2 emissions, scrap is increasingly being partially replaced (around25% (Gyllenram et al., 2022)) by Direct Reduced Iron (DRI). The resulting slag from this process is referred to as DRI-EAF slag (Heo & Park, 2022).

Steel slag, including both BOFS and EAFS, is produced at an estimated rate of 100-150 kg per tonne of raw steel. Approximately 72% of raw steel production is through the BOF process, while 28% is produced via EAF. In 2023, global BFS production was estimated at 330-390 Mt, while steel slag production, including BOFS and EAFS, was estimated to range from 190 to 290 Mt. For every tonne of pig iron produced, 250-300 kg of BFS is generated (Liu et al., 2021). Japan leads the world in steel slag utilisation with an impressive rate of 98.4%. The United States and Europe show similar rates, with the U.S. utilising 85.4% of its steel slag and Europe developed countries at 85.6%. In contrast, China, despite producing around 50% of the world's steel, utilises only 29.5% of its steel slag, leaving a large portion unutilised. India lags even further behind, utilizing just 15% to 20%, resulting in significant quantities being dumped and occupying land (Tiwari et al., 2016).

Therefore, the utilisation of steel slag is of great significance as it mitigates environmental burdens and recovers valuable resources, providing considerable economic value. Traditional utilisation pathways can be broadly categorised into internal recycling, secondary utilisation, and stockpiling (O'Connor et al., 2021). Internal recycling reintroduces slag into steelmaking to recover iron and alloying elements without external processing (Chen et al., 2011), yet its rate remains low, with Japan achieving only around 20% (Guo et al., 2018). Secondary utilisation offers the greatest potential for environmental and economic benefits but requires additional pre-treatment to address challenges related to particle size, reactivity, and heavy metal content (Gao et al., 2023). Common pre-treatment methods include natural

cooling, steam disintegration, hot splashing, and layer pouring, which are cost-effective but produce lower-quality slag primarily used as coarse aggregates in concrete or road bases (Guo et al., 2018). Advanced processes such as air quenching, water quenching, and the Baosteel Slag Short Flow (BSSF) method can enhance slag quality, enabling its application in cementitious materials. The most widespread use remains as aggregates in civil engineering, especially for road construction (Gencel et al., 2021; Hainin et al., 2015) and concrete (Anastasiou et al., 2014; J. Guo et al., 2018), accounting for 50–63% of total utilisation in developed countries. Further applications include partial substitution of cement raw materials, reducing both costs and CO_2 emissions (Gao et al., 2021), as well as soil amendment (Gao et al., 2020), wastewater treatment (Yi et al., 2012), flue gas desulphurisation (Zhou et al., 2011), and the production of glass-ceramics, ceramics, flame-retardant materials, rubber fillers, and abrasives, although most of these remain at an experimental stage (Liu et al., 2022).

Recently, steel slag's capacity to store CO_2 is regarded as one of its most promising applications, owing to its components' ready reaction with CO_2 to form stable carbonates (Zhang et al., 2023). This carbonation process not only helps reduce atmospheric CO_2, addressing climate change concerns, but also enhances the slag's physical properties, making it more suitable for use in construction materials like cement and concrete. Additionally, utilising steel slag for CO_2 absorption provides an efficient way to recycle industrial waste, transforming a by-product of steel production into a valuable resource for carbon capture and storage. As global efforts

to lower carbon emissions intensify, steel slag offers a cost-effective and sustainable solution for large-scale CO_2 sequestration.

The CO_2 fixation by steel slag has two approaches including (i) direct carbonation and (ii) indirect carbonation. Direct carbonation is a simple approach of steel slag carbonation, which is achieved through the reaction of steel slag with CO_2 either in the aqueous or gaseous phase. Slag can be pre-treated, but this approach does not involve using a solvent to extract the active components (such as Ca^{2+}) from steel slag, which is a feature of indirect carbonation. Direct carbonation shows many advantages, such as simple process, convenient operation and less consumption of chemical reagents (Wang et al., 2021). Direct carbonation has two different types: gas-solid carbonation and aqueous carbonation. Aqueous carbonation typically requires more complex handling of liquid phases, higher water consumption, and presents challenges in terms of process scalability and energy requirements (DiGiovanni et al., 2024). Therefore, it does not possess as much simplicity as gas-solid carbonation and is hence not considered in this study.

Past studies have investigated (direct) gas-solid carbonation and indirect carbonation of steel slags. Gas–solid carbonation generally requires elevated temperature and/or CO_2 partial pressure to overcome the diffusion barrier formed by the product layer and to accelerate the reaction rate (Tian et al., 2013). Kinetic studies at around 600 °C have shown good agreement with intraparticle diffusion and reaction models and have confirmed that higher CO_2 partial pressure sustains faster conversion, achieving approximately 0.07-0.086 kg CO_2 per kg slag uptake within 1 h under 5-100 % CO_2 (Tian

et al., 2013). Low-pressure CO_2 curing (10–60 psi) experiments have shown a pronounced exothermic temperature rise and have indicated that prolonged curing at high pressure can lead to calcite dissolution, so residence time must be carefully controlled (Shi & Wu, 2008). Even under low CO_2 pressure, carbonation of monolithic slag samples has produced significant strength development owing to carbonate bonding (Nielsen et al., 2020).

Indirect carbonation, which involves dissolution of calcium-and magnesium-bearing phases followed by precipitation of carbonates, generally achieves higher CO_2 uptakes when particle size is reduced and the liquid-to-solid ratio is optimised. For instance, thin-film and slurry experiments have reported approximately 176 g CO_2 per kg at a liquid-to-solid ratio of about 0.3 compared with approximately 280 g CO_2 per kg at a liquid-to-solid ratio of about 5 over 24 h (Baciocchi et al., 2015). Size-graded particles smaller than 0.105 mm have achieved 130–300 g CO_2 per kg for liquid-to-solid ratios between 0.2 and 0.4 (Polettini et al., 2016), and ladle slag slurries with median size around 12.8 μm at 60 °C have reached about 264 g CO_2 per kg within 3 h (Bonenfant et al., 2008). Elevated CO_2 pressure improves early dissolution rates but also increases calcite solubility, which requires careful optimisation of carbonation time to prevent re-dissolution (Chang et al., 2011). Enzyme-assisted systems have reported up to about 16.5 % sequestration efficiency at approximately 0.3 MPa before mass-transfer limitations dominate (Zhang et al., 2023).

Modelling studies have complemented these experimental findings by describing gas–solid routes using shrinking-core or grain models that include intraparticle diffusion

and external mass-transfer resistances, which enables accurate prediction of conversion profiles under different temperature, CO_2 partial pressure, and particle size conditions (Yu et al., 2021). For indirect carbonation, kinetic models frequently combine dissolution rate expressions, for example surface-controlled or diffusion-controlled leaching, with aqueous speciation and precipitation kinetics to simulate calcium release and carbonate formation over time (Huijgen & Comans, 2006; Tu et al., 2015). More recent research has incorporated energy balances to quantify the energy requirements for grinding, stirring, and gas sparging, although few studies link these results to life-cycle carbon performance, which highlights the need for the integrated modelling and LCA approach employed in this study (Yu & Wang, 2011).

Despite the above efforts, there is still a clear lack of consistent comparison between gas-solid carbonation and indirect carbonation of steel slag in terms of CO_2 removal potential and energetic performance, which hinders their practical applications. This study develops and compares these two carbonation models through consistent mathematical modelling and life cycle assessment to quantify their reaction kinetics, energy consumption, and material usage. An LCA model is established to evaluate the net carbon emissions of the accelerated carbonation industrial process based on CO_2 supplied from direct air capture. Finally, the potential for applying these carbonation technologies is assessed in countries with significant amounts of unrecycled steel slag, highlighting their role in achieving carbon reduction targets.

5.2 Methodology

5.2.1 Steel Slag Raw Materials

This study examines three types of steel slag as raw materials including Blast Furnace (BF) slag, Basic Oxygen Furnace (BOF) slag and Electric Arc Furnace (EAF) slag. The BF slag data were obtained from (Kumar et al., 2008; Liu et al., 2019), whereas information of the BOF and EAF slags was based on samples sourced from steelmaking plants in Indiana, United States (Yildirim & Prezzi, 2011). These slags originate from different stages of iron and steel production, resulting in notable variations in chemical composition and physical properties, which in turn influence their performance in mineral carbonation applications. In particular, differences in major oxide content and particle size distribution can significantly affect CO_2 uptake capacity and processing requirements. The fundamental physicochemical characteristics of these raw materials are summarized in **Table 5-1**.

Table 5-1 Physicochemical characteristics of modelled steel slags

	Chemical composition % (by weight)					***Density ($kg \cdot m^{-3}$)***	***Particle Size (mm)***
	CaO	**FeO**	**SiO_2**	**Al_2O_3**	**MgO**		
BF	38.44	0.35	30.58	14.04	10.57	2880	2.5
BOF	39.40	30.23	11.97	2.16	9.69	4070	15
EAF	47.52	7.61	4.64	22.59	7.35	3660	9.5

5.2.2 Modelling of Steel Slag Carbonation

5.2.2.1 Gas-solid Carbonation

5.2.2.1.1 Description of the Gas-solid Carbonation Process

An enclosed chamber with reference dimensions of $0.1m^3$ ($1m \times 1m \times 0.1m$) is considered to host a bed of steel slag particles, with a bed porosity of 0.4 (Myers & Nakagaki, 2020). The feed gas that contains CO_2 is supplied form one end of the chamber, travelling through the bed across the length, with a fan to overcome the pressure drop caused by the resistance of the steel slag particles to the gas flow. The carbonation process is conducted at an elevated temperature of approximately 600 °C. However, because the reaction is highly exothermic, the heat released during the process is sufficient to maintain the operating temperature without the need for an external heating system (Huang et al., 2024). In principle, an initial heat input is required to initiate the reaction; however, for continuous operations this requirement is considered insignificant and is therefore assumed to be negligible in this study. To prevent an excessive concentration of CO_2 in the outlet stream from the reaction chamber, a control strategy is implemented in which the inlet gas flowrate is gradually reduced when necessary. This ensures that the CO_2 flow in the exhaust remains below 0.1% of the inlet CO_2 flowrate. As the carbonation reaction rate declines over time, the process is terminated once 90% of the maximum achievable carbonation extent is reached, thereby avoiding unnecessarily extended operation with limited efficiency.

5.2.2.1.2 Mathematical Model of the Carbonation Chamber

To predict carbonation within the chamber, a one-dimensional multi-compartment model was formulated, wherein the chamber is discretized into n compartments along its longitudinal axis (Xi et al., 2016). A value of n=15 was adopted in the simulation to provide an appropriate balance between computational efficiency and model fidelity. Each compartment is assumed to be perfectly mixed and is linked to its downstream neighbour through gas-phase flow (L. Chen & Yang, 2025).

$$\frac{dC_{CO_2}(j)}{dt} = \frac{-R(j) + Q_{in}(j) \times C_{CO_{2in}}(j) - Q_{out}(j) \times C_{CO_2}(j)}{V(j)} \qquad (5-1)$$

Equation (5-1) presents the mass balance of CO_2 in the gas phase of compartment j, j = 1, 2, 3, …, n. $C_{CO_2}(j)$ (kg·m^{-3}) is CO_2 concentration in the gas phase. $C_{CO_{2in}}(j)$ (kg·m^{-3}) is CO_2 concentration of the gas entering compartment j, which is either the concentration of the feed gas if j = 1, or that leaving the previous compartment (j-1).

$Q_{in}(j)$ (m^3·s^{-1}) and $Q_{out}(j)$ (m^3·s^{-1}) are the velocity of the gas entering and leaving the compartment, respectively. $V(j)$ (m^3) is the gas phase volume of the compartment. $R(j)$ (kg·s^{-1}) is the carbonation rate, i.e., the rate at which CO_2 is removed from the gas phase and transferred to the steel slag particles. t (s) is the time. The gas flow rate leaving compartment j is given by:

$$Q_{out}(j) = Q_{in}(j) - \frac{R(j)}{G_t \times M_{CO_2}} \qquad (5-2)$$

where G_t (mol·m^{-3}) is the CO_2 mole in chamber, and M_{CO_2} (kg·mol^{-1}) is molar moss of CO_2. The carbonation rate, $R(j)$, is defined as the rate of increase in CO_2 uptake by the steel slag particles in compartment j:

$$R(j) = \frac{dCu(j)}{dt} = a_{max} \times m_{steel\ slag}(j) \times \frac{dX}{dt} \qquad (5-3)$$

where a_{max} (kg·(kg·tonne)$^{-1}$) is the maximum CO_2 uptake per unit kilogram of steel slag (X. Zhang et al., 2024), and $Cu\ (j)$ (kg) is the total CO_2 uptake by time t. $m_{steel\ slag}(j)$ (kg) is the mass of steel slag in compartment j. $\rho_{steel\ slag}$ (kg·m^{-3}) is steel slag density. $\frac{dX}{dt}$ (s^{-1}) is the percentage conversion rate of CaO, calculated using the following equation (5-4) derived for chemical conversion of solid particles through gas-solid reaction, based on the additive law of reaction times (Ranzani da Costa et al., 2013; Sohn, 2020):

$$\frac{dX}{dt} = \left\{\left[2 \cdot t_{Diff} \cdot (1-X)^{-\frac{1}{3}} - 1\right] + \left[\frac{t_{ch}}{3} \cdot (1-X)^{-\frac{2}{3}}\right]\right\}^{-1} \qquad (5-4)$$

where X is fractional CaO conversion. t_{Diff} (s) and t_{ch}(s) are the reaction time in diffusion process and chemistry control process, respectively.

$$t_{Diff} = \frac{\rho_{CaO} \cdot {d_p}^2}{24 \cdot D_o \cdot \left(C_{CO_2} - C_{CO_2,e}\right)} \qquad (5-5)$$

$$t_{ch} = \frac{\rho_{CaO} \cdot d_p}{2 \cdot C_{CO_2} \cdot k_s \cdot \left(C_{CO_2} - C_{CO_2,e}\right)} \qquad (5-6)$$

In this study, it is assumed that only CaO undergoes carbonation, and external mass transfer resistance is neglected. Let ρ_{CaO} (mol·m^{-3}) denote the molar density of CaO in steel slag particles. d_p (m) is the particle diameter (Tu et al., 2015), and D_o (m^2·s$^-$

[1]) is the overall diffusivity. The CO_2 concentration within the particle, C_{CO_2}, is approximately by $C_{CO_2}(j)$ as defined in equation (5-1). $C_{CO_2,e}$ (mol·m^{-3}) represents the equilibrium concentration of gas CO_2, which depends on the chamber temperature T (K). k_s (m·s^{-1}) is chemical reaction rate constant.

$$C_{CO_2,e} = \frac{1.826 \times 10^6}{8.314T} \exp\left(-\frac{19680}{T}\right) \quad (5-7)$$

$$D_o = \frac{\varepsilon}{\tau} \cdot \left(\frac{1}{D_k} + \frac{1}{D_{CO_2}}\right)^{-1} \quad (5-8)$$

In the above equations, ε is particle porosity, taken as 0.1205. τ is tortuosity, assigned a value of 13.47 (Li et al., 2024). D_k (m^2·s^{-1}) is Knudsen diffusivity. D_{CO_2}(m^2·s^{-1}) is CO_2 gas diffusivity.

$$D_k = \frac{2}{3} \cdot r_p \cdot \sqrt{\frac{8RT}{\pi M_{CO_2}}} \quad (5-9)$$

r_p (m) is the particle pore radius, which varies as the reaction progresses (see below). D_{CO_2} is estimated using the Chapman-Enskog equation:

$$D_{CO_2} = \frac{0.00143 \cdot T^{1.75} \times 4}{P\left(v_i^{\frac{1}{3}} + v_j^{\frac{1}{3}}\right)^2}\left(\frac{1}{M_i} + \frac{1}{M_j}\right) \quad (5-10)$$

where v_i and v_j respectively represent the diffusion volume of components i and j; M_i and M_j respectively represent the molar mass of meteorological components i and j (Hu et al., 2024). In this study, M_i=M_{CO_2}=44.01 g·mol^{-1}, v_{CO_2}=26.9 cm^3·mol^{-1}; M_j=M_{Air}=28.97 g·mol^{-1}, v_{air}=20.1 cm^3·mol^{-1}.

$$k_s = k_{s0} \cdot \exp\left(-\frac{E_k}{RT}\right) \quad (5-11)$$

R is the universal gas constant, equal to 8.314 J·(mol·K)$^{-1}$. E_k (J·mol^{-1}) is the activation energy. k_{s0} (m·s^{-1}) is the pre-exponential factor. The latter two parameters, together with the parameters for quantifying the dynamically changing pore radius r_p according to the empirical equation (5-12), are calibrated against experimental data reported in (Li et al., 2024).

$$r_p = r_{p0} \times \left(1 - \left(\frac{1}{1 + \sqrt{-c_1 \times \left(X + c_2 \times \left(\frac{T}{T_0}\right)^{c_3}\right)}}\right)\right) + c_4 \times \left(\frac{T}{T_0}\right)^{c_5} \quad (5-12)$$

where X (-) is the carbonation ratio, r_{p0} (m) is the initial pore radius (i.e., before carbonation starts, where X = 0), c_1– c_5 are empirical parameters depicting the change (reduction) in r_p as carbonation progresses, where the degree of change is also affected by carbonation temperature (T, normalised by a reference temperature, T_0 which is set to 273.15 K).

5.2.2.1.3 Calculation of Gas-solid Carbonation Energy Consumption

Energy consumption in steel slag gas-solid carbonation occurs in two steps. Firstly, the coarse steel slag freshly accumulated from steel plants is ground into fine steel slag particles with a characteristic size in the order of 10^{-6} m to meet the requirements for gas-solid carbonation process. Another step is the operation of the carbonation chamber fan for gas supply. Both are in the form of electricity. To quantify the specific energy consumption associated with grinding steel slag to a fine particle size, Bond's law was used as shown in Equation (5-13):

$$E_c = 10\,W_i\left(\frac{1}{\sqrt{D_{sp}}} - \frac{1}{\sqrt{D_{sm}}}\right) \quad (5-13)$$

where E_c (kWh·tonne^{-1}) is the specific energy consumption, W_i (kWh·tonne^{-1}) is the Bond Work Index and set to 13.5 kWh·tonne^{-1} for steel slag (Kohitlhetse et al., 2023), D_{sm} (μm) is the steel slag initial particle diameter, and D_{sp} (μm) is the steel slag final particle diameter.

To calculate fan energy consumption, the following equation is used:

$$E_f = \frac{1}{\varphi}\int_0^{t_c}\left\{P_{in}Q_{in}\frac{\gamma}{\gamma-1}\left[\left(\frac{P_{out}}{P_{in}}\right)^{\left(1-\frac{1}{\gamma}\right)} - 1\right]\right\}dt \quad (5-14)$$

$$P_{out} = P_{in} + \Delta p \quad (5-15)$$

E_f (J) is the energy consumption of the fan for the carbonation time duration, t_c (s). Q_{in} (m^3·s^{-1}) is the inlet gas flowrate of the fan. P_{in} (Pa) and P_{out} (Pa) are the inlet and outlet pressure of the fan, respectively. γ is the heat capacity ratio. φ is the efficiency coefficient. To calculate the pressure drop Δp in carbonation chamber to be overcome by the fan, the following method is adopted (Sivakumaran et al., 2014):

$$f_p = \frac{\Delta p}{L_c}\frac{D_p}{\rho_{gas}v_s^2}\left(\frac{{\epsilon_b}^3}{1-\epsilon_b}\right) \quad (5-16)$$

$$f_p = \frac{150}{Gr_p} + 1.75 \quad (5-17)$$

$$Gr_p = \frac{R_e}{(1-\epsilon_b)} \quad (5-18)$$

$$R_e = \frac{\rho_{gas}v_s D_p}{\mu} \quad (5-19)$$

f_p is the packed bed friction factor, R_e and Gr_p are the original and the modified Reynolds number, respectively. ρ_{gas} (kg·m^{-3}) is the density of the fluid. v_s (m·s^{-1}) is the gas flow velocity. μ (Pa·s) is the dynamic viscosity of the fluid. ϵ_b is the bed porosity.

5.2.2.2 Indirect Carbonation

5.2.2.2.1 Description of the Indirect Carbonation Process

Under ambient (room temperature) conditions, two reactors are employed sequentially including a dissolution reactor and a precipitation reactor (Z. Chen et al., 2021). The first reactor, with a volume of 1.5 m³, is used for the acidic dissolution of steel slag. It contains 1 m³ of 1M hydrochloric acid (HCl) and 10 kg of steel slag, based on a solid-to-liquid ratio of 10 g·L^{-1} (Luo & He, 2021; Ragipani et al., 2021). The HCl, along with the NaOH used in the subsequent precipitation step, is produced via Bipolar Membrane Electrodialysis (BPMED), an electrochemical process that uses bipolar membranes to split water into H^+ and OH^- ions, enabling the simultaneous generation of acid and base without external chemical inputs (Digdaya et al., 2020). This approach reduces chemical consumption and improves overall process sustainability. The entire liquid, including the undissolved slag, is transferred to a second reactor with a total volume of 3 m³, where the precipitation process takes place. In this stage, 1 m³ of 1M sodium hydroxide (NaOH), also generated by BPMED, is introduced to adjust the pH, while high concentration carbon dioxide gas is continuously bubbled into the system to induce the precipitation of carbonate or hydroxide species from the dissolved metal ions.

5.2.2.2.2 Mathematical Model of the Carbonation Reactors

In this study, only calcium dissolution is considered, primarily originating from the C3S and C2S phases of steel slag. The model is adopted from (Ragipani et al., 2019), employing a general dissolution model widely used to describe mineral dissolution by surface reaction. The model development is restricted to far-from-equilibrium conditions where the chemical affinities of dissolving minerals C3S and C2S are very high, allowing the influence of saturation state on the dissolution rate to be neglected. The general assumptions applied in deriving the model include acidic pH conditions with zero CO_2 concentration in the leaching agent. The partial pressure of oxygen is assumed to be constant. The formation of a silicon-rich leached layer on residual slag is neglected based on dissolution characteristics of orthosilicates. Mass transport limitations are ignored due to the non-porous nature of the slag and absence of significant stirring rate effects on dissolution. The leaching chemical reactions considered in the model are given in equations (5-20) and (5-21).

$$3CaO \cdot SiO_2 + 6H^+ \xrightarrow{K_{Ca}} 3Ca^{2+} + H_4SiO_4 + H_2O \qquad (5-20)$$

$$2CaO \cdot SiO_2 + 4H^+ \xrightarrow{K_{Ca}} 2Ca^{2+} + H_4SiO_4 \qquad (5-21)$$

The rate equations for leaching of calcium after neglecting the influences of ionic strength, chemical affinity, catalytic and inhibitory effects of species other than H^+ is given in equation (5-22):

$$\frac{d[Ca]}{dt} = \frac{k_{Ca}}{V_l M_{Ca}} S_{Ca} \left(\frac{\{H^+\}}{1 + K_{SCa}\{H^+\}} \right) \qquad (5-22)$$

where S_{Ca} (m^2) is the reactive mineral surface area, V_l ($mol \cdot L^{-1}$) is the leachate volume, M_{Ca} ($g \cdot mol^{-1}$) is the atomic wight of Ca. $\{H^+\}$ ($mol \cdot L^{-1}$) is the activity of H^+ in the aqueous solution. k_{Ca} ($g \cdot (m^2 \cdot min)^{-1} \cdot (L \cdot mol^{-1})$) is rate constant. k_{SCa}($L \cdot mol^{-1}$) is the surface stability constant.

Besides the reaction rate, the surface area evolution of Ca-rich phases is also considered. It can be modelled as equation (5-23):

$$S_{Ca}(t) = S_{Ca}(t_0)(1 - X_{Ca}) \qquad (5-23)$$

where $S_{Ca}(t_0)$ is the initial surface area corresponding to calcium-rich phases, conversion X_{Ca} is $[Ca]/[Ca]_{max}$ and $[Ca]_{max}$ ($mol \cdot L^{-1}$) is $x_{Ca} m_{i,slag}/V_l M_{Ca}$, $m_{i,slag}$ (g) is the initial slag mass used in the model, taken as 10 kg.

The matrix which is predominantly formed of calcium silicates also contains dicalcium ferrite which was found to be inert. In order to account for the volume occupied by inert material, an additional parameter *b* was introduced in equation (5-24).

$$S_{Ca}(t) = S_{Ca}(t_0)\left(1 - b\frac{[Ca]V_l M_{Ca}}{x_{Ca} m_{i,slag}}\right) \qquad (5-24)$$

After the steel slag dissolution process is completed, NaOH is added to adjust the pH to 10, and CO_2 is introduced into the reactor to react with Ca^{2+} ions in solution, thereby accelerating the precipitation of calcium carbonate (e.g., calcite; $CaCO_3$), as shown in equations (5-25) to (5-28).

$$CO_{2(g)} \rightarrow CO_{2(aq)} \qquad (5-25)$$

$$CO_{2(aq)} + H_2O \rightarrow H^+ + HCO_3^- \qquad (5-26)$$

$$HCO_3^- \rightarrow H^+ + CO_3^{2-} \quad (5-27)$$

$$Ca^{2+}_{(aq)} + CO_3^{2-}{}_{(aq)} \rightarrow CaCO_{3(s)} \quad (5-28)$$

For precipitation of $CaCO_3$, equation (5-29) is used to calculate the saturation index $\emptyset$ (-) and subsequently used to simulate the precipitation rate r_{prec} (mol·m^{-2}·h^{-1}) based on the calculated $\emptyset$ (Y. Zhang et al., 2025):

$$\emptyset = \frac{a_{Ca^{2+}} \times a_{CO_3^{2-}}}{K_{CaCO_3}} \quad (5-29)$$

$$r_{prec} = k \times (\emptyset - 1)^n \quad (5-30)$$

where K_{CaCO_3} (-) refers to the equilibrium constant of $CaCO_3$, a (-) refers to the activities of participating ions, and k (mol·m^{-2}·h^{-1}) refers to the specific rate constant. The precipitation was assumed to be seeded and was dominated by the growth of the solid seeds with an initial total surface area of 1 m^2 L^{-1}. Then, with the total surface area of seeds A (m^2·L^{-1}), equation (5-31) is used to calculate the rate of CO_2 capture r_{cap} (mol·L^{-1}·h^{-1}).

$$r_{cap} = r_{prec} \times A \quad (5-31)$$

Furthermore, equation (32) is used to calculate the rate of change in the total surface area r_A (m^2·L^{-1}·h^{-1}):

$$\frac{dA}{dt} = r_A = \frac{4 \times r_{prec} \times A \times M_{CaCO_3}}{\rho_{CaCO_3} \times \sqrt{\frac{A}{\pi \times n_s}}} \quad (5-32)$$

where M_{CaCO_3} (g·mol^{-1}) and ρ_{CaCO_3} (g·m^{-3}) refer to the molar mass and average density of $CaCO_3$, respectively, and n_s refers to the number of crystal seeds provided to the reactor.

5.2.2.2.3 Calculation of Indirect Carbonation Energy Consumption

The energy consumption in steel slag indirect carbonation primarily arises from five operations: (i) grinding of steel slag, (ii) stirring in the dissolution reactor, (iii) stirring in the precipitation reactor, (iv) CO_2 delivery via a fan, and (v) acid–base supply through the BPMED system.

The calculation of energy consumption by the grinding of steel slag is still by equation (5-13). The dissolution reactor operates as a stirred solid-liquid system, and its power input is determined using the ungassed power formula P_0. The precipitation reactor functions as a stirred gas-liquid system with CO_2 sparging. In this case, the gassed power P_G is calculated based on the ratio to P_0 according to the established empirical correlation, shown as equation (5-33):

$$\frac{P_G}{P_0} = 0.1\left(\frac{Q_G}{NV_L}\right)^{-0.25}\left(\frac{N^2D^4}{gD_iV_L^{\frac{2}{3}}}\right)^{-0.2} \quad (5-33)$$

where P_G (W) is the power consumption under gassed conditions, and P_0 (W) is the power input under ungassed conditions, as shown in equation (5-34). Q_G (m^3·s^{-1}) denotes the volumetric gas flow rate, while N represents the impeller rotational speed (rps). V_L (m^3) is the liquid volume, D (m) is the impeller diameter, and D_i (m)

is the width of the impeller blade. Finally, g stands for gravitational acceleration (9.81 m·s^{-2}). The ungassed power input is given by:

$$P_0 = \rho_L N^3 D^5 N_p \qquad (5-34)$$

where ρ_L (kg·m^{-3}) is the density of the liquid. N_p is the power number, a dimensionless parameter that characterizes the hydrodynamic performance of the impeller, which is calculated using the following equation (Scargiali et al., 2013):

$$N_p = min\left(19.5{Re_L}^{-0.3}; 24(Re_L Fr_L)^{-\frac{1}{3}}\right) \qquad (5-35)$$

Re_L is the Reynolds number, which characterizes the flow regime. $Fr_L$is the Froude number, representing the ratio of inertial to gravitational forces. They are defined as the following equations, where μ_L (Pa·s) is the liquid viscosity.

$$Re_L = \frac{\rho_L N D^2}{\mu_L} \qquad (5-36)$$

$$Fr_L = \frac{DN^2}{g} \qquad (5-37)$$

In dissolution reactor, the ungassed power input P_0 is calculated using the following parameters: liquid density ρ_L and liquid viscosity μ_L are 1049 kg·m^{-3} and 1.05 ×10^{-3} Pa·s for 1M hydrochloric acid, respectively (Haynes et al., 2016); impeller rotational speed N is 2 rps typical for solid-liquid mixing (Paul et al., 2003); impeller diameter D is 0.5 m based on 40% of tank diameter (Kumaresan & Joshi, 2006).

In prepetition reactor, assume the reactor has a diameter of 1.6 meters, with a liquid height of 1.0 meter and a total vessel height of 1.42 meters. Due to CO_2 sparging into solution containing dissolved metals and NaOH, the power consumption ratio should

be considered. The power input with gas P_G is calculated using the following parameters, i.e., V_L is 2 m^3; impeller diameter D is 0.6 m; impeller blade width D_i is set at 0.12 m. The liquid phase, composed of calcium chloride ($CaCl_2$) and sodium hydroxide (NaOH) solutions, has an estimated density of 1050 $kg \cdot m^{-3}$ and a dynamic viscosity of 1.2×10^{-3} Pa·s, which is representative of weakly alkaline inorganic mixtures. A moderate agitation speed of 1.5 rps is applied to ensure effective gas-liquid mixing (Kracík et al., 2020). CO_2 flow rate Q_G depends on the indirect carbonation modelling.

The energy demand associated with (iv) CO_2 delivery via a fan is calculated following equations (5-14) to (5-19), where the pressure drop in equation (5-14) is determined according to ΔP_c as defined in equation (5-38).

$$\Delta P_c = \rho_L \times g \times h_L \qquad (5-38)$$

which ρ_L ($kg \cdot m^{-3}$) is liquid density, the pressure difference required to push the gas through the liquid column of height (h_L), taken as 1 m.

The energy consumption of the BPMED system is calculated according to the following equations (Digdaya et al., 2020).

$$E_{BPMED} = \frac{\Delta Q_{total} \times V_{cell,practical}}{\varphi_{BPMED}} \qquad (5-39)$$

In this study, $V_{cell,practical}$ (V) is the practical total cell voltage, ΔQ_{total} (C) is the total charge requirement, and the BPMED efficiency φ_{BPMED} is assumed to be 0.8. The total charge requirement is calculated as:

$$\Delta Q_{total} = \Delta[H^+] \times V_a \times F \quad (5-40)$$

where $\Delta[H^+]$ (mol·L^{-1}) is the H^+concentration, taken as 0.1 mol·L^{-1}. V_a (L) is the volume of acidic compartment, taken as 1 L, and F is the Faraday constant, 9.6485×10^4 C·mol^{-1}. The practical cell voltage is expressed as:

$$V_{cell,practical} = \frac{RT}{F}\left(pH_{basified} - pH_{acidified}\right) + V_{BPM\ loss} + V_{CEMs} + V_{acidic} + V_{basic} + V_{electrode} \quad (5-41)$$

where $pH_{basified}$ is the pH of the solution in the basified compartment and $pH_{acidified}$ is the pH of the solution in the acidified compartment. $V_{BPM\ loss}$ (V) is the voltage loss across the BPM, V_{CEMs} (V) is the voltage loss across the CEMs, $V_{oceanwater}$ (V) and $V_{electrolyte}$ (V) are the voltage loss across the acidic and basic compartment, respectively, and $V_{electorde}$ (V) is the voltage loss at the two electrodes. Each part of them can be calculated by the following equations:

$$V_{BPMloss} = n_{BPM} \times R_{bpm} \times i \quad (5-42)$$

where i is current density, taken as 0.0766 A·cm^{-2}. The parameter n_{BPM} represents the number of BPM, which is taken as 1 in this study. The term R_{bpm} (Ω·cm^{-2}) refers to the BPM resistance, with a value of 5.2.

$$V_{CEMs} = n_{cem} \times R_{acem} \times i \quad (5-43)$$

The parameter n_{CPM} represents the number of CEM, which is taken as 2 in this study. The term R_{acem} (Ω·cm^{-2}) refers to the CEM/AEM resistance, with a value of 0.13.

In this study, assume these two parts can be calculated together as equation (5-44):

$$V_{acidic} + V_{basic} = i \times \left(\frac{L_a}{k_{acidic}} + \frac{L_c}{k_{basic}}\right) \quad (5-44)$$

where L_a (cm) and L_c(cm) denote the thickness of anode and cathode, respectively, with the values of 0.1 cm and 0.075 cm. The term k_{acidic} (S·cm^{-1}) represents the conductivity of seawater in the acidic compartment, while k_{basic} (S·cm^{-1}) corresponds to the conductivity of seawater after degassing in the basic compartment with respective values of 0.07735 and 0.07742. The electrode overpotential is given by:

$$V_{electrode} = \frac{RT}{F} \times \left(sinh^{-1}\left(\frac{i}{2i_{0,anode}}\right) + sinh^{-1}\left(\frac{i}{2i_{0,cathode}}\right)\right) \quad (5-45)$$

where $i_{0,anode}$ (A·cm^{-2}) and $i_{0,cathode}$(A·cm^{-2}) is the exchange current density for anode and cathode, respectively. Both values are taken 10^{-5} and 10^{-3} A·cm^{-2}.

5.2.3 Life Cycle Assessment

5.2.3.1 LCA for Gas-solid Carbonation Process

Two distinct cases are considered for supplying CO_2 to the carbonation chamber, leading to different LCA treatments. In the more complex case, a DAC facility produces pure CO_2, which is then delivered to the steel slag carbonation site through liquefaction, transportation, and vaporisation. In contrast, the simpler case considers low-purity CO_2 produced by a DAC facility, which requires lower energy input than producing pure CO_2. However, because transporting low-purity CO_2 is difficult, the DAC facility is assumed to be collocated with the carbonation chamber, resulting in a much-simplified supply chain. A key assumption in this study is that gas–solid

carbonation is modelled with pure CO_2 because its reaction rate strongly depends on CO_2 partial pressure, whereas indirect carbonation proceeds effectively at moderate CO_2 partial pressures and therefore only requires low-purity CO_2. Using pure CO_2 for the indirect route would add unnecessary energy and cost without significant performance gains.

For both cases, the functional unit chosen for the LCA is 1 tonne of steel slag (with the mass referring to that before carbonation) carbonated to 90%, that is, the achieved CO_2 uptake reaches 90% of the maximum value (as quantified by a_{max} in equation (5-3)). In terms of the system boundary, it should be noted that the transportation of steel slag to the carbonation site is not included, as such transportation would also be required for its conventional utilisation (i.e., in construction or road applications). Therefore, this step does not represent an additional burden specific to steel slag carbonation (O'Connor et al., 2021).

Table 5-1 shows the scope of the LCA for the case involving pure CO_2. In this study, two relatively mature technologies of DAC, wet scrubbing by carbon engineering (DAC Option1) (Keith et al., 2018) and solid sorbent by Climeworks (DAC Option2) (Deutz & Bardow, 2021) are chosen. The captured pure CO_2 is first liquefied and then transported to the carbonation site, where it is re-vaporised before feeding to the carbonation chamber. Two alternative fuels for road transport are considered, namely diesel and electricity. All other process steps, including DAC, liquefaction, vaporisation, grinding and crushing, and carbonation (for fan operation), require electricity. Accordingly, for gas solid carbonation, as pure CO_2 is typically introduced under the

experimental conditions, both industrially relevant DAC technologies are considered in order to evaluate which option can provide a greater contribution to net carbon reduction. These energy consumption data have been gathered from literature sources and are detailed in the Appendix B.1 **Table B-4**.

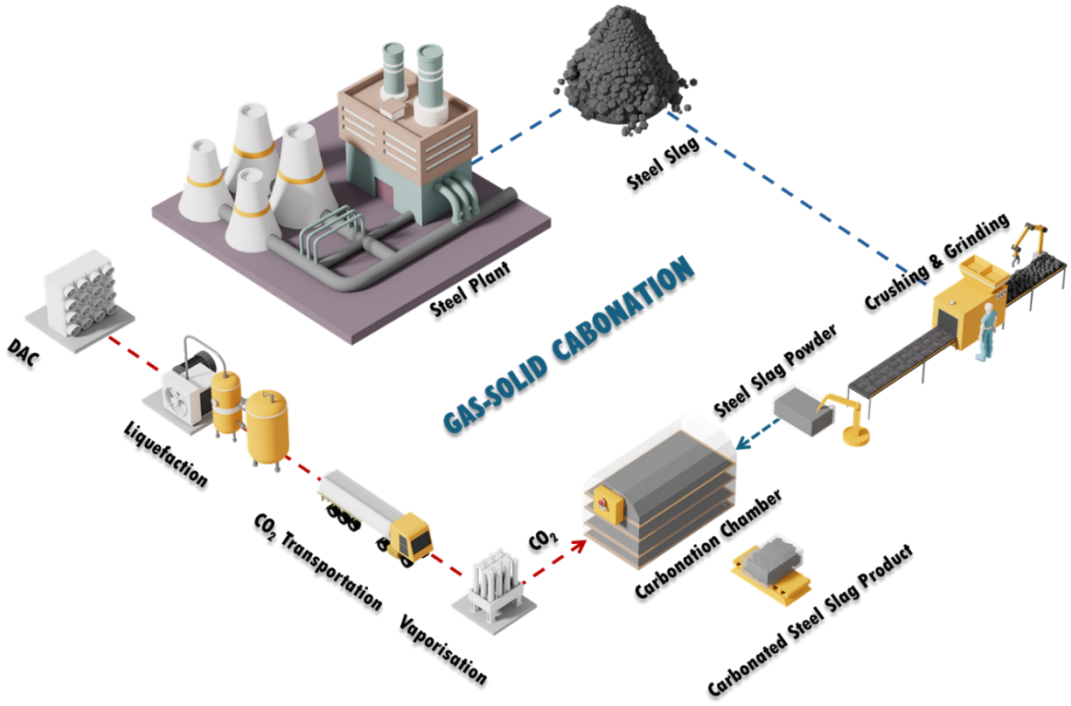

Figure 5-1 LCA of steel slag gas-solid carbonation with pure CO_2 supplied by DAC

The overall CO_2 emissions from the entire lifecycle include (i) the direct emission from the consumption of diesel fuel in the transportation step, (ii) the indirect emissions from the consumption of electricity at various steps, and (iii) the direct emission from the exhaust of the carbonation chamber due to the incomplete uptake of CO_2 (despite the strategy for controlling feed gas flowrate described in Section 5.2.2.1; determined by simulation). For (ii), the level of emissions depends on the carbon intensity of electricity, for which 37 countries and regions with available steel slag stocks are

considered. All corresponding emission factor data are provided in the Appendix C.1 **Table C-1**.

The equation for calculating total net CO_2 removal (R_{gsc}) in gas-solid carbonation process from the air is presented as:

$$R_{gsc} = R_{DAC} - (E_{DAC} + E_{liquefaction} + E_{vaporisation} + E_{transportation} + E_{crushing} + E_{gscfan} + E_{escape}) \quad (5-45)$$

In this equation, all the "E" terms represent emissions associated with energy consumption, whereas E_{escape} denotes the direct CO_2 release from the carbonation chamber resulting from incomplete CO_2 uptake. R_{DAC} corresponds to the amount of CO_2 captured from the atmosphere via DAC. It should be noted that R_{DAC} achieved by Option 1 is lower than that of Option 2 when both options deliver the same quantity of CO_2 to the carbonation chamber. This difference arises because the CO_2 supplied by Option 1 consists not only of air-derived CO_2 but also of CO_2 produced internally through the combustion of natural gas during the process. In contrast, the CO_2 stream from Option 2 originates exclusively from atmospheric capture. Therefore, four scenarios are considered in this section: (i) DAC Option 1 combined with diesel-powered transportation, (ii) DAC Option 2 combined with diesel-powered transportation, (iii) DAC Option 1 combined with electric vehicle transportation, and (iv) DAC Option 2 combined with electric vehicle transportation.

5.2.3.2 LCA for Indirect Carbonation Process

In contrast, for indirect carbonation, where only low concentration CO_2 can be supplied, DAC Option 2 represents the only technically feasible option. For the case using low-purity CO_2, liquefaction, transportation and vaporisation are removed, the steel slag carbonation step remains the same, and the DAC step is adapted to produce a low-purity product. As there are currently no well-established DAC processes producing non-pure CO_2, theoretical estimation of the energy (electricity) consumption, Elc_{low} (MJ/kg CO_2) was carried out, with reference to the energy consumption by DAC Option 2 introduced above (Elc_{opt2}):

$$Elc_{low} = \frac{Elc_{th-low}}{Elc_{th-pure}} \times Elc_{opt2} \qquad (5-46)$$

where Elc_{th-low} and $Elc_{th-pure}$ are the theoretical minimum energy consumption for achieving low-purity (as a function of the purity achieved) and that for producing pure CO_2, respectively. Like DAC option 2, the DAC for producing low-purity CO_2 is assumed to source CO_2 only from air.

Figure 2 shows the scope of the LCA for the case involving low-concentration CO_2. The overall CO_2 emissions from the entire lifecycle include (i) the DAC step energy consumption; (ii) the indirect emissions from the consumption of electricity at various steps, including the stirring process in dissolution reactor ($E_{stirring_{diss}}$), the stirring ($E_{stirring_{prec}}$) and the CO_2 delivery process (E_{icfan}) in precipitation reactor; and (iii) the BPMED system (E_{BPMED}) that supplies the HCl and NaOH.

The equation for calculating total net CO_2 removal (R_{ic}) in indirect carbonation process from the air is presented as:

$$R_{ic} = R_{DAC} - (E_{DAC} + E_{crushing} + E_{stirring_{diss}} + E_{stirring_{prec}} + E_{icfan} + E_{BPMED}) (5-47)$$

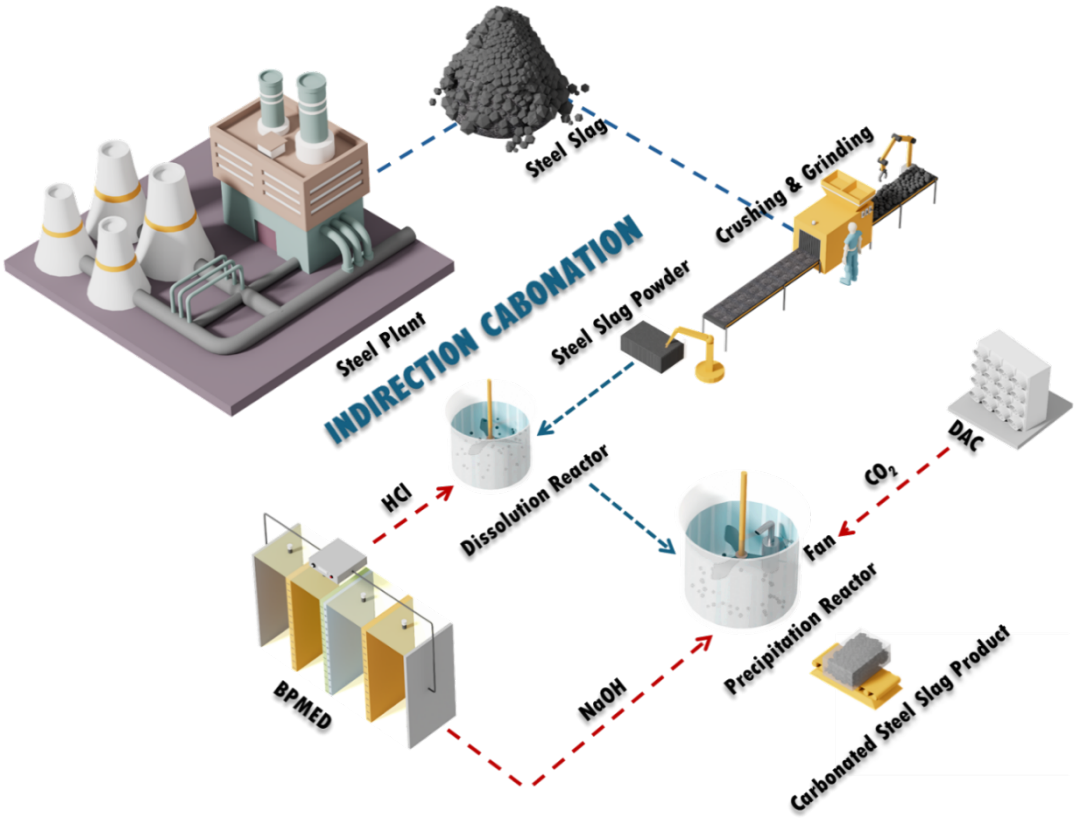

Figure 5-2 LCA of steel slag gas-solid carbonation with low-concentration CO_2 supplied by DAC

5.2.4 Model Features and Assumptions

Before analysing the results, this section outlines the principal features and assumptions of the models used to evaluate steel slag carbonation. The aim is to ensure that the process description, modelling scope and methodological consistency are explicitly defined prior to interpretation of the results. This clarification provides a clear understanding of how gas–solid and indirect aqueous carbonation are

represented, how they are coupled with DAC systems, and how life cycle boundaries are applied.

5.2.4.1 Model Features

The model evaluates two carbonation routes, gas–solid and indirect aqueous, both integrated with DAC and assessed within a unified life cycle framework. Three steel slag types are examined: BF, BOF, and EAF slag. The oxide compositions and densities of these materials are based on representative industrial data, and only CaO and MgO are considered reactive oxides that contribute to CO_2 fixation. The functional unit for the LCA is one tonne of steel slag carbonated to 90% of its theoretical CO_2 uptake calculated from the reactive CaO content. Transport between the steelworks and the carbonation facility is excluded, as it occurs in both baseline and carbonation cases.

The gas–solid process is modelled as a fixed-bed reactor with dimensions of $0.1 m^3$ (1m×1m×0.1m) operating at approximately 600 °C. Gas flow is assumed to follow plug-flow behaviour with uniform velocity and concentration profiles. The reaction is diffusion-controlled, described by a shrinking-core model that accounts for both intra-particle and external mass transfer. The exothermic heat released is assumed sufficient to maintain steady operating temperature. Kinetic parameters are derived from published experimental data and validated by comparison with reported CO_2 conversion levels. Pure CO_2 is assumed in all gas–solid cases to maintain a high concentration gradient and consistency with laboratory practice.

The indirect aqueous carbonation process is represented as a two-stage system

consisting of dissolution of Ca-bearing oxides followed by carbonate precipitation. Dissolution rates depend on particle size, liquid-to-solid ratio, and temperature, while precipitation is governed by equilibrium-based rate expressions. The energy requirements include grinding, stirring, gas handling, and operation of the BPMED unit used to generate acidic and alkaline streams. The CO_2 supply is assumed pure and available on site, with no additional transport considered. Both carbonation routes are coupled with DAC configurations equivalent to those in Chapter 4. Electricity consumption for DAC, BPMED operation, stirring, fans, and other auxiliary equipment is converted into emissions using grid intensities for 37 steel-producing countries. Net CO_2 removal is calculated as the total CO_2 mineralised minus all process emissions from energy use and transport. Only the climate-change category is considered in the LCA, while other impact categories such as leaching potential, durability, or long-term stability remain outside the system boundary.

5.2.4.2 Model Assumptions

All simulations are assumed to operate under steady-state conditions, excluding start-up or transient effects. Each slag type is considered compositionally homogeneous, and minor oxides or trace metals are not represented explicitly. Secondary reactions that do not form stable carbonate phases are omitted unless captured implicitly by kinetic calibration. Thermal losses are considered negligible relative to the heat of carbonation, and both DAC and carbonation systems are assumed to operate under a stable power supply. The potential reuse of carbonated slag in construction applications is acknowledged qualitatively but excluded from the quantitative carbon

balance. Electricity consumption, process efficiencies, and grid emission factors correspond to 2023 baseline values without adjustment for projected grid decarbonisation. These assumptions establish a consistent analytical basis for comparing the gas–solid and indirect aqueous carbonation processes and linking their kinetic performance with life cycle-based estimates of net CO_2 removal.

5.3 Results and Discussion

5.3.1 Results of Modelling the Gas-solid Carbonation Process

5.3.1.1 Comparison of Simulation Results with Experimental Data

To validate the model, CO_2 uptake predictions were compared against experimental data reported in a previous study under controlled conditions of 600 °C carbonation temperature and a 1-hour carbonation duration time (Tian et al., 2013b). Under low CO_2 concentrations (5%, 10%, and 15%), the model predicted CO_2 stored values of 0.0683, 0.0703, and 0.0717 kg CO_2/kg slag, closely matching the experimental values of 0.0731, 0.0761, and 0.0773 kg CO_2/kg slag, with an average relative error of only 7.15%. At 100% CO_2, the model slightly overestimated the CO_2 uptake at 0.0858 kg CO_2/kg slag compared to the experimental value of 0.0836 kg CO_2/kg slag, corresponding to a minimal relative error of just 2.63%.

For carbonation conversion, the model also showed strong agreement with experimental observations. At low CO_2 concentrations, the predicted conversions of 42.9%, 44.1%, and 45.0% were within 3–4% of the measured values (45.9%, 47.7%,

and 48.5%). At 100% CO_2, the model prediction of 53.8% was only 1.3% higher than the experimental value of 52.5%.

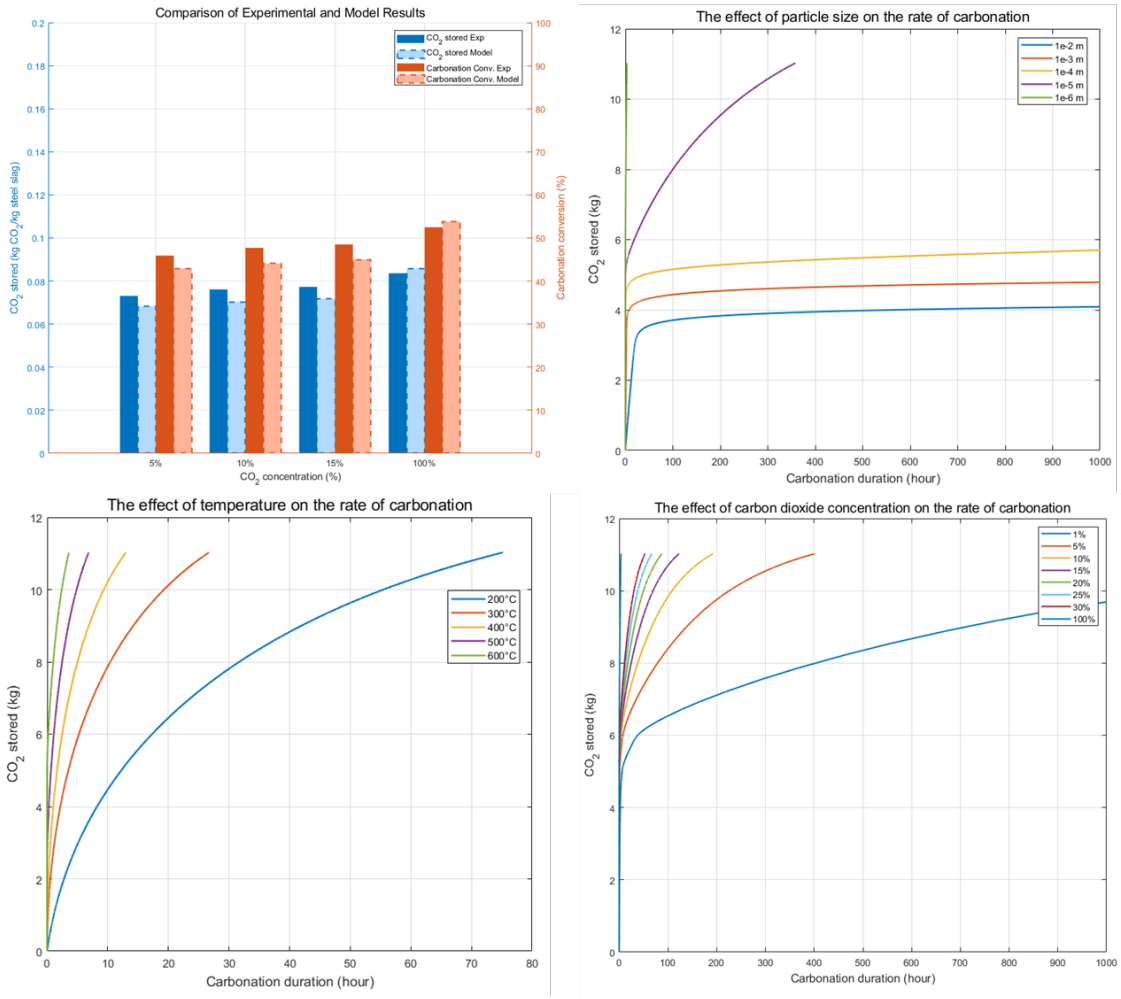

Figure 5-3 Gas-solid carbonation process simulation results. (a) comparison of experimental and model Results; (b) impact of particle size; (c) impact of temperature; (d) impact of CO_2 concentration

Overall, the close agreement between the model predictions and the experimental data across a range of CO_2 concentrations indicates that the model is capable of accurately capturing the trends and magnitudes of both CO_2 uptake and carbonation conversion. These results support the model's validity and suggest its suitability for

simulating carbonation behaviour under varying operational conditions (as shown in **Figure 5-3(a)**).

5.3.1.2 Impact of Key Factors on Process Performance

For the single-factor analysis, all other parameters are maintained at their default values to ensure consistency. The default settings are as follows: BOF steel slag as raw material, particle size is 1×10^{-6} m, CO_2 concentration is pure CO_2, and temperature is 600 °C. When stockpiled at steel plants without pretreatment, the slag typically has a particle diameter of approximately 15 mm. As shown in **Figure 5-3(b)**, gas–solid carbonation at this particle size requires more than 1,000 hours to reach completion, which is impractical under industrial conditions. However, reducing the particle size to 1 μm significantly improves carbonation efficiency, achieving approximately 90% conversion within around 4 hours. Under these conditions, the amount of CO_2 sequestered is 11.03 kg. **Figure 5-3 (c)** shows that the carbonation rate increases with increasing temperature due to enhanced reaction kinetics and improved diffusion of CO_2 through the slag matrix. Given that the carbonation reaction is exothermic, it has the potential to be self-sustaining without additional external energy input once initiated. However, excessively high temperatures may lead to the formation of dense carbonate layers on the slag surface, which can hinder further CO_2 penetration and reduce overall conversion efficiency (Z. Gao et al., 2024). Based on the simulation results, a temperature of 600 °C is considered optimal for achieving efficient carbonation under the studied conditions, as it provides a balance between high reaction rates and minimised diffusion limitations, while remaining feasible for

industrial applications. **Figure 5-3(d)** shows that the use of pure CO_2 exerts a significant influence on carbonation efficiency by accelerating reaction kinetics and promoting higher conversion rates. To enhance industrial feasibility, and since DAC technologies operate more effectively when providing concentrated CO_2 streams, pure CO_2 is assumed as the reactant in the gas–solid carbonation modelling presented in Section 5.2.2.1 and carried through to the LCA scenarios in Section 5.2.3.

5.3.1.3 LCA of Gas-solid Carbonation

5.3.1.3.1 Carbon Emission Analysis

Taking the UK as a scenario, per tonne of BOF steel slag can store 142.45 kg of CO_2. Without considering the transportation distance for DAC, the carbon emissions of the other five parts in DAC option 1 and option 2 are 59.97 kg and 123.38 kg, respectively.

Figure 5-4(a) illustrates the proportion of carbon emissions from various energy-consuming stages under different DAC options. In the absence of transportation, the steel slag crushing stage accounts for the largest share under DAC Option 1, contributing 53.04%, whereas under DAC Option 2, the DAC process itself dominates, representing 55.63%. When considering the transportation distance for DAC, it is evident that transportation has the lowest technical impact when using an EV truck combined with DAC option 1, while the highest technical impact occurs with a diesel truck combined with DAC option 2 (shown as **Figure 5-4(b)**).

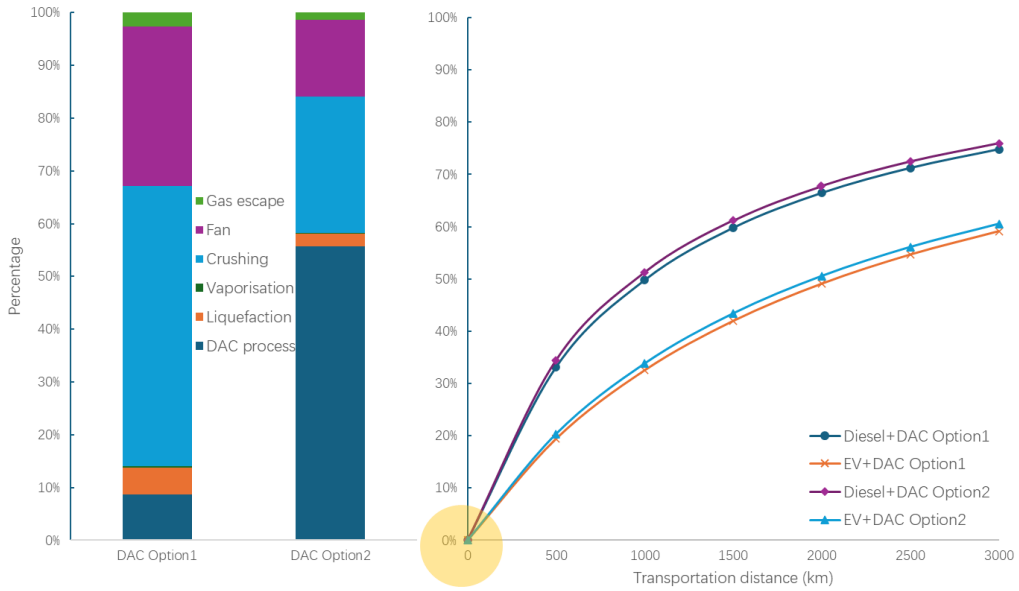

Figure 5-4 Gas-solid carbonation carbon emission analysis. (a) comparison of carbon emission proportions under different DAC options (transportation distance = 0 km); (b) impact of transportation distance on total carbon emissions under different scenarios (All results here refer to BOF slag and the UK grid electricity carbon intensity)

5.3.1.3.2 Impact of Carbon Intensity of Electricity Generation

A comparative analysis of net carbon emissions associated with BOF steel slag utilisation for CO_2 storage across multiple countries reveals a clear dependence on the carbon intensity of the local electricity supply. In regions where the electricity grid is predominantly supplied by low-carbon or renewable energy sources, adopting EV technology in combination with DAC Option 2 results in the lowest overall carbon emissions. This synergy is due to both the reduced emissions associated with electricity generation and the inherently lower carbon footprint of DAC Option 2, which captures CO_2 directly from the air without fossil fuel combustion.

In contrast, in countries where electricity generation relies largely on fossil fuels with high carbon emissions, the increased energy demand from EVs can offset their environmental benefits, leading to higher total emissions compared to conventional diesel-powered transport. Under these circumstances, diesel-powered vehicles paired with DAC options may prove to be more carbon-efficient despite the direct emissions from fuel combustion, as the overall carbon footprint of electricity consumption for EVs is comparatively higher. Therefore, the optimal choice of transport and DAC technology is highly context-dependent and must consider the national electricity generation mix to ensure genuine carbon reduction benefits. The map illustrating the optimal scenario selection across 37 countries is presented in **Figure 5-5**.

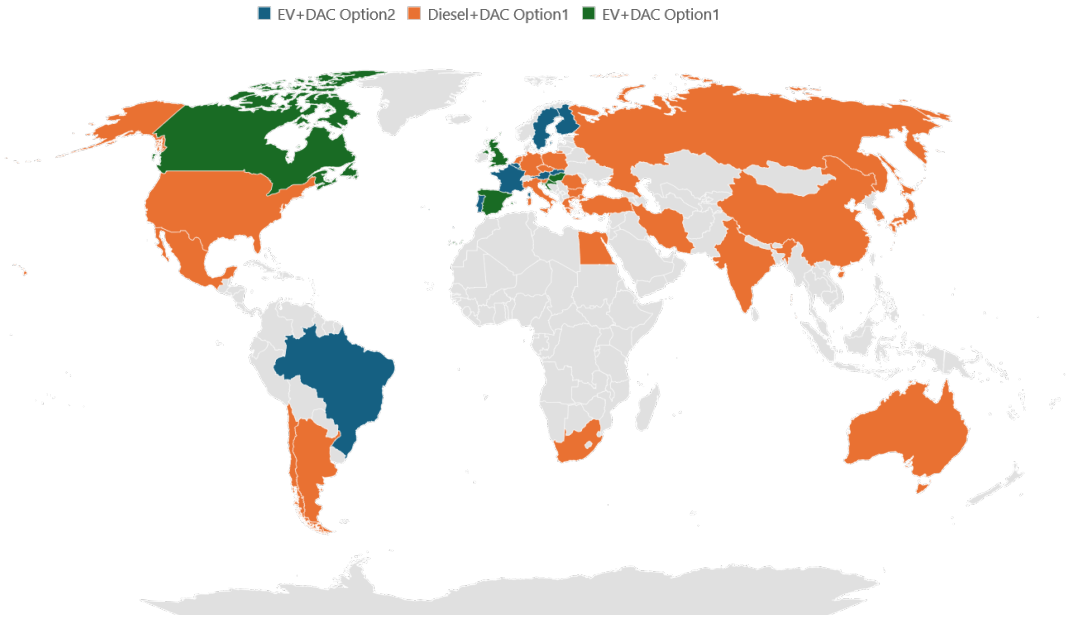

Figure 5-5 The optimal scenario selection across 37 countries

5.3.1.3.3 Net Carbon Removal

Considering the varying geographical sizes of different countries and typical CO_2 transportation distances, this study selects 50 km as the default transportation

distance. Building on the previously discussed optimal scenario for each country, a LCA analysis of net carbon removal is conducted using BF, BOF, and EAF steel slag as carbonation raw materials. Negative values indicate net CO_2 removal from the atmosphere, demonstrating the effectiveness of the technology, while positive values signify that the overall carbon footprint remains positive, meaning the amount of CO_2 stored is insufficient to offset the total carbon emissions generated throughout the entire process (shown in **Figure 5-6**).

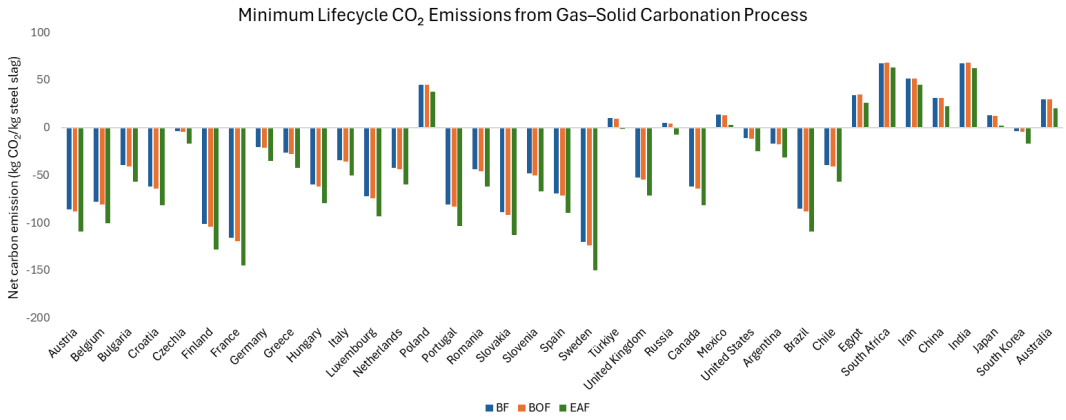

Figure 5-6 Net carbon emissions of BF, BOF and EAF steel slag gas-solid carbonation across 37 countries

A comparative analysis of the net carbon emissions reveals a clear dependence on the carbon intensity of electricity generation. Among the evaluated countries, approximately 81% achieve negative net emissions, indicating that accelerated carbonation using steel slag is an effective carbon removal strategy under most circumstances. In contrast, countries with electricity grids heavily reliant on fossil fuels such as India, China, South Africa, Iran and Egypt exhibit positive net emissions in

certain scenarios, where the emissions generated during DAC operations and slag processing exceed the CO_2 sequestered through carbonation.

The variation in performance across slag types demonstrates a consistent trend. EAF slag offers the highest net carbon removal potential, followed by BOF and then BF slag. This outcome is primarily attributable to the higher CaO content and carbonation reactivity of EAF slag. For instance, in decarbonised electricity systems such as those in Sweden, France and Finland, the net removal reaches up to 150 kg CO_2 per tonne of slag under EAF scenarios, underscoring the strong synergy between low-carbon energy and carbonation efficiency. Conversely, in high-carbon electricity grids, the energy-intensive steps of DAC and particle size reduction significantly reduce or even offset the carbon benefits, with the most unfavourable case observed in India under the BF scenario, yielding a net emission of approximately 67 kg CO_2 per tonne of slag.

Overall, the feasibility of steel slag carbonation for large-scale carbon removal is highly sensitive to the carbon intensity of regional power systems. Achieving meaningful climate benefits from this technology in coal-dominated grids requires parallel efforts in electricity decarbonisation or the integration of low-carbon energy sources for DAC and processing steps. Notably, even under unfavourable energy profiles, EAF slag consistently performs better than BF and BOF, reinforcing its role as the most promising candidate for future deployment.

5.3.2 Results of Modelling the Indirect Carbonation Process

5.3.2.1 Impact of Key Factors on Process Performance

To investigate the optimal parameters under varying conditions for the indirect carbonation process, all other parameters are maintained at their default values to ensure consistency. The default settings are as follows: BOF steel slag as the raw material, particle size of 1×10^{-5} m, CO_2 partial pressure of 0.1 bar, and a CO_2 gas flow rate of 24 m^3/h.

Figure 5-7(a) show that the smaller the particle size, the faster the dissolution rate. The original particle size of steel slag is approximately 1×10^4 μm. When the dissolution rate exceeds 95%, the corresponding dissolution times are 2880, 2500, 500, 60, and 20 minutes for particle sizes of 10^{-2} m, 10^{-3} m, 10^{-4} m, 10^{-5} m, and 10^{-6} m, respectively. At these points, the stirring energy input during dissolution, along with the crushing energy and total energy consumption, is evaluated. The minimum total energy consumption, 0.5 kWh per dissolution batch, is observed when the particle size is 1×10^{-5} m as shown in **Figure 5-7 (b)**. Therefore, this particle size is selected as the condition for the indirect carbonation process.

At a CO_2 gas flow rate of 24 m^3/h, the duration of the precipitation process is strongly influenced by CO_2 concentration. When the concentration is 0.05 bar, the process requires approximately 5.52 hours, whereas at 0.2 bar, the duration decreases to about 1.4 hours. Although higher CO_2 concentrations accelerate the precipitation rate, they also lead to a substantial increase in energy consumption for the DAC system.

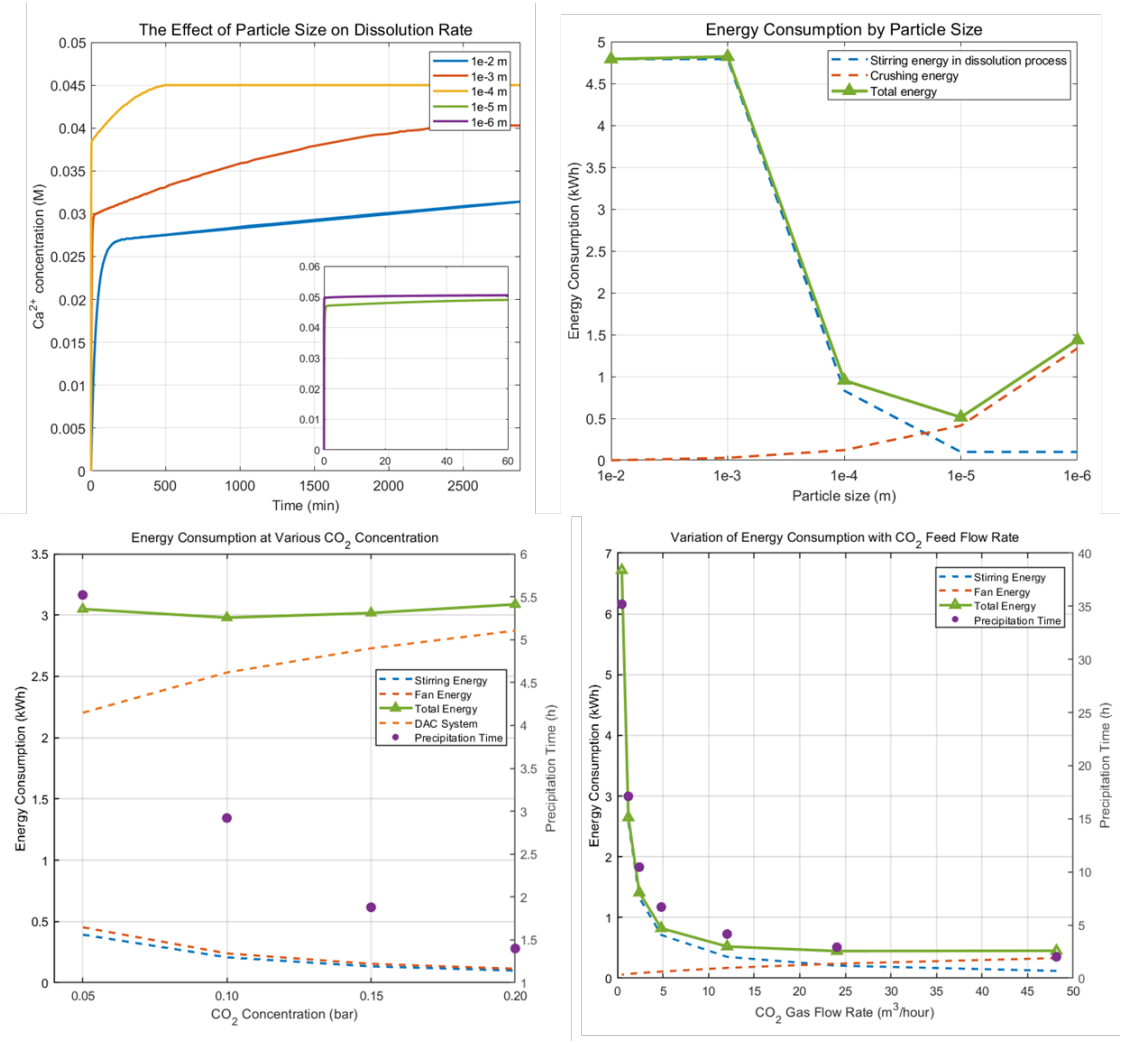

Figure 5-7 Indirect carbonation process simulation results (a) the effect of particle size on dissolution rate; (b) impact of particle size on energy consumption; (c) Effect of CO_2 concentration on energy consumption during the precipitation step; (d) Effect of CO_2 gas flow rate on energy consumption during the precipitation step

Taking both precipitation efficiency and energy demand into account, a partial pressure of 0.1 bar provides the most favourable trade-off and is therefore considered the optimal operating condition, as shown in **Figure 5-7 (c)**. When the CO_2 concentration is maintained at 0.1 bar and the gas flow rate is 24 m^3/h, the precipitation process lasts approximately 2.92 hours. Under these conditions, capturing 2.001 kg of CO_2 via DAC requires 2.531 kWh of energy. The stirring energy during the precipitation stage is 0.2078 kWh, while fan operation accounts for an

additional 0.2397 kWh. This results in a total energy consumption of 2.9785 kWh, which represents the lowest value among all evaluated scenarios, as presented in **Figure 5-7 (d)**.

5.3.2.2 LCA for Indirect Carbonation

5.3.2.2.1 Carbon Emission Analysis

Figure 5-8 summarises both the energy consumption and carbon emission profiles of the indirect carbonation process for BOF steel slag under the UK scenario. The pie chart presents the relative energy demand of each process step, showing that the BPMED system accounts for the largest share (58.4%), followed by DAC operation (20.7%), crushing (5.0%), stirring during precipitation (2.5%), fan operation (2.9%), and stirring in the dissolution stage (0.4%). This distribution indicates that energy consumption is dominated by electrochemical and gas-handling processes rather than by mechanical operations.

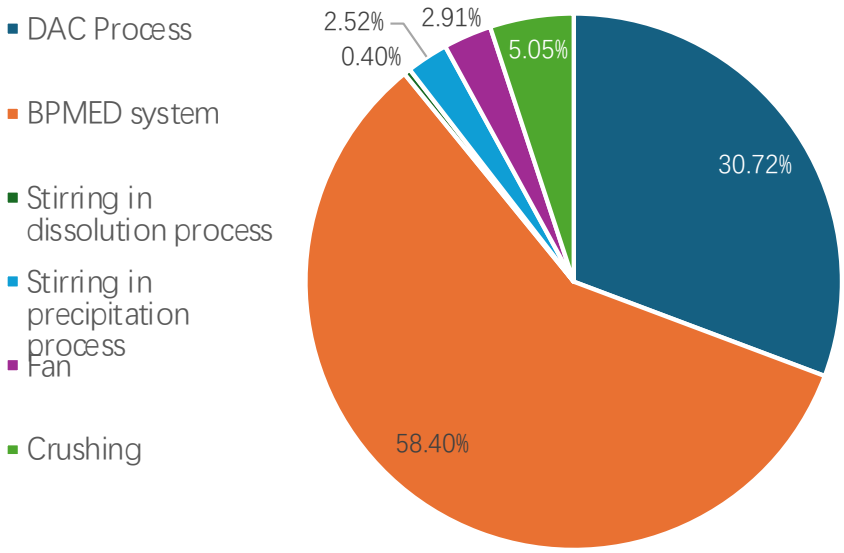

Figure 5-8 Energy consumption in the indirect carbonation of BOF steel slag under the UK scenario

The corresponding carbon emissions follow a similar pattern, as shown in the lower bar chart. The total carbon emission for the system is approximately 195.83 kg CO_2 per batch (10 kg of BOF slag). Crushing contributes 0.0988 kg CO_2 (5.05%), fan operation 2.91%, stirring during precipitation 2.52%, and stirring in dissolution 0.40%. The majority of emissions arise from the DAC and BPMED units, which together exceed 75% of the total footprint. From a carbon balance perspective, the process stores 200.23 kg CO_2 in mineral form while emitting 195.83 kg CO_2, achieving a net removal of 4.39 kg CO_2 per tonne of steel slag. Although energy-intensive, the process therefore remains net-negative in carbon terms under these operating conditions.

5.3.2.2.2 Net Carbon Removal

Figure 5-9 illustrates the net carbon emissions associated with indirect carbonation of BF, BOF, and EAF steel slags across 37 countries. Approximately 46% of the evaluated countries achieve negative net emissions, indicating that this pathway can be an effective carbon removal strategy where electricity supply is highly decarbonised. Conversely, in countries with fossil-fuel-intensive electricity systems, the process often results in positive emissions that outweigh the CO_2 stored.

Countries with decarbonised or low-carbon electricity systems perform best. Sweden achieves the largest net removal of CO_2, at approximately ~172 kg per functional unit under the EAF scenario, followed closely by France (~166 kg) and Finland (~143 kg). Other countries such as Portugal (~109 kg), Belgium (~105 kg), and Austria (~117 kg) also demonstrate substantial carbon removal benefits. In these cases, the differences

between BF, BOF, and EAF routes are relatively small, generally within ±2 kg CO_2, suggesting that electricity carbon intensity rather than slag type is the dominant factor. In contrast, South Africa records the highest emissions at approximately 383 kg CO_2 per functional unit across all slag types, followed by India (~383 kg), Iran (~328 kg), Egypt (~270 kg), and China (~260 kg). Poland also shows extremely high emissions, around 305 kg CO_2, ranking among the top contributors. Other high-emission regions include Mexico (~198 kg), Japan (~196 kg), and Australia (~253 kg). Thus, achieving negative emissions through indirect carbonation is contingent upon a largely decarbonised electricity supply.

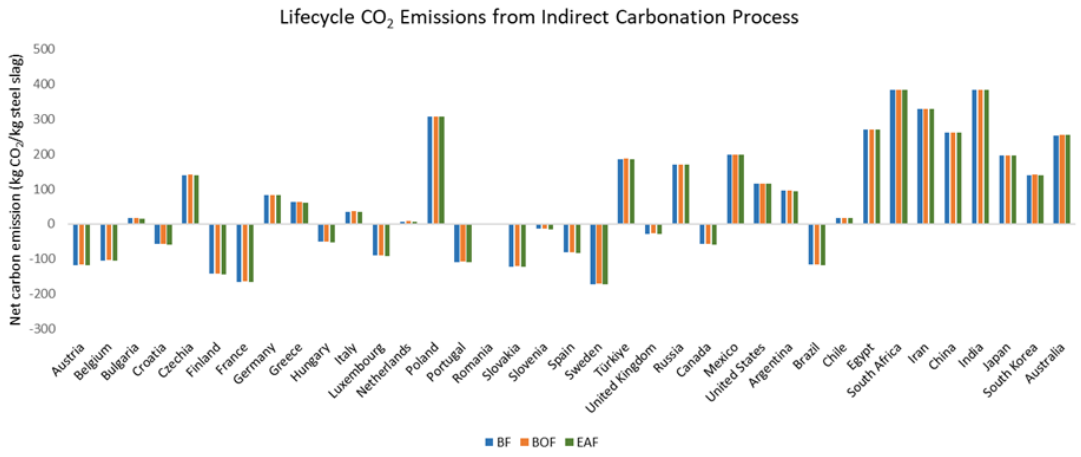

Figure 5-9 Net carbon emissions of BF, BOF and EAF steel slag indirect carbonation across 37 countries

5.3.2.2.3 Effect of Carbon Intensity on Carbonation Performance

To ensure consistency in the comparative analysis of LCA results between gas–solid carbonation and indirect carbonation, all boundary conditions are aligned. Specifically, the CO_2 transportation distance is assumed to be zero, eliminating variability associated with transport-related emissions and allowing for a direct evaluation of

process-level differences between the two carbonation pathways. The analytical expressions describing the variation of net emissions with CO_2 intensity for the three carbonation pathways are presented in **Figure 5-10**. For gas–solid carbonation employing DAC Option 1, the relationship is expressed as $y_{DAC_{O1}} = 245.6313x - 109.2084$. For gas–solid carbonation using DAC Option 2, the corresponding expression is $y_{DAC_{O2}} = 512.532x - 142.4536$. In the case of indirect carbonation, the analytical expression is given as $y_{indirect} = 824.21x - 220.2266$.

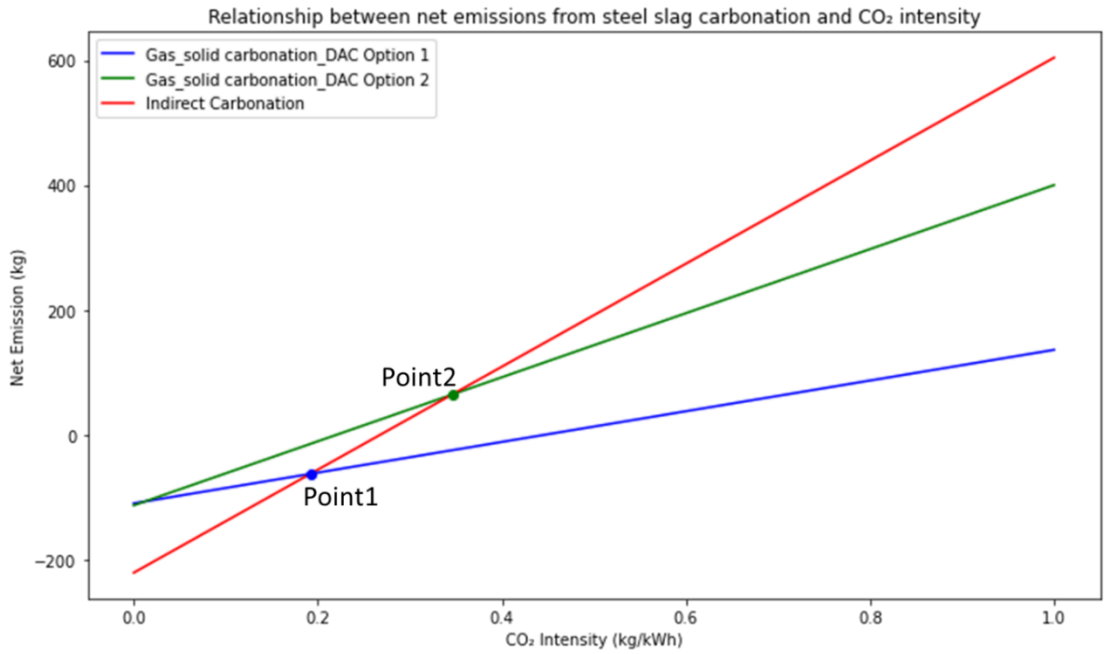

Figure 5-10 Relationship between net emissions from steel slag carbonation and CO_2 intensity

It can be observed that, when transportation distance is excluded, the three analytical curves intersect at two points. The first intersection, point 1, occurs at coordinates (0.192, −62.06), while the second intersection, point 2, is located at (0.3457, 64.632). This indicates that when the CO_2 intensity is below 0.192, indirect carbonation performs as the most effective option in terms of net emissions. When the CO_2

intensity exceeds 0.192, gas–solid carbonation under DAC Option 1 becomes the most favourable pathway. Within the range of CO_2 intensity between 0.192 and 0.3457, the performance of indirect carbonation remains intermediate, falling between that of DAC Option 1 and DAC Option 2.

5.3.3 Country-specific Comparison of the Two Carbonation Options in Net Carbon Removal

Figure 5-11 illustrates the top and bottom five countries in terms of net carbon emissions for both gas–solid carbonation and indirect carbonation pathways.

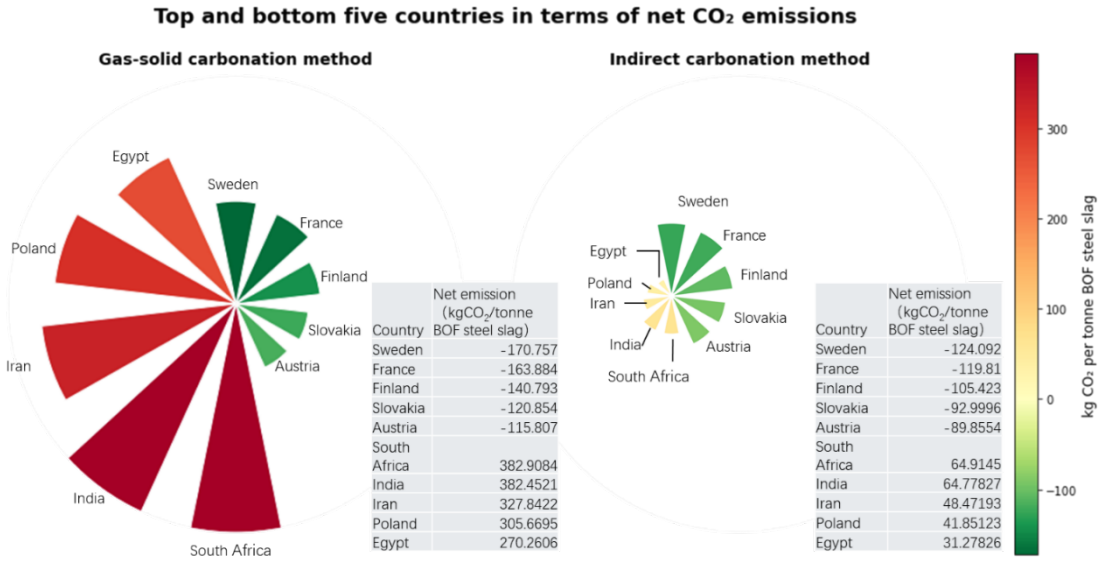

Country	Net emission ($kgCO_2$/tonne BOF steel slag)
Sweden	-170.757
France	-163.884
Finland	-140.793
Slovakia	-120.854
Austria	-115.807
South Africa	382.9084
India	382.4521
Iran	327.8422
Poland	305.6695
Egypt	270.2606

Country	Net emission ($kgCO_2$/tonne BOF steel slag)
Sweden	-124.092
France	-119.81
Finland	-105.423
Slovakia	-92.9996
Austria	-89.8554
South Africa	64.9145
India	64.77827
Iran	48.47193
Poland	41.85123
Egypt	31.27826

Figure 5-11 Top and bottom five countries in terms of net carbon emission

A comparative examination of these results highlights notable differences in the magnitude of emissions reduction and the overall effectiveness of each method across different regions. For the top five countries achieving the greatest carbon removal (negative emissions), gas–solid carbonation consistently outperforms indirect carbonation. The average net removal for gas–solid carbonation is ~142.42 kg CO_2 per

tonne of BOF steel slag, compared to ~106.63 kg for indirect carbonation, representing a shortfall of 35.79 kg, or approximately 25.1%. The smallest performance gap is observed in Austria (25.95 kg), while the largest occurs in Sweden (46.67 kg). The relative difference ranges between 22% and 27%, indicating that gas–solid carbonation remains the more effective pathway in highly decarbonised electricity systems.

Conversely, among the bottom five countries with the highest net emissions, both methods result in positive emissions, but indirect carbonation shows a substantial improvement. Gas–solid carbonation yields an average of 333.63 kg CO_2 per tonne, whereas indirect carbonation reduces this to 50.66 kg, corresponding to an average decrease of 282.97 kg, or about 84.8%. The reduction spans 83% to 88%, with the most significant absolute decrease recorded in South Africa (318 kg CO_2). Despite remaining a net carbon source in these regions, indirect carbonation markedly mitigates the carbon burden compared to gas–solid carbonation.

Figure 5-12 illustrates the annual average net carbon emissions associated with BOF steel slag carbonation via both gas–solid and indirect pathways across 37 countries. The emission outcomes are categorised into six discrete bands to aid in regional assessment. Countries exhibiting net emissions below -100 kg CO_2 per tonne are classified as highly suitable for the respective carbonation technology, reflecting strong decarbonisation potential. In contrast, any region with positive net emissions is deemed unsuitable for deployment, with those exceeding 1000 kg CO_2 per tonne

highlighted in red to indicate extremely unfavourable conditions due to excessive carbon intensity in the energy mix.

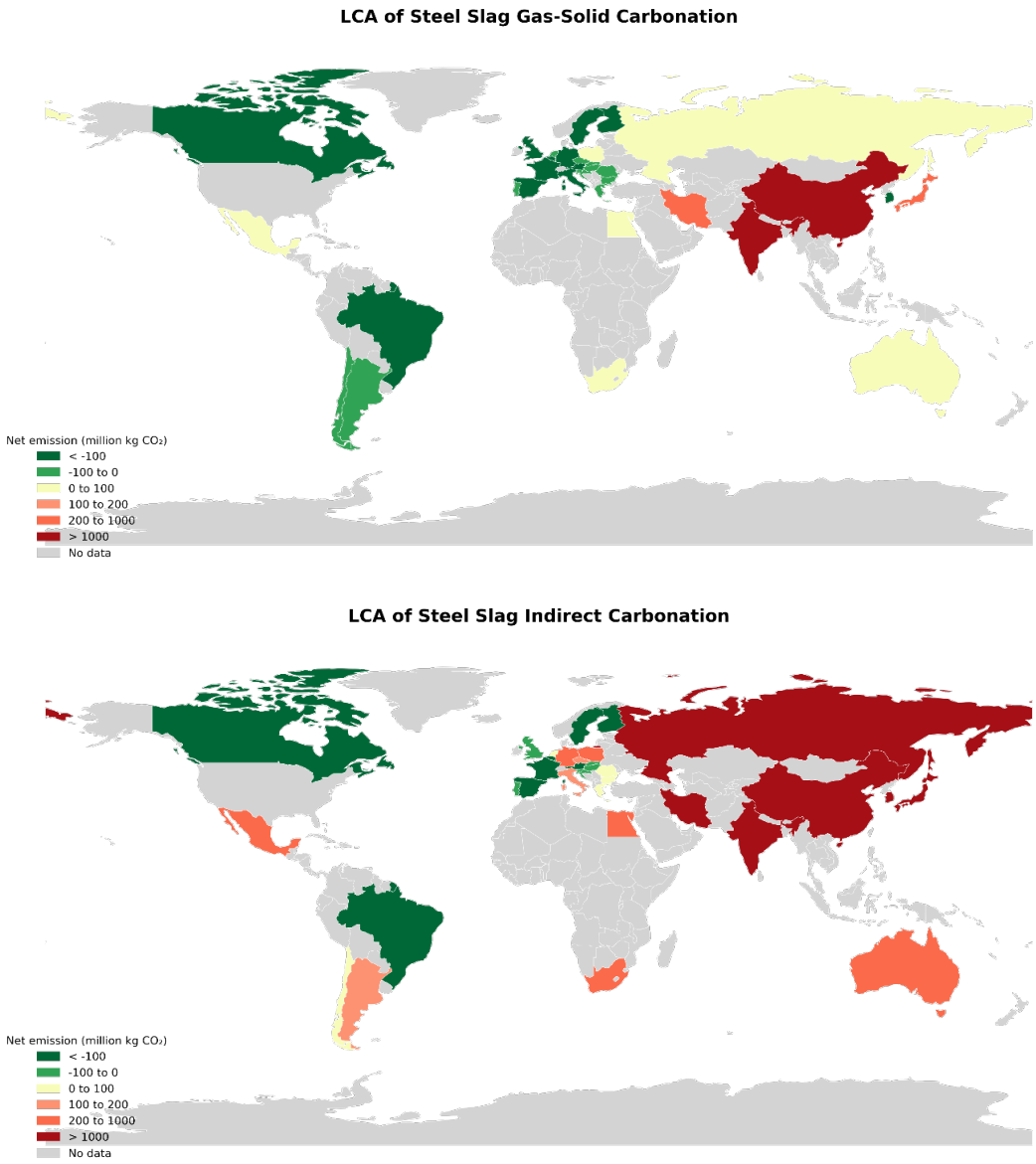

Figure 5-12 Comparison of global LCA net carbon emission results for steel slag (BF, BOF, and EAF) between gas-solid and indirect carbonation

Both carbonation methods display large variability across countries, primarily driven by differences in steel production volumes and electricity carbon intensity. Gas–solid carbonation generally exhibits smaller positive outliers, while indirect carbonation

shows extremely high positive values in fossil-fuel-dependent regions, indicating significant energy penalties associated with the dissolution and precipitation steps.

For gas–solid carbonation, 30 out of 37 countries achieve negative net emissions, with Brazil showing the most favourable performance at -1013.66 kg CO_2, followed by France (-392.98 kg) and the United States (-323.93 kg). These regions benefit from either low-carbon electricity grids or high carbon removal efficiency. For indirect carbonation, only 21 countries achieve negative emissions. The strongest performers are Brazil (-1310.97 kg CO_2), France (-530.50 kg), and Sweden (-231.52 kg). Compared with gas–solid, Brazil's advantage is even more pronounced for indirect carbonation.

Gas-solid carbonation shows moderately high emission cases in certain countries, such as China (10,416.79 kg CO_2), India (2484.49 kg CO_2), and Japan (238.89 kg CO_2). Indirect carbonation demonstrates extremely high emissions in certain regions, with China (96,900.25 kg CO_2) and India (15,075.26 kg CO_2) dominating due to their high steel production and fossil-fuel-intensive grids. Other large contributors include Japan (5590.02 kg CO_2) and South Korea (2895.92 kg CO_2). These results confirm that indirect carbonation is far more sensitive to grid carbon intensity and energy demand than gas-solid carbonation.

In most regions with decarbonised electricity (e.g., France, Sweden, Canada), both methods achieve negative emissions, but indirect carbonation tends to remove more CO_2 per functional unit than the gas-solid option. For example, France improves from -392.98 kg (gas-solid) to -530.50 kg (indirect). Conversely, in fossil-intensive regions,

indirect carbonation performs significantly worse than the gas-solid case. For instance, in China, emissions increase from 10,416.79 kg (gas-solid) to 96,900.25 kg (indirect), a difference of nearly 9-fold.

Overall, Brazil and France consistently rank among the top performers for both methods, indicating their electricity grids provide a strong foundation for carbon removal. China and India are outliers, contributing the highest global emissions for both methods, and their values for indirect carbonation dominate the global scale, making this pathway impractical without grid decarbonisation. On average, indirect carbonation is more advantageous only in countries with extremely low-carbon electricity, while gas-solid carbonation remains more robust across regions.

5.4 Conclusion

This study systematically evaluates the potential of steel slag carbonation as a CO_2 storage pathway through integrated process modelling, life cycle assessment, and global scenario analysis. Two carbonation pathways were considered: gas–solid carbonation and indirect carbonation, with a focus on process performance, energy requirements, and carbon balance under diverse operating conditions.

For the gas solid carbonation pathway, the model showed strong predictive accuracy, with an average relative error of 7.15% for CO_2 uptake and minimal deviation for carbonation conversion. Under optimized conditions of 600 °C and a particle size of 1 micrometre, the process achieved approximately 90% conversion within four hours, corresponding to a CO_2 sequestration amount of ~11 kilograms per batch. Using pure

CO_2 further enhanced carbonation efficiency, making it the preferred option for industrial application.

For the indirect carbonation pathway, the optimal conditions were identified as a particle size of 1×10^{-5} metres and a CO_2 partial pressure of 0.1 bar, combined with a gas flow rate of 24 cubic metres per hour. Under these conditions, the process captured ~2 kilograms of CO_2 per cycle with a total energy consumption of 2.98 kWh. LCA results indicated that the total emissions from the process were approximately 1.96 kilograms CO_2 per cycle, leading to a net removal of 4.39 kilograms CO_2 per tonne of steel slag.

A comparative analysis of net emissions under varying electricity carbon intensities revealed that when the intensity is below 0.192 kilograms CO_2 per kilowatt hour, indirect carbonation performs best, whereas above this threshold gas solid carbonation with DAC Option 1 becomes more favourable. When the electricity carbon intensity is low, gas solid carbonation can remove up to 150 kilograms CO_2 per tonne of slag, whereas indirect carbonation achieves an average of 106.63 kilograms, about 25% lower. In high carbon grids, indirect carbonation significantly reduces net emissions by 83% to 88% compared with gas solid carbonation, although both remain positive emitters in these regions.

The global analysis of 37 countries shows that approximately 81% of cases result in negative net emissions, confirming the feasibility of this approach as a carbon removal strategy. Among slag types, EAF slag consistently shows the highest removal potential,

followed by BOF and BF slag. In decarbonised energy systems, EAF slag enables net removals of up to 150 kilograms CO_2 per tonne, while in fossil fuel dominated grids such as those in India and South Africa, the most unfavourable cases can result in net emissions of up to 67 kilograms CO_2 per tonne under BF slag scenarios.

Overall, accelerated carbonation of steel slag represents a technically viable and scalable pathway for CO_2 removal. Its overall climate benefit depends strongly on the carbon intensity of electricity and on process optimisation. Indirect carbonation achieves the greatest net CO_2 removal when electricity is highly decarbonised, whereas gas–solid carbonation becomes the more favourable option as grid carbon intensity increases. In very carbon-intensive regions, both routes may still lead to net positive emissions unless paired with low-carbon energy sources. These results highlight the importance of aligning carbonation deployment with regional energy profiles to maximise climate benefit and provide guidance for integrating steel slag carbonation into global industrial decarbonisation strategies.

References

Anastasiou, E., Georgiadis Filikas, K., & Stefanidou, M. (2014). Utilization of fine recycled aggregates in concrete with fly ash and steel slag. *Construction and Building Materials*, *50*, 154–161. https://doi.org/10.1016/J.CONBUILDMAT.2013.09.037

Baciocchi, R., Costa, G., Di Gianfilippo, M., Polettini, A., Pomi, R., & Stramazzo, A. (2015). Thin-film versus slurry-phase carbonation of steel slag: CO2 uptake and effects on mineralogy. *Journal of Hazardous Materials*, *283*, 302–313. https://doi.org/10.1016/j.jhazmat.2014.09.016

Bonenfant, D., Kharoune, L., Sauvé, S., Hausler, R., Niquette, P., Mimeault, M., & Kharoune, M. (2008). CO2 sequestration potential of steel slags at ambient pressure and temperature. *Industrial and Engineering Chemistry Research*, *47*(20), 7610–7616. https://doi.org/10.1021/ie701721j

Chang, E.-E., Pan, S.-Y., Chen, Y.-H., Chu, H.-W., Wang, C.-F., & Chiang, P.-C. (2011). CO2 sequestration by carbonation of steelmaking slags in an autoclave reactor. *Journal of Hazardous Materials*, *195*, 107–114. https://doi.org/10.1016/j.jhazmat.2011.08.006

Chen, B., Yang, J. X., & Ouyang, Z. Y. (2011). Life Cycle Assessment of Internal Recycling Options of Steel Slag in Chinese Iron and Steel Industry. *Journal of Iron and Steel Research, International*, *18*(7), 33–40. https://doi.org/10.1016/S1006-706X(11)60087-3

Chen, L., & Yang, A. (2025). Assessing the net carbon removal potential by a combination of direct air capture and recycled concrete aggregates carbonation. *Resources, Conservation and Recycling*, *212*, 107940. https://doi.org/10.1016/j.resconrec.2024.107940

Chen, Z., Cang, Z., Yang, F., Zhang, J., & Zhang, L. (2021). Carbonation of steelmaking slag presents an opportunity for carbon neutral: A review. *Journal of CO2*

Utilization, *54*, 101738. https://doi.org/10.1016/j.jcou.2021.101738

Deutz, S., & Bardow, A. (2021). Life-cycle assessment of an industrial direct air capture process based on temperature–vacuum swing adsorption. *Nature Energy*, *6*(2), 203–213. https://doi.org/10.1038/s41560-020-00771-9

Devlin, A., Kossen, J., Goldie-Jones, H., & Yang, A. (2023). Global green hydrogen-based steel opportunities surrounding high quality renewable energy and iron ore deposits. *Nature Communications*, *14*(1), 2578. https://doi.org/10.1038/s41467-023-38123-2

Digdaya, I. A., Sullivan, I., Lin, M., Han, L., Cheng, W.-H., Atwater, H. A., & Xiang, C. (2020). A direct coupled electrochemical system for capture and conversion of CO2 from oceanwater. *Nature Communications*, *11*(1), 4412. https://doi.org/10.1038/s41467-020-18232-y

DiGiovanni, C., Hisseine, O. A., & Awolayo, A. N. (2024). Carbon dioxide sequestration through steel slag carbonation: Review of mechanisms, process parameters, and cleaner upcycling pathways. *Journal of CO2 Utilization*, *81*, 102736. https://doi.org/10.1016/j.jcou.2024.102736

Gao, D., Wang, F.-P., Wang, Y.-T., & Zeng, Y.-N. (2020). Sustainable Utilization of Steel Slag from Traditional Industry and Agriculture to Catalysis. *Sustainability*, *12*(21), 9295. https://doi.org/10.3390/su12219295

Gao, T., Dai, T., Shen, L., & Jiang, L. (2021). Benefits of using steel slag in cement clinker production for environmental conservation and economic revenue generation. *Journal of Cleaner Production*, *282*, 124538. https://doi.org/10.1016/j.jclepro.2020.124538

Gao, W., Zhou, W., Lyu, X., Liu, X., Su, H., Li, C., & Wang, H. (2023). Comprehensive utilization of steel slag: A review. *Powder Technology*, *422*, 118449. https://doi.org/10.1016/J.POWTEC.2023.118449

Gao, Z., Zhao, Q., Tao, M., Wang, Z., Liu, C., Saxén, H., & Zevenhoven, R. (2024).

Recent research progress on the direct carbon capture of steel slag to prepare building materials. *Green and Smart Mining Engineering*, *1*(4), 387–395. https://doi.org/10.1016/j.gsme.2024.11.003

Gencel, O., Karadag, O., Oren, O. H., & Bilir, T. (2021). Steel slag and its applications in cement and concrete technology: A review. *Construction and Building Materials*, *283*, 122783. https://doi.org/10.1016/j.conbuildmat.2021.122783

Geological Survey, U. (2024). *MINERAL COMMODITY SUMMARIES 2024*.

Guo, J., Bao, Y., & Wang, M. (2018). Steel slag in China: Treatment, recycling, and management. *Waste Management*, *78*, 318–330. https://doi.org/10.1016/j.wasman.2018.04.045

Guo, Y., Xie, J., Zheng, W., & Li, J. (2018). Effects of steel slag as fine aggregate on static and impact behaviours of concrete. *Construction and Building Materials*, *192*, 194–201. https://doi.org/10.1016/J.CONBUILDMAT.2018.10.129

Gyllenram, R., Arzpeyma, N., Wei, W., & Jönsson, P. G. (2022). Driving investments in ore beneficiation and scrap upgrading to meet an increased demand from the direct reduction-EAF route. *Mineral Economics*, *35*(2), 203–220. https://doi.org/10.1007/s13563-021-00267-2

Hainin, Mohd. R., A. Aziz, Md. M., Ali, Z., Putra Jaya, R., El-Sergany, M. M., & Yaacob, H. (2015). Steel Slag as A Road Construction Material. *Jurnal Teknologi*, *73*(4). https://doi.org/10.11113/jt.v73.4282

Haynes, W. M., Lide, D. R., & Bruno, T. J. (Eds.). (2016). *CRC Handbook of Chemistry and Physics*. CRC Press. https://doi.org/10.1201/9781315380476

Heo, J., & Park, J. H. (2022). Interfacial reactions between magnesia refractory and electric arc furnace (EAF) slag with use of direct reduced iron (DRI) as raw material. *Ceramics International*, *48*(4), 4526–4538. https://doi.org/10.1016/j.ceramint.2021.10.238

Hu, J., Li, Z., Liu, L., Wang, X., Wang, C., & Jin, Z. (2024). Investigation of the electrochemical performance of solid oxide fuel cells with methanol internal reforming. *International Journal of Electrochemical Science*, *19*(5), 100550. https://doi.org/10.1016/j.ijoes.2024.100550

Huang, X., Zhang, J., & Zhang, L. (2024). Accelerated carbonation of steel slag: A review of methods, mechanisms and influencing factors. *Construction and Building Materials*, *411*, 134603. https://doi.org/10.1016/j.conbuildmat.2023.134603

Huijgen, W. J. J., & Comans, R. N. J. (2006). Carbonation of steel slag for CO2 sequestration: Leaching of products and reaction mechanisms. *Environmental Science and Technology*, *40*(8), 2790–2796. https://doi.org/10.1021/es052534b

Keith, D. W., Holmes, G., St. Angelo, D., & Heidel, K. (2018). A Process for Capturing CO2 from the Atmosphere. *Joule*, *2*(8), 1573–1594. https://doi.org/10.1016/j.joule.2018.05.006

Kohitlhetse, I., Rutto, H., Motsetse, K., & Manono, M. (2023). Grindability, Energy Requirements and Gravity Separation of Quartz from Blast Furnace Ironmaking Slag by Shaking Table and Falcon Concentrator †. *Engineering Proceedings*, 17–31. https://doi.org/10.3390/xxxxx

Kracík, T., Moucha, T., & Petříček, R. (2020). Gas-Liquid Contactors' Aeration Capacities When Agitated by Rushton Turbines of Various Diameters. *ACS Omega*, *5*(10), 5072–5077. https://doi.org/10.1021/acsomega.9b04005

Kumar, S., Kumar, R., Bandopadhyay, A., Alex, T. C., Ravi Kumar, B., Das, S. K., & Mehrotra, S. P. (2008). Mechanical activation of granulated blast furnace slag and its effect on the properties and structure of portland slag cement. *Cement and Concrete Composites*, *30*(8), 679–685. https://doi.org/10.1016/j.cemconcomp.2008.05.005

Kumaresan, T., & Joshi, J. B. (2006). Effect of impeller design on the flow pattern and

mixing in stirred tanks. *Chemical Engineering Journal*, *115*(3), 173–193. https://doi.org/10.1016/j.cej.2005.10.002

Li, P., Ji, J., Wen, L., Chen, H., Bian, L., Zhou, W., & Wu, Y. (2024). Quantitative characterization and evaluation of key physicochemical characteristics of steel slag. *Construction and Building Materials*, *414*, 134959. https://doi.org/10.1016/j.conbuildmat.2024.134959

Liu, L., Liu, J., Liu, T., Zhang, Y., Liang, H., Ning, T., Lin, X., Bai, Z., & Lu, A. (2022). Preparation, crystallization kinetics and stabilization behavior of the heavy metal ions of all-solid waste-based glass-ceramics from steel slag and coal gangue. *Journal of Non-Crystalline Solids*, *592*, 121750. https://doi.org/10.1016/J.JNONCRYSOL.2022.121750

Liu, W., Teng, L., Rohani, S., Qin, Z., Zhao, B., Xu, C. C., Ren, S., Liu, Q., & Liang, B. (2021). CO2 mineral carbonation using industrial solid wastes: A review of recent developments. *Chemical Engineering Journal*, *416*, 129093. https://doi.org/10.1016/j.cej.2021.129093

Luo, Y., & He, D. (2021). Research on Indirect Carbonation of Two-step Leaching for the Purpose of Utilizing the Alkalinity of Steel Slag. *Journal of Sustainable Metallurgy*, *7*(3), 947–963. https://doi.org/10.1007/s40831-021-00384-w

Myers, C., & Nakagaki, T. (2020). Direct mineralization of atmospheric CO_2 using natural rocks in Japan. *Environmental Research Letters*, *15*(12), 124018. https://doi.org/10.1088/1748-9326/abc217

Nielsen, P., Boone, M. A., Horckmans, L., Snellings, R., & Quaghebeur, M. (2020). Accelerated carbonation of steel slag monoliths at low CO2 pressure – microstructure and strength development. *Journal of CO2 Utilization*, *36*, 124–134. https://doi.org/10.1016/j.jcou.2019.10.022

O'Connor, J., Nguyen, T. B. T., Honeyands, T., Monaghan, B., O'Dea, D., Rinklebe, J., Vinu, A., Hoang, S. A., Singh, G., Kirkham, M. B., & Bolan, N. (2021). Production,

characterisation, utilisation, and beneficial soil application of steel slag: A review. *Journal of Hazardous Materials*, *419*, 126478. https://doi.org/10.1016/j.jhazmat.2021.126478

Paul, E. L., Atiemo-Obeng, V. A., & Kresta, S. M. (Eds.). (2003). *Handbook of Industrial Mixing*. Wiley. https://doi.org/10.1002/0471451452

Polettini, A., Pomi, R., & Stramazzo, A. (2016). CO2 sequestration through aqueous accelerated carbonation of BOF slag: A factorial study of parameters effects. *Journal of Environmental Management*, *167*, 185–195. https://doi.org/10.1016/j.jenvman.2015.11.042

Ragipani, R., Bhattacharya, S., & Suresh, A. K. (2019). Kinetics of steel slag dissolution: from experiments to modelling. *Proceedings of the Royal Society A: Mathematical, Physical and Engineering Sciences*, *475*(2224), 20180830. https://doi.org/10.1098/rspa.2018.0830

Ragipani, R., Bhattacharya, S., & Suresh, A. K. (2021). A review on steel slag valorisation *via* mineral carbonation. *Reaction Chemistry & Engineering*, *6*(7), 1152–1178. https://doi.org/10.1039/D1RE00035G

Ranzani da Costa, A., Wagner, D., & Patisson, F. (2013). Modelling a new, low CO2 emissions, hydrogen steelmaking process. *Journal of Cleaner Production*, *46*, 27–35. https://doi.org/10.1016/j.jclepro.2012.07.045

Ren, L., Zhou, S., Peng, T., & Ou, X. (2021). A review of CO2 emissions reduction technologies and low-carbon development in the iron and steel industry focusing on China. *Renewable and Sustainable Energy Reviews*, *143*, 110846. https://doi.org/10.1016/j.rser.2021.110846

Scargiali, F., Busciglio, A., Grisafi, F., Tamburini, A., Micale, G., & Brucato, A. (2013). Power Consumption in Uncovered Unbaffled Stirred Tanks: Influence of the Viscosity and Flow Regime. *Industrial & Engineering Chemistry Research*, *52*(42), 14998–15005. https://doi.org/10.1021/ie402466w

Shi, C., & Wu, Y. (2008). Studies on some factors affecting CO2 curing of lightweight concrete products. *Resources, Conservation and Recycling*, *52*(8–9), 1087–1092. https://doi.org/10.1016/j.resconrec.2008.05.002

Sivakumaran, K. S., Korol, R. M., & Fan, X. (2014). Energy absorption potential of concrete floors containing secondary (shrinkage and temperature) reinforcements. *Frontiers of Structural and Civil Engineering*, *8*(3), 282–291. https://doi.org/10.1007/s11709-014-0269-3

Sohn, H. Yong. (2020). *Fluid-solid reactions*. Elsevier.

Tian, S., Jiang, J., Chen, X., Yan, F., & Li, K. (2013). Direct Gas–Solid Carbonation Kinetics of Steel Slag and the Contribution to In situ Sequestration of Flue Gas CO_2 in Steel-Making Plants. *ChemSusChem*, *6*(12), 2348–2355. https://doi.org/10.1002/cssc.201300436

Tiwari, M., Bajpai, Dr. S., & Dewangan, Dr. U. (2016). Steel Slag Utilization — Overview in Indian Perspective. *International Journal of Advanced Research*, *4*(8), 2232–2246. https://doi.org/10.21474/IJAR01/1442

Tu, M., Zhao, H., Lei, Z., Wang, L., Chen, D., Yu, H., & Qi, T. (2015). Aqueous Carbonation of Steel Slag: A Kinetics Study. *ISIJ International*, *55*(11), 2509–2514. https://doi.org/10.2355/isijinternational.ISIJINT-2015-142

Wang, J., Zhong, M., Wu, P., Wen, S., Huang, L., & Ning, P. (2021). A Review of the Application of Steel Slag in CO_2 Fixation. *ChemBioEng Reviews*, *8*(3), 189–199. https://doi.org/10.1002/cben.202000021

Xi, F., Davis, S. J., Ciais, P., Crawford-Brown, D., Guan, D., Pade, C., Shi, T., Syddall, M., Lv, J., Ji, L., Bing, L., Wang, J., Wei, W., Yang, K.-H., Lagerblad, B., Galan, I., Andrade, C., Zhang, Y., & Liu, Z. (2016). Substantial global carbon uptake by cement carbonation. *Nature Geoscience*, *9*(12), 880–883. https://doi.org/10.1038/ngeo2840

Yi, H., Xu, G., Cheng, H., Wang, J., Wan, Y., & Chen, H. (2012). An Overview of

Utilization of Steel Slag. *Procedia Environmental Sciences*, *16*, 791–801. https://doi.org/10.1016/J.PROENV.2012.10.108

Yildirim, I. Z., & Prezzi, M. (2011). Chemical, Mineralogical, and Morphological Properties of Steel Slag. *Advances in Civil Engineering*, *2011*, 1–13. https://doi.org/10.1155/2011/463638

Yu, C., Cui, C., Wang, Y., Zhao, J., & Wu, Y. (2021). Strength performance and microstructural evolution of carbonated steel slag stabilized soils in the laboratory scale. *Engineering Geology*, *295*, 106410. https://doi.org/10.1016/j.enggeo.2021.106410

Yu, J., & Wang, K. (2011). Study on Characteristics of Steel Slag for CO_2 Capture. *Energy & Fuels*, *25*(11), 5483–5492. https://doi.org/10.1021/ef2004255

Zhang, X., Zhao, J., Liu, Y., & Li, J. (2024). Use of steel slag as carbonation material: A review of carbonation methods and evaluation, environmental factors and carbon conversion process. *Journal of CO2 Utilization*, *88*, 102947. https://doi.org/10.1016/j.jcou.2024.102947

Zhang, Y., Long, S., Duret, M. T., Bullock, L. A., Lam, P., & Yang, A. (2025). Modeling and Feasibility Assessment of Mineral Carbonation Based on Biological pH Swing for Atmospheric CO_2 Removal. *ACS Sustainable Chemistry & Engineering*, *13*(19), 6972–6981. https://doi.org/10.1021/acssuschemeng.4c10708

Zhang, Y., Yu, L., Cui, K., Wang, H., & Fu, T. (2023). Carbon capture and storage technology by steel-making slags: Recent progress and future challenges. *Chemical Engineering Journal*, *455*, 140552. https://doi.org/10.1016/j.cej.2022.140552

Zhou, J. A., Zhong, S. J., Dang, J. X., & Li, X. (2011). Experimental Investigation of Sintering Flue Gas Desulfurization with Steel Slag Using Dry CFB Method. *Applied Mechanics and Materials*, *71–78*, 2547–2550. https://doi.org/10.4028/www.scientific.net/AMM.71-78.2547

Chapter 6 Conclusion

6.1 Summary of the PhD Study

This PhD research systematically evaluates the feasibility of integrating DACU with the carbonation of construction materials as a large-scale CO_2 removal pathway. The study addresses a fundamental question in the context of decarbonised infrastructure: whether CO_2 captured directly from air can be permanently stored within construction materials in a technically and energetically viable manner. It comprises three interrelated projects, namely the carbonation of cement and concrete, the carbonation of RCA, and the carbonation of steel slag. Together, these studies establish a consistent analytical framework that links experimental evidence, process modelling, and life cycle assessment to quantify the carbon removal potential and system-level feasibility of DACU.

Project 1 (Chapter 3) conducts a meta-analysis of 548 experimental datasets collected from 35 laboratories worldwide. The analysis harmonises previously inconsistent experimental results and provides the first standardised dataset for accelerated carbonation. Statistical and machine learning models, including RF, GB, SVR, and Ridge regression, are used to identify the most influential process parameters. The key variables controlling CO_2 uptake include CO_2 concentration, curing pressure, exposure duration, and water-to-cement ratio. The ensemble regression model achieves a determination coefficient of $R^2 = 0.81$ and a root mean square error below 5%. The results show that optimised curing conditions can achieve CO_2 uptake between 12%

and 25% of binder mass, depending on mix composition and curing atmosphere. High CO_2 concentration above 80% and moderate humidity enhance uptake while maintaining mechanical strength. These findings provide a quantitative basis for predictive curing design and resolve inconsistencies that have limited process optimisation in previous studies.

Project 2 (Chapter 4) develops an integrated process and life cycle model to assess the carbonation of RCA using CO_2 derived from DAC under conditions representative of industrial operation. The model incorporates material-level parameters such as CO_2 concentration, moisture content, particle size and contact duration, together with system-level factors including DAC energy demand and CO_2 transport. Simulation results indicate that for one tonne of RCA carbonated to 90%, total CO_2 uptake reaches approximately 70 kg. Depending on electricity carbon intensity and transport distance, the overall outcome ranges from a net removal of about 13 kg CO_2 to a net emission of about 14 kg CO_2. The use of on-site low-purity CO_2 (around 1%) enhances net removal by approximately 70% compared with high-purity off-site supply. Sensitivity analysis identifies electricity carbon intensity as the dominant factor, with a critical threshold of about 0.25 kg CO_2 kWh^{-1} separating net-positive from net-negative performance. Under low-carbon electricity conditions (below 0.20 kg CO_2 kWh^{-1}) and optimised logistics within 50 km, the combined DAC and RCA carbonation system achieves verifiable net-negative results. This model defines the operational boundary within which DACU-integrated RCA carbonation can be effectively deployed in regional construction supply chains.

Project 3 (Chapter 5) extends the analysis to steel slag, an abundant by-product of iron and steelmaking that contains reactive CaO suitable for mineral carbonation. The study develops comparative kinetic models for gas–solid and indirect carbonation and couples them with LCA under conditions representative of industrial practice. Gas–solid carbonation achieves up to 150 kg CO_2 per tonne of slag in net removal, while indirect aqueous carbonation reaches an average of about 106.6 kg CO_2 per tonne and up to 172 kg CO_2 per tonne in the most favourable cases. A threshold of approximately 0.192 kg CO_2 kWh^{-1} distinguishes the preferred route, with indirect aqueous carbonation performing better below this value and gas–solid carbonation above it. A global scenario analysis covering 37 countries shows that about 81% of the cases are net negative, with the highest carbon removal potential observed in regions where extensive slag reserves coincide with low-carbon electricity. These findings confirm the technical feasibility and regional suitability of large-scale slag carbonation and highlight the importance of coupling carbon utilisation with electricity decarbonisation.

A comparative analysis across the three material systems reveals complementary strengths and inherent limitations. Cement and concrete carbonation exhibit the highest reactivity per unit binder, achieving average uptakes of 0.16–0.18 kg CO_2 kg^{-1} binder and providing a statistically robust foundation for predictive modelling. RCA carbonation achieves 0.07–0.09 kg CO_2 kg^{-1} material, offering the largest overall storage capacity per bulk volume and clear circular-economy benefits by converting demolition waste into a durable CO_2 sink. Steel slag carbonation attains CO_2 uptakes

of 0.14–0.17 kg CO_2 kg^{-1} slag under industrially relevant conditions, consistent with the modelled net removals achieved in regions with low-carbon electricity.

Across all three studies, the process and life cycle models incorporate parameters that reflect realistic implementation, including batch size, CO_2 purity, flow rate and energy input. These consistent modelling frameworks enable direct quantitative comparison and demonstrate that both process design and energy context jointly determine achievable net removal outcomes. Collectively, the findings establish a unified, system-level understanding of DACU-enabled CO_2 mineralisation in construction materials, demonstrating that these processes can deliver verifiable net-negative emissions and make a substantive contribution to global carbon removal objectives.

6.2 Key Contributions

This PhD research makes both methodological and practical contributions:

This PhD study contributes to the scientific understanding of DACU-enabled CO_2 mineralisation in construction materials through methodological, analytical, and conceptual advances. The research provides new knowledge on how captured CO_2 interacts with cementitious and alkaline industrial residues, and it establishes quantitative frameworks that extend beyond experimental observation to predictive and system-level interpretation. The principal contributions can be summarised as follows.

(1) Development of a harmonised analytical foundation for CO_2 curing of cementitious materials

The study compiles and harmonises 548 experimental datasets from more than thirty-five independent laboratories, establishing the most comprehensive database currently available for accelerated carbonation of cement and concrete. The application of statistical and machine learning methods quantifies the relative influence of process parameters, clarifies inconsistencies reported in previous studies, and generates models capable of predicting CO_2 uptake with high accuracy ($R^2 = 0.81$). This approach transforms a fragmented body of empirical results into a coherent predictive framework, thereby advancing methodological rigour in the study of mineral carbonation.

(2) Advancement of integrated modelling linking process modelling with life-cycle metrics

A novel process model is developed for the carbonation of RCA using DAC-derived CO_2. Unlike conventional batch or laboratory models, this framework integrates material-level reaction kinetics with energy demand, transport distance, and DAC operation. Its coupling with LCA establishes a unified method for quantifying net CO_2 removal under different technological and regional conditions. This development represents a methodological step forward by connecting physical modelling with environmental evaluation, thereby enabling quantitative assessment of DACU systems at plant-relevant scale.

(3) Comparative kinetic and system analysis of gas–solid and indirect carbonation routes with steel slag

The research formulates and validates kinetic models for both gas–solid and indirect carbonation under consistent boundary conditions. Through integration with LCA, the work identifies the energy and carbon thresholds that determine the preferred process route, revealing a critical dependence on electricity carbon intensity (≈0.192 kg CO_2 kWh^{-1}). This provides a mechanistic and system-level understanding of how energy structure governs the net removal potential of mineral carbonation, an aspect not previously quantified across process routes.

(4) Establishment of a framework and indicators for future material and system design

Drawing on the methodologies developed, the thesis proposes generalised indicators for assessing emerging materials and configurations. These include CO_2 uptake per mass of reactive oxide, specific energy demand per kilogram of CO_2 captured, and net removal efficiency after accounting for energy inputs. The framework can be applied to materials such as fly ash, metakaolin, or alternative steel-slag derivatives, supporting systematic evaluation of future DACU–carbonation systems. This contribution provides a conceptual bridge between material-level kinetics and system-level design.

This research consolidates methodological and theoretical progress in CO_2 mineralisation by establishing a coherent link between experimental evidence, process modelling, and life-cycle assessment. It provides an integrated framework for quantifying the relationship between material reactivity, energy context, and system

design, thereby enabling a predictive evaluation of carbon removal performance in construction materials. The outcomes contribute to the broader understanding of carbon capture and utilisation by providing a scientifically grounded basis for model validation, process optimisation, and future scale-up assessment.

6.3 Limitations and Future Perspectives

Although this research establishes a quantitative and system-level framework for DACU-enabled CO_2 mineralisation, several limitations remain that define the scope of its applicability. The modelling and life-cycle assessments are conducted under process-relevant but not fully industrial operating conditions; therefore, the transition to continuous, plant-scale implementation requires further validation. The experimental datasets used in the meta-analysis originate from heterogeneous laboratory studies, introducing potential biases in measurement protocols, material compositions, and experimental control despite harmonisation efforts. The life-cycle analyses are further constrained by regional energy profiles and the assumption of steady-state operation, whereas future systems may involve dynamic or hybrid energy inputs. These factors collectively limit the precision with which large-scale system performance can be extrapolated from current results.

A further limitation arises from the focus on three representative material systems: cementitious binders, recycled concrete aggregates, and steel slags. While these materials capture major classes of reactive construction media, they do not encompass other alkaline residues or by-products that may hold significant potential

for CO_2 mineralisation. In addition, the modelling frameworks assume idealised reaction kinetics and uniform feedstock properties. In practice, the variability in industrial by-products, reactor configurations, and operational conditions could alter reaction efficiency and CO_2 storage stability. These uncertainties should be addressed through pilot-scale studies, improved kinetic data, and long-term monitoring to strengthen the robustness and transferability of the results.

Future research should extend the present framework to capture multiscale interactions between process design, material reactivity, and energy infrastructure. The quantitative indicators developed in this study, including CO_2 uptake per unit mass of reactive oxide, specific energy demand per kilogram of CO_2 captured, and net removal efficiency under regional energy contexts, provide a foundation for systematic evaluation of emerging materials and configurations. These may include fly ash, metakaolin, bottom ash, red mud, and steel-slag derivatives produced under different metallurgical and geographical conditions. Incorporating these indicators into comparative analyses would enable the consistent benchmarking of performance across materials and technologies.

Further model development should incorporate dynamic life-cycle inventory data and process simulations validated through pilot- and demonstration-scale testing. Integration of techno-economic assessment and uncertainty propagation will be essential to evaluate cost, sensitivity, and reliability of net-removal estimates under realistic boundary conditions. Such work would also identify the key economic and

operational drivers that influence the scalability and competitiveness of DACU technologies in construction supply chains.

From a broader perspective, future progress depends on collaboration between materials scientists, process engineers, and policy stakeholders to align technical innovation with regulatory and market frameworks. Standardised protocols for measuring CO_2 uptake, verifying storage permanence, and evaluating material performance will be critical for ensuring reproducibility and industrial adoption. Establishing certification schemes and integrating carbonated materials into construction codes will further accelerate deployment. By advancing towards a unified, data-driven framework that connects material innovation, system modelling, and policy implementation, future research can strengthen the scientific and practical foundations for DACU-enabled carbonation as a credible component of global carbon-removal strategies.

Appendix A

A.1 Tables

Designated concrete has two strength classes: CB and RC. CB is a designation for a series of designated cement-bound concretes used for foundations, pavements, hard standings, and reinstatement of openings in highways. RC is a designation for a series of designated concretes that are used in reinforced and prestressed concrete applications. The applications of a range of concrete classes are shown in **Table A-1.**

Table A-1 Typical reinforced concrete applications for designated concrete (British Standards Institution, n.d.)

Concrete designation	Use
RC20/25	Reinforced and prestressed concrete inside the enclosed building except in poorly ventilated rooms with high humidity
RC25/30	Wearing surface: light foot and trolley traffic
RC28/35	fully nominally reinforced, either ground bearing, suspended, or over sub-floor voids
RC30/37	External reinforced and prestressed vertical elements of buildings sheltered from or exposed to, rain
RC32/40	Wearing surface: general industrial
RC35/45	Wearing surface: general industrial
RC40/50	Wearing surface: heavy industrial

Table A-2 gives the target cement content to expect where concrete has been specified in terms of nominal proportions batched by volume. Where nominal proportions are by mass, the cement contents are significantly greater than the values

given in **Table A-2**. The other parameters of concrete manufacture follow **Table A-3** and **Table A-4**. (British Standards Institution, n.d.)

Table A-2 Target cement or combination contents for nominal proportions (British Standards Institution, n.d.)

Nominal proportions (Cement: Fine aggregate: Coarse aggregate)	Target cement or combination content (kg/m^3)
1:1:2	480
1:1:3	350
1:2:4	275
1:2:5	225
1:3:6	190
1:4:8	150
4:1 all in	330
5:1 all in	290
6:1 all in	250
7:1 all in	220
8:1 all in	195
9:1 all in	175
10:1 all in	160
12:1 all in	135
14:1 all in	120
15:1 all in	115
18:1 all in	95
20:1 all in	85

Table A-3 Summary of requirements for designated concretes

Concrete designation	Min. strength class	Characteristic compressive cub strength at 28 days that may be assumed for structural design (MPa)	Default slump class	Max. w/c ratio	Min. cement or combination content (kg/m^3) for 20 mm max.aggregate size
RC20/25	C20/25	25	S3	0.70	240
RC25/30	C25/30	30	S3	0.65	260
RC28/35	C28/35	35	S3	0.60	280
RC30/37	C30/37	37	S3	0.55	300
RC32/40	C32/40	40	S3	0.55	300
RC35/45	C35/45	45	S3	0.50	320
RC40/50	C40/50	50	S3	0.45	340

Table A-4 Mix proportions by weight

Standardised prescribed mix	Consistence class (slump in mm)	Cement (kg)	Fine aggregate (kg)	Coarse aggregate (kg)
ST1	S1 (10-40)	230	770	1155
ST2	S2 (50-90)	265	760	1135
ST2	S3 (100-150)	285	735	1105
ST2	S4 (160-210)	300	815	990
ST3	S2 (50-90)	295	745	1120
ST4	S2 (50-90)	300	735	1100
ST5	S2 (50-90)	375	720	1080

Table A-5 Chemical composition of different materials components

		SiO_2	CaO	Al_2O_3	MgO	Na_2O	K_2O	TiO_2	Fe_2O_3	MnO	P_2O_5	Cr_2O_3	V_2O_5	LOI/SO_3/Other
Cement products (OPC)		18.4-24.50	58.10-68	3.10-7.56	0.02-1.67	0-0.78	0.04-1.66		0.16-5.78					0-5.35
Natural aggregate	river sand	93.6-96.0	0.5-1.1	1.7-2.5	0.1-0.2	0.2-0.5	0.7-0.9	0.1-0.2	0.5-0.9					0-0.08
	gravel	97.03	0.26	0.34	0.65	0.16	0.01	0.01	0.10	0.00	0.02			1.41
SCM (RCA)	fine	58.6-75.8	17.1-27.5	4.1-5.8	0.9-2.1	0.4-0.6	1.1-1.5	0.3-0.5	1.7-3.3					0.93-1.62
	coarse	63.61-65.37	11.19-16.86	3.57-5.49	1.91-2.84	0.87-1.19	0.51-0.62	0.17-0.39	2.03-2.40	0.05-0.06	0.10-0.49			7.56-9.19
SCM (steel slag)	BFs	35-38	30-42	10-18	5-14									
	BOFs	8.45-16.93	40.82-54.29	0.33-5.85	1.93-9.15	0.27-0.84		0.16-1.57	16.78-29.49	1.2-8.7	0.89-7.14	0.14-0.33	0.42-0.53	1.14-2.01
	EAFs	12.2-20.3	25.08-45.9	1.55-12.2	2.82-7.68	0.62-0.63		0.37-1.06	22.3-38.51	1.3-5.87	0.5-1.37	0.8-2.0		0.31-3.48
SCM (fly ash)	Class F ash	43.6-64.4	0.7-6.7	19.6-30.1	0.9-1.7	0-2.8			3.8-23.9					0.4-7.2
	Class C ash	23.1-50.5	11.5-29.0	13.3-21.3	1.5-7.5	0.4-1.9			3.7-22.5					0.3-1.9

Table A-6 Elemental composition of timber & biomaterials

		Carbon	Oxygen	Hydrogen	Nitrogen	Sulphur	Ash
Timber		49-51	43-44	6-7	0.1-0.3		0.2-0.6
Other biomaterials	Biochar	59.24-82.77	13.96-37.25	2.12-2.90	1.08-1.73		
	Bio-based plastics	37.14-59.53	26.43-43.17	3.25-5.12	0.03-0.04	0.02-0.48	
	Bio-based asphalt bitumen	30.52-77.01	12.14-62.01	7.07-10.39	0.29-0.30	0.11-0.16	

Table A-7 Theoretical CO_2 uptake capacity of construction materials (CaO-based and C-based)

Material	Theoretical CO_2 uptake value (kg/kg material)	Midpoint (kg/kg material)
Cement products (OPC)	0.39–0.55	0.47
Recycled concrete aggregate (RCA, fine)	0.134–0.216	0.175
Recycled concrete aggregate (RCA, coarse)	0.088–0.132	0.110
Steel slag (BFs)	0.236–0.330	0.283
Steel slag (BOFs)	0.320–0.426	0.373
Steel slag (EAFs)	0.197–0.361	0.279
Fly ash (Class F)	0.0055–0.0526	0.029
Fly ash (Class C)	0.090–0.228	0.159
Timber	1.798–1.871	1.835
Biochar	2.174–3.037	2.606
Bio-based plastics	1.361–2.186	1.773
Bio-based asphalt bitumen	1.120–2.826	1.973

Table A-8 Theoretical annual CO_2 uptake potential by material

Material	Min (Mt CO_2/yr)	Max (Mt CO_2/yr)	Mid (Mt CO_2/yr)
Cement (OPC)	1638	2310	1974
RCA	47.52	116.64	76.95
Blast furnace slag (BFS)	77.88	128.7	101.88
Steel slag (BOFS)	42.56	86.48	62.66
Steel slag (EAFS)	11.23	31.41	20.09
Fly ash (Class F)	1.287	12.308	6.798
Fly ash (Class C)	14.04	35.57	24.8
Timber	3596	3742	3669
Biochar	0.761	1.063	0.912
Bioplastics	2.722	4.372	3.547

A.2 Data Resource

The dataset is available at: https://github.com/MayChenly/CO2-Curing-of-Cement-Data-Analysis-and-Regression-Modelling

Table A-9 The literature studies cited in Chapter 3

Study	Reference	Study	Reference
R1	(T. Chen & Gao, 2019)	R19	(Shi & Wu, 2008b)
R2	(Qin et al., 2019)	R20	(D. Wang et al., 2019)
R3	(X. Li & Ling, 2020)	R21	(B. J. Zhan et al., 2019)
R4	(D. Zhang & Shao, 2016a)	R22	(S. Zhang et al., 2021)
R5	(D. Zhang & Shao, 2016b)	R23	(Xian et al., 2021)
R6	(D. Zhang et al., 2020)	R24	(Hameed et al., 2020)
R7	(Rostami et al., 2011)	R25	(Z. Li et al., 2019)
R8	(El-Hassan & Shao, 2014)	R26	(Kang et al., 2019)
R9	(Zakir Morshed & Shao, 2013)	R27	(Seo et al., 2018)
R10	(El-Hassan & Shao, 2015)	R28	(Z. Li et al., 2018)
R11	(Shao & Morshed, 2015)	R29	(Moon & Choi, 2018)
R12	(El-Hassan et al., n.d.)	R30	(He et al., 2017)
R13	(Rostami et al., 2012)	R31	(Librandi et al., 2017)
R14	(El-Hassan et al., 2013)	R32	(T. Wang et al., 2017)
R15	(Rostami et al., 2012)	R33	(Sharma et al., 2023)
R16	(T. Liu, 2016)	R34	(L. Liu et al., 2023)
R17	(D. Zhang et al., 2016)	R35	(Bae et al., 2022)
R18	(Tang et al., 2021)		

A.3 References

Bae, J.-H., Kim, S., Amr, I. T., Seo, J., Jang, D., Bamagain, R., Fadhel, B. A., Abu-Aisheh, E., & Lee, H. K. (2022). Evaluation of physicochemical properties and environmental impact of environmentally amicable Portland cement/metakaolin bricks exposed to humid or CO2 curing condition. *Journal of Building Engineering*, *47*, 103831. https://doi.org/10.1016/j.jobe.2021.103831

British Standards Institution. (n.d.). *Concrete. Complementary British Standard to BS EN 206. Part 1, Method of specifying and guidance for the specifier.*

Chen, T., & Gao, X. (2019). Effect of carbonation curing regime on strength and microstructure of Portland cement paste. *Journal of CO2 Utilization*, *34*, 74–86. https://doi.org/10.1016/j.jcou.2019.05.034

El-Hassan, H., & Shao, Y. (2014). Dynamic carbonation curing of fresh lightweight concrete. *Magazine of Concrete Research*, *66*(14), 708–718. https://doi.org/10.1680/macr.13.00222

El-Hassan, H., & Shao, Y. (2015). Early carbonation curing of concrete masonry units with Portland limestone cement. *Cement and Concrete Composites*, *62*, 168–177. https://doi.org/10.1016/j.cemconcomp.2015.07.004

El-Hassan, H., Shao, Y., & Ghouleh, Z. (2013). Reaction Products in Carbonation-Cured Lightweight Concrete. *Journal of Materials in Civil Engineering*, *25*(6), 799–809. https://doi.org/10.1061/(asce)mt.1943-5533.0000638

Hameed, R., Seo, J., Park, S., Amr, I. T., & Lee, H. K. (2020). Co2 uptake and physicochemical properties of carbonation-cured ternary blend portland cement–metakaolin–limestone pastes. *Materials*, *13*(20), 1–14. https://doi.org/10.3390/ma13204656

He, Z., Li, Z., & Shao, Y. (2017). Effect of Carbonation Mixing on CO2 Uptake and Strength Gain in Concrete. *Journal of Materials in Civil Engineering*, *29*(10). https://doi.org/10.1061/(asce)mt.1943-5533.0002031

Kang, S. H., Kwon, Y. H., & Moon, J. (2019). Quantitative analysis of CO2 uptake and mechanical properties of air lime-based materials. *Energies*, *12*(15). https://doi.org/10.3390/en12152903

Li, X., & Ling, T. C. (2020). Instant CO2 curing for dry-mix pressed cement pastes: Consideration of CO2 concentrations coupled with further water curing. *Journal of CO2 Utilization*, *38*, 348–354. https://doi.org/10.1016/j.jcou.2020.02.012

Li, Z., He, Z., & Chen, X. (2019). The performance of carbonation-cured concrete. *Materials*, *12*(22). https://doi.org/10.3390/ma12223729

Li, Z., He, Z., & Shao, Y. (2018). Early age carbonation heat and products of tricalcium silicate paste subject to carbon dioxide curing. *Materials*, *11*(5). https://doi.org/10.3390/ma11050730

Librandi, P., Costa, G., Souza, A. C. B. de, Stendardo, S., Luna, A. S., & Baciocchi, R. (2017). Carbonation of Steel Slag: Testing of the Wet Route in a Pilot-scale Reactor. *Energy Procedia*, *114*, 5381–5392. https://doi.org/10.1016/j.egypro.2017.03.1674

Liu, L., Liu, Y., Su, B., Liu, C., & Chen, X. (2023). Assessing CO2 uptake of CO2-cured cement mortar through theoretical modeling and experimental validation. *Construction and Building Materials*, *383*, 131393. https://doi.org/10.1016/j.conbuildmat.2023.131393

Liu, T. (2016). *Effect of early carbonation curing on concrete resistance to weathering carbonation*.

Moon, E. J., & Choi, Y. C. (2018). Development of carbon-capture binder using stainless steel argon oxygen decarburization slag activated by carbonation. *Journal of Cleaner Production*, *180*, 642–654. https://doi.org/10.1016/j.jclepro.2018.01.189

Qin, L., Gao, X., & Chen, T. (2019). Influence of mineral admixtures on carbonation curing of cement paste. *Construction and Building Materials*, *212*, 653–662.

https://doi.org/10.1016/j.conbuildmat.2019.04.033

Rostami, V., Shao, Y., & Boyd, A. J. (2011). Durability of concrete pipes subjected to combined steam and carbonation curing. *Construction and Building Materials*, *25*(8), 3345–3355. https://doi.org/10.1016/j.conbuildmat.2011.03.025

Rostami, V., Shao, Y., & Boyd, A. J. (2012). Carbonation Curing versus Steam Curing for Precast Concrete Production. *Journal of Materials in Civil Engineering*, *24*(9), 1221–1229. https://doi.org/10.1061/(asce)mt.1943-5533.0000462

Seo, J. H., Amr, I. T., Park, S. M., Bamagain, R. A., Fadhel, B. A., Kim, G. M., Hunaidy, A. S., & Lee, H. K. (2018). CO2 uptake of carbonation-cured cement blended with ground volcanic ash. *Materials*, *11*(11). https://doi.org/10.3390/ma11112187

Shao, Y., & Morshed, A. Z. (2015). Early carbonation for hollow-core concrete slab curing and carbon dioxide recycling. *Materials and Structures/Materiaux et Constructions*, *48*(1–2), 307–319. https://doi.org/10.1617/s11527-013-0185-3

Sharma, R., Kim, H., Lee, N. K., Park, J.-J., & Jang, J. G. (2023). Microstructural characteristics and CO2 uptake of calcium sulfoaluminate cement by carbonation curing at different water-to-cement ratios. *Cement and Concrete Research*, *163*, 107012. https://doi.org/10.1016/j.cemconres.2022.107012

Shi, C., & Wu, Y. (2008). Studies on some factors affecting CO2 curing of lightweight concrete products. *Resources, Conservation and Recycling*, *52*(8–9), 1087–1092. https://doi.org/10.1016/j.resconrec.2008.05.002

Tang, W., Zhan, B., Wu, C., & Kou, S. cong. (2021). Experimental investigation and mathematical modelling of the carbon dioxide sequestration of cement pastes during pressurized CO2 curing. *Construction and Building Materials*, *302*. https://doi.org/10.1016/j.conbuildmat.2021.124383

Wang, D., Noguchi, T., & Nozaki, T. (2019). Increasing efficiency of carbon dioxide sequestration through high temperature carbonation of cement-based materials. *Journal of Cleaner Production*, *238*.

https://doi.org/10.1016/j.jclepro.2019.117980

Wang, T., Huang, H., Hu, X., Fang, M., Luo, Z., & Guo, R. (2017). Accelerated mineral carbonation curing of cement paste for CO2 sequestration and enhanced properties of blended calcium silicate. *Chemical Engineering Journal*, *323*, 320–329. https://doi.org/10.1016/j.cej.2017.03.157

Xian, X., Zhang, D., & Shao, Y. (2021). Flue gas carbonation curing of cement paste and concrete at ambient pressure. *Journal of Cleaner Production*, *313*. https://doi.org/10.1016/j.jclepro.2021.127943

Zakir Morshed, A., & Shao, Y. (2013). Influence of moisture content on co2uptake in lightweight concrete subject to early carbonation. *Journal of Sustainable Cement-Based Materials*, *2*(2), 144–160. https://doi.org/10.1080/21650373.2013.797373

Zhan, B. J., Xuan, D. X., Poon, C. S., & Shi, C. J. (2019). Mechanism for rapid hardening of cement pastes under coupled CO2-water curing regime. *Cement and Concrete Composites*, *97*, 78–88. https://doi.org/10.1016/j.cemconcomp.2018.12.021

Zhang, D., Asce, S. M., Cai, ; Xinhua, & Shao, Y. (2016). *Carbonation Curing of Precast Fly Ash Concrete*. https://doi.org/10.1061/(ASCE)MT.1943

Zhang, D., Cai, X., & Jaworska, B. (2020). Effect of pre-carbonation hydration on long-term hydration of carbonation-cured cement-based materials. *Construction and Building Materials*, *231*. https://doi.org/10.1016/j.conbuildmat.2019.117122

Zhang, D., & Shao, Y. (2016). Early age carbonation curing for precast reinforced concretes. *Construction and Building Materials*, *113*, 134–143. https://doi.org/10.1016/j.conbuildmat.2016.03.048

Zhang, S., Ghouleh, Z., Liu, J., & Shao, Y. (2021). Converting ladle slag into high-strength cementing material by flue gas carbonation at different temperatures. *Resources, Conservation and Recycling*, *174*. https://doi.org/10.1016/j.resconrec.2021.105819

Appendix B

B.1 Tables

Table B-1 Variables and parameters

Variable	Unit	Parameter value	Definition
$C_{CO_2}(j)$	kg/m^3		CO_2 concentration in the compartment j gas phase
$R(j)$	kg/s		carbonation rate, i.e. the rate at which CO_2 is removed from the gas phase and transferred to the RCA particles
$Q_{in}(j)$	m^3/s		velocity of the gas entering the compartment
$C_{CO_{2_{in}}}(j)$	kg/m^3		CO_2 concentration of the gas entering compartment j
$Q_{out}(j)$	m^3/s		velocity of the gas leaving the compartment
$V(j)$	m^3		gas phase volume of the compartment
G_t	mol/ m^3		CO_2 mole in chamber
M_{CO_2}	kg/mol	44*10^{-3}	molar moss of CO_2
$Cu(j)$	kg		total CO_2 update by time t
a_{max}	kg/m^3		maximum CO_2 update per unit volume of RCA
F_d			fraction of recycled concrete aggregates that are carbonated
t	s		time
$m_{RCA}(j)$	kg		mass of RCA in compartment j
ρ_{RCA}	kg/m^3		RCA density
a_{th}	kg/m^3		theoretical maximum CO_2 uptake
w		0.3 (Sereng et al., 2021)	adjustment factor to the theoretical maximum CO_2 update
β	% of CaO carbonated		CaO content in cement
C_e	kg/ m^3 RCA		cement content in the concrete

M_{CaO}	kg CaO/ kg cement		
M_r		0.7857	molar mass ratio of CO_2 to CaO
f_{CaO}		0.95 (Bediako & Amankwah, 2015)	ratio of the mass molar of CaO in C_2S, C_3S and C_3A to the mass molar of CaO in clinker
α_H			hydration degree and can be estimated as a function of water to cement ratio in cement
w/c			water to cement ratio
a	m		minimum diameter of RCA particles in given size distribution
b	m		maximum diameter of RCA particles in given size distribution
D	m		diameter of RCA particles, it's in range of a and b.
D_0	m		carbonated diameter of an RCA particle
d_0	m		thickness of the carbonated layer of an RCA particle
C_{CO_2}	kg/m^3		CO_2 concentration in the gas phase
D_{CO_2}	m^2/s		CO_2 diffusion coefficient
B	$m/s^{1/2}$	0.12 (Papadakis et al., 1991)	constant
ε_p			cement paste porosity
RH	%		relative humidity during RCA carbonation
K		0.39 (Fagerlund, 2006b)	coefficient of capillary porosity
E_c	kWh/kg		crashing electricity demand
W_i	kWh/kg	2.69×10^{-3} (Cui & Sheikh, 2010)	working index for recycled concrete aggregates
D_p	m		average of the upper and lower limits of the RCA particles

d_m	m	0.05-0.5 (Soni et al., 2022)	waste concrete pieces particle during the demolition stage
E_f	J		energy consumption of the fan for the carbonation time duration
t_c	s		carbonation time duration
P_{in}	Pa		inlet pressure of the fan
Q_{in}	m^3/s		inlet gas flowrate of the fan
φ		0.8075 (Sivakumaran et al., 2014)	the efficiency coefficient
γ		1.28 (Xing et al., 2022)	heat capacity ratio
P_{out}	Pa		out pressure of the fan
f_p			packed bed friction factor
Δp	Pa		pressure drop in carbonation chamber to be overcome by the fan
L_c	m	10	length of chamber
ρ_{gas}	kg/m^3	1.1691	liquid density
v_s	m/s		gas flow velocity
ϵ_b		0.4	bed porosity
Gr_p			the modified Reynolds number
R_e			the original Reynolds number
μ	Pa·s	18.37×10^{-6} (Sivakumaran et al., 2014)	the dynamic viscosity of the fluid

Table B-2 RCA types and characteristics

RCA type	w/c ratio	Cement content (kg/m^3)	CaO mass (%)	Density (kg/m^3)	Concrete designation
RCA1	0.70	240	65	2250	RC 20/25
RCA2	0.65	260	65	2300	RC 25/30
RCA3	0.60	280	65	2350	RC 28/35
RCA4	0.55	300	65	2400	RC 32/40
RCA5	0.50	320	65	2450	RC 35/45
RCA6	0.45	340	65	2500	RC 40/50

Based on the Concrete – Complementary British Standard to BS EN 206, Part 1: Method of specifying and guidance for the specifier and Part 2: Specification for constituent materials and concrete.

Table B-3 The derivation of the expressions

$$\frac{d\,F_d}{dD_0} = \begin{cases} -C_1 \times C_2 & a \geq D_0 \\ -C_1 \times C_2 & a < D_0 < b \\ 0 & b \leq D_0 \end{cases}$$

<table>
<tr><td rowspan="2">$a \geq D_0$</td><td>$F_d = 100\% - \dfrac{\int_a^b \frac{\pi}{6}(D-D_0)^3 dD}{\int_a^b \frac{\pi}{6} D^3 dD} \times 100\%$</td><td colspan="2">$F_d = 100\% - \dfrac{(b-D_0)^4 - (a-D_0)^4}{(b^4-a^4)} \times 100\%$</td></tr>
<tr><td>$\boldsymbol{\frac{d\,F_d}{dD_0} = -C_1 \times C_2}$</td><td>$C_1 = \dfrac{1}{(b^4-a^4)}$</td><td>$C_2 = -4(b-D_0)^3 + 4(a - D_0)^3$</td></tr>
<tr><td rowspan="2">$a < D_0 < b$</td><td>$F_d = 100\% - \dfrac{\int_{D_0}^b \frac{\pi}{6}(D-D_0)^3 dD}{\int_a^b \frac{\pi}{6} D^3 dD} \times 100\%$</td><td colspan="2">$F_d = 100\% - \dfrac{(b-D_0)^4}{(b^4-a^4)} \times 100\%$</td></tr>
<tr><td>$\boldsymbol{\frac{d\,F_d}{dD_0} = -C_1 \times C_2}$</td><td>$C_1 = \dfrac{1}{(b^4-a^4)}$</td><td>$C_2 = -4(b-D_0)^3$</td></tr>
<tr><td rowspan="2">$b \leq D_0$</td><td>$F_d = 100\%$</td><td colspan="2">$F_d = 1$</td></tr>
<tr><td>$\boldsymbol{\frac{d\,F_d}{dD_0} = 0}$</td><td></td><td></td></tr>
<tr><td colspan="4">$C_3 = -2C_0 \times C_1 \times C_2$</td></tr>
</table>

Table B-4 Calculation details for each step of the system

Step	Method	Reference
DAC Option1 (Elc_{opt1})	Raw data in reference: ◆ CO_2 produced at 150 bars: 1.3 tonne; ◆ CO_2 removed from air: 1 tonne; ◆ Electricity consumption including compression: 366 kWh per tonne of CO_2 removal from air; ◆ Compression electricity: 22 MWh for 171 tonnes of CO_2 produced; ◆ Natural gas consumption: 5.25 GJ per tonne of CO_2 removal from air; CO_2 emissions are only through electricity consumption, as natural gas derived emissions are captured by their system. To produce 1 tonne of pure CO_2 at 1 bar, electricity consumption is: (366*3.6*10^-3/1.3) – (22*3.6/171) = 0.55038 GJ (or 152.884 kWh). Out of 1 tonne of CO_2 produced, the amount of CO_2 removed from air is 1/1.3 = 0.7692 tonne.	(Keith et al., 2018)
DAC Option2 (Elc_{opt2})	Raw data in reference: ◆ CO_2 produced at 1 bar: 1 tonne; ◆ CO_2 removed from air: 1 tonne; ◆ Electricity supply for the heat pump system: 4.7 MJ per kg CO_2 ◆ Other electricity supply: 0.7 kWh per kg CO_2 To produce 1 tonne of pure CO_2 at 1 bar, (total) electricity consumption is: (0.7*3.6+4.7= 7.22 GJ (or 2005.6 kWh)	(Deutz & Bardow, 2021b)
Transportation	Diesel trucks: Carbon emission (kg CO_2) = Total_weight * return_distance * emission factor. Total_weight (tonne) = 2* Tare_weight + CO_2_weight Tare weight = 0.4212 tonne CO_2 weight = 1 tonne return_distance (km) is determined from 0 to 2000 km. The emission factor = 0.112 kg CO_2 per tonne per km ((Ravikumar et al., 2021)SI.page4).	

	Electric trucks: The linear relation between the consumption of the electric truck (E) and its total weight (W) is (Rizet et al., 2016): E(kWh/km) =0.43 + 0.033 x W (tonne) One-way: CO_2_weight (1 tonne) + tare_weight (0.4212 tonne) = 1.4212 kg Return: tare_weight =0.4212 kg So the electric truck energy consumption vaule is = (0.43+0.033*1.4212) + (0.43+0.033*0.4212) = 0.921 kWh/km Total CO2 emissions = energy consumption per km * one-way distance *emission factor, where emission factor follows data in Table S5.	
Vaporisation	Atmospheric ASCO CO_2 Vaporiser; energy consumption: 5.4 kWh per tonne of CO_2 https://www.ascoco2.com/fileadmin/PDF_Download/PDF_Produkte/PDF_CO2_und_Trockeneis_Zubehoer/Ergaenzendes_CO2_Zubehoer/en/ASCO_Atmospheric_CO2_Vaporisers.pdf	
Liquefaction	CO_2 liquefaction; 89 kWh per tonne of CO_2	(Kemp & Sola Kasim, 2010)

Table B-5 Carbon intensities of grid electricity

Entity	Carbon intensity of electricity - gCO_2/kWh
China	582
US	369
France	56

Source: Carbon intensity of electricity generation data (2023 version)

https://ourworldindata.org/grapher/carbon-intensity-electricity

Table B-6 Estimation of energy consumption of low-purity DAC

Step	Method	Reference
Elc_{th-low} & $Elc_{th-pure}$	Assuming 100% recovery of CO_2: $$E = RT\left[\ln\left(\frac{X_{CO2}^{feed}}{X_{CO2}^{air}}\right)n_{CO2}^{feed} + \ln\left(\frac{X_{inert}^{feed}}{X_{inert}^{air}}\right)n_{inert}^{feed} + \ln\left(\frac{1}{X_{inert}^{air}}\right)n_{inert}^{reject}\right]$$ where, X_{CO2}^{feed} is the mole fraction of CO_2 of the feed to carbonation chamber; X_{CO2}^{air} is mole fraction of CO_2 of the air; X_{inert}^{feed} is mole fraction of other gas in the feed to carbonation chamber; X_{inert}^{air} is mole fraction of other gas in the air; n_{inert}^{feed} is the mole number of other gas in the feed to carbonation chamber; n_{CO2}^{feed} is the mole number of CO_2 in the feed to carbonation chamber;n_{inert}^{reject} is the mole number of gas rejected by DAC.	(Xing et al., 2022)
To calculate the theoretical work for producing 1 tonne of CO_2 at a purity of 10% (as an example): Elc_{th-low}	X_{CO2}^{feed}=10% X_{CO2}^{air}=410e-6 n_{CO2}^{feed}=1e+06/44.01 = 2.27e+04 mole X_{inert}^{feed}=1-10%=90% X_{inert}^{air}=1-410e-6 n_{inert}^{feed}=$n_{CO2}^{feed} * \frac{X_{inert}^{feed}}{X_{inert}^{feed}}$ = 1*90%/10% =2.04e+05 mole $n_{inert}^{air} = n_{CO2}^{feed} * \frac{X_{inert}^{air}}{X_{CO2}^{air}}$ = 1*(1-410e-6)/(410e-6) = 5.54e+07 mole n_{inert}^{reject}=$n_{inert}^{air} - n_{inert}^{feed}$ =5.52e+07 mole	

	Elc_{th-low} = 3.13e+08 J	
$Elc_{th-pure}$ (per tonne CO_2)	4.96 e+08 J (derived from the above equation with X_{CO2}^{feed}=100%)	
Elc_{opt2} (per tonne CO_2)	7.22 e+09 J	See Table S4
Elc_{low} (10%) (per tonne CO_2)	3.13 e+08 / 4.96 e+08 *7.22 e+09 = 4.55 e+09 J	

Table B-7 Experimental conditions for data used for comparing with carbonation modelling results

Defination	The mass molar of CaO in C2S, C3S and C3A	RCA density	The CaO content in cement	Water to cement ratio in cement	The minimum diameters of RCA particles	The maximum diameters of RCA particles	RCA carbonation time	CO_2 concentration during RCA carbonation	Relative humidity during RCA carbonation	Cement content in the concrete of strength class i.	theoretical maximum CO_2 uptake	Experimental Total carbon uptake by the carbonation of a certain amount of RCA
unit	/	kg/m^3	/	/	cm	cm	hour	bar	%	kg	kg/kg RCA	kg/kg RCA
Test1	0.95	2461	0.6639	0.49	0.1	0.4	24	0.15	80	353	0.0230	0.0218
Test2	0.95	2461	0.6639	0.49	1.2	2	24	0.15	80	353	0.0230	0.0096
Test3	0.893	2456	0.6538	0.32	0.1	0.4	24	0.15	80	461	0.0180	0.0114
Test4	0.893	2456	0.6538	0.32	1.2	2	24	0.15	80	461	0.0180	0.0065

Table B-8 Supplementary LCA results

Scenario	CO_2 stored (kg)	DAC process(kg)	liquefaction (kg)	vaporisation (kg)	Crushing (kg)	Fan (kg)	CO_2 escape (kg)	CO_2 removal from air	transportation (kg)	Net CO_2 removal (kg)
1	15.24	1.46	0.85	0.05	0.28	0.00	1.18	12.63	3.39	5.41
2	15.24	0.93	0.54	0.03	0.18	0.00	1.18	12.63	3.39	6.38
3	15.24	0.14	0.08	0.00	0.03	0.00	1.18	12.63	3.39	7.81
4	15.24	1.46	0.85	0.05	0.28	0.00	1.18	12.63	8.70	0.11
5	15.24	0.93	0.54	0.03	0.18	0.00	1.18	12.63	5.58	4.19
6	15.24	0.14	0.08	0.00	0.03	0.00	1.18	12.63	0.85	10.35
7	15.24	19.17	0.85	0.05	0.28	0.00	1.18	16.42	3.39	-8.50
8	15.24	12.15	0.54	0.03	0.18	0.00	1.18	16.42	3.39	-1.05
9	15.24	1.84	0.08	0.00	0.03	0.00	1.18	16.42	3.39	9.89
10	15.24	19.17	0.85	0.05	0.28	0.00	1.18	16.42	8.80	-13.92
11	15.24	12.15	0.54	0.03	0.18	0.00	1.18	16.42	5.58	-3.25
12	15.24	1.84	0.08	0.00	0.03	0.00	1.18	16.42	0.85	12.43

B.2 References

Bediako, M., & Amankwah, E. O. (2015). Analysis of Chemical Composition of Portland Cement in Ghana: A Key to Understand the Behavior of Cement. *Advances in Materials Science and Engineering*, *2015*, 1–5. https://doi.org/10.1155/2015/349401

Cui, C., & Sheikh, S. A. (2010). Experimental Study of Normal-and High-Strength Concrete Confined with Fiber-Reinforced Polymers. *Journal of Composites for Construction*, *14*(5), 553–561. https://doi.org/10.1061/(ASCE)CC.1943-5614.0000116

Deutz, S., & Bardow, A. (2021). Life-cycle assessment of an industrial direct air capture process based on temperature–vacuum swing adsorption. *Nature Energy*, *6*(2), 203–213. https://doi.org/10.1038/s41560-020-00771-9

Fagerlund, G. (2006). Porosity and specific surface of Portland cement paste : an analysis of experimental work performed by Åke Grudemo during the years 1973-1979. *Lund University*.

Keith, D. W., Holmes, G., St. Angelo, D., & Heidel, K. (2018). A Process for Capturing CO2 from the Atmosphere. *Joule*, *2*(8), 1573–1594. https://doi.org/10.1016/j.joule.2018.05.006

Kemp, A. G., & Sola Kasim, A. (2010). A futuristic least-cost optimisation model of CO2 transportation and storage in the UK/UK Continental Shelf. *Energy Policy*, *38*(7), 3652–3667. https://doi.org/10.1016/j.enpol.2010.02.042

Papadakis, V. G., Vayenas', C. G., & Fardis, M. N. (1991). EXPERIMENTAL INVESTIGATION AND MATHEMATICAL MODELING OF THE CONCRETE CARBONATION PROBLEM. In *Chemicd Engineering Science* (Vol. 46, Issue 516).

Ravikumar, D., Zhang, D., Keoleian, G., Miller, S., Sick, V., & Li, V. (2021). Carbon dioxide utilization in concrete curing or mixing might not produce a net climate

benefit. *Nature Communications*, *12*(1), 855. https://doi.org/10.1038/s41467-021-21148-w

Rizet, C., Cruz, C., & Vromant, M. (2016). The Constraints of Vehicle Range and Congestion for the Use of Electric Vehicles for Urban Freight in France. *Transportation Research Procedia*, *12*, 500–507. https://doi.org/10.1016/j.trpro.2016.02.005

Sereng, M., Djerbi, A., Metalssi, O. O., Dangla, P., & Torrenti, J.-M. (2021). Improvement of Recycled Aggregates Properties by Means of CO2 Uptake. *Applied Sciences*, *11*(14), 6571. https://doi.org/10.3390/app11146571

Sivakumaran, K. S., Korol, R. M., & Fan, X. (2014). Energy absorption potential of concrete floors containing secondary (shrinkage and temperature) reinforcements. *Frontiers of Structural and Civil Engineering*, *8*(3), 282–291. https://doi.org/10.1007/s11709-014-0269-3

Soni, A., Das, P. K., Hashmi, A. W., Yusuf, M., Kamyab, H., & Chelliapan, S. (2022). Challenges and opportunities of utilizing municipal solid waste as alternative building materials for sustainable development goals: A review. *Sustainable Chemistry and Pharmacy*, *27*, 100706. https://doi.org/10.1016/j.scp.2022.100706

Xing, L., Pullin, H., Bullock, L., Renforth, P., Darton, R. C., & Yang, A. (2022). Potential of enhanced weathering of calcite in packed bubble columns with seawater for carbon dioxide removal. *Chemical Engineering Journal*, *431*, 134096. https://doi.org/10.1016/j.cej.2021.134096

Appendix C

C.1 Tables

Table C-1 Country emission factor data

Country	Carbon intensity of electricity (gCO_2/kWh)	Country	Carbon intensity of electricity (gCO_2/kWh)
Austria	102.6229	Slovenia	227.6471
Belgium	117.5764	Spain	146.1536
Bulgaria	264.2069	Sweden	35.82383
Croatia	174.4792	Türkiye	469.697
Czechia	413.8592	United Kingdom	210.8911
Finland	72.2488	Russia	449.1959
France	44.17909	Canada	174.8143
Germany	344.1399	Mexico	484.8317
Greece	319.7624	United States	383.5492
Hungary	182.8182	Argentina	358.9482
Italy	287.5335	Brazil	103.2123
Luxembourg	134.6154	Chile	265.5165
Netherlands	253.3115	Egypt	571.9383
Poland	614.9824	South Africa	708.8762
Portugal	112.2868	Iran	641.9362
Romania	245.5543	China	559.5517
Slovakia	96.48824	India	708.3216
Japan	482.3242	Australia	551.5898
South Korea	414.2726		

Table C-2 Steel slag amount by countries

Country	BOF_min_Million tonnes	BOF_max_Million tonnes	EAF_min_Million tonnes	EAF_max_Million tonnes	BF_min_Million	BF_max_Million	BOF_average_Million tonnes	EAF_average_Million tonnes	BF_average_Million tonnes
Austria	0.6825	1.02375	0.0675	0.10125	1.375	1.65	0.853125	0.084375	1.5125
Belgium	0.4851	0.72765	0.2149	0.32235	0.9	1.08	0.606375	0.268625	0.99
Bulgaria	0	0	0.05	0.075	0	0	0	0.0625	0
Croatia	0	0	0.02	0.03	0	0	0	0.025	0
Czechia	0.41323	0.619845	0.01677	0.025155	0.675	0.81	0.5165375	0.0209625	0.7425
Finland	0.19775	0.296625	0.15225	0.228375	0.55	0.66	0.2471875	0.1903125	0.605
France	0.81554	1.22331	0.39446	0.59169	1.55	1.86	1.019425	0.493075	1.705
Germany	2.58336	3.87504	1.09664	1.64496	5.9	7.08	3.2292	1.3708	6.49
Greece	0	0	0.15	0.225	0	0	0	0.1875	0
Hungary	0.06201	0.093015	0.02799	0.041985	0.05	0.06	0.0775125	0.0349875	0.055
Italy	0.3456	0.5184	1.8144	2.7216	0.775	0.93	0.432	2.268	0.8525
Luxembourg	0	0	0.19	0.285	0	0	0	0.2375	0
Netherlands	0.38247	0.573705	0.22753	0.341295	1.025	1.23	0.4780875	0.2844125	1.1275
Poland	0.34484	0.51726	0.39516	0.59274	0.675	0.81	0.43105	0.49395	0.7425
Portugal	0	0	0.19	0.285	0	0	0	0.2375	0
Romania	0.16302	0.24453	0.09698	0.14547	0.15	0.18	0.203775	0.121225	0.165
Slovakia	0	0	0.08229	0.123435	0	0	0	0.1028625	0
Slovenia	0	0	0.06	0.09	0	0	0	0.075	0
Spain	0.368	0.552	0.782	1.173	0.75	0.9	0.46	0.9775	0.825

Sweden	0.28688	0.43032	0.15312	0.22968	0.725	0.87	0.3586	0.1914	0.7975
Türkiye	1.00035	1.500525	2.50965	3.764475	2.175	2.61	1.2504375	3.1370625	2.3925
United Kingdom	0.4854	0.7281	0.1146	0.1719	1.125	1.35	0.60675	0.14325	1.2375
Russia	4.6475	6.97125	2.36665	3.549975	13.65	16.38	5.809375	2.9583125	15.015
Canada	0.65219	0.978285	0.55781	0.836715	1.45	1.74	0.8152375	0.6972625	1.595
Mexico	0.26426	0.39639	1.54574	2.31861	0.25	0.3	0.330325	1.932175	0.275
United States	2.4955	3.74325	5.5545	8.33175	5.15	6.18	3.119375	6.943125	5.665
Argentina	0.22746	0.34119	0.28254	0.42381	0.5	0.6	0.284325	0.353175	0.55
Brazil	2.56091	3.841365	0.81158	1.21737	6.425	7.71	3.2011375	1.014475	7.0675
Chile	0.07308	0.10962	0.04692	0.07038	0.15	0.18	0.09135	0.05865	0.165
Egypt	0	0	0.65954	0.98931	0	0	0	0.824425	0
South Africa	0.2904	0.4356	0.1496	0.2244	0.725	0.87	0.363	0.187	0.7975
Iran	0.25092	0.37638	2.80908	4.21362	0.875	1.05	0.31365	3.51135	0.9625
China	93.37076	140.05614	10.50924	15.76386	220.8	264.96	116.71345	13.13655	242.88
India	5.73874	8.60811	6.79126	10.18689	21.575	25.89	7.173425	8.489075	23.7325
Japan	6.53836	9.80754	2.38164	3.57246	15.75	18.9	8.17295	2.97705	17.325
South Korea	4.5073	6.76095	2.0727	3.10905	11.3	13.56	5.634125	2.590875	12.43
Australia	0.41895	0.628425	0.15105	0.226575	0.875	1.05	0.5236875	0.1888125	0.9625

Table C-3 Variables and Parameters

Symbol	Unit	Definition	Value
$C_{CO_2}(j)$	kg·m^{-3}	CO_2 concentration in the gas phase	
$C_{CO_{2in}}(j)$	kg·m^{-3}	CO_2 concentration of the gas entering compartment j	
$Q_{in}(j)$	m^3·s^{-1}	velocity of the gas entering the compartment	
$Q_{out}(j)$	m^3·s^{-1}	velocity of the gas leaving the compartment	
$V(j)$	m^3	gas phase volume of the compartment	
$R(j)$	kg·s^{-1}	carbonation rate	
t	s	time	
G_t	mol·m^{-3}	CO_2 mole in chamber	
M_{CO_2}	kg·mol^{-1}	molar moss of CO_2	
a_{max}	kg·(kg·tonne)$^{-1}$	maximum CO_2 uptake per unit kilogram of steel slag	
$Cu\ (j)$	kg	total CO_2 uptake by time	
$m_{steel\ slag}(j)$	kg	mass of steel slag in compartment j	
$\rho_{steel\ slag}$	kg·m^{-3}	steel slag density	
$\frac{dX}{dt}$	s^{-1}	percentage conversion rate of CaO	
X	/	fractional CaO conversion	
t_{Diff}	s	reaction time in diffusion process	
t_{ch}	s	reaction time in chemistry control process	
ρ_{CaO}	mol·m^{-3}	molar density of CaO in steel slag particles	
d_p	m	particle diameter	
D_o	m^2·s^{-1}	overall diffusivity	
C_{CO_2}	mol·m^{-3}	CO_2 concentration within the particle	
$C_{CO_2,e}$	mol·m^{-3}	equilibrium concentration of gas CO	
T	K	chamber temperature	
k_s	m·s^{-1}	chemical reaction rate constant	
ε	/	particle porosity	0.1205

τ	/	tortuosity	13.47
D_k	$m^2 \cdot s^{-1}$	Knudsen diffusivity	
D_{CO_2}	$m^2 \cdot s^{-1}$	CO_2 gas diffusivity	
r_p	m	particle pore radius	2×10^{-9} (initial value)
v_i	$cm^3 \cdot mol^{-1}$	diffusion volume of components i	26.9 (CO_2)
v_j	$cm^3 \cdot mol^{-1}$	diffusion volume of components j	20.1 (air)
M_i	$g \cdot mol^{-1}$	molar mass of meteorological components i	44.01 (CO_2)
M_j	$g \cdot mol^{-1}$	molar mass of meteorological components j	28.97 (air)
E_k	$J \cdot mol^{-1}$	activation energ	$10^{-1.8254}$
k_{s0}	$m \cdot s^{-1}$	pre-exponential factor	$10^{4.0309}$
R	$J \cdot (mol \cdot K)^{-1}$	universal gas constant	8.314
E_c	$kWh \cdot tonne^{-1}$	specific energy consumption	
W_i	$kWh \cdot tonne^{-1}$	Bond Work Index	13.5
D_{sm}	µm	steel slag initial particle diameter	
D_{sp}	µm	steel slag final particle diameter	
E_f	J	energy consumption of the fan for the carbonation time duration	
t_c	s	carbonation time	
Q_{in}	$m^3 \cdot s^{-1}$	inlet gas flowrate of the fan	
P_{in}	Pa	inlet pressure of the fan	
P_{out}	Pa	outlet pressure of the fan	
γ	/	heat capacity ratio	
φ	/	efficiency coefficient	
Δp	Pa	pressure drop in carbonation chamber to be overcome by the fan	
f_p	/	packed bed friction factor	
R_e	/	original Reynolds number	
Gr_p	/	modified Reynolds number	
ρ_{gas}	$kg \cdot m^{-3}$	density of the fluid	
v_s	$m \cdot s^{-1}$	gas flow velocity	
μ	Pa·s	dynamic viscosity of the fluid	
ϵ_b	/	bed porosity	
S_{Ca}	m^2	reactive mineral surface area	
V_l	$mol \cdot L^{-1}$	leachate volume	

M_{Ca}	g·mol^{-1}	atomic wight of Ca	
$\{H^+\}$	mol·L^{-1}	activity of H^+ in the aqueous solution	
k_{Ca}	g·(m^2·min)$^{-1}$·(L·mol^{-1})	rate constant	
k_{SCa}	L·mol^{-1}	surface stability constant	
$S_{Ca}(t_0)$	/	initial surface area corresponding to calcium-rich phases	
X_{Ca}	/	conversion corresponding to calcium-rich phases	
$m_{i,slag}$	g	initial slag mass used in the model	10000
$\emptyset$	/	saturation index	
r_{prec}	mol·m^{-2}·h^{-1}	precipitation rate	
K_{CaCO_3}	/	equilibrium constant of $CaCO_3$	
A	m^2·L^{-1}	total surface area of seeds	
r_{cap}	mol·L^{-1}·h^{-1}	rate of CO_2 capture	
r_A	m^2·L^{-1}·h^{-1}	rate of change in the total surface area	
M_{CaCO_3}	g·mol^{-1}	molar mass of $CaCO_3$	
ρ_{CaCO_3}	g·m^{-3}	average density of $CaCO_3$	
P_0	W	power input under ungassed conditions	
P_G	W	power consumption under gassed conditions	
Q_G	m³·s^{-1}	volumetric gas flow rate	
V_L	m³	liquid volume	2 (prepetition reactor)
D	m	impeller diameter	0.5 (dissolution reactor); 0.6 (prepetition reactor)
D_i	m	width of the impeller blade	0.12 (prepetition reactor)
g	m·s^{-2}	gravitational acceleration	9.81
ρ_L	kg·m^{-3}	density of the liquid	1049 (dissolution reactor);

			1050 (prepetition reactor)
N_p	/	power number	
Re_L	/	Reynolds number	
Fr_L	/	Froude number	
μ_L	Pa·s	liquid viscosity	1.05 $\times 10^{-3}$ (dissolution reactor); 1.2 $\times$ 10^{-3} (prepetition reactor)
N	rps	impeller rotational speed	2 (dissolution reactor); 1.5 (prepetition reactor)
ΔP_c	Pa	pressure difference required to push the gas through the liquid column	
h_L	m	Liquid column height	1
$V_{cell,practical}$	V	practical total cell voltage	
ΔQ_{total}	C	total charge requirement	
φ_{BPMED}	/	BPMED efficiency	0.8
$\Delta[H^+]$	mol·L^{-1}	H^+concentration	0.1
V_a	L	volume of acidic compartment	1
F	C·mol^{-1}	Faraday constant	9.6485$\times 10^4$
$pH_{basified}$	/	pH of the solution in the basified compartment	
$pH_{acidified}$	/	pH of the solution in the acidified compartment	
$V_{BPM\ loss}$	V	voltage loss across the BPM	
V_{CEMs}	V	voltage loss across the CEMs	
$V_{oceanwater}$	V	voltage loss across the oceanwater	
$V_{electrolyte}$	V	voltage loss across the electrolyte compartment	
$V_{electorde}$	V	voltage loss at the two electrodes	
i	A·cm^{-2}	current density	0.0766
n_{BPM}	/	number of BPM	1
R_{bpm}	Ω·cm^{-2}	BPM resistance	5.2
n_{CPM}	Ω·cm^{-2}	number of CEM	2
R_{acem}	Ω·cm^{-2}	CEM/AEM resistance	0.13

L_a	cm	thickness of anode	0.1
L_c	cm	thickness of cathode	0.075
k_{acidic}	$S \cdot cm^{-1}$	conductivity of seawater in the acidic compartment	0.07735
k_{basic}	$S \cdot cm^{-1}$	conductivity of seawater after degassing in the basic compartment	0.07742
$i_{0,anode}$	$A \cdot cm^{-2}$	exchange current density for anode	10^{-5}
$i_{0,cathode}$	$A \cdot cm^{-2}$	exchange current density for cathode	10^{-3}